Structure and Reactivity of Mono- and Diiron Synthetic Models of Nonheme Iron-containing Enzymes

A DISSERTATION
SUBMITTED TO THE FACULTY OF
UNIVERSITY OF MINNESOTA
BY

Saikat Banerjee

IN PARTIAL FULFILLMENT OF THE REQUIREMENTS
FOR THE DEGREE OF
DOCTOR OF PHILOSOPHY

Professor Lawrence Que, Jr., Adviser

August 2020

Acknowledgments

Firstly, I want to thank my advisor Lawrence Que, Jr. for accepting me as a graduate student in his lab and making state-of-the-art resources available to do research. This has helped me to test my ideas and has contributed to my development as an independent scientist. I appreciate his patience with the pace of my development, which was stunted at the beginning, but I hope I have repaid his patience with results during the last year of my graduate school. I am grateful for the humble personality that surely sets him apart from his peers. This strongly helped me voice my concerns, both scientific and non-scientific, which he never took personally. This taught me to always have an open mind and receptive to new ideas no matter how successful I become. I also must thank the National Science Foundation and the National Institute of Health for funding my research in Que lab.

I have to thank Letitia Yao, who played an important role in helping me understand the realities of variable temperature studies on highly reactive compounds. Without her help, I would not have been able to publish my work on mononuclear high-valent systems. I thank Waqas Rasheed for his continued support and hard work as a collaborator on the same project. I thank Dr. Oloo for his guidance in the initial stages of this project. I want to thank Andrew Jasniewski for many insightful discussions about diiron enzymes and model complexes, which shaped my interests and helped me discover a novel diiron system of my own. For the diiron project, I am grateful to Apparao Draksharapu for his guidance and hard work to obtain beautiful spectroscopic data that made my story stand out even more. I thank Patrick Crossland for his continued support and hard work as a collaborator on the same project. I am grateful to Ruixi Fan and Yisong Guo from CMU for continued support with Mössbauer spectroscopy that played key roles in developing my projects. I also had the pleasure to work with Marcel Swart on theoretical investigations and I thank him for being an excellent collaborator.

Recent updates from him on my diiron results have a bright future. A special thanks to Mayank Puri for being so helpful to me during his time in Que group and beyond. I also thank all the Que group members, past and present that have contributed to my development as a research scholar.

Lastly, I am grateful to my wife, Amanda for her unconditional love and support. Her presence in the last year of my graduate school made a huge difference. I am thankful to her for her feedback on my grammar and sentence construction throughout my thesis, which improved my thesis. I am very lucky to have her in my life.

Dedication

This thesis is dedicated to my family – Dolu, Ma, Khokon, and Amanda – who always stayed on my side in exchange for nothing.

Abstract

Metalloenzymes are utilized to perform different physiological functions in biology. Nonheme iron-containing enzymes are one such class of metalloenzymes that can catalyze a wide array of reactions at ambient temperature and pressure. Several mononuclear nonheme iron enzymes carry out a range of oxidative transformations via a common oxoiron(IV) oxidant with high-spin iron(IV) centers. Within the past two decades, many small-molecule analogs of these highly reactive species have been synthesized, and under favorable circumstances, some have even been crystallized. These models shed light on the structural and functional properties of the Fe^{IV}=O unit in biological systems. Dinuclear nonheme iron enzymes such as soluble methane monooxygenase (**sMMO**) activate oxygen to carry out challenging transformations like hydroxylation of strong C-H bonds in methane. The enzymatic cycle of **sMMO** involves the formation of a peroxodiiron(III) intermediate (**P**) that gives rise to a diiron(IV) complex (**Q**), which is the species responsible for methane hydroxylation. Synthetic models for **Q** are rare, and none of these are formed by mimicking the conversion of **P** to **Q.** This thesis describes work on synthetic models that will enhance our understanding of enzymes and contribute to future catalyst design.

In Chapter 2, reaction optimization studies along with an array of spectroscopy studies have been utilized to elucidate the solution-state structure of a highly reactive oxoiron(IV) complex $[Fe^{IV}(O)(Me_3NTB)]^{2+}$ (Me_3NTB=tris[(1-methyl-benzimidazol-2-yl)methyl]amine). This chapter presents evidence that the spin-state of the iron(IV) center is not the sole determinant in governing reactivity of oxoiron(IV) complexes as previously proposed in the literature. Our results emphasize the need to identify factors besides the ground spin state of the Fe^{IV}=O center to rationalize nonheme oxoiron(IV) reactivity.

In Chapter 3, a diiron cluster supported by Me_3NTB ligand is used to carry out oxygen activation. This generates an unstable μ-1,2-peroxo species, which is characterized using various spectroscopic techniques. The structural analyses of

this complex highlight the unique properties of this model. Even more interesting is the observation that this peroxodiiron(III) complex undergoes O–O bond cleavage upon treatment with strong Lewis acids and transforms into a bis(μ-oxo)diiron(IV) complex, thus providing a synthetic precedent for an analogous reaction in the diiron enzyme **sMMO**.

In Chapter 4, oxygen activation chemistry is further explored using a quinoline rich framework to generate diiron intermediates with high-spin configurations. In this work, we have used the tripodal ligand TQA (TQA = tris(2-quinolylmethyl)amine) to support a diferrous center that upon exposure to O_2 leads to the isolation of a bis(μ-oxo)diferric complex. This is the first crystal structure of such a complex that is formed by oxygen activation. The formation of a $[Fe_2(\mu\text{-}O)_2]^{2+}$ complex through oxygen activation also provides indirect evidence that the oxygen activation in our model passes through a similar mechanism like the diiron enzymes. Interesting solvent dependence is also reported for the oxygen activation process with this system.

In Chapter 5, key results in the preceding chapters are summarized and future directions evaluated.

Table of Contents

Abbreviations

α-KG - α-ketoglutarate

TauD - Taurine dioxygenase

PheH - Phenylalanine hydroxylase

CarC - Carbapenem synthase

sMMO - Soluble methane monooxygenase

RNR - Ribonucleotide reductase

EXAFS - Extended X-ray Absorption Spectroscopy

DFT - Density Functional Theory

D - Zero field splitting parameter

k_2 - second order rate constant

KIE - Kinetic Isotope Effect

NRVS - Nuclear Resonance Vibrational Spectroscopy

MCD - Magnetic Circular Dichroism

NIH - National Institutes of Health

PhIO - Iodosylbenzene

DHA - Dihydroanthracene

Me_3NTB - tris((1-methyl-1*H*-benzo[*d*]imidazol-2-yl)methyl)amine

Me_3NTB* - tris((1,5,6 -trimethyl-1*H*-benzo[*d*]imidazol-2-yl)methyl)amine

TMC - 1,4,8,11-tetramethyl-1,4,8,11-tetraazacyclotetradecane

TPA - tris(2-pyridylmethyl)amine

TPA* - tris(4-methoxy-3,5-dimethyl-2-pyridylmethyl)amine

TQA - tris(2-quinolylmethyl)amine

ArIO - 2-(*t*BuSO_2)-C_6H_4IO

NMR - Nuclear Magnetic Resonance

XAS - X-ray Absorption Spectroscopy

HERFD XAS - High Energy Resolution Fluorescence Detected X-ray Absorption

6Me_3TPA - tris(6-methyl-2-pyridylmethyl)amine

6Me_2BPP - bis(6-methyl-2-pyridylmethyl)-3-aminopropionate

BnBQA - *N*-benzyl-*N*-bis(2-quinolinylmethyl)amine

BQPA - 2-pyridylmethyl)bis(2-quinolylmethyl)amine)

BPPE - 1,2-bis[2-(bis(2-pyridyl)methyl)-6-pyridyl]ethane)

6-HPA - 1,2-bis[2-{bis(2-pyridylmethyl)aminomethyl}-6-pyridyl]ethane

N-Et-HPTB - tetrakis(2-benzimidazolylmethyl)-2-hydroxy-1,3-diaminopropane

XRD - X-ray diffraction

ORTEP - Oak Ridge Thermal Ellipsoid Plot Program

TPA* - tris(3,5-dimethyl-4-methoxypyridin-2-ylmethyl)amine

CAN - ceric ammonium nitrate

*m*CPBA - *meta*-chloroperbenzoic acid

TFE - 2,2,2-trifluoroethanol

BDE - bond dissociation energy

TBP - trigonal bipyramidal

COSY - homonuclear correlation spectroscopy

TMC - 1,4,8,11-tetramethyl-1,4,8,11-tetraazacyclotetradecane

TSR - Two-State Reactivity

HAT - hydrogen atom transfer

OAT - oxygen atom transfer

GOF - goodness of fit

hDOHH - human deoxyhypusine hydroxylase

DBU - 1,8-diazabicyclo[5.4.0]undec-7-ene

XANES - X-ray Absorption Near-Edge Structures

CHD - 1,4-cyclohexadiene

MLCT - metal-to-ligand charge transfer

LMCT - ligand-to-metal charge transfer

FWHM - full peak width at half-maxima

FTIR - Fourier Transformed Infrared Spectroscopy

ESI-MS - Electrospray Ionization Mass Spectrometry

List of Figures

List of Tables

Chapter 1:
Nonheme Mono- and Diiron Enzymes and Related Synthetic Model Systems

1.1 Iron in Nature

Iron is one of the abundant elements and the most abundant transition metal in Nature. It is present in many biological systems and involved in important transformations in living organisms. In iron-dependent metalloproteins, it plays roles that include dioxygen delivery and storage in hemoglobin and hemerythrin, electron transfer in iron-sulfur proteins, and redox catalysis in oxygenases, oxidases, hydrogenase, and nitrogenase.[1–4] There are heme-based proteins that contain an iron-protoporphyrin and play key roles as oxygen carriers and activators. There are also unwanted reactive oxygen species (ROS) and reactive nitrogen species (RNS) that are produced in the presence of iron and lead to serious diseases.[5] Lastly, there are nonheme enzymes that incorporate nonheme ligands to bind the iron center and carry out oxygen activation. This thesis focuses specifically on the sub-category of these nonheme iron enzymes that contains one (mono-) or two (di-) iron centers in their active sites to activate oxygen and carry out important and versatile transformations in biology. In this chapter, the focus is on well-studied nonheme mono- and diiron enzymes and key intermediates involved in their catalytic cycles including high-valent oxoiron(IV) complexes that act as potent oxidants to carry out various transformations. We will elaborate on the unique structural features of the active sites found in these enzymes, the mechanism by which they activate dioxygen, characterization of key intermediates, including high-valent oxidants, and how they functionalize substrates. More importantly, progress on synthetic models of the intermediates found in these enzymes will be discussed.

1.2. Monoiron Enzymes and Synthetic Models

1.2.1. Nonheme Monoiron Enzymes

Nonheme monoiron enzymes utilize oxygen to carry out diverse reactions (Figure 1.1) such as selective hydroxylation and halogenation of unactivated substrate C–H bonds, N-demethylation, epoxidation, desaturation, and oxidative cyclization.[6–8] These play key roles in major functions such as biosynthesis of natural products including antibiotics and collagen, oxygen sensing and protection against hypoxia, alkylated DNA repair, and transcription regulation by histone demethylation.[9] A major subset of these enzymes uses an α-ketoglutarate (**α-KG**) moiety as a reducing co-substrate to supply two electrons for the oxidation. For ligands, these enzymes generally have two histidines as N-donors and a carboxylate as an O-donor to the iron center. These motifs are part of the coordination sphere in these enzymes, which is named 2-His-1-carboxylate “facial triad”. This ligand arrangement can be described with these motifs occupying one face of an octahedron and the other three sites are occupied by water molecules that are replaced later. Activation of oxygen by **α-KG** enzymes has been shown to generate a high-valent oxoiron(IV) species, which carries out the oxidative functions of these enzymes.[9] These oxoiron(IV) species have been spectroscopically characterized in several enzymes such as taurine dioxygenase (**TauD**),[10–12] the halogenases **CytC3**[13] and **SyrB2**[14], phenylalanine hydroxylase (**PheH**)[15], carbapenem synthase (**CarC**)[16] and others (Figure 1.2).[17,18] Mössbauer spectroscopy has been used to determine that the iron centers in these enzymatic oxoiron(IV) species have four unpaired d-electrons giving it an $S = 2$ spin state with isomer shifts (δ) in the range of 0.22 – 0.30 mms^{-1}.[13–18] Weak-field ligands such as histidines and carboxylates in these enzymes are responsible for enforcing an $S = 2$ spin state among these high-valent complexes. In 2003, **TauD** became the first nonheme

enzyme where the oxoiron(IV) species was trapped and characterized.[10] This intermediate named **TauD-*J*** was generated rapidly with rates of 130 mM^{-1} s^{-1} at 278 K and showed an absorption feature around 318 nm. Mössbauer spectroscopy revealed the iron(IV) center in this intermediate to be high-spin (δ = 0.31 mm/s, ΔE_Q = -0.88 mm/s)[10] and an axial S = 2 ground state with a zero-field splitting parameter D of 10.5 cm^{-1} was determined.[10,19] Resonance Raman and Extended X-ray Absorption Spectroscopy (EXAFS) have also been used to confirm the presence of an iron(IV)-oxo bond in **TauD-*J***.[11,12] An 821 cm^{-1} vibration observed through resonance Raman spectroscopy was assigned to an Fe=O stretching frequency[12] that downshifts by 34 cm^{-1} upon ^{18}O labeling. EXAFS results revealed a short 1.62 Å distance that was assigned to the Fe=O bond in **TauD-*J***.[11] Furthermore, density functional theory (DFT) calculations have been used to predict that **TauD-*J*** has either a trigonal bipyramidal or an octahedral environment around the iron center.[20]

The oxygen activation at the active site in the **α-KG**-dependent enzymes like **TauD** is shown in Figure 1.2 below.[8,21] The **α-KG** first binds to the iron(II) center of the resting state of the enzyme as a bidentate ligand, displacing water molecules bound to the iron center. As taurine comes into the vicinity of the active site, another water molecule leaves, thus making way for the binding of oxygen from the air. This results in the coordinative saturation of the iron center, and its oxidation to form an iron(III)-superoxide intermediate. Next, this species is proposed to act as a nucleophile and attack the carbonyl moiety of the **α-KG** ligand to form an iron(IV)-alkylperoxo intermediate. O–O bond cleavage follows this step along with the elimination of CO_2 to generate a high-valent oxoiron(IV) species. This is the active oxidant that performs the hydroxylation of the C–H bond in taurine through hydrogen atom abstraction followed by a radical rebound

to produce the final hydroxylation product. The iron center is brought back to the +2 state for the catalytic cycle to start another round. After monitoring the disappearance of **TauD-*J*** through UV-vis spectroscopy in the presence of taurine, the breaking of the C–H bond was confirmed to be carried out by this high valent intermediate. This also follows from similar experiments with perdeuterated taurine, where the C–H bonds in taurine have been replaced with C–D bonds, and observing a significantly slower rate with kinetic isotope effect (KIE) of ~50.[22,23] This deuterium modification has also been instrumental in obtaining detailed characterization for **TauD-*J*** as it was pivotal in increasing the stability of this fleeting intermediate. The high KIE observed in taurine hydroxylation reaction was also confirmed by carrying out similar experiments in the prolyl-4-hydroxylase enzyme.[17] In this case, a value of ~60 was obtained that confirms the hydrogen abstraction from the proline residue. More interestingly, the oxoiron(IV) complex in prolyl-4-hydroxylase has similar spectroscopic properties as **TauD-*J***, with Mössbauer parameters that are consistent with $S = 2$ iron(IV) centers ($\delta = 0.30$ mm/s, $\Delta E_Q = -0.82$ mm/s) and a zero-field parameter D of 15.5 cm^{-1}.[17] The existence of high-valent oxoiron(IV) intermediates in these distantly related enzymes and similar KIE values suggest that they carry out hydroxylation through a common mechanism.

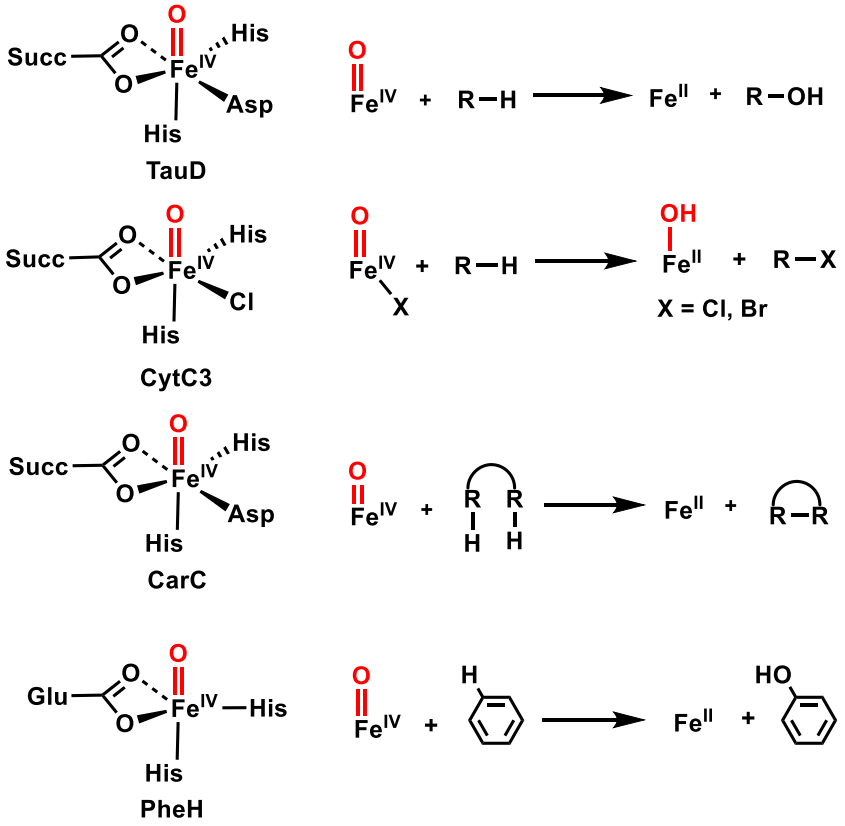

Figure 1.1. Premier functions of the nonheme iron-dependent enzymes that are carried out by high-valent oxoiron(IV) species.[7–9]

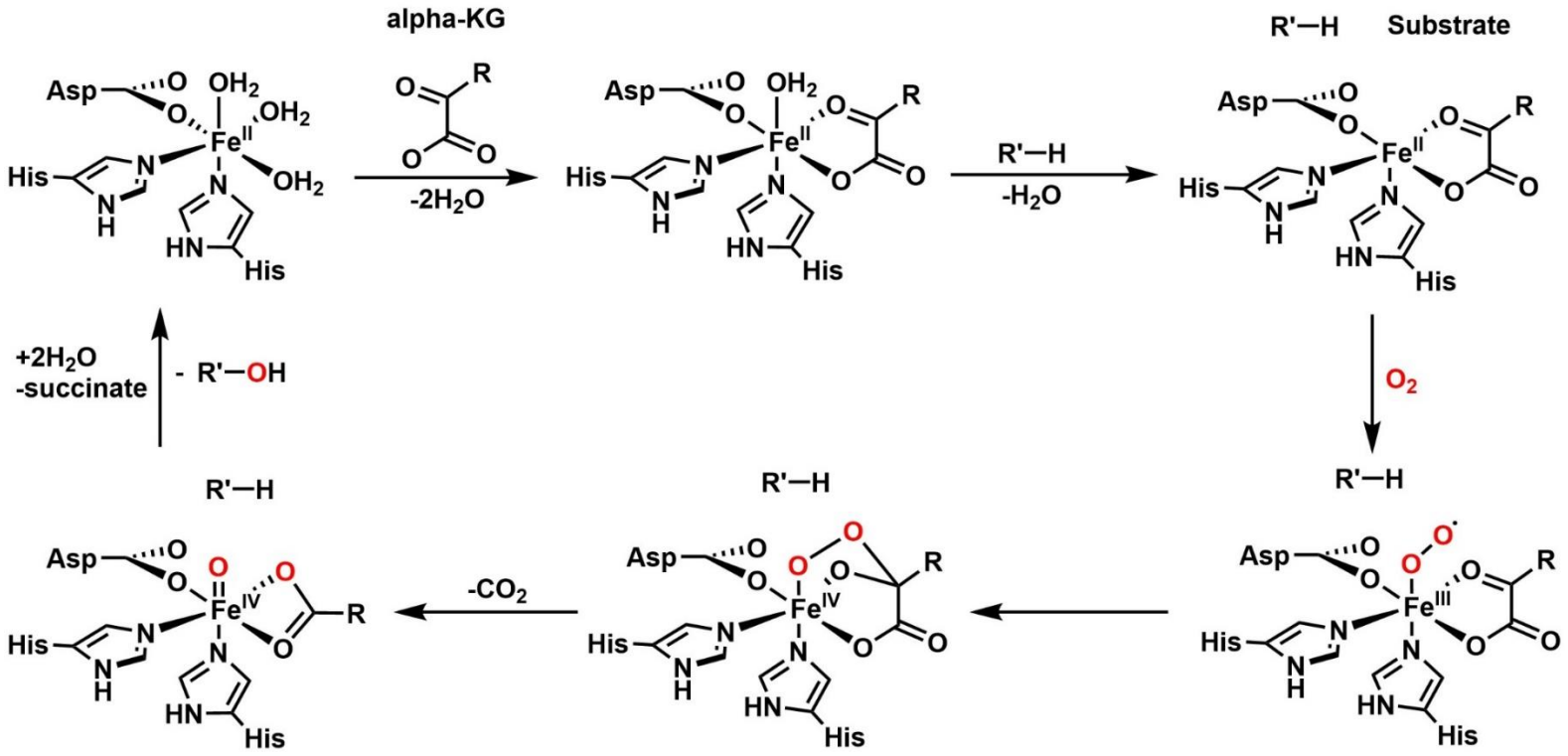

Figure 1.2. Mechanism of oxygen activation in **α-KG** dependent enzymes.

R = $-CH_2CH_2COO^-$ and R' is the rest of the substrate chain that varies in these enzymes

Another well-studied group of **α-KG** dependent enzymes are the halogenases, where the aspartate ligand in the generic active site is replaced by an alanine residue to open up a binding site for the halide anion. This is a different ligand arrangement from what was discussed in related enzymes like **TauD**.[10] Several halogenating enzymes have been explored to varying degrees in recent years[24–28] with carbon-halogen bonds ubiquitous in industrial chemicals.[29,30] **SyrB2** and **CytC3** are the enzymes that will be discussed here as representatives. **SyrB2** was the first enzyme to be reported where the coordination of the ligands to the iron center was established[24] and later reaffirmed by **CytC3**[25] and others.[26–28] **SyrB2** and **CytC3** are involved in the biosynthesis of natural product syringomycin E and cytotrienin, respectively. The involvement of these enzymes in such important syntheses has motivated biochemists to learn more about them. It has been shown through various spectroscopies[9,14,31–33] that high-valent oxoiron(IV) intermediates are involved in the halogenating enzymes like in hydroxylating enzymes such as **TauD.** Mössbauer spectroscopy has shown the iron(IV) center to be $S = 2$ in these cases but an important distinction from **TauD** is the existence of two different iron(IV) sites ($\delta \sim 0.23$ mm/s, $\delta \sim 0.30$ mm/s) in both **CytC3** and **SyrB2** enzymes.[8] Computations suggest that the two Mössbauer doublets originate from positional isomers of X–Fe═O unit with oxo and halide anions exchanging their positions in the calculated isomers.[34] Nuclear resonance vibrational spectroscopic (NRVS) studies[32] and magnetic circular dichroism (MCD) studies[33] have shown the high-valent oxoiron(IV) species has a trigonal bipyramidal geometry with the oxo as the axial and halide as the equatorial ligand. EXAFS studies revealed short Fe═O distances of 1.6 – 1.7 Å and longer distances of 2.3 – 2.4 Å that were assigned to Fe-halide interactions.[14,31] The deuteration of the substrate in the catalytic cycle of **SyrB2** retarded the decay of the high-valent Cl–

Fe(IV)=O and produced a significant kinetic isotope effect of ~20.[14] This is reminiscent of the high KIE (~50) observed for C–H bond cleavage in the **TauD** enzyme[22] and suggests that hydrogen bond abstraction is the rate-determining step in halogenases as well. This results in the formation of a substrate radical that combines with the halide moiety to produce halogenated products.[8]

Carbepenem synthase (**CarC)** enzyme is another α-KG-dependent iron enzyme that needs mentioning here for its unique epimerization and desaturation reactions.[8] A *S* = 2 oxoiron(IV) center (δ = 0.28 mm/s, ΔE_Q = -0.87 mm/s) has been characterized as the active oxidant for **CarC** like the other enzymes discussed so far.[16] The epimerization mechanism has been studied and shown to involve a C–H bond cleavage reaction. The following desaturation step has not been confirmed mechanistically but one can visualize desaturation as a derivative of hydroxylation mechanism. The initial hydrogen atom abstraction would happen similarly as described for enzymes like **TauD**. Next, instead of a hydroxyl radical rebound to the incipient alkyl free radical observed in hydroxylases, a second hydrogen atom is abstracted adjacent to the initial abstraction position. This will generate a C═C double bond in the product. This will need to be verified by experiments and related isotope labeling studies in the future.

Another versatile subset of nonheme iron-dependent enzymes employs tetrahydrobiopterin as the source of two electrons (instead of α-ketoglutarate in α-KG dependent enzymes) and performs aromatic hydroxylations in crucial amino acid side chains. Three major enzymes fall into this category. They are phenylalanine, tryptophan, and tyrosine hydroxylase, all of them carry out hydroxylations of the corresponding amino acids. Phenylalanine hydroxylase (**PheH**) enzyme is crucial to

mammalian liver functioning and, if found to be deficient, can lead to diseases like phenylketonuria. Tryptophan and tyrosine hydroxylases are vital to the production of neurotransmitters such as dopamine, norepinephrine, epinephrine, and serotonin.[8,9] This class of enzymes has been studied in detail and the crystal structure of the **PheH** active site shows the presence of a 2-His-1-carboxylate facial triad around the iron center.[35] Activation of oxygen by this enzyme produces a generic high-valent oxoiron(IV) species, although the pathway leading to this intermediate is yet to be clarified. The steps before the formation of the high-valent intermediate[8] remain unclear and will need further experiments to be determined. Nonetheless, the oxoiron(IV) intermediate has been characterized and found to have an S = 2 iron(IV) center by Mössbauer spectroscopy (δ = 0.28 mm/s, $|\Delta E_Q|$ = 1.26 mm/s),[15] which is reminiscent of similar parameters found in other hydroxylases.[8] The oxidative attack of the high-valent intermediate, however, happens differently from what was discussed for hydroxylases and halogenases. In the **PheH** enzyme, the oxoiron(IV) complex carries out aromatic electrophilic substitution and not a homolytic C–H bond cleavage as observed in hydroxylases and halogenases. This mechanistic picture is supported by an inverse KIE effect with the deuterated substrate instead of a high positive KIE as observed in hydroxylases and halogenases. Also, an NIH shift or a 1,2–hydride shift in the mechanism reveals the presence of a positively charged intermediate, which is common in classical aromatic electrophilic substitution reactions.[8] Interestingly, a high positive KIE of ~10 is observed if non-native aliphatic substrates are used instead of aromatic side chains,[36] which suggests that hydrogen atom abstraction is the rate-determining step in the absence of aromatic side chains. This is reminiscent of similar oxidation mechanisms of hydroxylases and

halogenases and is a reminder of the versatility of the roles oxoiron(IV) species play in nonheme enzymes.

1.2.2. Nonheme Monoiron Synthetic Models

The characterization of these high-valent intermediates in the enzymes has facilitated a golden age for synthetic model complexes. As discussed earlier, nonheme iron-dependent enzymes carry out diverse functionalizations using generic oxoiron(IV) complexes. Several limitations such as inability to change reaction conditions and short lifetimes of the enzymatic intermediates prevent biochemists from studying these high-valent species in detail. Studying synthetic models of the enzymes is an attractive way to shed light on the catalytic cycle of the enzymes. Synthetic models will allow us to modify the reaction conditions and extend the lifetimes of the studied intermediates to enhance the breadth of possible studies. In this context, 2003 was a golden year when the enzymatic **TauD-*J*** intermediate was characterized[10] and the first crystallized synthetic oxoiron(IV) complex ($[(TMC)Fe^{IV}(O)]^{2+}$, where TMC = 1,4,8,11-tetramethyl-1,4,8,11-tetraazacyclotetradecane) was reported.[37] The high-valent complex was prepared by the reaction of the corresponding iron(II) precursor and iodosylbenzene (PhIO), which was used as an oxo-transfer agent. This complex had a light-green color and its UV-vis spectrum showed a unique near-IR feature at 824 nm (ε = 400 M^{-1} cm^{-1}). Unlike **TauD**, TMC contains primarily N-donor ligands with four tertiary amines forming the macrocycle supporting the iron(IV) center. The sixth ligand was shown to be the solvent (MeCN) in which the oxoiron(IV) was generated (Figure 1.3). Despite these differences in ligands and visible spectra, $[(TMC)Fe^{IV}(O)]^{2+}$ matches the enzymes well in terms of having a short Fe═O bond (1.646 Å) and an 834 cm^{-1} Fe═O stretching vibration, which is very close to what is observed for **TauD-*J*** intermediate.[38] Besides, X-ray

diffraction studies on $[(TMC)Fe^{IV}(O)]^{2+}$ showed the Fe=O bond length to be 1.646 Å which is comparable to 1.62 Å distance found in **TauD-*J*** intermediate. However, the two high-valent species have different ground spin-states for the iron(IV) centers. While **TauD-*J*** exhibits an *S* = 2 iron(IV) center as determined by Mössbauer spectroscopy, iron(IV) center in $[(TMC)Fe^{IV}(O)]^{2+}$ has an *S* = 1 spin state, possibly due to the presence of stronger field tertiary amines as ligands in the latter case. More importantly, while **TauD** enzyme can oxidize taurine, which has theoretically calculated C–H bond strength of over 100 kcal mol^{-1},[39] $[(TMC)Fe^{IV}(O)]^{2+}$ can only oxidize weak C–H bonds in dihydroanthracene (DHA) with a bond strength of 78 kcal mol^{-1}.

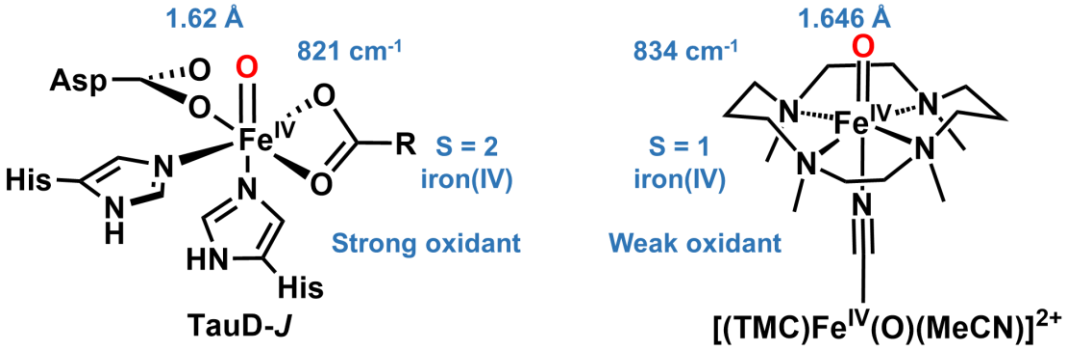

Figure 1.3. Comparison of the first characterized biological and synthetic nonheme oxoiron(IV) intermediates and their related properties at a glance.

The discovery of $[(TMC)Fe^{IV}(O)]^{2+}$ opened the gates to the exploration of different ligand frameworks to support iron(IV) centers. The near-IR feature of $[(TMC)Fe^{IV}(O)]^{2+}$ became a benchmark for the identification of similar model complexes. The most important report after $[(TMC)Fe^{IV}(O)]^{2+}$ came in the later part of 2003 when a tetradentate ligand (TPA) comprising a mixture of tertiary amine and pyridines was used to support an iron(IV) center along with a labile site *cis* to the oxo moiety.[40] The labile site was assumed to be occupied by the solvent (MeCN). This high-valent complex

was found to be pale green with an absorption feature at 724 nm (ε = 400 M^{-1} cm^{-1}). Mössbauer spectroscopy confirmed the presence of an *S* = 1 iron(IV) center like in $[(TMC)Fe^{IV}(O)]^{2+}$ while EXAFS measurements found a short 1.67 Å, which was assigned to a Fe═O bond. The generation of this high-valent intermediate was carried out by the reaction of oxo transfer agents such as peracetic acid or meta-chloroperbenzoic acid with the iron(II) precursor. This is reminiscent of how $[(TMC)Fe^{IV}(O)]^{2+}$ was generated using PhIO. Unlike $[(TMC)Fe^{IV}(O)]^{2+}$, $[(TPA)Fe^{IV}(O)]^{2+}$ was found to be relatively unstable and could not be crystallized. While $[(TPA)Fe^{IV}(O)]^{2+}$ was found to only be stable for days at 233 K, $[(TMC)Fe^{IV}(O)]^{2+}$ could survive for at least a month at the same temperature. Intriguingly, it was more reactive toward hydrogen atom transfer and oxygen atom transfer than $[(TMC)Fe^{IV}(O)]^{2+}$. Ligand variations on $[(TPA)Fe^{IV}(O)]^{2+}$ helped us understand both structural and functional effects of varying the electronics and steric demands around the iron(IV) center. Figure 1.4 shows the summary of ligand changes that were reported on the TPA framework. Changing the sixth ligand from the solvent to different anions such as Cl^-, Br^-, and $CF_3CO_2^-$ decreased the stabilities of the corresponding oxoiron(IV) complexes.[41] While the parent $[(TPA)Fe^{IV}(O)]^{2+}$ has a half-life of 1 hour at 283 K, the anion substituted variants turned out to be much less stable with the halide-bound species exhibiting a half-life of ~2 minutes at the same temperature. The addition of an anionic sixth ligand also brought intriguing changes to the spectroscopic signatures of $[(TPA)Fe^{IV}(O)]^{2+}$. The most important one was the red-shift of the near-IR feature in the range of 724 nm to 800 nm, the magnitude of the shift being dependent on the ligand-field strength of the anions used. This lends further support to the assignment of the near-IR feature to ligand-field d-d transitions.[42,43] Ligand variations were also made on the α substituents of the pyridine arms in $[(TPA)Fe^{IV}(O)]^{2+}$, where

the introduction of a methyl group at the sixth position (6-Me) or replacing pyridines with quinolines brought similar changes to the spectroscopy and the stability of $[(TPA)Fe^{IV}(O)]^{2+}$.[44] These substitutions increased the steric congestion around the iron center, thus causing a weakening of the ligand field. In addition to lowering the stability, these substitutions also enhanced the reactivity of the iron(IV) center toward substrates like thioethers.[44] Although the weakening of the ligand field can aid in accessing an *S* = 2 spin state, these mono-substitutions were not enough to convert *S* = 1 $[(TPA)Fe^{IV}(O)]^{2+}$ complex into an *S* = 2 derivative. It is possible that introducing additional substituents would further weaken the ligand field to a point where the spin-state of the iron(IV) center changes but such efforts have not been reported at this point.[44]

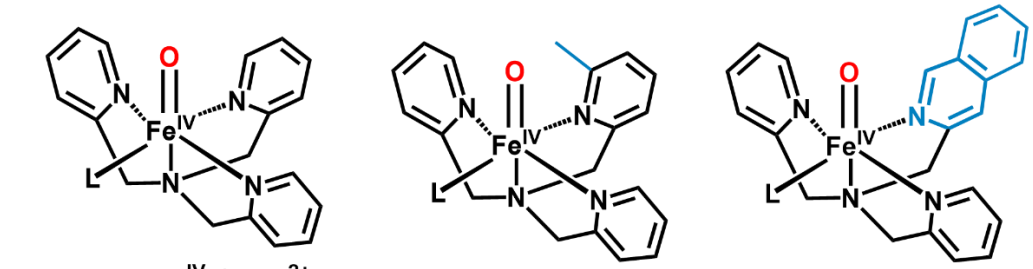

Figure 1.4. Ligand variations reported for $[(TPA)Fe^{IV}(O)]^{2+}$.

The success of these ligand variations on TPA and others[38] emphasizes the importance of ligands in modulating the properties of oxoiron(IV) complexes. A major goal for synthetic chemists is to mimic the high reactivity of the enzymatic intermediates and the *S* = 2 spin state of the iron(IV) center has been proposed to be behind this high reactivity.[45] However, out of 100 reported synthetic oxoiron(IV) complexes, only 10% have *S* = 2 iron(IV) centers.[7,46] The first synthetic *S* = 2 oxoiron(IV) complex $[(H_2O)_5Fe^{IV}(O)]^{2+}$ was generated in water at pH 1 with five weak-

field aqua ligands bound to the high-valent iron-oxo center.[47,48] This complex was generated using ozone as the oxidant and had a half-life of ~7 seconds at 298 K. The short lifetime of this species limited elaborate spectroscopic characterization and contributed to its lower yield (~25%). The use of water instead of a low-melting organic solvent did not help, as it seriously limited the accessibility of lower temperatures to increase the lifetime of such a short-lived species. Nonetheless, Mössbauer spectroscopy was able to confirm the *S* = 2 spin state (δ = 0.38 mm/s, ΔE_Q = 0.33 mm/s) of the iron(IV) center in this complex. This model was the closest structural mimic of **TauD-*J*** intermediate at the time with very similar Mössbauer isomer shifts. Another strategy to synthesize *S* = 2 oxoiron(IV) complexes utilized C_3-symmetric ligand architectures to make d_{x2-y2} and d_{xy} orbitals of the iron center degenerate in a trigonal bipyramidal geometry.[49–52] An *S* = 2 oxoiron(IV) complex using this strategy was generated by using TMG_3tren (TMG_3tren = 1,1,1-tris{2-[N2-(1,1,3,3-tetramethylguanidino)]ethyl}amine) as a ligand (Figure 1.5).[49] This complex was found to be relatively unstable with a half-life of just 30s at 298 K. The stability of this complex was increased by perdeuteration of the methyl groups in the ligand framework, which even allowed this complex to be crystallized.[53] EXAFS and Raman studies showed that the Fe═O distance (1.66 Å) and Fe═O vibration (843 cm^{-1}) for this *S* = 2 complex were comparable to those of *S* = 1 counterparts, thus suggesting that the iron-oxygen bond order has not been affected by the spin-state of the iron(IV) center. Despite having an *S* = 2 iron(IV) center like the enzymatic oxoiron(IV) intermediates, this synthetic model had lower Mössbauer isomer shifts (0.09 mm/s) compared to the enzymatic intermediates (0.22 – 0.30 mm/s). The steric congestion introduced in the TMG_3tren framework was designed to prevent the formation of a (μ-oxo)diiron(III) byproduct, which is commonly found as one of the thermal decay products in high-

valent iron-oxo chemistry.[7] However, because of the significant steric interactions, this novel *S* = 2 oxoiron(IV) complex fell well short of biological *S* = 2 oxoiron(IV) intermediates in terms of reactivity.[7] This notion was proved when a derivative ligand TMG_2dien (TMG_2dien = 2′,2′-(2,2′-(methylazanediyl)bis(ethane-1,2-diyl))bis(1,1,3,3-tetramethylguanidine) (Figure 1.5),[52] where one the arms had been removed to decrease the steric bulk, produced an oxoiron(IV) complex with significantly enhanced reactivity. This was the closest functional model for the enzymatic intermediates such as **TauD-*J***. Buoyed by this success, the search for more *S* = 2 oxoiron(IV) complexes continued.

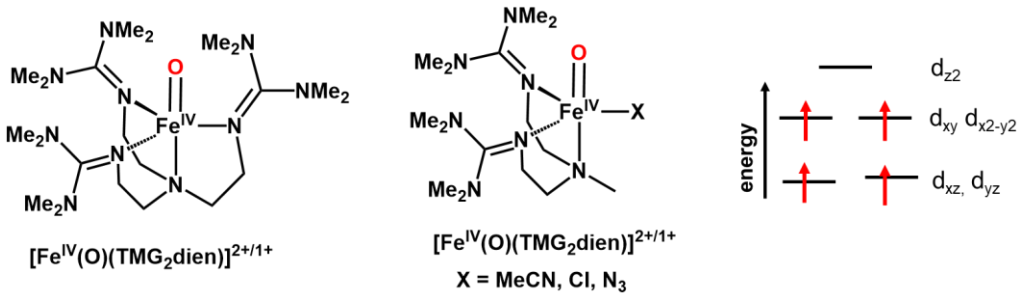

Figure 1.5. (Left) Bulky ligand frameworks (TMG_3tren and TMG_2dien) that forced an iron(IV) center to be in a trigonal bipyramidal geometry and exhibit *S* = 2 ground spin state. (Right) d-orbital splitting around an iron(IV) center in a trigonal bipyramidal geometry.

Using weak-field ligands to decrease the energy gap between d_{x2-y2} and d_{xy} orbitals to a point where they become degenerate and enforces an *S* = 2 configuration is another promising design. However, this strategy has failed to generate *S* = 2 oxoiron(IV) complexes most notably in the report of TPA ligand variations by Paine et al. (Figure 1.4).[44] However, using similar strategies, Biswas et al. reported a variant of the TPA ligand framework where all the pyridines have been replaced with quinolines to give rise to the TQA ligand framework (TQA = tris(quinolyl-2-methyl)amine) (Figure

1.6).[54] More importantly, a different oxidant in 2-(*t*BuSO$_2$)-C$_6$H$_4$IO (ArIO) was used here instead of peracetic acid or *t*-BuOOH, which were the oxidants employed by Paine et al..[44] ArIO is a far more efficient O-atom donor for iron(II) precursors and this oxidant has been widely used in the synthesis of reactive *S* = 2 oxoiron(IV) complexes ever since.[7,46] This underscores the importance of reaction conditions including the choice of oxidants in stabilizing *S* = 2 oxoiron(IV) complexes like [(TQA)Fe^{IV}(O)]$^{2+}$ (TQA = tris(quinolyl-2-methyl)amine). *S* = 2 oxoiron(IV) complexes are proposed to be more reactive toward C–H bonds than the *S* = 1 complexes,[45,55] which is generally supported by experimental observations.[52,56] Also, *S* = 2 complexes tend to be shorter-lived than most of the *S* = 1 complexes.[44] This change is most prominently seen between TPA and TQA ligand frameworks, where quinolines have weakened the ligand field to such an extent that the spin-pairing energy is greater than the energy difference between d_{x2-y2} and d_{xy} orbitals. This results in the unpairing of two more d-electrons in going from pyridine rich TPA to quinoline rich TQA (see Figure 1.6 below).

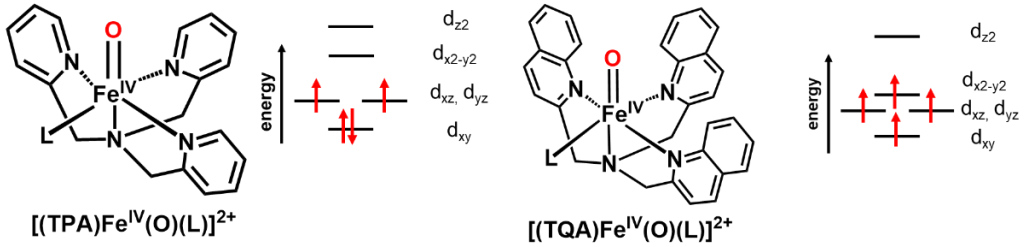

Figure 1.6. (Left) [(TPA)Fe^{IV}(O)]$^{2+}$ and the splitting of the d-orbitals of the iron(IV) center in a pseudo-octahedral geometry (Right) [(TQA)Fe^{IV}(O)]$^{2+}$ and the splitting of the d-orbitals of the iron(IV) center in a pseudo-octahedral geometry. Note the decrease in energy difference between d_{x2-y2} and d_{xy} orbitals that lead to four unpaired d-electrons.

The discovery of $[(TQA)Fe^{IV}(O)]^{2+}$ produced the first synthetic model that can act as both structural and functional mimics of the enzymatic intermediates such as **TauD-*J*** (See figure 1.7 below). The isomer shift (δ) as measured through Mössbauer spectroscopy for $[(TQA)Fe^{IV}(O)]^{2+}$ is 0.24 mm/s, which falls within the range of isomer shifts of enzymatic intermediates (δ = 0.22 – 0.30 mm/s).[10] The isomer shift is a measure of the electron density around the iron(IV) center and TQA is a great mimic of the biological ligand environment. Furthermore, high-field Mössbauer studies showed that the magnetic hyperfine splitting parameters for $[(TQA)Fe^{IV}(O)]^{2+}$ are comparable to those found in high-valent intermediates in **TauD**[10] and prolyl-4-hydroxylase.[17] This was the first time that a synthetic oxoiron(IV) model exhibited such close spectroscopic similarity with the biological systems. In addition to the spectroscopic modeling, the oxidation rates observed for $[(TQA)Fe^{IV}(O)]^{2+}$ are significantly higher than the pyridine containing $[(TPA)Fe^{IV}(O)]^{2+}$. While $[(TPA)Fe^{IV}(O)]^{2+}$ cannot oxidize cyclohexane at 233 K, $[(TQA)Fe^{IV}(O)]^{2+}$ oxidizes cyclohexane (C–H BDE = 99.3 kcal/mol) with a respectable rate constant of 0.4 M^{-1} s^{-1}. Intriguingly, when the temperature differences between rate measurements are considered, oxidation rates for **TauD-*J*** and $[(TQA)Fe^{IV}(O)]^{2+}$ are comparable. (k_{obs} (**TauD-*J***) = 13 s^{-1} at 278 K (rate of decay of **TauD-*J*** in the presence of taurine[22]) vs 0.4 s^{-1} at 233 K, assuming that rates double for every 10 degrees in temperature).

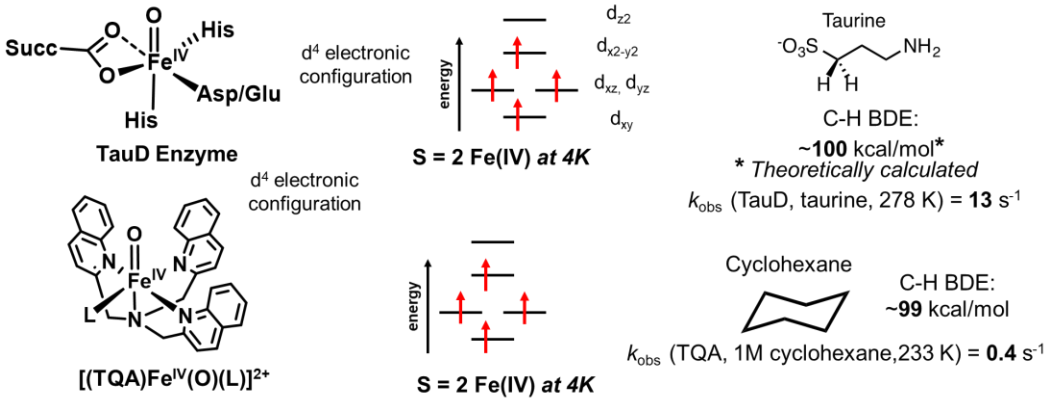

Figure 1.7. Structural and functional modeling of **TauD-*J*** by $[(TQA)Fe^{IV}(O)]^{2+}$, where not only the high-spin state with close isomer shifts were mirrored by the synthetic model but also the rates of oxidation for strong and unactivated C–H bonds.[54]

Interestingly, an *S* = 1 oxoiron(IV) complex supported by the Me_3NTB ligand (Me_3NTB = tris((N-methylbenzimidazol-2-yl)methyl)amine) where pyridines/quinolines are replaced with benzimidazoles exhibit comparable oxidation rates as $[(TQA)Fe^{IV}(O)]^{2+}$.[57] This complex oxidizes the strong and unactivated C–H bonds of cyclohexane (1M) at a rate of 0.25 s^{-1}, comparable to the rate for $[(TQA)Fe^{IV}(O)]^{2+}$ (0.4 s^{-1}). Also, olefin oxidation rates and the C–H bond activation mechanism are very similar for these two reactive species.[58] This was the first time an *S* = 1 oxoiron(IV) complex exhibited comparable reactivity with a closely related *S* = 2 framework. This anomalous observation was rationalized using a two-state reactivity model that was originally proposed by Shaik.[45] This model proposed that, even though an oxoiron(IV) complex has an *S* = 1 ground spin state, it can access an excited *S* = 2 spin state to achieve higher than expected oxidation rates. This was proposed to be happening for $[(Me_3NTB)Fe^{IV}(O)]^{2+}$, where the *S* = 2 state for this complex is a low-lying excited state and can be accessed during the reaction with C–H bonds.

Another attractive rationale was the possibility that $[(Me_3NTB)Fe^{IV}(O)]^{2+}$ undergoes a spin-crossover as we raise the temperature (See figure 1.8 below), which was thought to happen through the loss of the sixth ligand from the iron center. This loss of the sixth ligand would lead to a trigonal bipyramidal geometry that would enforce an S = 2 configuration at higher temperatures.[59] It is important to emphasize here that ground spin state measurements for this complex were done by Mössbauer spectroscopy at 4 K whereas oxidation rates were measured at 233 K. This makes the identity of this high-valent complex unclear at 233 K, which holds the key to explain its high reactivity. Thus, there is a significant need to develop strategies to measure spin-state and electronic structure information at the same temperatures as kinetic measurements. Besides theoretical conjectures, no experimental evidence has been put forward to shed light on the true nature of $[(Me_3NTB)Fe^{IV}(O)]^{2+}$ and its anomalous reactivity. This is mainly due to the extreme instability of this model complex ($t_{1/2}$ ~1 min at 233 K) and its modest yield (57%) that limits detailed spectroscopic characterization. It is of paramount importance that we understand the structure of this reactive S = 1 complex and ask the question: Is spin-state the only determining factor in governing C–H bond oxidation rates in oxoiron(IV) complexes as believed in the current literature?

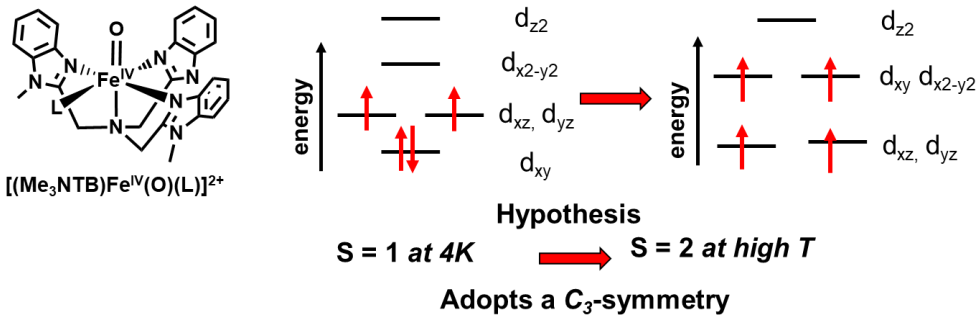

Figure 1.8. Proposed spin-crossover hypothesis for $[(Me_3NTB)Fe^{IV}(O)]^{2+}$ from ref[57,59]

It is important to note here that there is no perfect way to determine the spin-state and geometry of this reactive species in solution. Evans method using NMR spectroscopy is an obvious consideration for spin-state measurements but the short-half life and possible high-spin ferric decay product will complicate Evans measurements. An additional challenge is to obtain an analyzable NMR spectrum for such a short-lived complex even at lower temperatures. Finally, the paramagnetic nature of $[(Me_3NTB)Fe^{IV}(O)]^{2+}$ makes it doubtful that even if an NMR spectrum is obtained that we can use it to answer questions about geometry and spin-state in the liquid solution. This is because there exist very few examples of extensive NMR studies on oxoiron(IV) model complexes and none of them have benzimidazoles as part of the ligand framework. This seriously limits the amount of information one can extract from an NMR spectrum of a paramagnetic compound like $[(Me_3NTB)Fe^{IV}(O)]^{2+}$. On the flip side, the paramagnetic shifts of NMR signals are a function of the number of unpaired d-electrons, and they can be used as a metric of spin-state at higher temperatures. Achieving the same can be challenging using other techniques like Mössbauer spectroscopy. NMR studies showing the dependence of the paramagnetic shifts on the spin-state of the metal center have been shown in the case of nonheme iron(II) complexes where the change in spin-state resulted in significant differences in the paramagnetic shifts experienced by the protons in the ligands.[60] This was specifically observed in iron(II) complexes of TPA and $6Me_3TPA$ ($6Me_3TPA$ = tris(6-methyl-2-pyridylmethyl)amine). In the latter complex, the steric demands of the 6-methyl groups force a spin-state change of the iron(II) center from $S = 0$ to $S = 2$. This spin change was manifested in the ^1H NMR of the corresponding iron(II) precursors, where $S = 0$ $[(TPA)Fe^{II}(MeCN)](ClO_4)_2$ has pyridine based proton signals only in the diamagnetic region but $S = 2$ $[(6Me_3TPA)Fe^{II}(MeCN)](ClO_4)_2$ has pyridine

based signals paramagnetically shifted close to 100 ppm (Figure 1.9).[61] This results from the increase in the number of unpaired d-electrons during the change from an S = 0 spin-state to S = 2 spin-state. Electrons have larger magnetic moments than protons; and will cause the ^{1}H nuclei of TPA ligand to experience greater spin density in high-spin configurations (S = 2) compared to intermediate spin (S = 1) or low-spin configurations (S = 0).[60] Therefore, the NMR spectra of paramagnetic compounds have respective signals significantly shifted, the extent of which is directly related to the available unpaired spin density in a system. However, studies that utilize this knowledge have been limited for high-valent oxoiron(IV) complexes,[62–65] and have not been explored at all for reactive models. Therefore, figuring out an NMR based strategy to shed light on the solution state geometry and spin state of a reactive model like $[(Me_3NTB)Fe^{IV}(O)]^{2+}$ is desired.

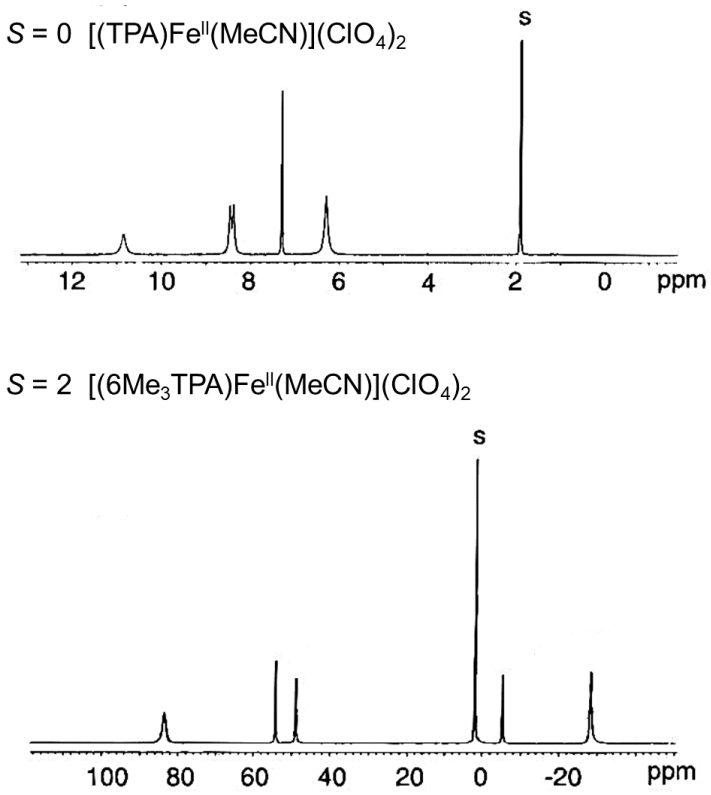

Figure 1.9. ^{1}H NMR comparison of iron(II) precursor complexes with two different spin states. The picture is reprinted (adapted) with permission from Y. Zang, J. Kim, Y. Dong, E. C. Wilkinson, E. H. Appelman, L. Que, *J. Am. Chem. Soc.* **1997**, *119*, 4197–4205. Copyright 1997, American Chemical Society.

1.3. Diiron Enzymes and Synthetic Models

1.3.1. Nonheme Diiron Enzymes

Nonheme diiron enzymes represent another well-studied class of nonheme iron-containing enzymes where the active site contains two irons, which come together to activate oxygen and achieve challenging transformations in Nature.[66,67] Two of the well-studied examples are soluble methane

monooxygenase (**sMMO**) and ribonucleotide reductase (**RNR**). **sMMO** is the soluble variant of methane monooxygenase that carries out selective oxidation of methane to methanol. The particulate variant employs copper in the active site for methane and is beyond the scope of this thesis.[68] The selective oxidation of methane is essential to methanotrophic organisms that depend on methane as the sole source of carbon and energy.[69] **sMMO** contains three different parts: a hydroxylase, a regulatory component B, and a reductase.[68,70] It is the hydroxylase part in **sMMO** that carries out the selective oxidation of methane using oxygen. **RNR** enzymes carry out the conversion of ribonucleotides into deoxyribonucleotides, which is integral to DNA biosynthesis.[71,72] **RNR** enzymes have been characterized in different classes depending on the presence of iron, manganese, cobalamin, or iron-sulfur clusters as part of their active site. In this thesis, we focus on the Class 1a **RNR** enzyme with a diiron active site. Furthermore, this class of **RNR** consists of two components: an R1 subunit, which is responsible for substrate binding, allosteric regulation, and hosting a catalytic cysteine residue and an R2 subunit where a catalytically essential tyrosyl radical is generated via an oxygen activation process like that of the **sMMO** enzyme.

In both **sMMO** and class 1a **RNR** enzymes, the active sites contain diferrous motifs that bind 2 histidines and 4 carboxylates as ligands.[67] Although they both employ similar ligand design, the denticity of one or more of the carboxylate ligands is different in these enzymes. Interestingly, there are three broad classifications for diferrous enzyme active sites based on the binding of the carboxylate ligands in the active sites (Figure 1.10). Class 1 is where only μ-1,3-carboxylate ligands are used, class 2 is where both μ-1,1-carboxylate and μ-1,3-carboxylate ligands are used, and lastly, class 3 is where a single-atom bridge is introduced in addition to

carboxylate ligands. The **sMMO** active site involves class 2 binding, while the class 1a **RNR** involves class 1 binding of carboxylates. Diiron enzymes that fall in class 3 classification such as frog M ferritin and others[67] are outside the scope of this thesis.

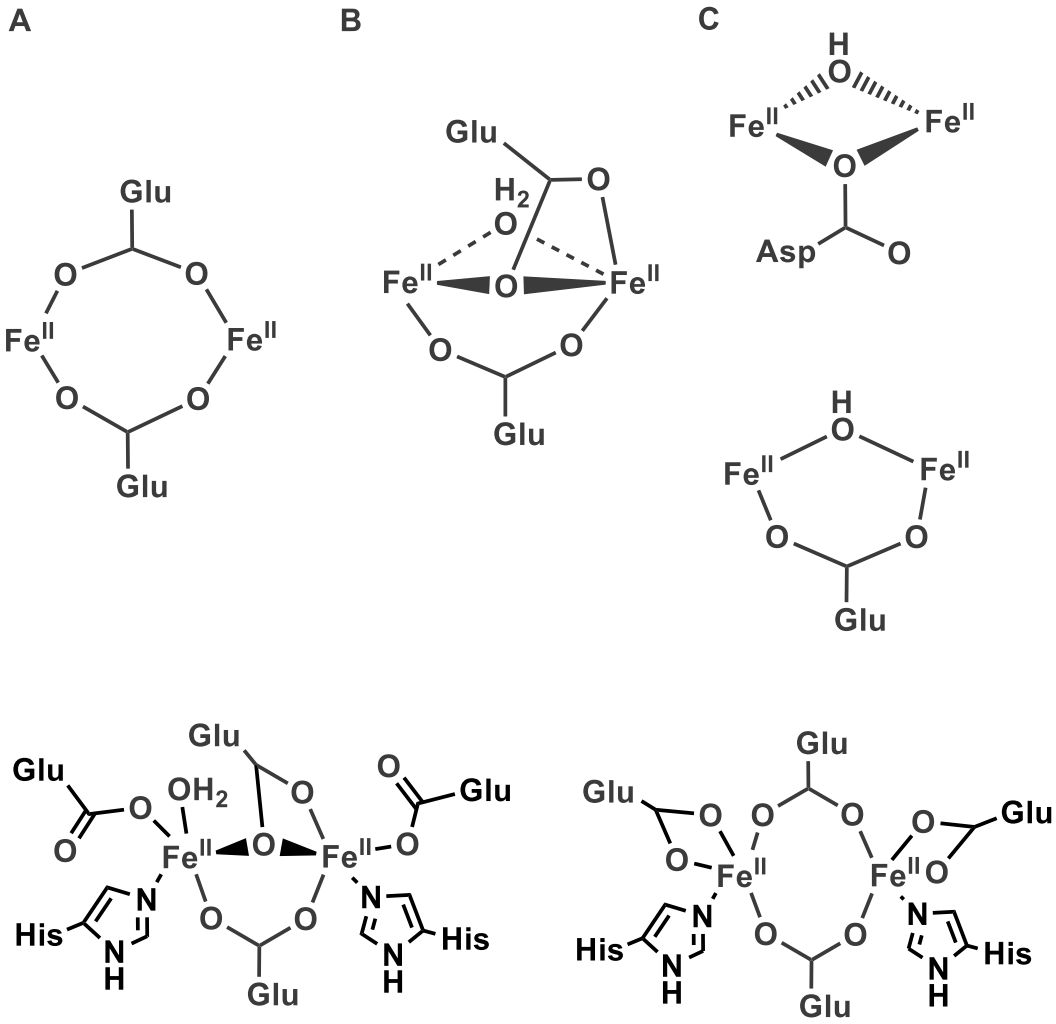

Figure 1.10. (Top) Summary of diferrous active site structural classes. **A**: Class 1 uses exclusively *μ*-1,3-carboxylate ligands; **B**: Class 2 uses both *μ*-1,1-carboxylate and *μ*-1,3-carboxylate ligands; **C**: Class 3 only uses single atom bridging groups such as hydroxyl moiety and either a *μ*-1,1-carboxylate or a *μ*-1,3-carboxylate ligand. (Bottom) Diferrous active site structures in **sMMO** (Left) and class 1a **RNR** enzyme (Right). The picture

is reprinted (adapted) with permission from A. J. Jasniewski, L. Que, *Chem. Rev.* **2018**, *118*, 2554–2592. Copyright 2018 American Chemical Society.

Several mechanistic studies have allowed us to discuss the catalytic cycles of **sMMO** and class 1a **RNR** enzymes in two parts: oxygen activation and substrate attack.[67,68] In the **sMMO** enzyme, a diferrous active site is generated by reducing the diferric state by 2 electrons. This diferrous site (A in Figure 1.10 and 1.11), which is characterized by an EPR signal of g = 16 (S_{tot} = 4 system with ferromagnetically coupled high-spin iron(II) centers) is primed for oxygen binding to start the catalytic cycle. Oxygen has been shown to bind to the iron center to generate a peroxodiiron(III) intermediate through metal-to-ligand electron transfer. This peroxodiiron(III) intermediate called **P** (B in Figure 1.11) has been characterized using various spectroscopic techniques.[68] The presence of an intense absorption feature at 700 nm (ε_{700} = 2500 M^{-1} cm^{-1}) is a characteristic of a peroxo species that is reminiscent of similar charge transfer features in related synthetic models (See later for more details).[67,73] Mössbauer spectroscopy confirmed that **P** contains diferric centers (δ = 0.66 mm/s, ΔE_Q = 1.53 mm/s). Unfortunately, resonance Raman studies were not successful in obtaining an O–O stretching frequency for the peroxide moiety in this intermediate, preventing the O–O binding mode in **sMMO-P** from being established. However, based on comparison with related systems, it is believed that the peroxide moiety is bound in a cis- or a trans-μ-1,2 fashion.[67,74]

In the next step, this peroxodiiron(III) species undergoes O–O bond cleavage to generate a high-valent diiron(IV) cluster **Q** (C in Figure 1.11). This step is accelerated by the lowering of pH, indicating a proton transfer

facilitates O–O bond cleavage in sMMO.[68,75] **sMMO-Q** has absorption features at 330 and 430 nm (ε_{330} = 9800 M^{-1} $cm^{-1,}$ ε_{430} = 7500 M^{-1} cm^{-1}). Mössbauer spectroscopy shows that **Q** contains two *S* = 2 (high-spin) iron(IV) centers that are anti-ferromagnetically coupled with one another in identical environments (δ = 0.17 mm s^{-1}, ΔE_Q = 0.53 mm s^{-1}) or almost identical environments (δ_1 = 0.21 mm s^{-1}, ΔE_{Q1} = 0.68 mm s^{-1}; δ_2 = 0.14 mm s^{-1}, ΔE_{Q2} = 0.55 mm s^{-1}), depending on the methanotrophic bacteria studied.[68] The isomer shift for **Q** is much smaller than what is observed in diferric systems like **P** and related synthetic models, and thus underscores the presence of a ferryl moiety or iron(IV) center in **Q**. The fact that the iron(IV) centers are anti-ferromagnetically coupled comes from high-field Mössbauer studies, which confirm that the ground state of this high-valent intermediate is diamagnetic.[76] Further structural insights on **Q** come from time-resolved resonance Raman spectroscopy, where a 690 cm^{-1} signal is observed that downshifted by 34 cm^{-1} with $^{18}O_2$ used instead of $^{16}O_2$ as the oxidant.[77] When compared with related studies of synthetic models, the 690 cm^{-1} vibration along with a ~30 cm^{-1} isotope shift is reminiscent of $Fe_2(\mu\text{-}O)_2$ tetratomic closed or “diamond” core vibrations.[78] Furthermore, using a mixed isotope-labeled gas $^{18}O^{16}O$, the 690 cm^{-1} vibration in the proposed $Fe_2(\mu\text{-}O)_2$ closed core of **Q** shifted by 17 cm^{-1}, which suggests that both the oxygen atoms in **Q** come from O_2. The retention of both O_2-derived O-atoms suggests that the O–O bond cleavage proceeds by a homolytic mechanism. This closed core structure of **Q** has also been supported by early EXAFS (Extended X-ray Absorption Spectroscopy) studies that reveal a diiron distance of 2.46 Å, which is indicative of a closed core diiron species.[79] More recently however, significant advancements in the X-ray absorption (XAS) techniques that use high energy resolution fluorescence detected (HERFD) XAS have improved the quality of the data, and the diiron distance of **Q** has been revised to a much longer ~3.4

Å, which is indicative of an open core structure for **Q**.[80] Besides, studies of related synthetic models show that open core high-valent diiron complexes are much more reactive than the closed core ones[56], which suggests that an open core **Q** is possibly more reactive than one with a closed core. This makes the open core version of **Q** more likely to be the active oxidant that carries out highly challenging oxidation of a 105 kcal mol^{-1} C–H bond in methane. The debate surrounding the actual structure of **Q** is still developing, and the best picture is an equilibrium between a closed core **Q** (observed through resonance Raman) and an open core **Q** (observed through HERFD XAS).[68] Moving towards the reactivity of **Q**, the oxidation of methane proceeds through a hydrogen-atom abstraction and exhibits a significant C–H/C–D kinetic isotope effect of 50-100 [81,82], which is followed by the rebound of the hydroxyl moiety on the methyl free radical to produce methanol. This is reminiscent of the well-studied mechanism of heme-containing cytochrome P450 enzyme[83] and also nonheme enzymes discussed above.[8]

As mentioned before, another well-studied diiron enzyme is the Class 1a ribonucleotide reductase (**RNR**) that catalyzes the conversion of ribonucleotides into deoxyribonucleotides in *E. coli* and mammals.[71,72] The diiron active site in this enzyme contains a 2-His-4-carboxylate as well but differentiated from **sMMO** by the denticity of some of the carboxylates. The oxygen activating mechanism of **RNR** is very similar to **sMMO**, where the diferrous active site reacts with oxygen to form a peroxo intermediate (**RNR-P**). Mössbauer spectroscopy finds very similar parameters for **RNR-P** to those of **sMMO-P** (δ = 0.66 mm s^{-1}, ΔE_Q = 1.68 mm s^{-1}).[84] But unlike for **sMMO-P**, resonance Raman experiments were successful in observing the O–O stretching frequency for the **RNR**-**P** intermediate to be at 870 cm^{-1} with an ^{18}O isotope shift of 46 cm^{-1}.[85] These features lead to the

assignment of a μ-1,2 binding peroxide for **RNR**-**P** upon comparison with synthetic peroxodiiron(III) complexes.[67,73] This peroxodiiron(III) intermediate then undergoes concurrent 1-e^- reduction and O–O bond cleavage to generate a mixed-valent diiron(III,IV) complex **X** (E in Figure 1.11 below).[86–89] This high-valent complex then abstracts a hydrogen atom from a tyrosine residue to produce a tyrosyl radical that in turn oxidizes a cysteine moiety integral to DNA biosynthesis. In this process, **X** is reduced to the diiron(III) resting state of the enzyme (F in Figure 1.11 below).

The generation of a mixed-valent diiron(III,IV) intermediate in **RNR** in contrast to a diiron(IV) intermediate in **sMMO** from very similar peroxodiiron(III) intermediates is intriguing and a testament to the flexibility of the active sites of these enzymes. **RNR-X** was also characterized by different spectroscopic techniques like **sMMO-Q**. Mössbauer spectroscopy showed an anti-ferromagnetically coupled pair consisting of a high-spin S = 5/2 iron(III) center (δ = 0.56 mm/s) and a high-spin S = 2 iron(IV) center (δ = 0.26 mm/s).[86,88] The anti-ferromagnetic nature of **X** was also observed in EPR spectroscopy where a g = 2 signal confirmed the presence of a S_{tot} = ½ system.[86] The exact identity of the core in **X** is still under debate like in **sMMO**-**Q**. EXAFS studies were successful in fitting a Fe−O distance of 1.75 Å and a Fe···Fe distance of 2.78 Å, in agreement with computational results on a $Fe^{III}Fe^{IV}(\mu\text{-}O)_2$ core.[90] However, magnetic circular dichroism[91] and electron nuclear double resonance[87,92] results for **X** contradicted the assignment of a $Fe^{III}Fe^{IV}(\mu\text{-}O)_2$ core and favored a mono-oxo bridged structure. The former study favored a $Fe^{III}Fe^{IV}(\mu\text{-}O)(\mu\text{-}OH)$ core and the latter one favored a $Fe^{III}Fe^{IV}(\mu\text{-}O)$(μ-1,1-carboxylate) core. Therefore, further studies are needed to put all these results into one picture to confirm the exact structure of **X**.

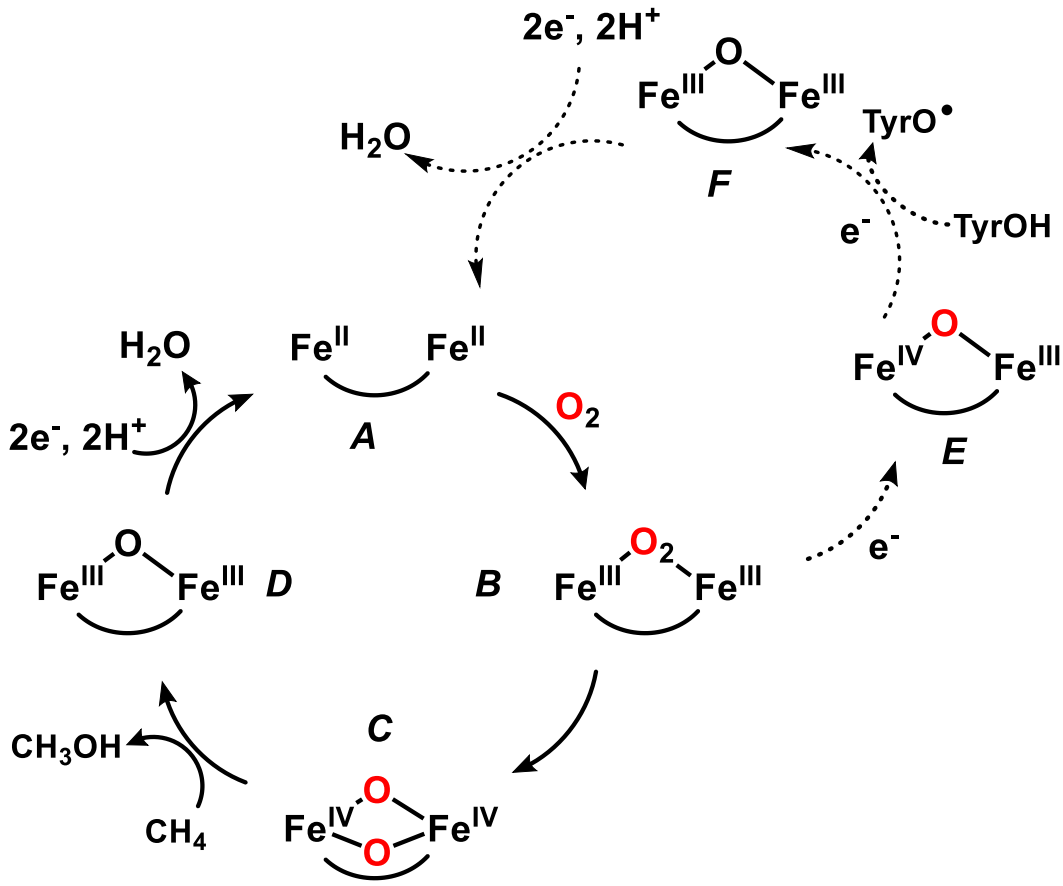

Figure 1.11. Schematic representation of the catalytic cycle for **sMMO** and class 1a **RNR** enzymes. A is the diferrous starting point of O_2 activation; B is a peroxodiiron(III) species; C and E are the high-valent active oxidants in the cycles, represented here as the bis(μ-oxo)diiron(IV) species **Q** from **sMMO** and **X** from class 1a **RNR** respectively; D and F represent the resting diferric state; Representative examples: **sMMO** proceeds through the A→B→C→D cycle; class 1a **RNR** proceeds through the A→B→E→F cycle; The picture is reprinted (adapted) with permission from A. J. Jasniewski, L. Que, *Chem. Rev.* **2018**, *118*, 2554–2592. Copyright 2018 American Chemical Society.

1.3.2. Nonheme Diiron Synthetic Models

The significance of the high-valent intermediates found in the diiron enzymes and the ambiguity surrounding the structure of such intermediates warrant extensive studies of synthetic diiron models. Synthetic complexes can help us understand the structures and functions of the species involved in the catalytic cycles of the enzymes discussed above. There are various guidelines synthetic chemists can use to direct their ligand design and modeling studies. Nitrogen donors used in the 2-His-4-carboxylate framework in **sMMO** and class 1a **RNR** enzymes are histidines. Histidines offer a five-membered ring for the ligation. They are used as a flexible acid-base source in the active sites of the enzymes. and involved in various hydrogen bonding interactions that play crucial roles in the enzymes. To emulate similar interactions in synthetic models, heterocycles analogous to histidines must be used in ligand design. Next, oxygen activation generates peroxodiiron(III) intermediates in **sMMO** and **RNR** enzymes, which then generate high-valent oxidants to perform substrate fuctionalizations. Oxygen is a cheap, green oxidant that Nature finds a way to use to form important oxidants in these enzymes. With that in mind, oxygen activation and the use of oxygen as the terminal oxidant in synthetic modeling studies must be an important goal to understand the mechanism of similar processes in Nature. This will aid in the design of efficient and green catalysts that can perform substrate fuctionalizations seen in Nature and beyond. Finally, synthetic chemists need to consider the essential variables that make the high-valent intermediates so potent in the enzymes. One of the most important properties is the spin-state of the iron(IV) center. The iron centers in the enzymes are bound to weak-field ligands like histidines and carboxylates. These make the high-valent iron(IV) centers in the enzymes high-spin. Similarly, ligand choice can play a major role in dictating whether synthetic models can support a high-spin

iron(IV) center or not.[46] This is an important parameter and has been discussed for monoiron enzymes and related models,[8,46] but it is also significant in the design of diiron models.

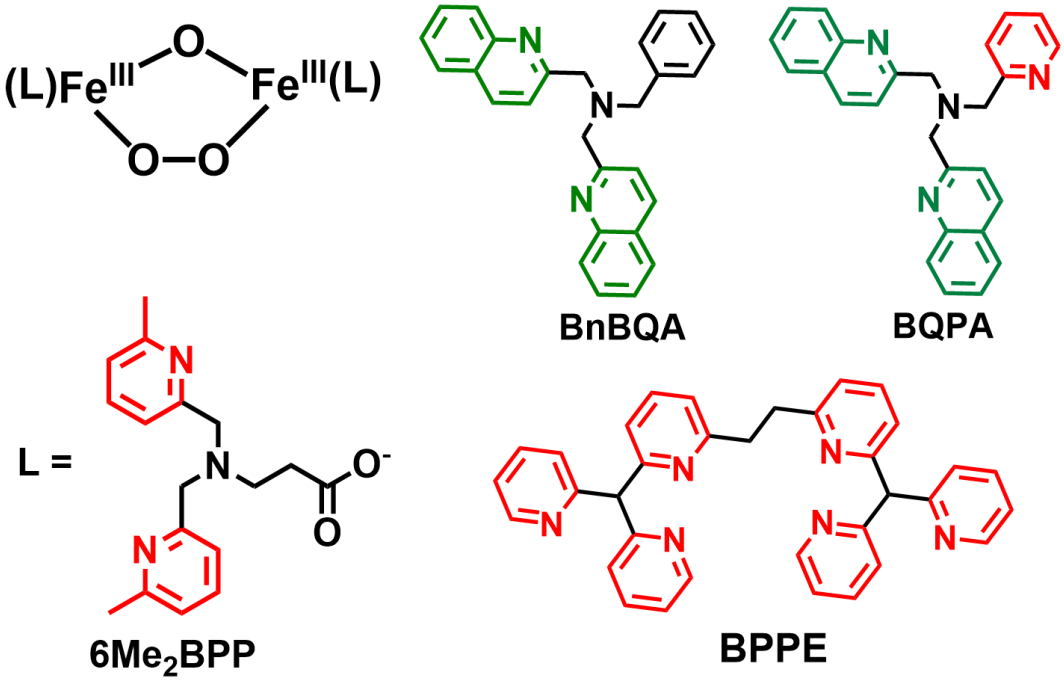

Figure 1.12. Mononucleating and dinucleating ligands used in diiron modeling chemistry.

In the last three decades, synthetic models have been able to support ***P**-like* peroxodiiron(III) intermediates with a variety of ligand frameworks.[67] These include polydentate ligands with N-donors like pyridines, quinolines and tertiary amines, and O-donors like carboxylates or alkoxides. Ligands such as $6Me_2BPP$ ($6Me_2BPP$ = bis(6-methyl-2-pyridylmethyl)-3-aminopropionate), BnBQA (BnBQA = *N*-benzyl-*N*-bis(2-quinolinylmethyl)amine), BQPA (BQPA = bis(2-quinolylmethyl)-*N*-2-pyridylmethylamine) bind the iron center, leaving vacant sites available for oxo or hydroxo bridges to form diiron synthetic models (Figure 1.12).[67,73] Alternatively, dinucleating ligands such as BPPE (BPPE = 1,2-bis[2-(bis(2-

pyridyl)methyl)-6-pyridyl]ethane), 6-HPA (6-HPA = 1,2-bis[2-{bis(2-pyridylmethyl)aminomethyl}-6-pyridyl]ethane) or N-Et-HPTB (N-Et-HPTB-H = tetrakis(2-benzimidazolylmethyl)-2-hydroxy-1,3-diaminopropane) bind two iron centers and directly give rise to diiron models.[67,73] More than thirty peroxodiiron(III) models have been reported so far. They have predominantly been made either by bubbling oxygen into solutions of diiron(II) precursor complexes or by adding hydrogen peroxide to diferric complexes. The use of organic solvents in these studies allowed chemists to reach lower temperatures and extend the lifetimes of relevant intermediates.

All of these peroxodiiron(III) complexes exhibit intense ligand-to-metal charge transfer bands in the visible region of the electromagnetic spectrum with the absorption maxima dependent on the basicity of the ligands. Six of these peroxodiiron(III) complexes have been crystallized and studied by X-ray diffraction (XRD). This provides high-resolution structural insights related to similar structures found in the enzymes.[67,93] Others have been studied using X-ray absorption spectroscopy when diffraction quality crystals were not obtainable. Interestingly, in most of these structures, the peroxide moiety is bound in a *cis*-μ-1,2 fashion (see Figure 1.13 for two examples), which has been proposed for **sMMO-P** and class 1a **RNR-P** enzymatic intermediates.[67] The average O–O distance in these models was found to be around 1.4 Å, consistent with an O–O single bond. The diiron distance varied significantly (3.1 – 4.0 Å) and so did the Fe–O_{peroxo} distance (1.86 – 2.1 Å), as the basicity of the bridging motifs changed from oxo to hydroxo or alkoxo to carboxylates. This highlights the structural differences that can exist in different biological systems with such subtleties in ligation.

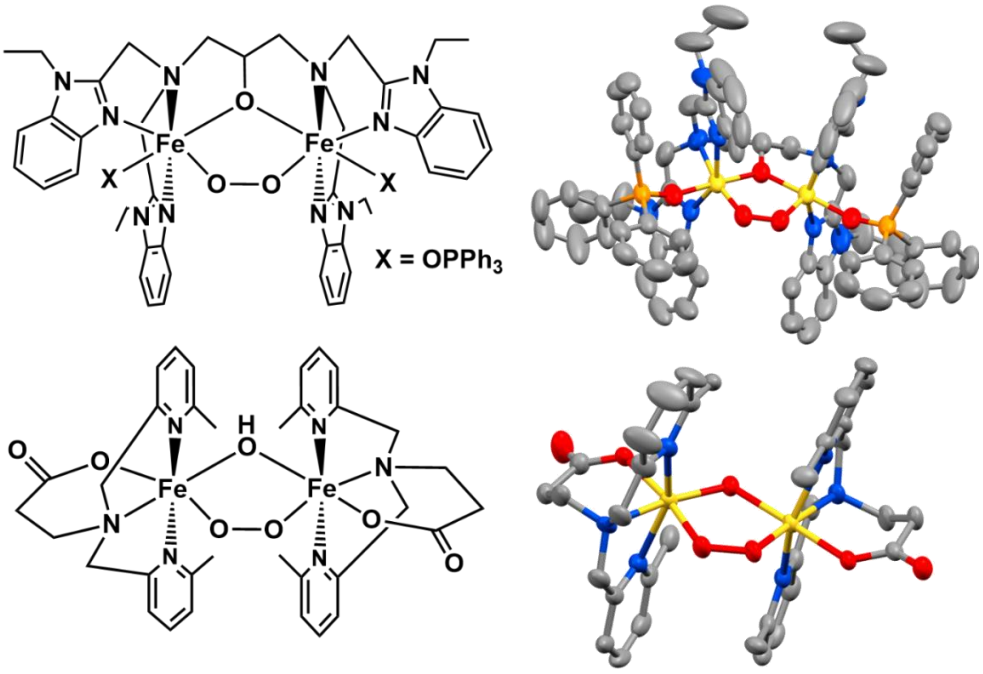

Figure 1.13. Crystal structures of peroxodiiron(III) complexes demonstrating the *cis*-μ-1,2 peroxide coordination supported by a dinucleating ligand (top) and two mononucleating ligands (bottom). The pictures are reprinted (adapted) with permission from X. Zhang, H. Furutachi, S. Fujinami, S. Nagatomo, Y. Maeda, Y. Watanabe, T. Kitagawa, M. Suzuki, *J. Am. Chem. Soc*. **2005**, 127, 826–827, Copyright 2005 American Chemical Society and Y. Dong, S. Yan, V. G. Young, L. Que, *Angew. Chem. Int. Ed. Engl.* **1996**, *35*, 618–620, Copyright 1996 Wiley VCH.

Mössbauer studies on several synthetic peroxodiiron(III) complexes show the iron centers to be high-spin iron(III) with isomer shifts in the range of 0.47 – 0.66 mm/s. Most interestingly, among these models, the crystallized model, $[(Tp^{i}Pr_2)_2Fe^{III}_2(O_2)(PAA)_2]$ ($Tp^{i}Pr_2$ = tris(3,5-diisopropyl-1-pyrazolyl)borate, PAA = phenylacetic acid) exhibits Mössbauer parameters (δ = 0.66 mm/s, ΔE_Q = 1.40 mm/s), which fall close to values observed for

the peroxo intermediates in **sMMO**, **RNR R2**, enzymes.[67] Another key parameter obtainable from Mössbauer studies is the strength of the coupling between the iron(III) centers, which is denoted by *J* from Hamiltonian $\hat{\mathrm{H}} = JS_1S_2$. Nearly all the models exhibit *S* = 0 ground states with the iron(III) centers antiferromagnetically coupled with each other. The strength of this coupling is usually measured by the *J* value. The lowest *J* value reported among the models was for a carboxylate-rich system $[Fe^{III}_2(dxlCO_2)_4(O_2)(Py)_2]$ ($dxlCO_2^-$ = 2,6-bis[(2,6-dimethylphenyl)methyl]-4-tert-butylbenzoate) (*J* = 30 cm^{-1}). Incidentally, this complex also exhibited a relatively low v(O-O) of 822 cm^{-1} that was obtained from resonance Raman studies. Similar studies have shown the O–O stretching frequency to be 870 cm^{-1} for **RNR-P** intermediate[85] but were unsuccessful in obtaining similar information for **sMMO-P.** Peroxodiiron(III) species in other diiron enzymes[67] have shown considerable variability with **CmlI-P** having the lowest value at 791 cm^{-1} and **Δ^9D-P** with the highest side with 898 cm^{-1}. For synthetic models as well, the O–O stretching frequency can span quite a large range, depending on the ligands. The frequencies range from 820 cm^{-1} to over 928 cm^{-1}, which is quite interesting and speaks to the importance of ligands regulating this variable in the biological peroxodiiron(III) intermediates.[67]

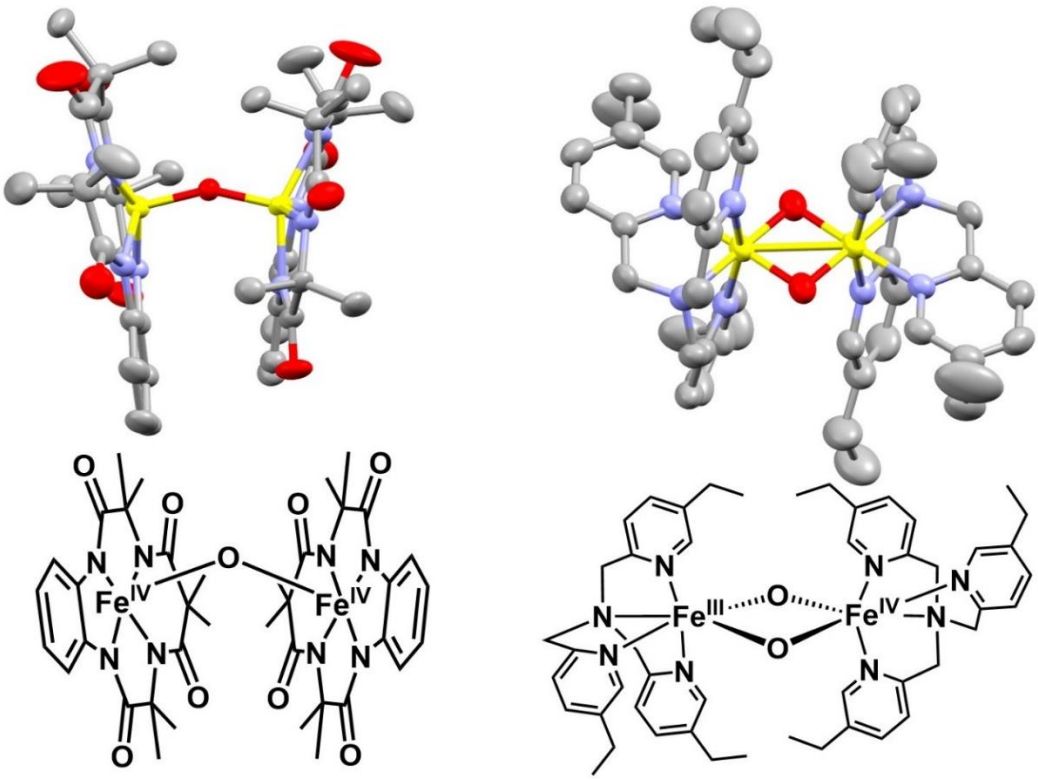

Figure 1.14. (Left) Crystal structures of high-valent diiron(IV) ($[Fe^{IV}_2O(TAML)_2]^{2-}$) complex and (Right) mixed-valent diiron(III,IV) ($[Fe^{III}Fe^{IV}(\mu\text{-}O)_2(5Et_3TPA)_2]^{3+}$) model complexes. The pictures are reprinted (adapted) with permission from H. F. Hsu, Y. Dong, L. Shu, V. G. Young, L. Que, *J. Am. Chem. Soc.* **1999**, *121*, 5230–5237, Copyright 1999 American Chemical Society and A. Ghosh, F. T. De Oliveira, T. Yano, T. Nishioka, E. S. Beach, I. Kinoshita, E. Münck, A. D. Ryabov, C. P. Horwitz, T. J. Collins, *J. Am. Chem. Soc.* **2005**, *127*, 2505–2513, Copyright 2005 American Chemical Society.

Biological peroxodiiron(III) intermediates in **sMMO** and **RNR** enzymes act as precursors to high-valent intermediates like **Q** and **X** respectively. Models for **Q** and **X** have been far fewer than corresponding peroxodiiron(III) models. Only fifteen high-valent diiron model complexes

have been reported so far with seven of them having diiron(IV) cores and the rest being diiron(III,IV) complexes. The suite of spectroscopic tools used for these high-valent models is the same as that used for peroxodiiron(III) models. Mössbauer spectroscopy has been utilized to identify the iron(IV) centers in these complexes with most of them reported being *S* = 1, while the open core or single bridged complexes of TPA* and 6-HPA ligand exhibit *S* = 2 iron(IV) centers.[67] To date, there is no report of either a closed core bis(μ-oxo)diiron(IV) or a bis(μ-oxo)diiron(III,IV) complex with *S* = 2 iron(IV) centers. Only high-valent diiron complexes with open cores exhibit *S* = 2 iron(IV) centers. It is not currently well understood what may cause this outcome. We need a more diverse set of ligand frameworks to identify the rationale behind this observation.

XAS studies have also been instrumental in obtaining important structural information, with the diiron distance being key to differentiating open core structures intermediates from closed core structures. Overall, upon comparison with diferric precursors, there is always a contraction of bond lengths going to high-valent intermediates due to the increase in the oxidation state of the iron(IV) center. In addition, only two of them, $[Fe^{IV}_2O(TAML)_2]^{2-}$ (TAML = 3,3,6,6,9,9-hexamethyl-3,4,8,9-tetrahydro-1H-1,4,8,11-benzotetraazacyclo-tridecine-2,5,7,10(6H,11H)-tetraone)[96] and $[Fe^{III}Fe^{IV}(\mu\text{-}O)_2(5Et_3TPA)_2]^{3+}$ (5Et$_3$TPA = tris(5-ethyl-2-pyridylmethyl)amine)[95] have high resolution structural information from crystallography. The former has a structure with a single oxo bridge, while the latter has a closed core with two oxo bridges (Figure 1.14).

Resonance Raman studies have been instrumental in studying key vibrations in high-valent diiron complexes, most notably by Que and co-workers for a rare synthetic closed core model of **Q**. In these reports,[97,98]

both chemical and electrochemical methods were used to generate a high-valent bis(μ-oxo)diiron(IV) complex supported by the electron-rich ligand TPA* (TPA* = tris(3,5-dimethyl-4-methoxypyridin-2-ylmethyl)amine).[97,98] This complex showed an intense vibrational feature at 674 cm^{-1} with an ^{18}O isotopic shift of 30 cm^{-1}, which has been a signature for $M_2(\mu\text{-}O)_2$ complexes.[78,99] Using the same ligand framework, an open core (μ-oxo)diiron(III,IV) complex was formed where the iron(III) (S = 5/2) and iron(IV) (S = 2) centers were both high-spin in nature, which acted as a structural model for **X** intermediate in class 1a **RNR**.[ref?] Unfortunately, no peroxodiiron(III) intermediates were seen in these cases, and hence the biological precedent of a peroxo intermediate giving rise to high-valent intermediates has not yet been modeled in these reports. Indeed, there are only two peroxodiiron(III) complexes $[Fe^{III}_2(\mu\text{-}O)(O_2)(6\text{-}Me_3\text{-}TPA)_2]^{2+}$ (6-Me_3-TPA = tris(6-methyl-2-pyridylmethyl)amine) and $[Fe^{III}_2(\mu\text{-}O)(O_2)(BnBQA)_2]^{2+}$ (BnBQA = N-benzyl-N,N-bis(2-quinolinylmethyl)amine) that have been shown to generate high-valent diiron(III,IV) complexes[100,101] through O–O bond cleavage and thus being mechanistically similar to enzymes. In both these cases, it was observed that a proton is necessary to form the high-valent complexes, which is reminiscent of how **Q** is generated from **sMMO-P** where the lowering of pH has been shown to enhance the rates of formation of the active oxidant.[74,75] However, there is no example of any peroxodiiron(III) model that has been shown to form a high-valent bis(μ-oxo)diiron(IV) core, similar to what has been characterized by Raman studies for **Q** in **sMMO**. The closest example would be the 6-HPA system (6-HPA = 1,2-bis{2-[bis(2-pyridylmethyl)-aminomethyl]pyridin-6-yl}ethane) developed by Kodera et al.,[102] which used a diferric system and hydrogen peroxide to generate a peroxodiiron(III) complex that produced a diferryl species with two terminal iron(IV) oxo moieties connected by an oxo bridge. Therefore, to this date,

a diiron(II) system has not been reported that can use O_2 to form a peroxodiiron(III) species and in turn generate a high-valent diiron(IV) species. Such a transformation is highly desired and would be analogous to the **P**-to-**Q** transformation in the **sMMO** cycle.

1.4 Objective of this thesis

This thesis will cover the study of synthetic models that span from monoiron models to diiron models, and detail spectroscopic and reactivity studies on these models. The most unique part about the research presented here is that it will cover the study of monoiron(IV) and diiron(IV) models supported by the same ligand, which will allow the rare comparison between them. Often, comparison of structure and reactivity properties between monoiron(IV) oxo complexes with diiron(IV) complexes are flawed because they are supported by different ligands or have other variables to consider, for instance, different donor capabilities from different ligand structures. The use of the same ligand in Chapter 2 for the monoiron(IV) model and Chapter 3 for the diiron(IV) model makes for intriguing comparisons. In the current literature, there is just one ligand (TPA*) capable of supporting both monoiron(IV) and diiron(IV) models, and their comparison produced interesting spectroscopic and at least a thousandfold difference in reactivity.[56] Me_3NTB ligand used in Chapter 2 and Chapter 3 will be the second framework in this highly exclusive group. Specifically, Chapter 2 will cover the importance of understanding the variables behind making oxoiron(IV) models reactive and introduce NMR as a tool to obtain electronic and structural information in solution state for unstable models. With this information, future studies can exploit NMR to gather information to correlate structure and reactivity at comparable temperatures, which has been challenging especially for reactive complexes. Chapter 3 will cover the diiron-based oxygen activation chemistry and introduce an

unprecedented way to promote O–O bond cleavage in peroxoxdiiron(III) complexes to successfully generate a high-valent diiron(IV) complex. The use of oxygen and generation of a **P**-like intermediate and conversion into a **Q**-like intermediate is unprecedented and our strategy here will pave the way for similar studies that will add to the currently small number of high-valent diiron complexes. Chapter 4 will cover the introduction of weaker-field ligands that have the potential to generate $S = 2$ high-valent diiron(IV) complexes, which will mimic the electronic structure of similar species found in the enzymes. Very few studies have utilized ligands that produce high-spin iron(IV) complexes in a diiron framework. Our exploration in this chapter will build on the knowledge from Chapter 3 and take us one step closer to the goal of modeling the enzymatic high-valent intermediates. This will have far-reaching implications in reactivity as the difference in spin-states of the iron center is often attributed to differences in reactivities while comparing enzymes and synthetic systems. This issue has been widely explored in mononuclear systems but more dinuclear systems need to be studied to test this hypothesis in diiron models.

Chapter 2:
Use of ^{1}H NMR Spectroscopy in Elucidating Solution Structure and Spin State of Oxoiron(IV) Complexes

This chapter is reprinted (adapted) with permission from Banerjee, S.; Rasheed, W.; Fan, R.; Draksharapu, A.; Oloo, W. N.; Guo, Y.; Que, L. *Chem. Eur. J.* **2019**, *25* (41), 9608-9613.

2.1 Introduction

Mononuclear nonheme iron enzymes carry out a range of oxidative transformations *via* a recurring $S = 2$ oxoiron(IV) oxidant.[8,103] 2003 proved to be a "golden" year for nonheme iron enzymes when Krebs and Bollinger trapped and characterized the first oxoiron(IV) intermediate (labeled as ***J***) in the α-ketoglutarate dependent enzyme TauD that oxidizes the strong C-H bonds of taurine[104] and regulate sulfur metabolism in *Escherichia coli*.[105] This enzymatic oxoiron(IV) intermediate was shown to possess an $S = 2$ ground spin state for the iron(IV) center, which is bound to histidine and carboxylate ligands in this enzyme. Around the same time, Que and coworkers reported the crystal structure of the first synthetic oxoiron(IV) complex,[37] which was supported by a nitrogen-containing macrocycle and was shown to have an $S = 1$ iron(IV) center. Within the past two decades, many small-molecule analogs of these highly reactive species have been synthesized and some have even been crystallized,[7,38,106] which shed light on the structural and functional properties of the Fe^{IV}=O unit. Most of these complexes have $S = 1$ ground states, which theory predicts to be less reactive than their $S = 2$ counterparts.[45,55] This reactivity pattern is generally borne out by experiments.[56,107] However, a notable exception to this trend is the $[Fe^{IV}(O)(Me_3NTB)]^{2+}$ complex (**1**, Figure 2.1; Me_3NTB = tris((benzimidazolyl-2-methyl)amine), which is established by Mössbauer analysis at 4.2 K to have an $S = 1$ ground state,[57] but oxidizes hydrocarbon substrates at rates comparable to those found for the highly reactive $S = 2$ complex $[Fe^{IV}(O)(TQA)]^{2+}$ (TQA = tris(quinolyl-2-methyl)amine), despite having different spin states.[54] These two complexes represent two of the most reactive Fe^{IV}=O complexes synthesized thus far.[7,38,106] The comparable reactivity of these two complexes clouded the reasoning, which dictates that to achieve enzyme-like reactivity an $S = 2$ iron(IV) center is needed. There is thus a gap in our understanding of why Nature

uses an S = 2 iron(IV) center in TauD and other nonheme iron-containing enzymes. Filling this gap in knowledge is essential for the bioinorganic community to facilitate the development of catalysts that can achieve enzyme-like reactivity and capable of versatile oxidation reactions.

It is necessary to summarize the arguments that have been put forward to explain the anomalous reactivity of **1**. While the high reactivity of $[Fe^{IV}(O)(TQA)]^{2+}$ is attributed to its S = 2 spin state, the comparably high reactivity of **1** has been rationalized in two different ways. One is the two-state reactivity rationale postulated by Shaik, which posits that the S = 1 complex can access a low-lying S = 2 excited state along the reaction coordinate to carry out substrate oxidation.[57] This hypothesis considers the involvement of the transition-state whereby the activation energy of the oxidation reactions is reduced, resulting in enhanced rates. As this phenomenon is proposed to involve the transition-state, experimental verification is not possible. An alternative hypothesis invokes the presence of a thermal equilibrium between a more stable S = 1 six-coordinate species, which predominates at 4.2 K where Mössbauer studies have been carried out and a more reactive S = 2 trigonal bipyramidal species that is accessible at higher temperature upon dissociation of a bound solvent, where oxidation reactions are carried out.[59] This hypothesis is an attractive one given the fact that enforcement of trigonal bipyramidal geometry to achieve S = 2 configurations has been shown in oxoiron(IV) models before.[49] Therefore, it is perfectly reasonable to assume that the solvent, which is the most weakly bound ligand may come off as the temperature is raised. Another rationale behind this postulate is the crystal structure of the iron(II) complex of Me_3NTB, which shows the iron center is in a trigonal bipyramidal geometry. However, the thermal instability of **1** ($t_{1/2}$ < 1 min at 233 K in MeCN)[108] has made it difficult to obtain experimental support for the latter hypothesis. We have thus sought to identify reaction

conditions that could increase the lifetime of **1** and allow its characterization in liquid solution by ^{1}H NMR spectroscopy. This goal has been achieved by using acetone-d_6 as the solvent (Figure 2.1), which allows **1** to be characterized in solution down to 193 K. This will allow us to study the structure and the spin state of this reactive complex at higher temperatures where the oxidation reactions are done, unlike at 4.2 K where the Mössbauer data is reported.

2.2 Results

2.2.1 Generation of oxoiron(IV) complexes and their electronic absorption spectral characterization

All complexes in this series can be generated from their ferrous precursors in acetone-d_6/acetonitrile at appropriate temperatures. **1, 1a, 1b** can be generated upon addition of 2 equivalents of 2-(^{t}BuSO$_2$)-C$_6$H$_4$IO (ArIO) in 2,2,2-trifluoroethanol to the corresponding iron(II) precursors and **2** can be generated by adding 4 equivalents of ceric ammonium nitrate (CAN) as the oxidant to the respective iron(II) precursors, recrystallized and dissolved in acetone-d$_6$ for comparison with **1**.

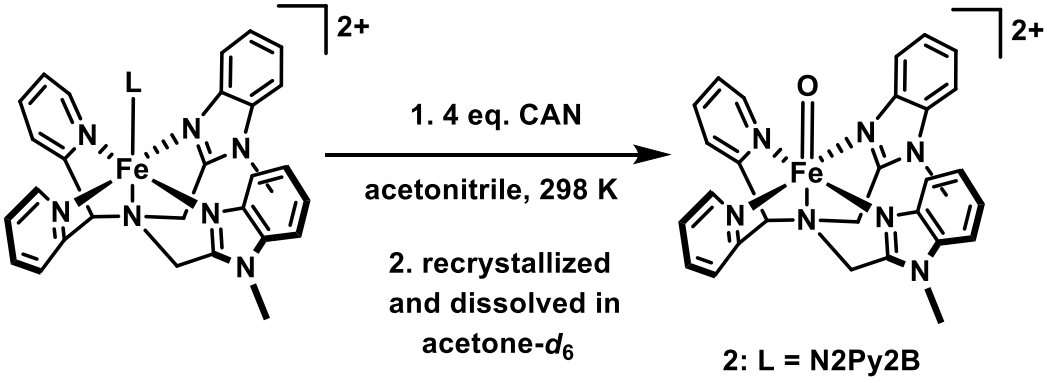

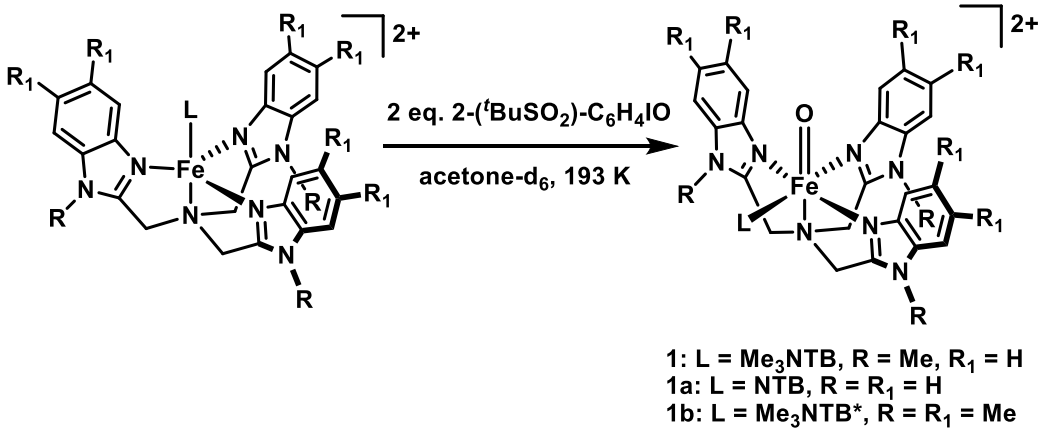

Figure 2.1. Generation of oxoiron(IV) complexes that are studied here.

Addition of 2 equiv. 2-(^{t}BuSO$_2$)-C$_6$H$_4$IO (ArIO) to a solution of [Fe^{II}(Me$_3$NTB)(CH$_3$CN)](CF$_3$SO$_3$)$_2$ in acetone-d_6 at 193 K under N_2 generates **1** (Figure 2.2 left), which exhibits a near-IR band with a λ_{max} at 770 nm that is identical to that reported in CH$_3$CN and arises from *d-d* transitions of the Fe=O unit.[109] This spectrum derives from a sample obtained from the reaction of a 2-mM solution of iron(II) precursor in acetone-d_6 with 2 equiv. ArIO, for which Mössbauer analysis shows it to contain 70% **1** (vide infra). A comparison of these data in acetone-d_6 with those reported by Seo *et al*. in CH$_3$CN[57] shows that a larger fraction of **1** is formed under the conditions presented here. The larger yield is likely not due to the change in solvent or temperature but, because of the use of ArIO as oxidant instead of *m*-ClC$_6$H$_4$CO$_3$H (*m*CPBA), as the same absorbance is obtained in CH$_3$CN with 2 equiv. ArIO at 233 K (Figure 2.2). When the Mössbauer-derived fraction of **1** (see a later section for details) is considered together with the observed absorbance, an extinction coefficient of 540 M^{-1} cm^{-1} can be associated with this complex, much higher than the originally reported value of 200 M^{-1} cm^{-1}.[57] More importantly, its half-life at 233 K also increases from ~1 min[57] to ~4 min with the use of ArIO as the oxidant.

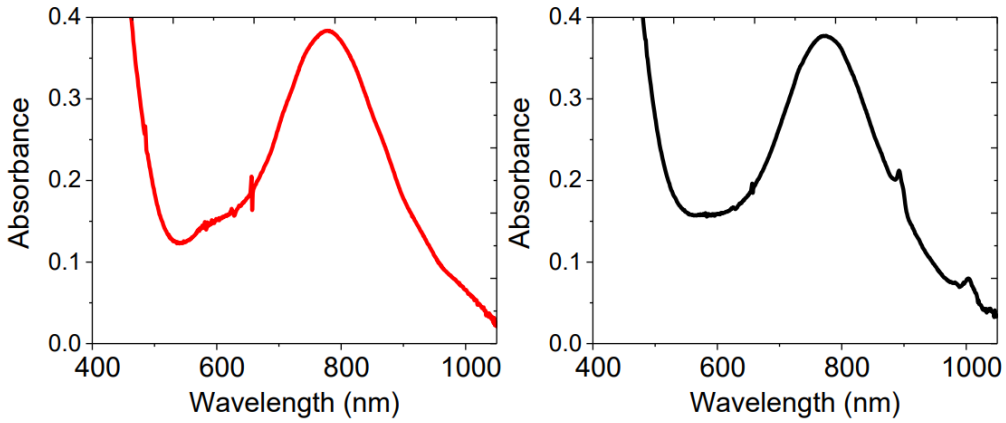

Figure 2.2. Electronic absorption spectra of **1** prepared from the reaction of a 1-mM solution made from solid $[Fe^{II}(Me_3NTB)(CH_3CN)](CF_3SO_3)_2$ with 2 equiv. ArIO (in TFE) in acetone-d_6 (red trace on the left) and acetonitrile (black trace on the right) at 233 K.

2.2.2 Reactivity of 1 with hydrocarbon substrates

To ascertain that the oxidative reactivity of **1** is unaffected by the change of solvent, we have measured the second-order rate constants (k_2) for the reactions of **1** with a range of hydrocarbon substrates in acetone-d_6 at 233 K for comparison with data reported by Seo *et al.* in CH_3CN.[57] As evidenced from the plot of log(k_2') versus C−H bond dissociation energies (BDE), where k_2' = k_2/number of equivalent substrate C−H bonds (Figure 2.3 right), the logarithms of the rate constants are found to decrease linearly with an increase in the C−H bond dissociation energies. More importantly, the values of the second-order rate constants for **1** in acetone-d_6 are comparable to the ones reported by Seo *et al.* in CH_3CN at 233 K,[57] within experimental uncertainty (Table 2.1), suggesting that the oxidative power of **1** is not significantly affected by the change in the solvent.

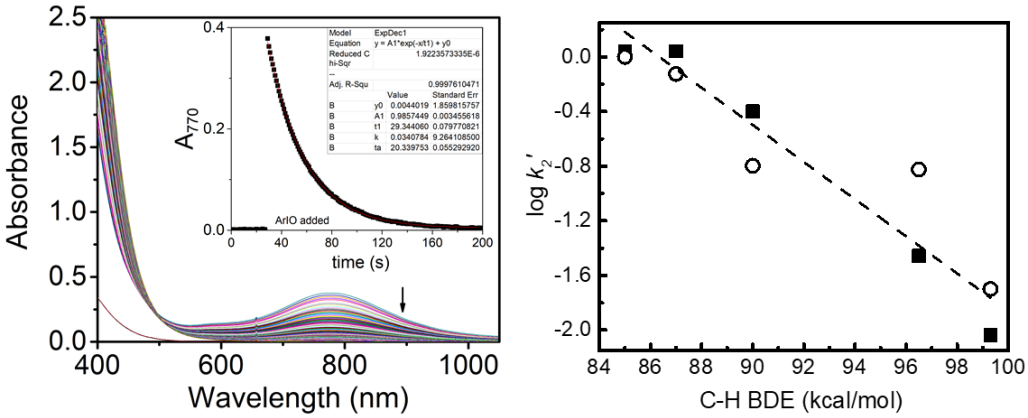

Figure 2.3. (Left) Spectral changes observed over time in the reaction of **1** generated by adding 2 equiv. of ArIO to a 1-mM solution of $[Fe^{II}(Me_3NTB)(CH_3CN)](CF_3SO_3)_2$ in acetone-d_6 with 278 equivalents of cyclohexane at 233K. (Inset) Absorption-vs-time decay profile upon the reaction of **1** with cyclohexane obtained following absorbance changes at 770 nm. It can be fitted well with an exponential function. The decay profiles from other experiments were fit similarly. **(Right)** Plot of log k_2' values for the oxidations of different substrates with **1** generated in acetone-d_6 at 233 K with ArIO as the oxidant (squares) vs substrate C−H BDE's. Open circles denote previously reported values by Seo *et al*. with **1** generated in CH_3CN solvent using mCPBA as the oxidant.[57] The dashed line represents the best fit to the data in acetone-d_6.

Table 2.1. 2nd-order rate constants (k_2) for **1** at 233 K.

Substrates	Bond Dissociation Energies (kcal/mol)	2nd order rate constants in CH_3CN from Seo *et al.*[57] (k_2) M^{-1} s^{-1}	2nd order rate constants in acetone-d_6 from this work (k_2) M^{-1} s^{-1}
Cumene	85	1	1.1
Ethylbenzene	87	1.5	2.2
Toluene	90	0.47	1.2
2,3-DMB	96.5	0.29	0.07
Cyclohexane	99.3	0.25	0.11

Interestingly, the oxidation rates of **1** with hydrocarbon substrates such as cyclooctane, 2,3-dimethylbutane and cyclohexane are comparable with that of $[(TQA)Fe^{IV}(O)]^{2+}$, which is a S = 2 oxoiron(IV) complex and the Compound I model $[(TDCPP\bullet)Fe^{IV}(O)]^{+}$ (H_2TDCPP = *meso*-tetrakis(2,6-dichloro-phenyl)porphin). [57] (Table 2.2) This suggests that high-valent iron complexes can achieve comparable rates of oxidation despite having differences in the ligand architecture and the spin state. More importantly, this warrants that we should look at other factors besides these two when explaining the enhanced oxidation reactivity of oxoiron(IV) complexes.

Table 2.2. 2nd-order rate constants (k_2) comparison of **1** 233 K.

Complex / Substrate	**1** in CH_3CN	**1** in acetone-d_6	$[(TQA)Fe^{IV}(O)]^{2+}$ in CH_3CN	$[(TDCPP\bullet)Fe^{IV}(O)]^{+}$ in 1:1 CH_3CN:CD_2Cl_2
Cyclooctane	2.2	Not measured	3.5	0.51
2,3-DMB	0.29	0.07	0.13	0.076
Cyclohexane	0.25	0.11	0.37	0.11

Furthermore, an Eyring analysis carried out for the oxidation of toluene by **1** between 193 and 263 K affords a $\Delta H^{\ddagger}$ of 29(3) kJ/mol and a $\Delta S^{\ddagger}$ = -132(20) J/mol K (Figure 2.4). The linearity of this plot suggests no dramatic change in the nature of **1** occurs within this temperature range.

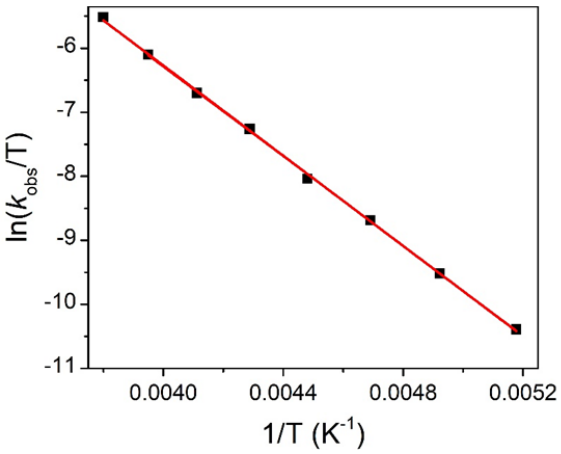

Temperature (K)	Rate constant (s^{-1}) (0.198 M toluene)
193	0.006
203	0.015
213	0.036
223	0.072
233	0.164
243	0.299
253	0.567
263	1.056

Figure 2.4. Eyring plot of the reaction of **1** with toluene (0.198 M) in acetone-d_6 (193 – 263 K) by following the decay of the 770 nm feature of **1**. Upon analysis, the plot yields activation parameters of $\Delta H^{\ddagger}$ = 29(3) kJ/mol and $\Delta S^{\ddagger}$ = -132(20) J/mol K.

2.2.3 Mössbauer characterization of 1 under the new reaction conditions

Mössbauer spectroscopy has been used to study the electronic structure of **1**. The simulation of the Mössbauer spectra of **1** was carried out by the following spin Hamiltonian model:

$$\widehat{H} = D\left(\left(S_z^2 - \frac{1}{3}S(S+1)\right) + \frac{E}{D}\left(S_x^2 - S_y^2\right)\right) + \beta\widehat{\boldsymbol{S}}\cdot\boldsymbol{g}\cdot\boldsymbol{B} + \widehat{\boldsymbol{S}}\cdot\boldsymbol{A}\cdot\hat{\boldsymbol{I}} + \widehat{H}_Q + \widehat{H}_Z \quad (1)$$

$$\widehat{H}_Q = \frac{eQV_{zz}}{12}\left[3\hat{I}_z^2 - \frac{15}{4} + \eta\left(\hat{I}_x^2 - \hat{I}_y^2\right)\right] \quad (1a)$$

$$\widehat{H}_Z = -g_n\beta_n \boldsymbol{B}\cdot\hat{\boldsymbol{I}} \qquad (1b)$$

where the $\widehat{H}_Q$ represents the nuclear quadrupole terms and the $\widehat{H}_Z$ represents the nuclear Zeeman term. All symbols have their conventional definitions. When performing theoretical simulations on different spin systems, we only need to change the electronic spin value *S* in the above expressions.

By applying various magnetic fields on the sample at 4.2 K, it is clear that the sample contains 15% of a high-spin ferric component indicated by the six-line feature (Figure 2.5, simulated by the red curves). To eliminate its interference to the spectral simulations on the major Fe^{IV} species, we simulated the high-spin ferric species by a generic *S* = 5/2 spin model. Subtracting the high-spin ferric component from the raw data effectively helps us perform accurate simulations on the major species, $[Fe^{IV}O(Me_3NTB)(L)]^{2+}$ (**1**), that contributes up to 70% of the total iron in the sample. The spectral simulations for **1** have been shown in Figure 2.6. One exception is that we did not subtract the high-spin ferric component from the zero-field spectrum in Figure 2.6 (Left Panel) because at such a condition, it broadly underlies the baseline of the whole spectrum (from -10 mm/s to 10 mm/s) and therefore the theoretical simulation becomes ineffective. The zero-field spectrum provided the values for the isomer shift and the magnitude of the quadrupole splitting for **1**. These values are similar to those reported for **1** in CH_3CN,[57] suggesting that changing the conditions here did not affect the structure of **1** significantly.[57] It was also identified that there exists another diamagnetic species, which could be a diferric species generated by the decay of **1** (simulated by the parameters in Table 2.3, column "(μ-oxo)-diiron(III)byproduct". Its isomer shift (0.49 mm/s) and quadrupole splitting (1.47 mm/s) reflect the characteristics of a diiron(III) species.

To determine the spin Hamiltonian parameters of **1**, such as *A* and *D* values, in addition to the variable field data measured at 4.2 K, we also performed higher temperature studies on the same sample at 15 K, 20 K, 25 K, 35 K, and 50 K under a 7-T applied field. We noticed that the spectra recorded at 15~25 K may still be in the intermediate electronic relaxation region, which was difficult to simulate theoretically. Thus, we only chose the spectra at 35 K and 50 K to perform our theoretical simulations at the fast electronic relaxation limit, in which we replaced the <S> by $<S_{thermo}>$, the thermo-averaged spin expectation value, in computing the internal magnetic field for the nuclear Zeeman term. To determine *A* and *D* values accurately for **1**, both 4.2 K and higher temperature data are needed, because for complex **1** with an $S = 1$ ground state and a large positive *D* value, 4.2 K high field spectra mainly depend on the magnetic hyperfine field in the xy plane, $\boldsymbol{B}_{hf}(i) = -\langle S_i \rangle A_i / g_n \beta_n$ (i = x,y). Since $\langle S_{x,y} \rangle$ is inversely proportional to *D* for a large positive *D* system, one cannot obtain $A_{x,y}$ accurately from the 4.2 K spectra. However, at an elevated temperature, such as 35 K or 50 K, $\langle S_{x,y} \rangle$, is independent of *D*, allowing one to determine $A_{x,y}$. By group fitting both 4.2 K, 35 K, and 50 K spectra, we obtained a *D* value of 33(3) cm^{-1}, which is typical for an $S = 1$ oxoiron(IV) center. The simulation also estimated the z-direction of the A tensor (A_z). Seo *et al*. obtained $D = 28$ cm^{-1} but with a large variance of 20 - 35 cm^{-1}.[3] It is likely because 1) the purity of the sample was not as high as the one reported in this study, so the spectral features of the impurity in the sample could interfere with the spectral features of the species of interest; and 2) they performed the high-temperature study only at 80 K, at which $<S_{thermo}>$ is generally much smaller than that at 35 K due to the 1/T dependent of $<S_{thermo}>$ with temperature (the Curie Law), which could introduce a larger uncertainty in determining the spin Hamiltonian parameters.[57] Subsequently, their hyperfine tensor values at x and y directions were also

under-estimated, because there exists a positive correlation between the $A_{x/y}$ and the *D* value from the same dataset. Finally, it is worthwhile to notice that we did not subtract out the high-spin ferric component from the high-temperature spectra because its relaxation behavior remains unclear to us; however, with only 15% present in the sample, it should not significantly affect our high-temperature simulations on the major Fe^{IV} species. Also, we kept the *E*/*D* as zero with the current simulations.

Taken together, our Mossbauer data indicate that **1** is formed in a 70% yield under our reaction conditions, which is a value higher than the 57% reported by Seo *et al.*.[57] The remaining 30% of the sample is completed by the diferric (15%) and mononuclear ferric (15%) byproducts. Besides, due to the higher purity of **1** and by carrying out a temperature dependence study at carefully chosen multiple temperature data points, we were able to get a much more reliable value for the *D* value for **1**.

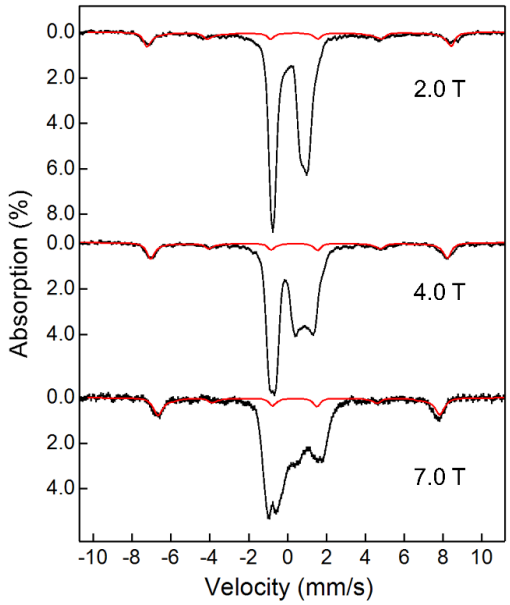

Figure 2.5. 4.2 K Mössbauer spectra of **1** (prepared by adding 2 equiv of ArIO to a 2-mM solution made by dissolving solid

$[Fe^{II}(Me_3NTB)(CH_3CN)](CF_3SO_3)_2$ in acetone-d_6) with various applied magnetic fields (2.0T, 4.0T, 7.0T respectively). Black: experimental spectra for the sample; red: theoretical simulation of the high-spin ferric impurity in the sample.

Table 2.3. Theoretical simulation parameters in the spin Hamiltonian for **1.**

Species	Iron(IV) Component	(μ-oxo)diiron(III) byproduct
Spin state	$S = 1$	$S_{tot} = 0$
Isomer shift (mm/s)	0.03	0.49
D (cm^{-1})	33(3)	-
E/D	0.0	-
Quadrupole splitting (mm/s)	1.62	1.47
η	0.5	0.6
Ax/gnβn (kG)	-225	-
Ay/gnβn (kG)	-225	-
Az/gnβn(kG)	n.d.*	-
Line width (mm/s)	0.28	0.36
Percentage	70%	15%

*n.d = not determined due to the small spin expectation value in the z-direction.

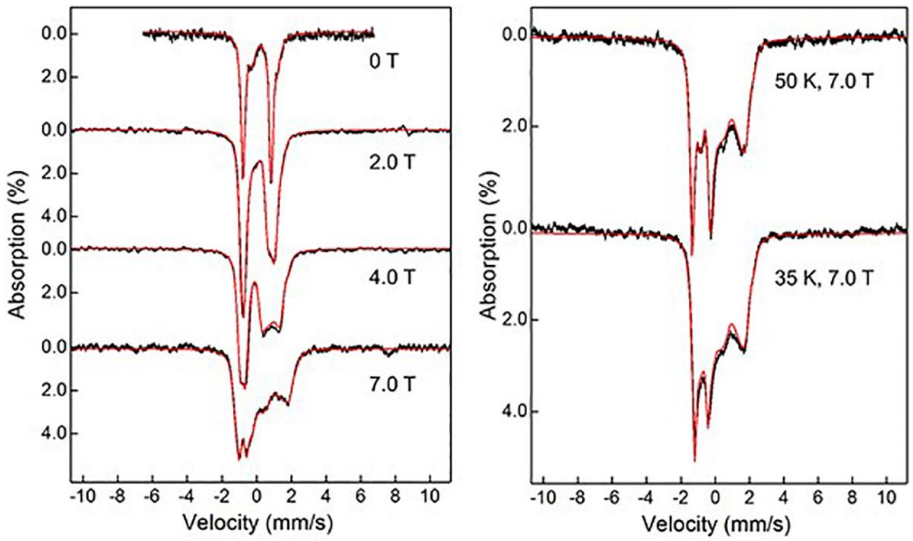

Figure 2.6. Left panel: 4.2 K Mössbauer spectra of **1** with various applied magnetic fields. Black: experimental spectra with a high-spin ferric component removed. Red: theoretical simulation at the slow-relaxation limit. Right panel: Mössbauer spectra of **1** under a 7.0-T applied magnetic field at 35 and 50 K.

2.2.4 XAS characterization of 1 to elucidate its structure at low temperature

Owing to the high instability of **1**, no crystallization attempts were made. However, X-ray absorption spectroscopy has been used to shed light on the structural parameters of this reactive species. A higher concentration sample was prepared under similar conditions to get a reasonable S/N ratio for **1** using this spectroscopic technique. Data collection was done at 10 K and has been processed to elucidate the valence state of iron and the bond metrics in **1**. (Figures 2.7 and 2.8). It exhibits an Fe K-edge energy of 7125.8 eV, like those of other Fe^{IV}=O complexes, and a single pre-edge feature due to 1s→3d transitions at 7114.2 eV with an area of 30 units, which falls into the range typically found for Fe^{IV}=O complexes (27-45 units).[38] The Fourier transformed EXAFS spectrum of **1** shows two prominent features at R + Δ ~ 1.5 and 2.9 Å. The first shell is best fit with 0.7 N/O scatterer at 1.65 Å (arising from the Fe=O unit) and N/O scatterers at 1.98 and 2.17 Å arising from the ligating atoms of the Me_3NTB ligand and the solvent (Table 2.4). The outer shell is best fit with C scatterers at 3.05 and 3.26 Å, which are associated with carbon atoms on the benzimidazole rings, as observed in the crystal structures of iron-benzimidazole complexes.[57,110–112] The average Fe–N/O distance of 2.06 Å is within experimental error essentially the same as the values predicted by DFT for a 6-coordinate **1** in an *S* = 1 state (2.03 Å) and for an *S* = 2

trigonal bipyramidal **1** (2.04 Å), but is much smaller than the 2.14-Å distance calculated for its *S* = 2 six-coordinate counterpart (Table 2.5),[59] which excludes the latter as a proper description for **1** at 10 K.

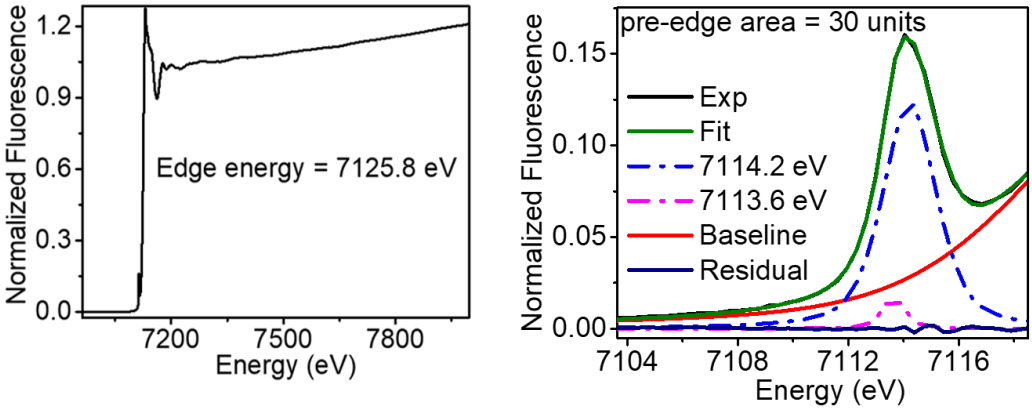

Figure 2.7. (**Left**) Fe K-edge X-ray absorption near-edge structures (XANES, fluorescence excitation) of **1**. (**Right**) Pre-edge region analysis of **1**. The experimental data (black), baseline (red), pre-edge peak components (blue and pink), residuals (dark blue), and total fit (green) are shown.

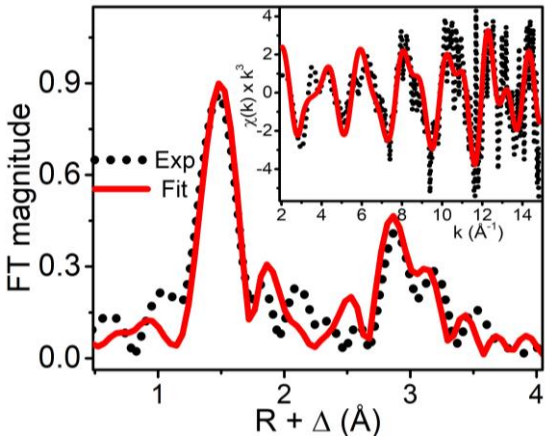

Figure 2.8. Fourier-transformed *k*-space EXAFS data of **1** in acetone-d_6 at 10 K the first shell of which is fit with 0.7 O @ 1.65 Å, 3 N @ 1.98 and 2 N @ 2.17 Å. The inset shows the *k*-space spectrum.

Table 2.4. Fit parameters for the EXAFS data of **1**. Fit 9 gives the most reasonable fit of the experimental data.

	Fe-N/O			Fe-N/O			Fe-O			Fe•••C			Fe•••C			GOF		
Fit	N	r(Å)	σ^2(x 10^{-3})	N	r(Å)	σ^2(x 10^{-3})	N	r(Å)	σ^2 (x 10^{-3})	N	r(Å)	σ^2(x 10^{-3})	N	r(Å)	σ^2(x 10^{-3})	F	F-factor (x10^3)	E_0
1	5	1.95	9.2													898	928	-17.2
2	4	1.93	5.1													836	896	-21.9
3	4	1.94	5.2	1	2.19	1										823	889	-9.3
4	3	1.96	2.2	2	2.13	2.4										736	840	-6.5
5	3	1.95	2.9	2	2.13	4.4	1	1.65	3.6							590	753	-4.3
6	3	1.96	3.2	2	2.14	3.9	0.7	1.65	1.8							594	755	-3.1
7	3	1.98	3.8	2	2.17	3.5	0.7	1.65	1.3	4	3.26	0.1				542	721	0.5
8	3	1.98	3.7	2	2.17	3.2	0.7	1.65	1.3	5	3.26	1.2				569	739	1.1
9	**3**	**1.98**	**3.6**	**2**	**2.17**	**2.9**	**0.7**	**1.65**	**1.3**	**5**	**3.26**	**1.2**	**3**	**3.05**	**2.8**	**511**	**700**	**1.9**
10	3	1.98	2.8	2	2.16	1.7				5	3.25	1.4	3	3.04	2.5	680	808	-0.4
11	3	1.96	3.2	2	2.14	3.9	0.7	1.65	1.8				3	2.91	13.1	582	748	-2.5

Fit 9 represents the best fit; Fit 10 shows the importance of the O scatterer at
1.65 Å; Fit 11 shows the importance of C shell at 3.26 Å

Table 2.5. Comparison of XAS bond metrics for 1 with results from DFT calculations

Units	DFT-calculated values for $S = 1$ $[Fe^{IV}(O)(Me_3NTB)-(CH_3CN)]^{2+}$	DFT-calculated values for $S = 2$ $[Fe^{IV}(O)(Me_3NTB)-(CH_3CN)]^{2+}$	DFT-calculated values for $S = 2$ TBP $[Fe^{IV}(O)(Me_3NTB)]^{2+}$	XAS-based metrics for **1**
reference	[59]	[59]	[59]	This work
average Fe–N (Å)	2.026	2.135	2.043	2.06
average $Fe–L_{equatorial}$ (Å)	1.982	2.116	1.998	3 Fe-N/O at 1.98 Å,
$Fe–N_{amine}$ (Å)	2.201	2.212	2.18	2 Fe-N/O at 2.17 Å,
Fe–NCMe (Å)	2.005	2.326	N/A	
Fe=O (Å)	1.625	1.619	1.618	Fe-O 1.65 Å

2.2.5 NMR characterization of 1 and analysis of the structure and the spin state at higher temperatures

The XAS and Mössbauer spectroscopic studies we have described thus far have been carried out at liquid helium temperatures and support the assignment of an $S = 1$ ground state for **1** at this temperature.[57] However, such experiments do not address the DFT-derived possibility that **1** may convert into a C_3-symmetric trigonal bipyramidal (TBP) isomer at higher temperatures by loss of the solvent ligand to gain access to a highly reactive $S = 2$ species.[59] We have thus carried out ^{1}H NMR experiments in acetone-d_6 solution at 193 K to probe the symmetry of the complex and

assess its spin state at this temperature, but our results described below do not support the trigonal bipyramidal hypothesis.

In previous work, Fe^{IV}=O complexes have been shown to exhibit relatively sharp, paramagnetically shifted peaks in the +100 to −100 ppm region that arise from ligand protons.[113–116] COSY cross peaks could also be observed under favorable circumstances.[113] We first present the ^{1}H NMR spectrum of $[Fe^{IV}(O)(N2Py2B)]^{2+}$ [111,117] (N2Py2B = *N*,*N*-bis((1-methyl-1*H*-benzoimidazol-2-yl)-methyl)-1,1-di(pyridin-2-yl)-methanamine) (**2**, Figures 2.9, 2.10a and 2.11) to guide us in interpreting the NMR data for **1**. Complex **2** has a mirror plane of symmetry that gives rise to a relatively simple ^{1}H-NMR spectrum with seven sharp peaks corresponding to protons on the heterocyclic ligands; all have unit intensity except for the peak at -0.9 ppm, which represents 3 H's and therefore is easily assigned to the *N*-Me group of the *N*-Me-benzimidazole donor. The peaks at 48, 9 and -19 ppm can be assigned respectively to pyridine β-, γ-, and β'-protons by analogy to peaks in the spectrum of $[Fe^{IV}(O)(N4Py)]^{2+}$ (Figure 2.11 and 2.12) (N4Py = *N,N*-bis(pyridyl-2-methyl)-bis(2-pyridyl)methylamine),[113] while peaks at 15, 12, and 5 ppm can be associated with benzimidazole C4-H, C5-H, and C6-H protons. Their assignments follow from their T_1's and linewidths that reflect their varying distances from the metal center (Table 2.7). Moreover, the assignment of C5-H and C4-H is also supported by the cross peak between these two signals observed in the COSY spectrum of the complex (Figure 2.12). The remaining benzimidazole C7-H and pyridine α protons are likely to have broader linewidths due to their proximity to the Fe=O unit.

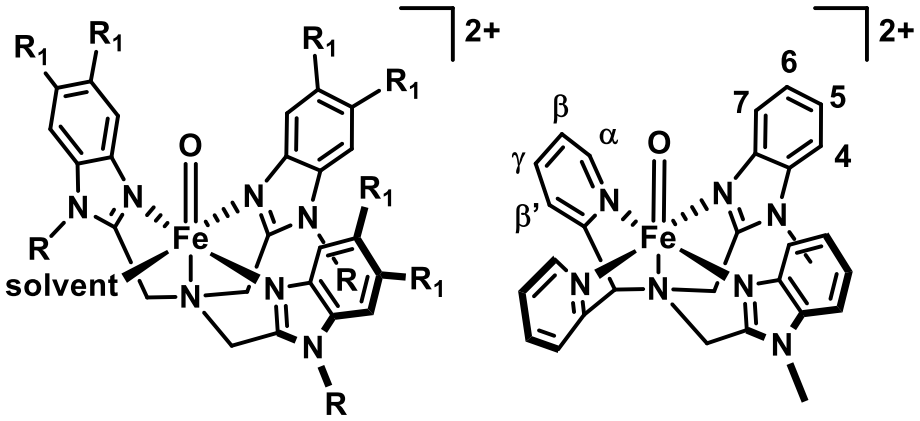

1: L = Me_3NTB, R = Me, R_1 = H **2: L = N2Py2B**
1a: L = NTB, R = R_1 = H
1b: L = Me_3NTB*, R = R_1 = Me

Figure 2.9. $[Fe^{IV}(O)(L)]^{2+}$ complexes used for the ^{1}H NMR study. The labeling protocol for protons on the heterocyclic rings used is shown for **2**.

Assuming ideal symmetry, a C_3-symmetric trigonal bipyramidal $[Fe^{IV}(O)(Me_3NTB)]^{2+}$ complex should exhibit only one set of benzimidazole ring proton peaks, while a six-coordinate complex with C_s symmetry should give rise to two sets of peaks with a 2:1 intensity ratio, respectively arising from the two benzimidazoles trans to each other and from the benzimidazole trans to the bound solvent (Figure 2.9). As shown in Figure 2.10d, the ^{1}H NMR spectrum of **1** at 193 K exhibits nine relatively sharp features with unit intensity in the 0 – 25 ppm region, which are absent in the spectrum of the decayed complex (Figure 2.14). The number of peaks observed argues against a C_3- or a C_s-symmetric complex. Signal assignment is aided by the ^{1}H NMR spectra of $[Fe^{IV}(O)(NTB)]^{2+}$ (**1a**) and $[Fe^{IV}(O)(Me_3NTB^*)]^{2+}$ (**1b**) (Figure 2.9). While **1a** shows nine peaks very similar to those found for **1** (Figures 2.15 and 2.17), **1b** has only 3 peaks (Figures 2.10c and 2.16), which are assigned to the C4-H protons due to the replacement of the C5- and C6-H atoms with methyl groups (see

Figures 2.14 - 2.18 for the full spectra of **1**, **1a** and **1b**). Thus, there is no element of symmetry in solutions of **1**, **1a** and **1b**, and each benzimidazole is in a unique environment.

Closer scrutiny of the spectrum of **1** in Figure 2.10d shows that two of the C4-H peaks are similar to each other in chemical shift and linewidth but distinct from the third one (Table 2.6). Similar patterns can be found for the C-4H peaks of **1a** (Figure 2.15) and **1b** (Figures 2.10c and 2.16), reflecting a slight distortion of the six-coordinate Fe^{IV}=O center by a twist of the two trans benzimidazole planes relative to each other along the N–Fe–N axis. Thus, the NMR data point to a six-coordinate structure with bound solvent as the dominant species for **1** in solution, with no detectable evidence for a C_3-symmetric isomer.

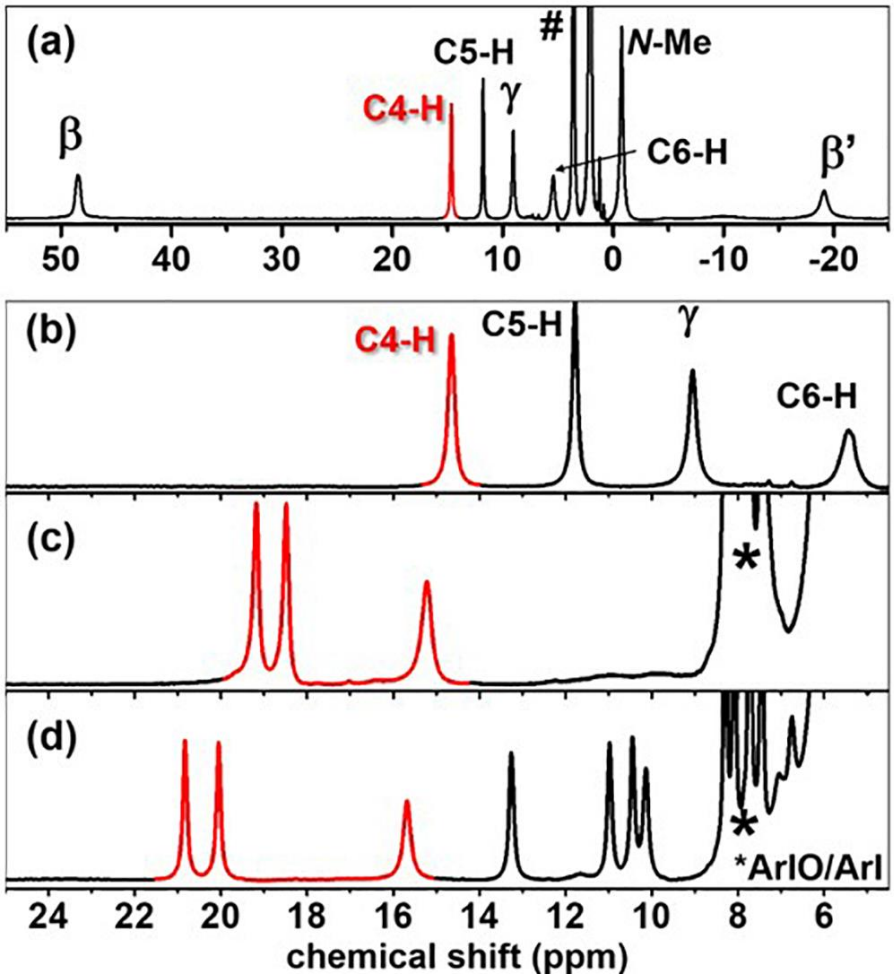

Figure 2.10. The ^{1}H NMR spectra of a) **2** (55 to -25 ppm), b) **2** (25 to 4.5 ppm), c) **1b** (25 to 4.5 ppm), and d) **1** (25 to 4.5 ppm) in acetone-d_6 at 193 K. The peaks highlighted in red are assigned to the benzimidazole C4-H protons. See Figures 2.14 – 2.18 and Table 2.8 for more information. Peaks marked with # derive from residual solvent signals.

Table 2.6. ^{1}H NMR properties of the benzimidazole C4-H protons of **1**, **1a**, **1b**, and **2** in acetone-d_6.

Complex	Experimental shifts, ppm (FWHM in Hz) at 193 K	DFT-predicted shifts for **1** and **2** (ppm) at 193 K
1	21 (45), 20 (45), 16 (80)	22, 23, 2 (*S* = 1, 6-coordinate) 60, 67,110 (*S* = 2, 6-coordinate) 77 (*S* = 2 TBP)
1a	20 (58), 19.5 (51), 16 (86)	
1b	19 (62), 18.5 (59), 15 (110)	
2	15 (75)	17 (*S* = 1); 86 (*S* = 2)

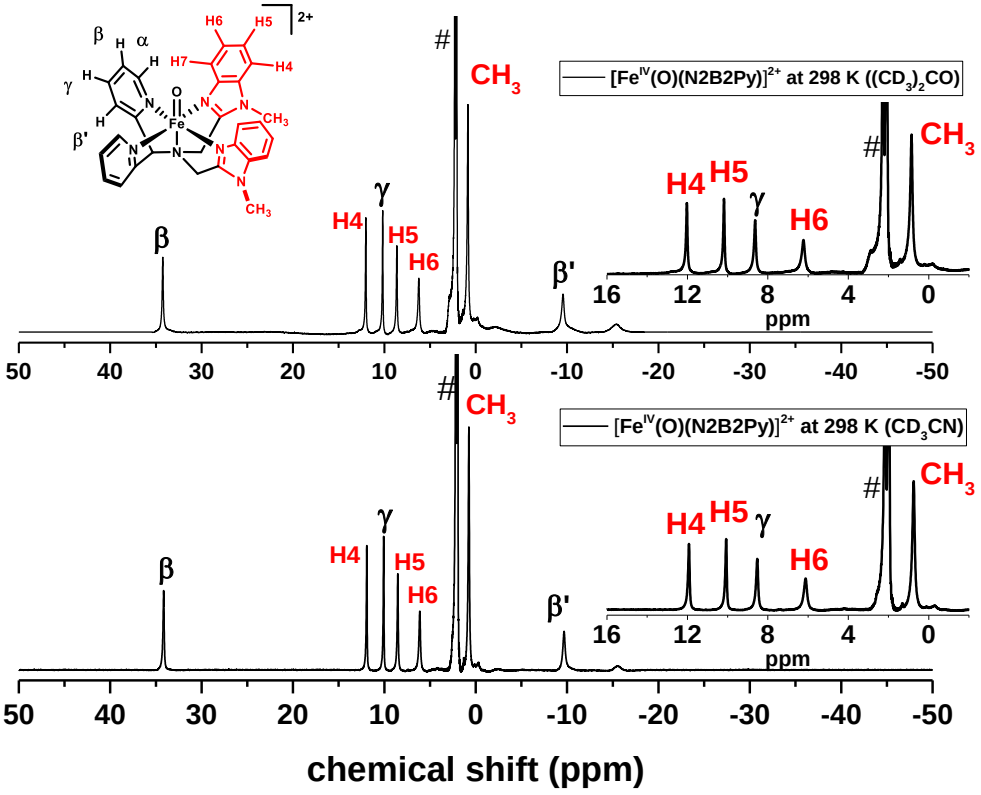

Figure 2.11. ^{1}H NMR spectra for $[Fe^{IV}(O)(N2Py2B)]^{2+}$ (**2**) in acetone-d_6 (top) and CD_3CN (bottom) at 298 K. The stacked insets show the expanded regions from –2 to 16 ppm.

Table 2.7. ^{1}H NMR properties of complex **2** obtained in acetone-d_6 at 298 K.

Legend	H4	H5	H6	CH_3	py-γ	py-β'	py-β
δ (ppm)	12	10	6.2	0.8	8.6	-9.6	34
FWHM (Hz)	56	44	96	72	68	185	85
T_1 (ms)	36	59	13	9.8	24	10	15
*d (Fe•••H) (Å)	6.3	6.8	5.7	5.3	5.7	4.8	5.0

*Distance estimated from the crystal structure of **2**, shown from its cross-section.[111]

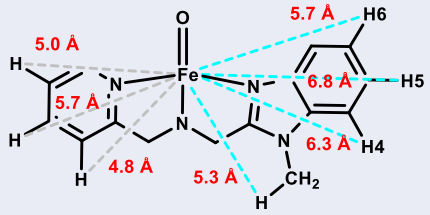

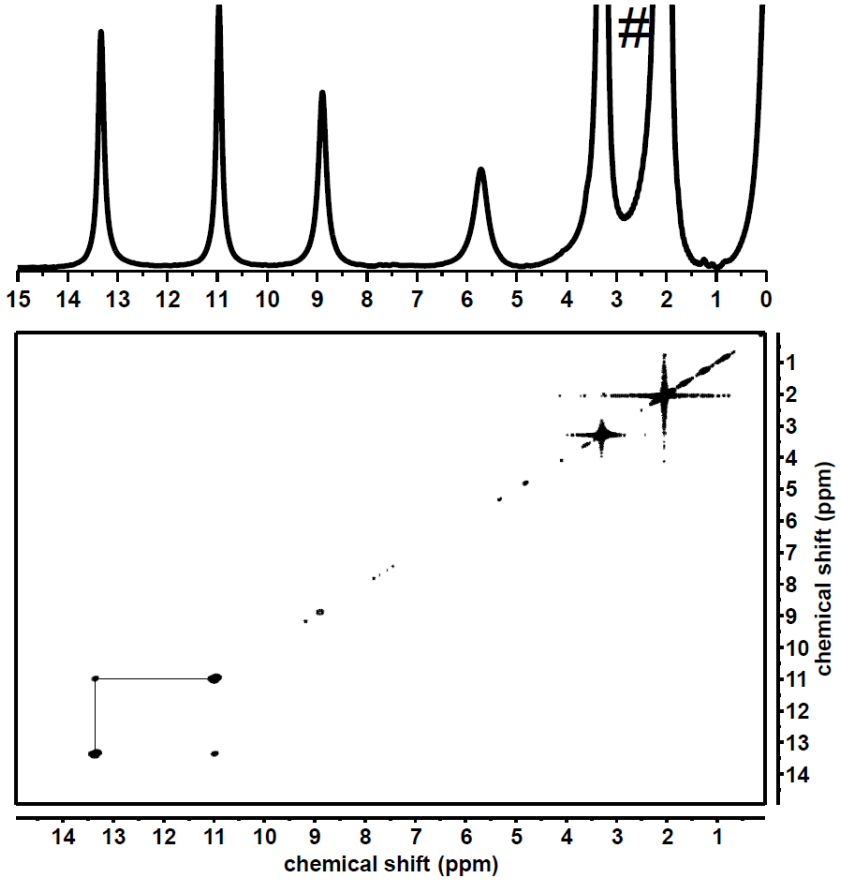

Figure 2.12. ^{1}H COSY NMR spectrum of complex **2** in acetone-d_6 at 233 K from 0 to 15 ppm. Only the cross peak between the resonances at 13 and 11 ppm was observed. The lower temperature was chosen to minimize the self-decay of **2** over the course of data collection of over 12 hours on a 10-mM sample. The faster relaxation of C6-H at 5.9 ppm likely prevented cross peaks to be observed.

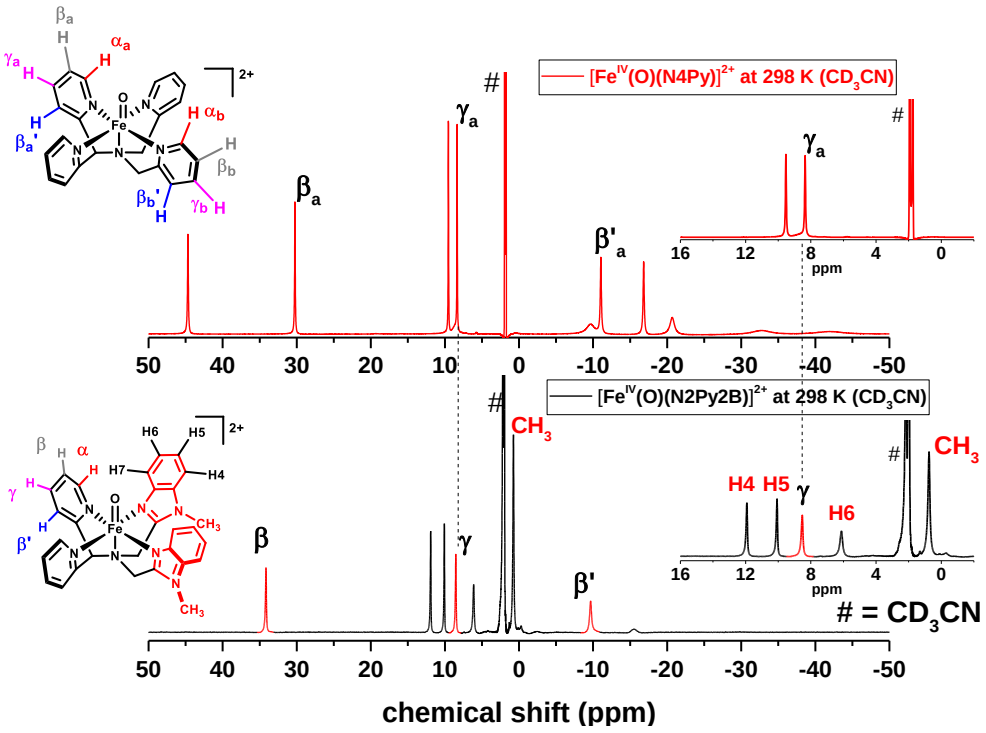

Figure 2.13. Stacked ^{1}H NMR spectra of **2** (bottom) and $[Fe^{IV}(O)(N4Py)]^{2+}$ (top) in CD_3CN at 298 K, along with assignments. The stacked insets show the expanded regions from –2 to 16 ppm. A dotted black line is drawn across the insets and the full spectra to distinguish the pyridine γ protons from benzimidazole protons.

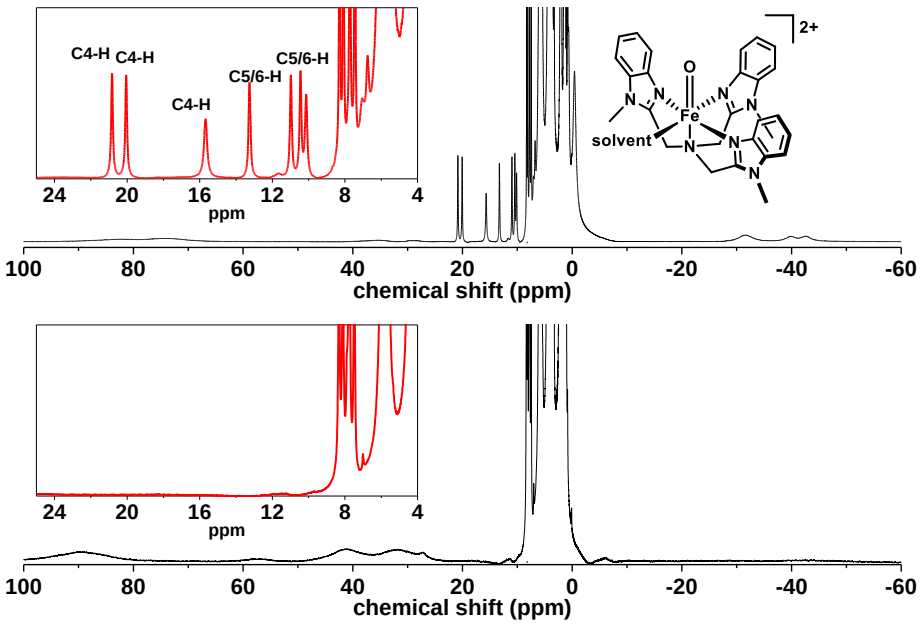

Figure 2.14. Stacked ^{1}H NMR spectra of complex **1** (prepared by adding 2 equiv of ArIO to a 4-mM solution made by dissolving solid $[Fe^{II}(Me_3NTB)(CH_3CN)](CF_3SO_3)_2$ in acetone-d_6) (top) and after it has decayed (bottom), obtained in acetone-d_6 at 193 K. Insets show the expanded region from 4 to 25 ppm.

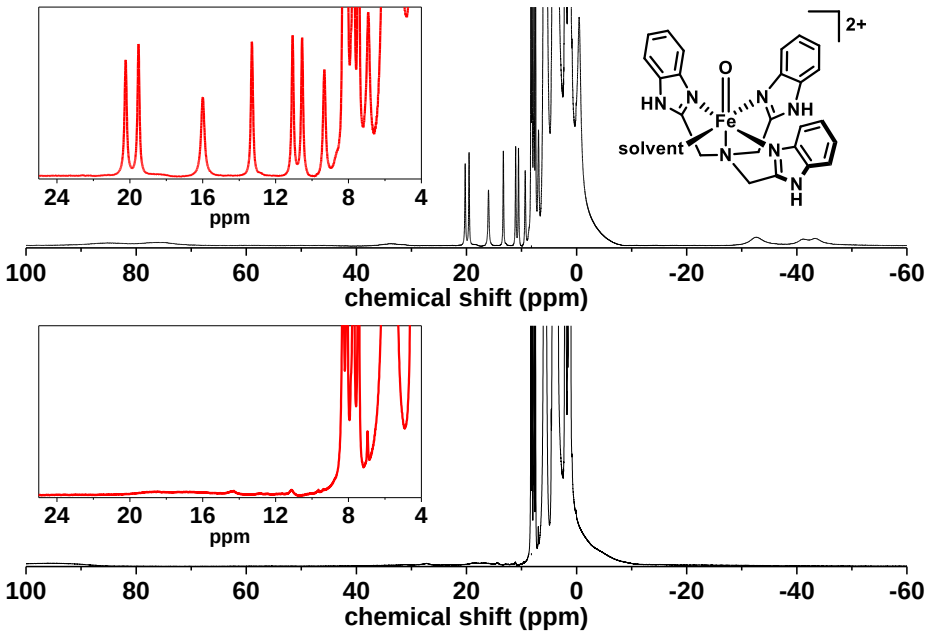

Figure 2.15. Stacked ^{1}H NMR spectra of complex **1a** (prepared by adding 2 equiv of ArIO to a 4-mM solution made by dissolving solid $Fe^{II}(NTB)(CF_3SO_3)_2$ in acetone-d_6) (top) and after it has decayed (bottom), obtained in acetone-d_6 at 193 K. Insets show the expanded regions from 4 to 25 ppm.

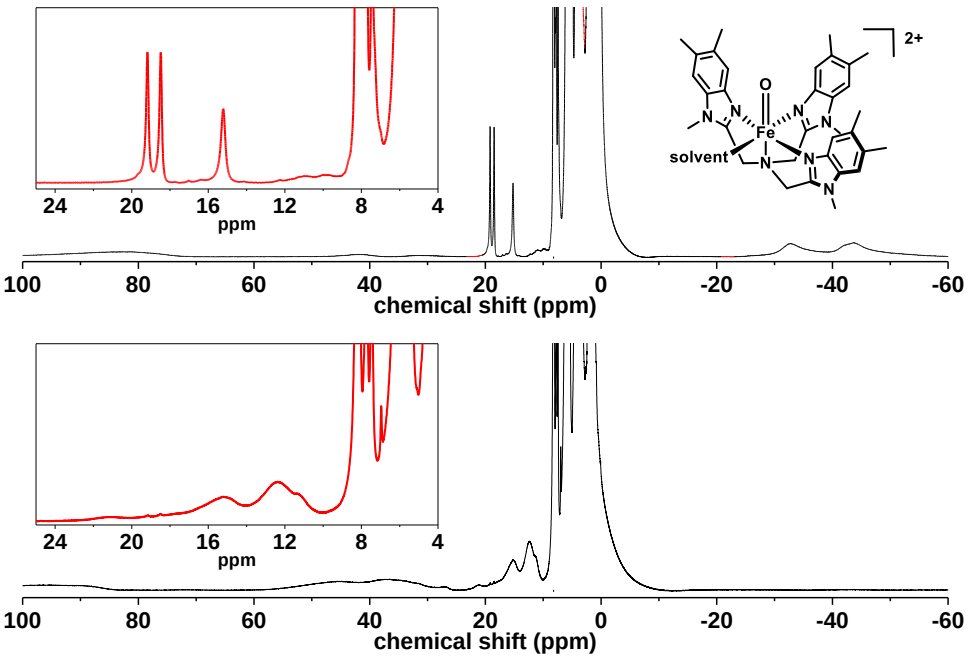

Figure 2.16. Stacked ^{1}H NMR spectra of complex **1b** (prepared by adding 2 equiv of ArIO to a 4-mM solution made by dissolving solid $Fe^{II}(Me_3NTB^*)(CF_3SO_3)_2$ in acetone-d_6) at 193 K (top) and after its thermal decay (bottom). Insets show the expanded region from 4 to 25 ppm.

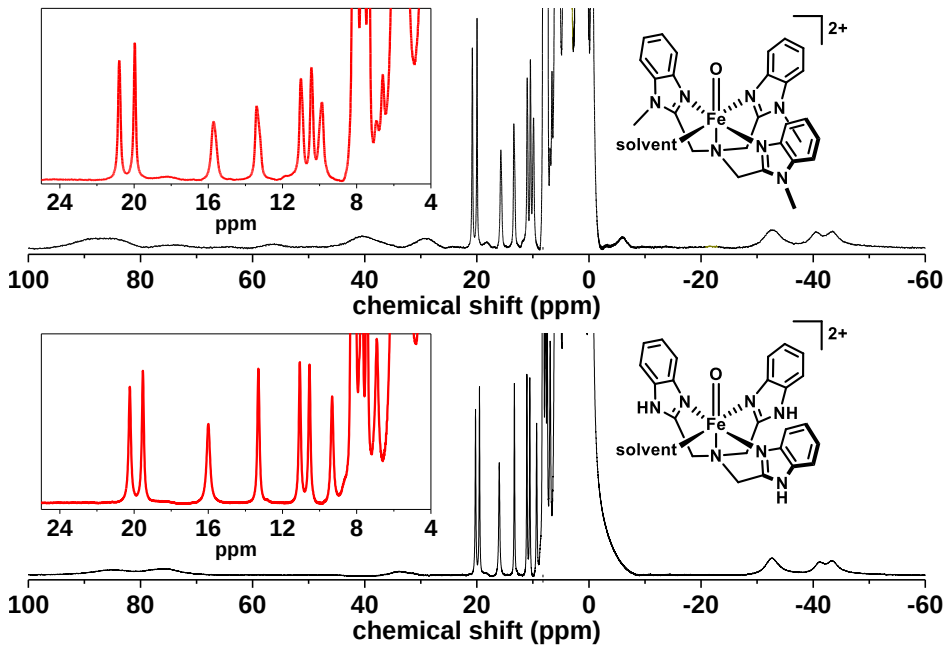

Figure 2.17. Stacked ^{1}H NMR spectra of complex **1** (top) and complex **1a** (bottom), (prepared by adding 2 equiv of ArIO to a 4-mM solution of $[Fe(R_3NTB)(L)]^{2+}$ in acetone-d_6) at 193 K. Insets show the expanded regions from 4 to 25 ppm.

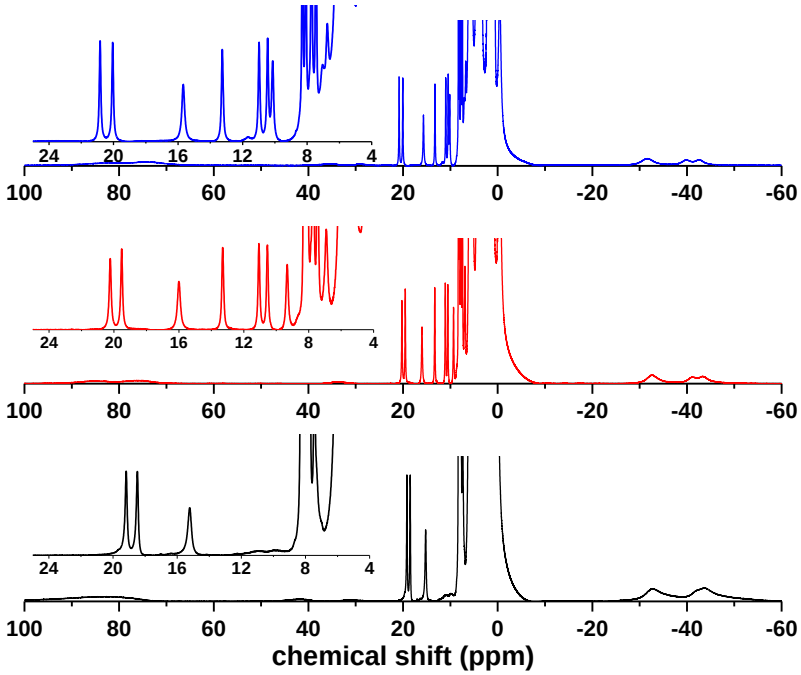

Figure 2.18. Stacked ^{1}H NMR spectra of complex **1** (top), complex **1a** (middle) and complex **1b** (bottom) at 193 K. Insets show the expanded regions from 4 to 25 ppm.

Table 2.8. ^{1}H NMR assignment table for benzimidazole containing complexes

Complex	H4, ppm (FWHM in Hz)	H5/H6, ppm (FWHM in Hz)	CH_3 at C5/C6, ppm (FWHM in Hz)	N-CH_3/N-H, ppm (FWHM in Hz)	H7, ppm (FWHM in Hz)
$[Fe^{IV}(O)(Me_3NTB)(L)]^{2+}$ (**1**)	20.8 (45), 20.0 (45), 15.7 (80)	13.3 (50), 11.0 (48), 10.5 (48), 10.1 (61), 7.0 (-)*, 6.8 (-)*			
$[Fe^{IV}(O)(Me_3NTB*)(L)]^{2+}$ (**1b**)	19.2 (62), 18.5 (59), 15.2 (110)	-	5.1 (47), 4.9 (46)		
$[Fe^{IV}(O)(NTB)(L)]^{2+}$ (**1a**)	20.2 (58), 19.5 (51), 16.0 (86)	13.3 (54), 11.0 (50), 10.5 (50), 9.3 (65), 6.9 (-)*			
$[Fe^{IV}(O)(N2Py2B)]^{2+}$ (**2**)	14.9 (75)	11.9 (64), 5.4 (170)	-	-0.9 (170)	-
$[Fe^{II}(Me_3NTB)(L)]^{2+}$	37.3 (130)	-0.6 (190), 0.5 (330)	-	22.8 (200)	
$[Fe^{II}(Me_3NTB*)(L)]^{2+}$	36.2 (110)	-	0.5 (65), 3.8 (70)	27.1 (140)	
$[Fe^{II}(NTB)(L)]^{2+}$	37.4 (110)	-0.2 (110), 2.0* (-)	-	63.6 (650)	
$[Fe_2$(N-Et-HPTB)-$(O_2CC_6H_5)]^{2+}$ [26] in CD_3CN at 298 K (T_1 in ms listed in place of FWHM)	δ: 20.6 (37 ms)	β: 7.3 (21 ms) / γ: 4.5 (53 ms)	-	N-CH_2: 8.6 (18 ms), 7.4 (21 ms); N-CH_3: 0.1 (30 ms)	α: 18.3 (1 ms)

* Signals close to residual signals of ArIO/ArI or acetone-d_6, making FWHM less reliable.

Solvent used is acetone-d_6 and the temperature for the measurements is 193 K unless otherwise specified.

The observation of well-resolved paramagnetically shifted peaks in the ^{1}H NMR spectra of **1**, **1a** and **1b** at 193 K provides a means to evaluate the spin state of the Fe^{IV}=O center at this temperature, by comparison to those of **2**, which is unequivocally an *S* = 1 complex. Figure 2.10 shows that the benzimidazole C4-H protons of **1** and **1b** have chemical shifts comparable to those of **2**, leading us to favor an *S* = 1 spin state assignment for **1** and **1b**. Given a threefold increase in its magnetic susceptibility, the corresponding *S* = 2 isomer should exhibit significantly larger paramagnetic shifts. Unfortunately, there are no reported examples to date of NMR data for *S* = 2 Fe^{IV}=O complexes, but this notion is supported by the NMR data for mononuclear *S* = 2 Fe^{II}(NTB) complexes (Table 2.8). To fill this knowledge gap, we have turned to DFT methods (See Experimental Section for computational details) to predict the paramagnetic shifts of **1** in the *S* = 1 and 2 states using a protocol[118] that Borgogno *et al.* have successfully applied in reproducing the paramagnetic shifts observed for the *S* = 1 complexes $[Fe^{IV}(O)(TPA)]^{2+}$ (TPA = tris(pyridyl-2-methyl)amine) and $[Fe^{IV}(O)(TMC)]^{2+}$ (TMC = 1,4,8,11-tetramethyl-1,4,8,11-tetraazacyclotetradecane).[114–116] As shown in Table 2.6, there is good agreement between the experimental data for **1** and **2** and values calculated for the *S* = 1 complexes, but the shifts predicted for their *S* = 2 counterparts are generally much larger, commensurate with the higher paramagnetism expected for an *S* = 2 center. Thus, the NMR data show that **1** has an *S* = 1 spin state in acetone solution at 193 K. In addition, the linear Eyring plot for the oxidation of toluene by **1** between 193 and 233 K confirms that the ground spin state of **1** does not change in this temperature range.

2.3 Discussion

In summary, we have extended the lifetime of thermally unstable and highly reactive complex **1** by a solvent change to acetone-d_6, allowing its characterization at 193 K by ^{1}H NMR to probe its solution-state geometry and spin state. The number of NMR peaks observed for **1** excludes the C_3-symmetric trigonal bipyramidal structure favored by DFT to be the major species in solution.[59] Furthermore, the ^{1}H-NMR shifts observed for the benzimidazole ring protons of **1** are not very different from those of the bona fide S = 1 complex **2** but much smaller than predicted for its 6-coordinate or trigonal bipyramidal S = 2 counterparts (Table 2.6), so **1** must be in an S = 1 state in solution. Thus, its high reactivity at 193-233 K cannot arise from its thermal conversion to a more reactive S = 2 form by loss of a solvent ligand, an attractive hypothesis proposed by Nam.[12]

A rationale commonly invoked to explain the reactivity of nonheme oxoiron(IV) complexes is the notion of Two-State Reactivity (TSR) as first postulated by Shaik.[45,55] This idea has been applied to **1** in 2011,[57] for which spin crossover to the more reactive S = 2 reaction surface occurs as the Fe^{IV}=O unit interacts with a substrate C–H bond along the reaction coordinate. As these are events postulated to occur in the transition state, experimental confirmation is not possible.

Alternatively, a more thermodynamic approach could be applied, as favored by Mayer,[119] in which the toluene HAT reactivity of a metal-oxo species is demonstrated to correlate with the bond dissociation energy (BDE) of the MO–H bond formed (Figure 2.19),[120–124] even though the properties of the oxidants in this correlation have been measured in solvents that range in polarity from benzene to water. To obtain the MO–H bond dissociation energy requires the measurement of the redox potential of the oxidized metal-oxo species and the pK_a of the reduced MO–H

proton, but such values have been challenging to obtain. Indeed, only for one nonheme Fe^{IV}=O complex has its Fe^{III}O–H bond dissociation energy been reliably assessed.[125,126] This unique complex $[Fe^{IV}(O)(H_3buea)]^-$ (H_6buea = tris[(N'-*tert*-butylureaylato)-*N*-ethylene]amine) has been characterized by Borovik and found to have an Fe^{III}O–H bond dissociation energy of 87 kcal mol^{-1}.[125,126] Unfortunately, very little has been reported about its HAT reactivity, which may be significantly attenuated by the bulky groups that surround the Fe^{IV}=O unit.

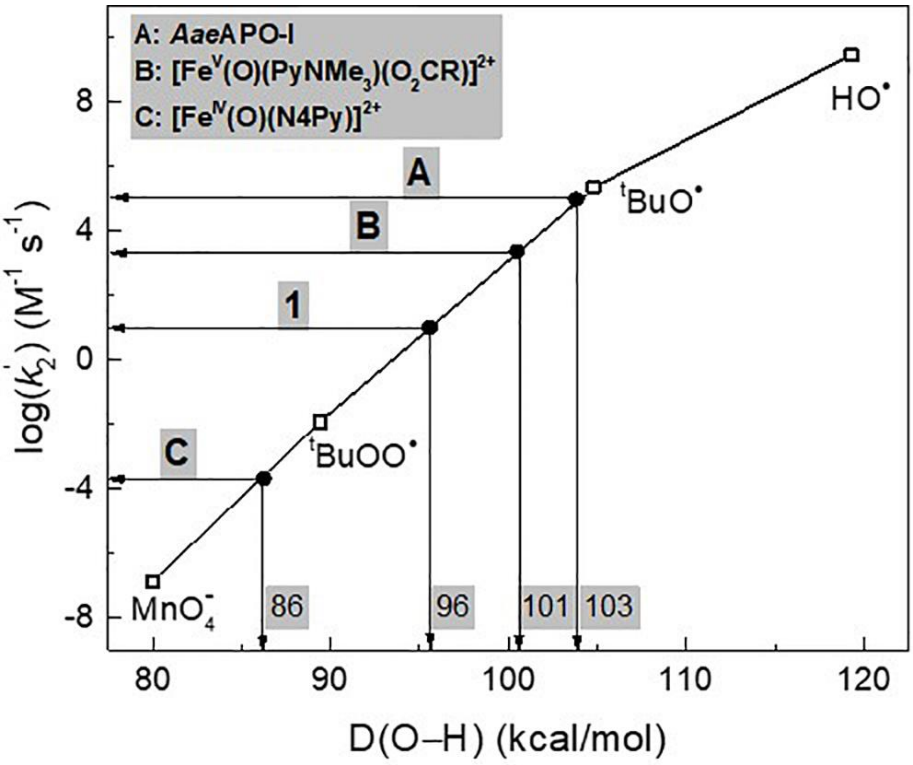

Figure 2.19. Plot of log k_2' values for toluene oxidation by various oxidants vs. the strength of the O**–**H bond formed at room temperature. Log k_2' values for *Aae*APO-I, $[Fe^V(O)(PyNMe_3)(O_2CR)]^{2+}$ and $[Fe^{IV}(O)(N4Py)]^{2+}$ were reported in refs [127–129]; values for the oxidants represented by the open squares were reported in refs [130–133]. The black line passes through open squares, which correspond to rate constants for permanganate and

tert-butylperoxyl, *tert*-butoxyl and hydroxyl radicals. The solid circles in the plot represent other high-valent Fe=O oxidants A, B, and C for which toluene oxidation rates have been measured.

The plot in Figure 2.19 may be used to estimate the BDE of the FeO–H bond formed after HAT by measuring the toluene oxidation rate of the corresponding Fe=O oxidant at 25 °C. For the prototypical $[Fe^{IV}(O)(N4Py)]^{2+}$ complex, the BDE of the corresponding $Fe^{III}O$–H bond can be estimated to be 86 kcal mol^{-1} based on a toluene k_2' value of 2 x 10^{-4} $M^{-1}s^{-1}$.[129] Similarly, respective $Fe^{IV}O$–H bond dissociation energies of 103 and 101 kcal mol^{-1} have been associated with the much more reactive Cpd-I intermediate of the peroxygenase *Aae*APO characterized by Groves[127,134] and the nonheme iron(V) oxidant $[Fe^{V}(O)(PyNMe_3)(O_2CR)]^{2+}$ ($PyNMe_3$ = 3,6,9-trimethyl-3,6,9-triaza-1(2,6)-pyridinacyclodecaphane) described by Costas and coworkers.[128] Based on k_2' value of 9.2 $M^{-1}s^{-1}$ estimated for **1** at 25 °C from the Eyring plot for toluene oxidation shown in Figure 2.4, **1** is deduced to have an $Fe^{III}O$–H bond dissociation energy of 96 kcal mol^{-1}, which is 10 kcal mol^{-1} higher than that for $[Fe^{IV}(O)(N4Py)]^{2+}$, reflecting a difference in toluene oxidation rates of over four orders of magnitude. As they have substrate oxidation rates comparable to those of **1**, the S = 2 $[(TQA)Fe^{IV}(O)]^{2+}$ complex and the Compound I model $[(TDCPP\bullet)Fe^{IV}(O)]^{+}$ (H_2TDCPP = *meso*-tetrakis(2,6-dichloro-phenyl)porphin)[57] must have similar FeO–H bond dissociation energies despite differences in iron(IV) ligand environment and overall spin state. Clearly, the big challenge presented by the above comparisons is to devise ways to independently assess FeO–H bond dissociation energies for these oxidants, and the evidence we have obtained for the geometry

and spin state of **1** serves as a basis for future efforts to determine the key thermodynamic factors that govern these reactions.

2.4 Conclusion

It is of paramount importance that we understand the variables that are responsible for high oxidation rates in the enzymes. This will help us incorporate similar strategies in synthetic models and develop better catalysts for versatile chemical transformations. Our work here clearly shows that having a high-spin iron(IV) center is not mandatory to have a highly reactive complex as previously proposed. Our publication will drive the search for other factors such as thermodynamic forces that need to be explored while evaluating the reactivity of oxoiron(IV) models in C–H bond activation reactions. Moreover, most of the spin-state determinations for oxoiron(IV) complexes are done in the frozen state using Mössbauer spectroscopy. However, the oxidation rates are measured in liquid solution at much higher temperatures, where the spin-state determinations are more challenging for reactive complexes. These are the complexes we are most interested in as they can mimic the high rates of oxidation that are seen in the biological systems. Our strategy to utilize paramagnetic NMR shifts solves this problem where magnetic susceptibility is a function of unpaired electrons on the iron(IV) center and will, therefore, be a determinant of the spin-state. Of course, appropriate reaction optimization needs to be carried out to be able to use NMR as a viable tool to gather such information for often unstable complexes.

2.5 Experimental Section

2.5.1 Materials

Commercially available solvents like anhydrous acetonitrile, 2,2,2-trifluoroethanol (TFE) and deuterated acetone were used without further purification, unless otherwise noted. 2-(*tert*-butylsulfonyl)iodosylbenzene (2-(^{t}BuSO$_2$)C$_6$H$_4$IO),[135,136] (*Caution*: An injury was recently reported while attempting to synthesize this oxidant, so this synthetic procedure should be carried out with the appropriate safety precautions and protective equipment) NTB,[137] Me$_3$NTB,[57] NTB*,[138] and [Fe^{II}(Me$_3$NTB)(CH$_3$CN)](CF$_3$SO$_3$)$_2$[57] were synthesized as reported. Fe^{II}(OTf)$_2$•2CH$_3$CN was prepared according to the published procedure.[139] All oxygen- and moisture-sensitive compounds were synthesized in a nitrogen-filled glovebox. The substrates cyclohexane, 2,3-dimethylbutane, toluene, ethylbenzene, and cumene used in kinetic experiments were passed through a plug of silica before use. All kinetic experiments were carried out under nitrogen.

Ligand names and structures

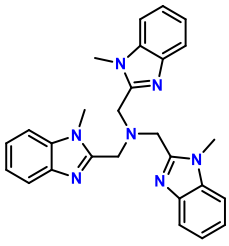	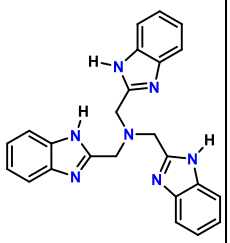	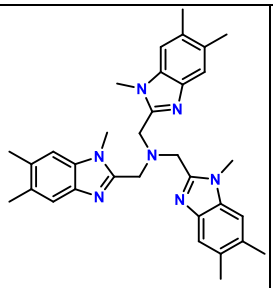	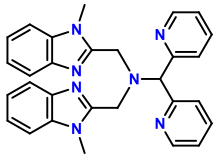
Me$_3$NTB	**NTB**	**Me$_3$NTB***	**N2Py2B**
tris((1-methyl-1*H*-benzo[d]imidazol-2-yl)-methyl)amine	tris((1*H*-benzo[d]imidazol-2-yl)-methyl)amine	tris((1,5,6-trimethyl-1*H*-benzo[d]imidazol-2-yl)methyl)amine	*N*,*N*-bis((1-methyl-1*H*-benzoimidazol-2-yl)-methyl)-1,1-di(pyridin-2-yl)-methanamine
Ligand supporting complex **1**	Ligand supporting complex **1a**	Ligand supporting complex **1b**	Ligand supporting complex **2**

Synthesis of Me_3NTB* ligand

NTB* (tris((5,6-dimethyl-1*H*-benzo[d]imidazol-2-yl)methyl)amine) was synthesized according to the reported method[138] with modifications detailed below, followed by a methylation reaction to obtain the Me_3NTB* ligand.

Modified synthesis of NTB*

In a 250-mL Schlenk flask, nitrilotriacetic acid (1.41 g, 7.35 mmol) was stirred under argon in 60 mL of propylene glycol to produce a white suspension at room temperature. 4,5-dimethyl-1,2-phenylenediamine (3 g, 22.04 mmol) was then added to this suspension, and the mixture was refluxed under argon at 180-190°C overnight. This resulted in a clear, dark red solution, which was cooled back to room temperature and then poured into 500 mL ice-cold water. A white precipitate formed, which was then filtered and subsequently refluxed in methanol containing activated charcoal for 1 hour. This solution was then filtered hot over a sintered fine frit, and the filtrate was left overnight to yield beige-colored crystals. These crystals were then recrystallized from ethanol to give a white solid (1.5 g, 42% yield).

Methylation of NTB*

This solid NTB* was suspended in dry THF (0.93 g, 1.89 mmol) and stirred overnight with NaOH (0.45 g, 11.34 mmol) under Ar to finally give a clear solution. Iodomethane (0.8 g, 5.7 mmol) was added to this solution and stirred for two days at room temperature. This resulted in the precipitation of a white solid. This solid was filtered and washed thoroughly with acetone to produce a white solid (0.45 g, 45% yield). ^{1}H NMR (400 MHz, DCM-d_2): 7.0 ppm (3H, Benz-*H*), 7.4 ppm (3H, Benz-*H*), 4.1 ppm (6H, -CH_2), 3.2 ppm (9H, N-CH_3), 2.4 ppm (18H, -CH_3). ^{13}C NMR (400 MHz, DCM-d_2): 150.8

ppm, 141.4 ppm, 135.0 ppm, 132.1 ppm, 131.0 ppm, 119.8 ppm, 109.8 ppm, 50.6 ppm, 29.4 ppm, 20.6 ppm, 20.3 ppm.

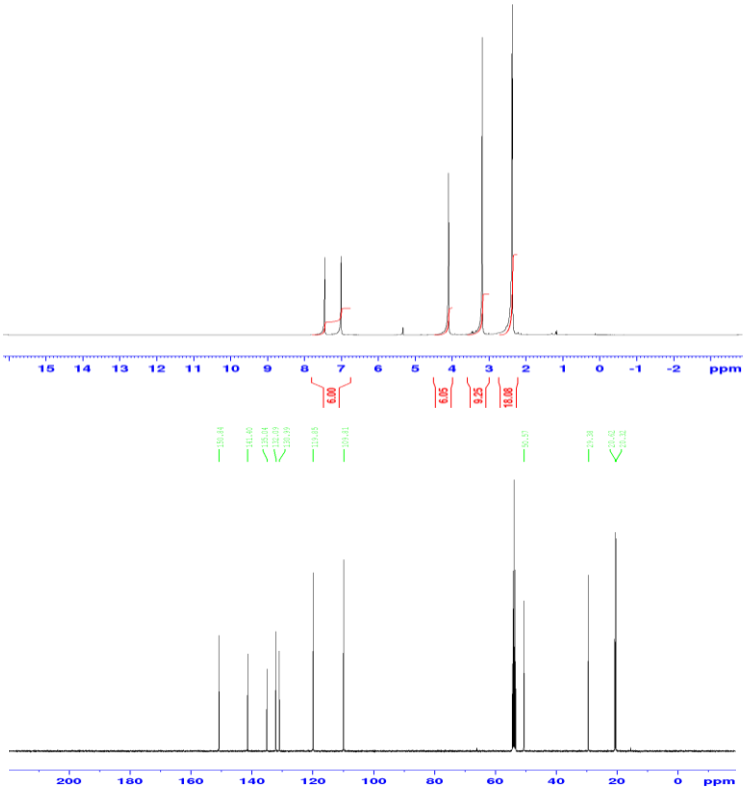

Figure 2.20. ^{1}H NMR (top) and ^{13}C NMR (bottom) spectra of the Me_3NTB* ligand in CD_2Cl_2.

Synthesis of $Fe^{II}(NTB)(OTf)_2$

To a suspension of NTB (150 mg, 0.368 mmol) in acetonitrile inside an inert glovebox, 1 equiv. of $Fe(OTf)_2$•$2CH_3CN$ (160 mg, 0.368 mmol) was added and the mixture was stirred overnight to give a clear solution. This solution was then poured into a diethyl ether bath to produce a white precipitate, which was filtered and washed with diethyl ether, to give a white colored solid. This solid was dissolved back in acetonitrile and crystallized by vapor diffusion using diethyl ether to give crystalline white solid of the complex. (150 mg, 50%). Anal. calcd. for $C_{26}H_{21}F_6FeN_7O_6S_2$ for $Fe^{II}(NTB)(OTf)_2$: C, 41.01; H, 2.78; N, 12.88. Found: C, 40.77; H, 3.13; N, 12.90.

Synthesis of $Fe^{II}(Me_3NTB^*)(OTf)_2$

To a suspension of Me_3NTB^* (125 mg, 0.234 mmol) in acetonitrile inside an inert glovebox, 1 equiv. of $Fe(OTf)_2 \bullet 2CH_3CN$ (102 mg, 0.234 mmol) was added and the mixture was stirred overnight to give a clear solution. This solution was then poured into a diethyl ether bath to produce a white precipitate, which was filtered and washed with diethyl ether to give a white solid. This solid was subsequently dissolved back in acetonitrile and recrystallized by a vapor diffusion method using diethyl ether to give a white solid of the complex. (110 mg, 53%) Anal. calcd. for $C_{35}H_{39}F_6FeN_7O_6S_2$ for $Fe^{II}(Me_3NTB^*)(OTf)_2$: C, 47.36; H, 4.43; N, 11.05. Found: C, 47.41; H, 4.51; N, 11.16.

Syntheses of 1, 1a, 1b and 2

Complexes **1**, **1a** and **1b** were generated by the addition of 2 equiv. 2-(^{t}BuSO$_2$)-C_6H_4IO (ArIO) dissolved in 2,2,2-trifluoroethanol to 1-mM solutions of iron(II) precursors of Me_3NTB, NTB and Me_3NTB^* in acetone-d_6, respectively, at 193 K under N_2. **2** was isolated according to a previously reported method[111] and then dissolved in acetone-d_6/acetonitrile-d_3 for various studies reported herein.

2.5.2 Physical methods

UV-vis absorption spectra were recorded with an HP 8453A diode array spectrophotometer equipped with a cryostat from UNISOKU Scientific Instruments, Japan. All UV-vis absorption experiments were carried out in 1-cm pathlength cuvettes.

Iron K-edge X-ray absorption spectra for **1** were collected on SSRL beamline 9−3 using a 100-element solid-state Ge detector (Canberra) with a SPEAR storage ring current of ~500 mA at a power of 3.0 GeV. The incoming X-rays were unfocused using a Si(220) double crystal

monochromator, which was detuned to 40% of the maximal flux to attenuate harmonic X-rays. Seven scans of the fluorescence excitation spectra for **1** were collected from 6882 to 8000 eV at a temperature (10 K) that was controlled by an Oxford Instruments CF1208 continuous-flow liquid helium cryostat. An iron foil was placed in the beam pathway prior to the ionization chamber I_0 and scanned concomitantly for an energy calibration, with the first inflection point of the edge assigned to 7112.0 eV. A 6 μm Mn filter and a Soller slit were used to increase the signal-to-noise ratio of the spectra. Photoreduction was monitored by scanning the same spot on the sample twice and comparing the first derivative peaks associated with the edge energy during collection, but none was observed in the present study. The detector channels from the scans were examined, calibrated, averaged, and processed for EXAFS analysis using EXAFSPAK[140] to extract χ(k). Theoretical phase and amplitude parameters for a given absorber−scatterer pair were calculated using FEFF 8.40[141] and were utilized by the “opt” program of the EXAFSPAK package during curve fitting. In all analyses, the coordination number of a given shell was a fixed parameter and was varied iteratively in integer steps, while the bond lengths (R) and mean-square deviation (σ^2) were allowed to freely float. The amplitude reduction factor S_0 was fixed at 0.9, while the edge-shift parameter E_0 was allowed to float as a single value for all shells. Thus, in any given fit, the number of floating parameters was typically equal to (2 × num shells) + 1. The k range of the data is 2−15 $Å^{-1}$. The pre-edge analysis was performed on data normalized in the “process” program of the EXAFSPAK package, and pre-edge features for **1** were fit using the Fityk[142] program with pseudo-Voigt functions composed of 50:50 Gaussian/Lorentzian functions.

NMR spectra were recorded on a Bruker 400 MHz spectrometer at 298 K unless otherwise mentioned. Temperatures cited for low-temperature experiments were determined by calibration using a solution of methanol and TMS as the standard.

Mössbauer spectra were recorded with two spectrometers using Janis Research (Wilmington, MA) SuperVaritemp dewars that allow studies in applied magnetic fields up to 8 T in the temperature range from 1.5 to 200 K. Isomer shifts are quoted relative to iron metal at 298 K. Mössbauer spectral simulations were performed using the WMOSS software package (SEE Co, Edina, MN), and all the spectral figures were prepared by using SpinCount software.[143]

2.5.3 Reactivity and kinetics of 1

All experiments were conducted with an acetone-d_6 solution of **1** generated from the reaction of a 1-mM iron(II) precursor with 2 equiv. of ArIO at 233 K, unless otherwise stated. The pseudo-first order decay curves from time profiles were obtained by monitoring the decrease in absorbance at 770 nm (see Figure 2.3) with time. These profiles at various substrate concentrations were fit with an exponential decay function using Origin Pro 2016. The rates (k_{obs}) were plotted against different concentrations of substrates, and their slopes represent 2nd order rate constants (k_2).

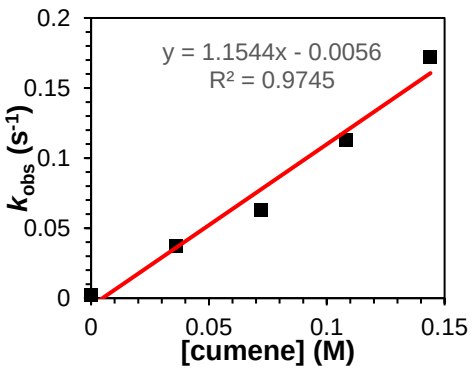

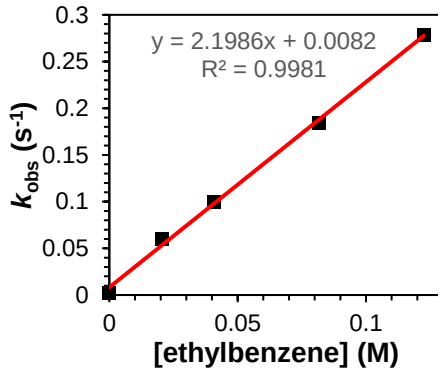

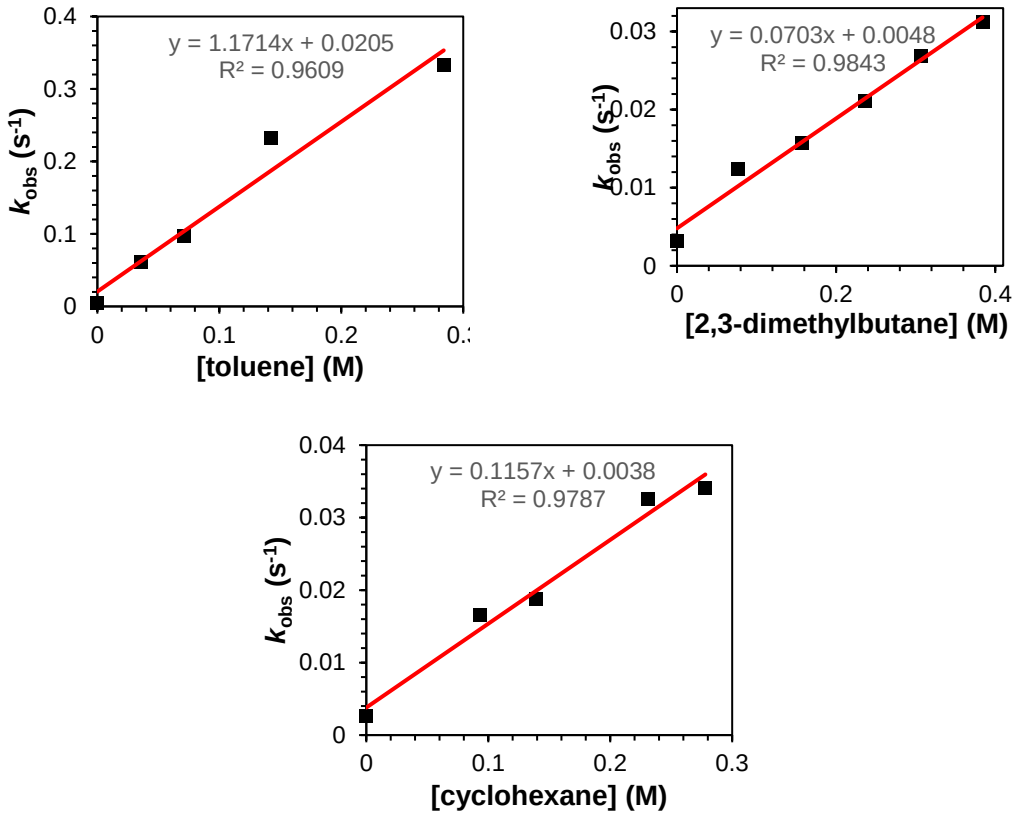

Figure 2.21. k_2 plots for the reactions of different HAT substrates with **1** under N_2. The slopes of the fitted red lines represent the second-order rate constants (k_2) at 233 K.

2.5.4 Structural analysis of complex 1 using XAS

Sample preparation: A XAS sample of **1** was generated by the addition of 2 equiv. 2-(^{t}BuSO$_2$)-C$_6$H$_4$IO (ArIO) dissolved in 2,2,2-trifluoroethanol to 5-mM solutions of iron(II) precursor of Me$_3$NTB in acetone-d_6 at 193 K under N_2.

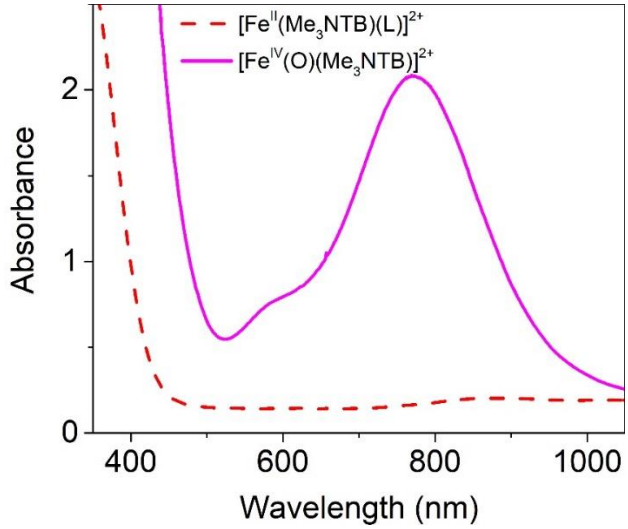

Figure 2.22. Electronic absorption spectra of **1** (pink trace) prepared from the reaction of a 5-mM solution made by dissolving solid $[Fe^{II}(Me_3NTB)(CH_3CN)](CF_3SO_3)_2$ in acetone-d_6 (red dotted trace) with 2 equiv. ArIO (in TFE) at 193 K.

General EXAFS considerations: In the fit table of EXAFS data, N refers to the number of scatterers used for a particular shell, r is the distance of the scattering shell, σ^2 is the mean squared deviation (or Debye-Waller factor), E_0 is the edge shift parameter, and the goodness of fit (GOF) parameters are calculated as following:

Scale Factor S_0^2=0.9. GOF= Goodness-of-fit calculated as $F = \sqrt{\sum k^6 \left(\chi_{\exp} - \chi_{calc}\right)^2}$

$F' = \sqrt{\sum k^6 \left(\chi_{\exp} - \chi_{calc}\right)^2 / \sum k^6 \chi_{\exp}{}^2}$ / = double scattering pathway

2.5.5 Computational details for predicting NMR shifts

The calculations were carried out by following the protocol described by Bagno and coworkers.[118,144–146] Geometries were optimized starting from X-ray structures (when available) or pre-optimized structure from MM2 force-field method (when XRD structure is not available). All the optimization were performed at the B3LYP*/6-31G(d',p') level. Final energies and NMR parameters were computed with the B3LYP*/cc-pVTZ level.[147] All calculations were carried out with Gaussian 16.[148] The B3LYP* functional is invoked through the following route: B3LYP IOp(3/76 = 1000001500) IOp(3/77 = 0720008000) IOp(3/78 = 0810010000).

The calculated NMR shifts were determined by the following formula:[149,150]

$$\sigma = \sigma_{ref} - (\sigma_{orb} + \sigma_{FC} + \sigma_{PC})$$

where σ_{ref} = 31.02 ppm for TMS was obtained at the same theoretical level as those for the Fe(IV) complexes included in this study. σ_{orb} is the orbital contribution to the proton, which is equivalent to the shielding for diamagnetic systems. The Fermi contact term, σ_{FC}, which originates from the scalar interaction between magnetic field from unpaired electrons and the magnetic momentum of target proton, dominates the paramagnetic component in the NMR shift. The Fermi contact term can be calculated from Fermi's hyperfine interaction parameters as the following:

$$\sigma_{FC} = \frac{2\pi}{\gamma_I} g_{iso} \mu_B A \frac{S(S+1)}{3kT}$$

in which γ_I is the magnetogyric ratio of the nucleus I and g_{iso} is the isotropic g factor of electron, μ_B is the Bohr magneton and A is the Fermi hyperfine interaction parameter. The contribution from pseudo-contact term σ_{PC}, can be approximated by the theory developed by Hrobárik et al.[151] Usually it is small and can be ignored compared with σ_{FC}. In this work we estimate the NMR shift only by the orbital term and Fermi-contact term. All

calculations were done at 193 K, the same temperature as the NMR measurements performed in this work.

2.6 Acknowledgments

I am grateful to have worked with immensely helpful collaborators like Dr. Waqas Rasheed for helping me collect NMR data, Dr. Apparao Draksharapu for XAS results and Dr. Ruixi Fan for carrying out DFT calculations in addition to Mössbauer results. I gratefully acknowledge the support of the U.S. National Science Foundation (grants CHE-1665391 to L.Q. and CHE-1654060 to Y.G.). The Bruker Avance III HD nanobay 400 MHz NMR spectrometer used in this study was purchased from funds provided by the Office of the Vice President of Research, College of Science and Engineering, and the Department of Chemistry at the University of Minnesota. We thank Dr. Letitia Yao for her advice on our NMR experiments and Prof. John Lipscomb and Shuangning Xu for their valuable input into the interpretation of our kinetic data.

Chapter 3:

Sc^{3+}-promoted O–O bond cleavage of a (μ-1,2-peroxo)diiron(III) species formed from an iron(II) precursor and O_2 to generate a complex with an $Fe^{IV}_2(\mu\text{-}O)_2$ core

This chapter is reprinted (adapted) with permission from Banerjee, S.; Draksharapu, A.; Crossland, P. M.; Fan, R.; Guo, Y.; Swart, M.; Que, L. Sc^{3+}-promoted O–O bond cleavage of a (μ-1,2-peroxo)diiron(III) species formed from an iron(II) precursor and O_2 to generate a complex with an $Fe^{IV}_2(\mu\text{-}O)_2$ core. *J. Am. Chem. Soc.* **2020**, *142* (9)**,** 4285-4297.

3.1 Introduction

Dioxygen activation is carried out by nonheme diiron enzymes such as soluble methane monooxygenase (sMMO), ribonucleotide reductase (RNR), fatty acid desaturases, human deoxyhypusine hydroxylase (hDOHH) and others.[67,68,89,152] These enzymes are involved in various important transformations such as the conversion of methane to methanol, the conversion of ribonucleotides to deoxyribonucleotides, the desaturation of fatty acids, and the selective hydroxylation of the eukaryotic initiation factor 5a. Dioxygen binding to the diiron(II) center gives rise to a peroxodiiron(III) species, as observed for sMMO,[153,154] RNR R2,[84,155] fatty acid desaturases,[156,157] and hDOHH.[158–160] This, in turn, converts to high-valent intermediates that play key roles in enzyme action, such as the diiron(III,IV) species "**X**" in RNR class 1A[86–88] or the diiron(IV) species "**Q**" in sMMO.[75,77,161]

Various synthetic models have been produced to mimic dioxygen activation steps in nonheme diiron enzymes.[67,152,162] The polydentate ligands used for these models incorporate various nitrogen heterocycles, with pyridine and quinoline donors most often represented. Closer analogs of the histidine ligands in the enzyme active sites are imidazoles and benzimidazoles, but there are only a handful of polydentate ligands with these heterocycles that are reported to form (μ-1,2-peroxo)diiron(III) intermediates.[93,110,148,163–166], and not one has been shown to transform into a higher-valent diiron species. Herein, we present a study of $[Fe^{II}(Me_3NTB)(CH_3CN)](CF_3SO_3)_2$ (**1**)[57] (Scheme 1), which in the presence of DBU (1,8-diazabicyclo[5.4.0]undec-7-ene) reacts with O_2 in MeCN at -40 °C to form a (μ-1,2-peroxo)diiron(III) species (**2**). Subsequent treatment of this intermediate with $Sc(OTf)_3$ converts **2** to a diiron(IV)

complex **3**, thereby providing a biomimetic precedent for the steps in dioxygen activation by sMMO, from diiron(II) precursor to diiron(IV) oxidant.

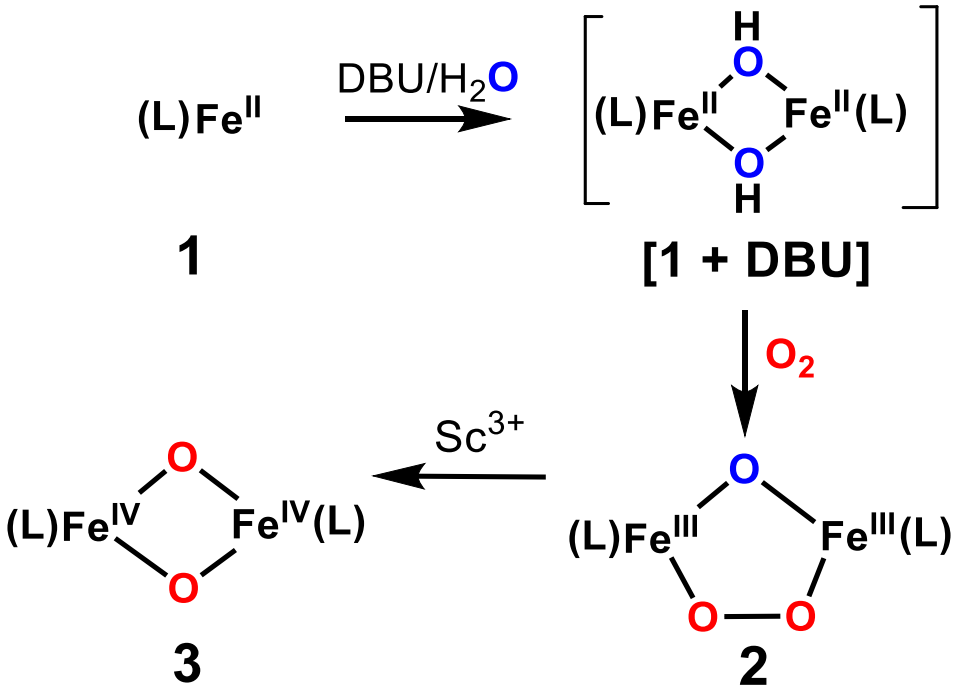

Figure 3.1. Reaction of O_2 with **1** in the presence of DBU and water to form **2**, and subsequent conversion to **3** upon treatment with Lewis acid $Sc(OTf)_3$.

3.2 Results

3.2.1 Generation of a diiron(II) species, oxygen activation, and related electronic absorption spectral characterization

A colorless 1-mM solution of **1** prepared in CH_3CN under N_2 at -40 °C turns yellow upon the addition of 1.5 equiv. DBU/H_2O, corresponding to the appearance of a broad absorption band around 390 nm (Figure 3.1 and 3.2). Such spectral changes have been observed when related Fe^{II}(N4) complexes are treated with Et_3N to form dihydroxo-bridged diiron(II) complexes.[101,167] The use of Et_3N does not generate such a complex and

it does not produce a significant change in the absorption spectrum of **1**. A stronger base like DBU (pKa = ~24 vs pKa of Et_3N = ~18 in CH_3CN[168]) is needed to form the putative dihydroxo-bridged diiron(II) complex with Me_3NTB as the ligand framework. Isolation of this complex has proved challenging and only electronic absorption characterization has been obtained. Oxygenation of this [**1 + DBU**] solution produces a deep-green species **2** within ~15 s, with absorption bands at 485, 595 and 750 nm (ε ~ 1200, 1000, 300 M^{-1} cm^{-1}, respectively), features like those associated with (*μ*-oxo)(*μ*-1,2-peroxo)diiron(III) complexes.[101,167]

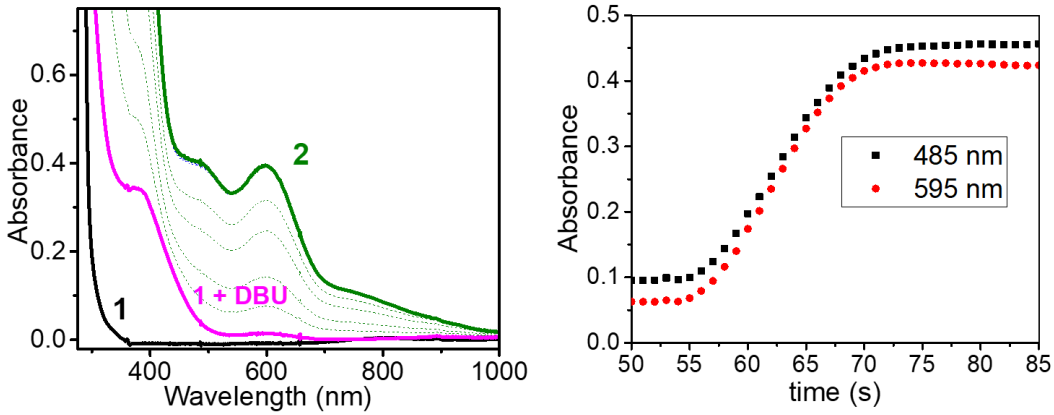

Figure 3.2. (**Left**) UV-vis absorption spectra of **1** (1 mM, black), [**1 + DBU**] (pink) formed after addition of 1.5 equiv. DBU, **2** (green) obtained upon oxygenation of **1** in the presence of DBU, all in CH_3CN at -40 ºC. (**Right**) Time trace showing the rate of oxygenation of [**1 + DBU**] to generate **2** in CH_3CN at -40 ºC at multiple wavelengths.

The stability of **2** is low and its half-life is roughly 13 minutes in CH_3CN at -40 ºC. This contrasts with most of the other peroxodiiron(III) models where much higher stability was observed.[100–102,163,169–171] The self-decay of **2** can be followed through the use of UV-vis spectroscopy (Figure 3.3) and the rate of decay can be fit using a first-order exponential function. This

suggests that the decay of **2** most likely goes through a single reaction pathway.

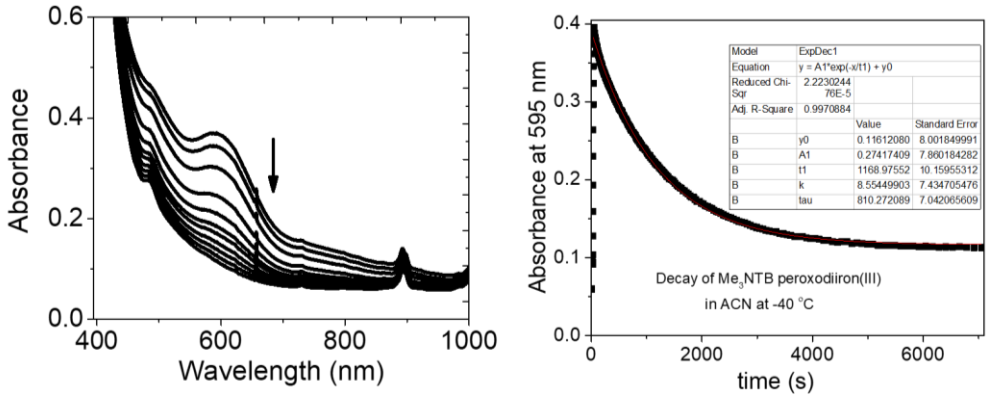

Figure 3.3. (**Left**) UV-vis absorption spectra of the decay process of **2** in CH_3CN at -40 ºC. (**Right**) Time trace showing the rate of decay of **2** in CH_3CN at -40 ºC by following the 595 nm absorption feature. The red line denotes the first-order exponential fit to the curve obtained after data collection for the whole decay process.

3.2.2 Resonance Raman characterization of 2 to elucidate its vibrational structure

Resonance Raman spectroscopy was carried out on frozen samples of **2** to gain structural information by observing potential vibrational signals. The resonance Raman spectrum of **2** obtained with 561-nm excitation of a frozen solution at 77 K shows resonance-enhanced bands at 825, 715, 527, 518, and 454 cm^{-1} (Figure 3.4). With $^{18}O_2$, the 825-cm^{-1} band downshifts by 46 cm^{-1}, as predicted by Hooke's law for an O–O stretch. This value is among the smallest v(O–O)'s found for peroxodiiron(III) complexes (Tables 3.1 and Figure 3.5). Two other vibrations at 454 and 518 cm^{-1} also downshift by about 24 cm^{-1} upon $^{18}O_2$ incorporation, leading to their respective assignments as the ν_{sym}(Fe−O_2−Fe) and the

ν_{asym}(Fe−O_2−Fe) modes. On the other hand, the features at 527 and 715 cm^{-1} are sensitive to $H_2{}^{18}O$ labeling, respectively downshifting by 25 and 34 cm^{-1} (Figure 3.4), supporting their assignments as the ν_{sym} and ν_{asym} modes of the Fe−O−Fe unit. Taken together, these results strongly suggest that this deep green intermediate is an Fe^{III}_2(μ-O)(μ-1,2-O_2) complex based on its spectroscopic resemblance to the previously reported complexes with Fe^{III}_2(μ-O)(μ-1,2-O_2) cores.[67]

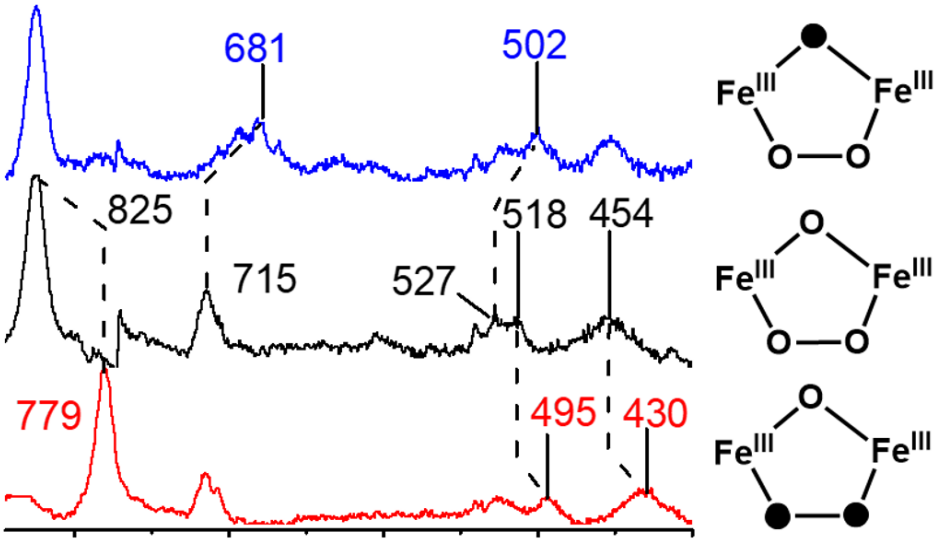

Figure 3.4. Resonance Raman difference spectra of **2** generated with $^{16}O_2$ in CH_3CN (black), with $^{16}O_2$ in the presence of 150 equiv. $H_2{}^{18}O$ (blue) and with $^{18}O_2$ in CD_3CN (red). Dotted lines highlight isotope shifts. Isotopic composition for different spectra are shown on the right-hand side of the figure. Filled oxygen atoms denote ^{18}O-labeled atoms.

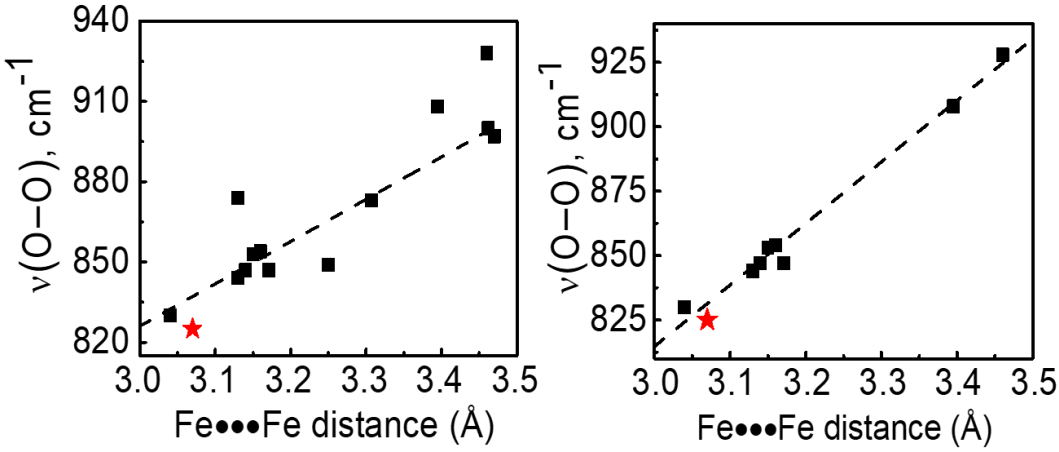

Figure 3.5. (**Left**) Plot of Fe•••Fe distance vs. *ν*(O–O) stretching frequencies for model peroxodiiron(III) complexes having an additional oxo, hydroxo or alkoxo bridge.[73,101,170] (**2** is plotted as a red star.) (**Right**) A better correlation was observed when the alkoxo bridged and negatively charged ligand-based peroxodiiron(III) complexes were removed. This is significant because it suggests in the right-hand side plot we are comparing systems that are more similar in coordination environments, where the relationship between ν(O–O) and Fe•••Fe is more strongly observed.

Table 3.1. Comparison of resonance Raman features of **2** with other peroxodiiron(III) model complexes

	ν **(O–O)** **[$\Delta^{18}O$,** **$\Delta^{18}O_2$]**	***ν*$_{sym}$(Fe** **–O_2–Fe)** **[$\Delta^{18}O$,** **$\Delta^{18}O_2$]**	***ν*$_{asym}$(Fe** **–O_2–Fe)** **[$\Delta^{18}O$,** **$\Delta^{18}O_2$]**	***ν*$_{sym}$(Fe–** **O–Fe)** **[$\Delta^{18}O$,** **$\Delta^{18}O_2$]**	***ν*$_{asym}$(Fe–** **O–Fe)** **[$\Delta^{18}O$,** **$\Delta^{18}O_2$]**	**Ref**
2	825 [-, -46]	454 [-, -24]	518 [-, -23]	527 [-25, -]	715 [-34, -]	This work
A	854 [0, -47]	460 [0, -13]	511 [0, -19]	523 [-16, 0]	714 [- 42, -]	[101,167]

B	928 [-2,-53]	468 [0, -6]	550 [-4, -17]	424 [-7, -11]		[101]
C	847 [0, -44]	463 [-, -21]	533 [-, -25]	511 [-12, -]	696 [-30, -6]	[100]
D	816 [-45], 830			537 [-20, -]		[73]
E	847 [-, -33]	465 [-, -19]			695 [-, -2]	[169]
F	908 [-, -47]	460 [0, -13]	548 [-, -18]	498 [-, -5]		[169]
G	844 [0, -44]	464 [0, -17]	523 [0, -20]	522 [-13, 0]	708 [-32, -4]	[73,167]
H	853 [0, -45]	463 [-, -15]	529 [0, -26]	510 [-16, 0]	698 [-31, -4]	[73]
I	874 [-, -38]	458 [-, -13]		520 [−16, 0]	560 [–12, 0]	[170]
J	826 [-, -51]					[172]
K	900 [-, -50]	471 [-, -16]				[110]
L	845, 853 [-, -42]	470 [-, -15]				[148]
M	897 [-, -49]	477 [-, -19]				[148]
N	845 [-, -49]	464 [-, -21]				[164]

O	876 [-, -48]	421 [-, -12]				[173]
P	822 [-, - 43]					[174]
Q	873 [-, -50]	480 [-, -16]				[165]
R	840 [-, -45]	459 [-, -20]				[165]
S	883 [-, -51]	451 [-, -11]	556 [-, -13]			[175]
T	840	461	521			[175]

A = $[Fe^{III}_2(\mu\text{-}O)(\mu\text{-}O_2)(BnBQA)_2]^{2+}$, BnBQA = *N*-benzyl-*N*,*N*-bis(2-quinolinylmethyl)amine; **B** = $[Fe^{III}_2(\mu\text{-}OH)(\mu\text{-}O_2)(BnBQA)_2]^{3+}$; **C** = $[Fe^{III}_2(\mu\text{-}O)(\mu\text{-}O_2)(6\text{-}Me_3TPA)_2]^{2+}$, 6-Me$_3$TPA = tris(6-methyl-2-pyridylmethyl)-amine; **D** = $[Fe^{III}_2(\mu\text{-}O)(O_2)(OAc)(BPPE)]^{+}$, BPPE=1,2-bis[2-(bis(2-pyridyl)methyl)-6-pyridyl]ethane; **E** = $[Fe^{III}_2(\mu\text{-}O)(\mu\text{-}O_2)(6\text{-}Me_2BPP)_2]$, 6-Me$_2$BPP = bis(6-methyl-2-pyridylmethyl)-3-aminopropionate; **F** = $Fe^{III}_2(\mu\text{-}OH)(\mu\text{-}O_2)(6\text{-}Me_2BPP)_2]^{+}$; **G** = $[Fe^{III}_2(\mu\text{-}O)(\mu\text{-}1,2\text{-}O_2)(BQPA)_2]^{2+}$,BQPA = bis(2-quinolylmethyl)-*N*-2-pyridylmethylamine; **H** = $[Fe^{III}_2(\mu\text{-}O)(\mu\text{-}O_2)(6\text{-}Me\text{-}BQPA)_2]^{2+}$, 6-Me-BQPA = bis(2-quinolylmethyl)(6-methylpyridyl-2-methyl)amine]; **I =** $[Fe^{III}_2(\mu\text{-}O)(\mu\text{-}O_2)(IndH)_2]^{2+}$, IndH = 1,3-bis(2'-pyridylimino)isoindoline; **J** = $[Fe^{III}_2(O)(O_2)(6\text{-}HPA)]^{2+}$, 6-HPA = 1,2-bis[2-{bis(2-pyridylmethyl)amino-methyl}-6-pyridyl]ethane; **K** = $[Fe^{III}_2(O_2)(N\text{-}Et\text{-}HPTB)(OPPh_3)_2]^{3+}$, *N*-Et-HPTB = tetrakis(2- benzimidazolylmethyl)-2-hydroxy-1,3-diaminopropane; **L** = $[Fe^{III}_2(O_2)(O_2PPh_2)(N\text{-}Et\text{-}HPTB)]^{2+}$; **M** = $[Fe^{III}_2(O_2)(N\text{-}Et\text{-}HPTB)(\eta^1\text{–}O_2PPh_2)(MeCN)]^{2+}$; **N** = = $[Fe^{III}_2(Ph\text{-}bimp)(O_2)(OBz)]^{2+}$,Ph-bimp = 2,6-Bis[bis-2-(1-methyl-4,5-

diphenylimidazolyl)methyljaminomethyl]-4-methylphenolate; **O** = $[Fe^{III}_2(O_2)(Tp^{iPr2})_2(OBz)_2]$, Tp^{iPr2} = tris(3,5-diisopropyl-1-pyrazolyl)borate; **P** = $[Fe^{III}_2(dxlCO_2)_4(O_2)(Py)_2]$, $dxlCO_2^-$ = 2,6-bis[(2,6-dimethylphenyl)methyl]-4-*tert*-butylbenzoate; **Q** = $[Fe^{III}_2(O_2)(LPh_4)(Ph_3CCO_2)]^{2+}$, LPh_4 = N,N,N′,N′-tetrakis[(1-methyl-2-phenyl-4- imidazolyl)methyl]-1,3-diamino-2-propanolate; **R** = $[Fe^{III}_2(O_2)(LPh_4)(PhCO_2)]^{2+}$; *S* = $[Fe^{III}_2(OH)(O_2)(L)]^{3+}$, L = 1,2- bis(2,2'-bipyridyl-6-yl)ethane; **T** = $[Fe^{III}_2(O)(O_2)(L)]^{2+}$.

Previous studies of synthetic *μ*-oxodiiron(III) and *μ*-1,2-peroxodiiron(III) complexes have uncovered patterns that correlate vibrational frequencies linearly with structural features of these complexes. Sanders-Loehr et al. have found that the ν_{sym}(Fe−O−Fe) and ν_{asym}(Fe−O−Fe) correlate with the Fe–O–Fe angle of the complex (Figure 3.8),[176] while Fiedler et al. have shown a linear correlation between the *ν*(O−O) of a complex and its diiron distance (Figure 3.5).[73,101] When analyzed within this context, the vibrational data of **2** predict an Fe−O−Fe angle of 117° and an Fe•••Fe distance of 3.04 Å for **2**.

3.2.3 XAS characterization of 2 to elucidate its structure

Owing to the instability of **2** as discussed above, no crystallization attempts were made. However, X-ray absorption spectroscopy (XAS) was used on higher concentration samples of **2** (4 mM) to achieve a reasonable signal to noise ratio. This helped us get X-ray absorption data at Fe K-edge on the frozen samples of **2**. The resultant XANES (X-ray Absorption Near-Edge Structures) spectrum of **2** is shown in Figure 3.6. This figure focuses on the near-edge region of **2** that provides information regarding the oxidation states and coordination environments of the metal centers. The

first inflection point of the rising edge was assigned as the edge energy (E_0) associated with the transition of an electron from the Fe 1s orbital to the continuum. This has been determined to be 7126.3 eV, consistent with values for high-spin iron(III) centers. The energy of the pre-edge feature ($E_{pre\text{-}edge}$), at about 8-10 eV below the edge jump, corresponds to the Fe 1s to Fe 3d transitions. The pre-edge region of **2** can be fitted with one peak centered at 7114.5 with an area of 18.2 units (Table 3.2), values comparable to those reported for other complexes with $Fe^{III}_2(\mu\text{-}O)(\mu\text{-}1,2\text{-}O_2)$ cores.

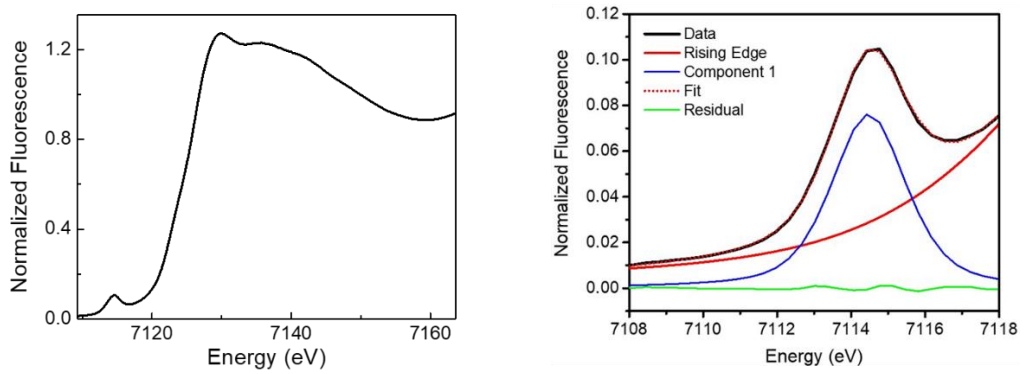

Figure 3.6. (**Left**) Fe K-edge XANES (X-ray Absorption Near-Edge Structures) data of **2**. (**Right**) Pre-edge features and their fitting in **2**. The experimental data is shown in black, rising edge in red, pre-edge peak component in blue and residual in green color.

Table 3.2. Pre-edge fitting parameters and K-edge energy for **2**

Species	K-edge (eV)	Peak Position (eV)	Area (units)	Relative Area
2	7126.3	7114.5	18.2	1
			Total = 18.2	

The Fe K-edge EXAFS data for complex **2** along with the corresponding Fourier transforms are shown in Figure 3.7. The best fit of the EXAFS data

obtained for **2** consists of 2 N/O scatterers at 1.84 Å, 4 N/O scatterers at 2.11 Å, and a diiron distance of 3.07 Å. (Table 3.3) The 2.11 Å scatterers can be assigned to Fe–N bonds and the two O scatterers with an average Fe–O distance of 1.84 Å would then be assigned to the oxo bridge and the 1,2-peroxo bridge. These conclusions gain more support when we compare similar values of related peroxodiiron(III) complexes. (Table 3.4) Of particular interest is the fact that the diiron distance of **2** (3.07 Å) is among the shortest of the peroxodiiron(III) model complexes reported so far. This observation is tied to the fact that **2** has one of the lowest observed *v*(O–O)'s among such complexes. (Figure 3.5) Furthermore, the 113˚ Fe–O–Fe angle obtained from just the EXAFS data agrees well with that derived from the Sanders-Loehr correlation relating the Fe–O–Fe vibrations with the Fe–O–Fe angle. (Figure 3.8)

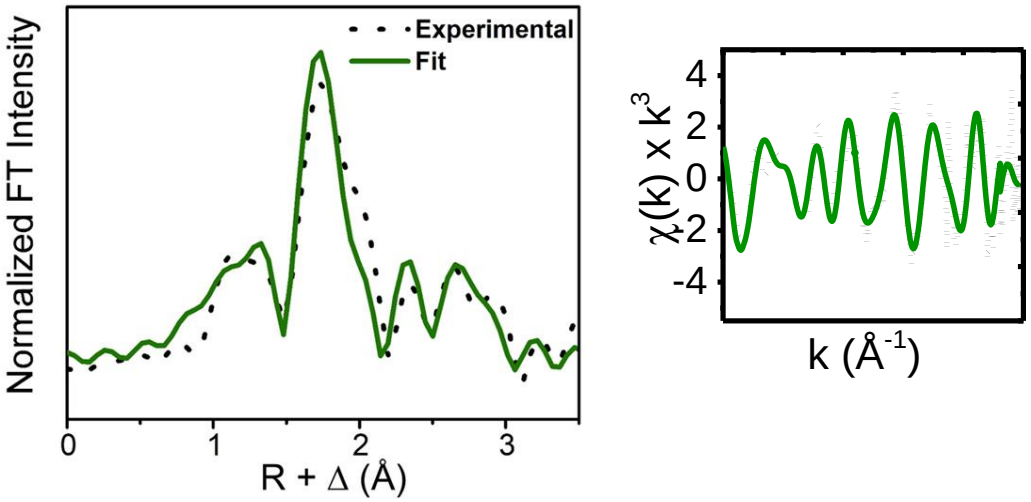

Figure 3.7. (Left) Fourier-transformed k-space EXAFS data for **2**. (Right) k-space EXAFS data for **2**. Data is represented by black dots, and the best fits are in green solid lines.

Table 3.3. EXAFS fitting parameters for **2;** best fits in bold font

2	**Fe-N/O**			**Fe-O/N**			**Fe•••C/N**			**Fe•••Fe**				**GOF**	
Fit	**N**	**R (Å)**	**σ^2 (10^{-3})**	**N**	**R(Å)**	**σ^2 (10^{-3})**	**N**	**R(Å)**	**σ^2 (10^{-3})**	**N**	**R(Å)**	**σ^2 (10^{-3})**	**E_0**	**F**	**F'**
1	4	2.13	7.31	-	-	-	-	-	-	-	-	-	1.72	955	658
2	4	2.12	4.55	2	1.85	5.03	-	-	-	-	-	-	-4.01	601	655
3	4	2.12	4.61	2	1.85	5.14	-	-	-	1	3.06	6.95	-3.41	539	653
4	4	2.11	4.85	2	1.84	4.90	3	2.91	3.57	1	3.06	3.57	-5.37	508	649
5	4	2.11	5.08	2	1.84	4.92	3	2.94	-0.70	1	3.07	0.20	-3.24	466	646
							3	3.24	0.68						
6	**4**	**2.11**	**5.03**	**2**	**1.84**	**4.94**	**4**	**2.94**	**1.37**	**1**	**3.07**	**0.31**	**-3.56**	**468**	**646**
							3	**3.24**	**0.56**						

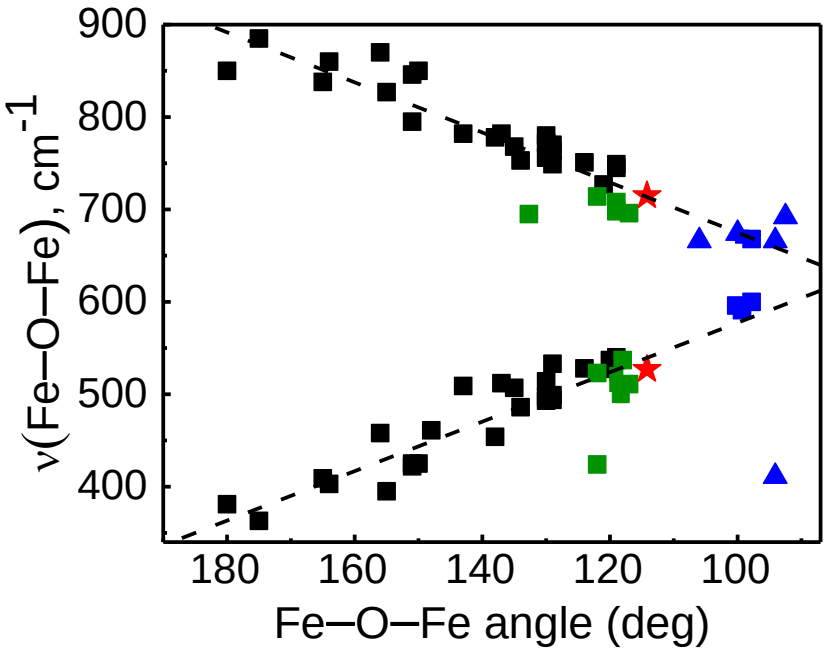

Figure 3.8. Correlation between Fe–O–Fe angles of oxo-bridged diiron complexes and ν_s(Fe–O–Fe) (bottom) and ν_{as}(Fe–O–Fe) values (top). Data from the original Sanders-Loehr study (black),[176] augmented by data for species with $Fe_2(\mu\text{-}O)(\mu\text{-}1,2\text{-}O_2)$ (green)[73,100,101,167,169,170], $Fe_2(\mu\text{-}O)_2$ cores (blue triangles) and $Fe_2(\mu\text{-}O)(\mu\text{-}OH)$ cores (blue squares).[78,177,178] *The Fe–O–Fe vibrations of **2** are shown as red stars*. The black dashed lines show the best linear fit of the data points available. The relationship between the vibrations of the Fe–O–Fe unit and the related Fe–O–Fe bond angle has been studied originally using secular equations.[179]

Table 3.4. Comparison of EXAFS-derived iron-scatterer distances for **2** and related complexes

Complex	**d(Fe–O) (Å)**	**d(Fe–N) (Å)**	**d(Fe••Fe) (Å)**	**Ref.**
$Fe^{III}_2(\mu\text{-}O)(\mu\text{-}1,2\text{-}O_2)$ complexes				
2	2 @ 1.84	4 @ 2.11	3.07	This work
A BPPE (μ-O_2CCH_3)	1 @ 1.77 2 @ 1.94	3 @ 2.16	3.04	[73]
B BQPA	2 @ 1.82	1 @ 2.03 3 @ 2.21	3.13	[73]
C $6Me_3TPA$	2 @ 1.84	4 @ 2.23	3.14	[73,100]
D 6MeBQPA	2 @ 1.83	1 @ 2.05 3 @ 2.23	3.15	[73]
E BnBQA	1 @ 1.81 1 @ 1.92	4 @ 2.21	3.16	[101]

A = $[Fe^{III}_2(\mu\text{-}O)(\mu\text{-}1,2\text{-}O_2)(OAc)(BPPE)]^+$, BPPE = 1,2-bis[2-(bis(2-pyridyl)methyl)-6-pyridyl]-ethane; **B** = $[Fe^{III}_2(\mu\text{-}O)(\mu\text{-}1,2\text{-}O_2)(BQPA)_2]^{2+}$, BQPA = bis(2-quinolylmethyl)-*N*-2-pyridylmethylamine; **C** = $[Fe^{III}_2(\mu\text{-}O)(\mu\text{-}1,2\text{-}O_2)(6\text{-}Me_3TPA)_2]^{2+}$, 6-$Me_3$TPA = tris(6-methyl-2-pyridylmethyl)-amine; **D** = $[Fe^{III}_2(\mu\text{-}O)(\mu\text{-}1,2\text{-}O_2)(6\text{-}Me\text{-}BQPA)_2]^{2+}$, 6-Me-BQPA = bis(2-quinolylmethyl)(6-methylpyridyl-2-methyl)amine]; **E** = $[Fe^{III}_2(\mu\text{-}O)(\mu\text{-}1,2\text{-}O_2)(BnBQA)_2]^{2+}$, BnBQA = *N*-benzyl-*N*,*N*-bis(2-quinolinylmethyl)amine;

3.2.4 Mössbauer characterization of 2

Mössbauer spectroscopy of **2** at 4.2 K and zero applied field reveals a single quadrupole doublet with an isomer shift (δ) of 0.49 mm/s and a quadrupole splitting (ΔE_Q) of 1.06 mm/s (Figure 3.9), representing the two equivalent high-spin iron(III) sites of the (*μ*-oxo)(*μ*-1,2-peroxo)diiron(III) complex. Notably, the quadrupole splitting of **2** is among the smallest of the values previously reported for peroxodiiron(III) complexes (Table 3.5).[101] High-field measurements show that the doublet originates from a diamagnetic species that corresponds to 75-80% of the iron in the sample (Figure 3.10).

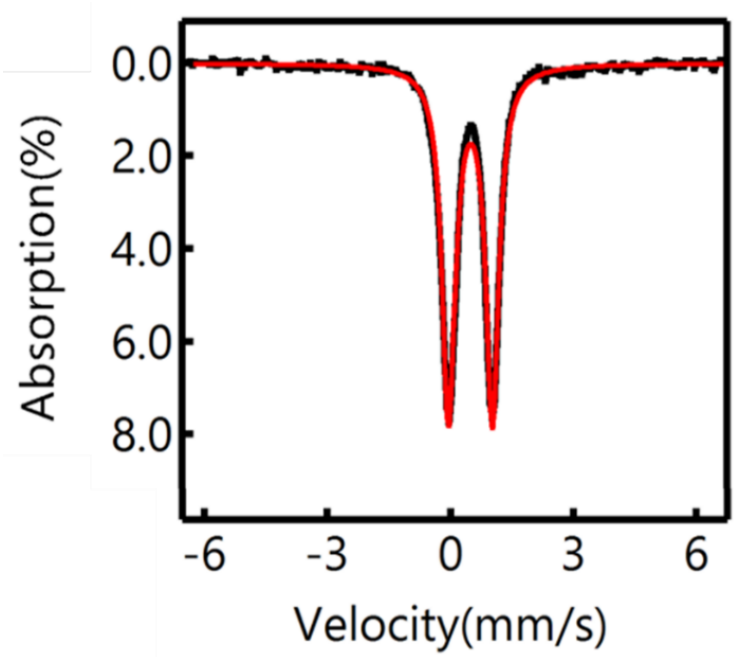

Figure 3.9. Mössbauer spectra of **2** at 4.2 K and 0 T.

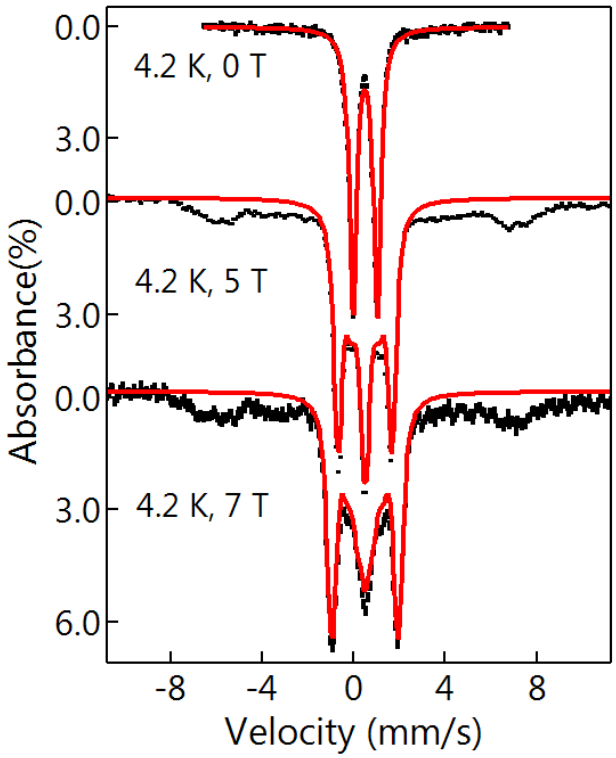

Figure 3.10. Mössbauer spectra of **2** measured at 4.2 K with various applied fields (0 T, 5 T, 7 T). The red solid lines represent the spectral simulation of an *S* = 0 peroxodiiron(III) species, representing ~80% iron in the sample. The black arrows indicate possible high-spin ferric impurities.

Table 3.5. Comparison of spectroscopic properties of (*μ*-1,2-peroxo)-diiron(III) complexes

Complex [$t_{1/2}$] @ -40 °C	**λ_{max} (ε) nm (M^{-1} cm^{-1})**	***ν*(O–O) (cm^{-1}) [$\Delta^{18}O_2$]**	**d (Fe••Fe) (Å) [b]**	**δ [ΔE_Q] (mm/s)**	**Ref.**
***μ*-oxo complexes**					
2 [13 mins]	595 (990)	825 [-46]	3.07	0.49 [1.06]	This work
A BPPE (*μ*-O_2CCH_3) [8 h/27 °C]	595 (1400)	816 [-45] 830	3.04	0.53 [1.67]	[171] [73]
B BQPA	620 (1000)	844 [-44]	3.13	-	[73]
C $6Me_3TPA$ [7.5 min/-30 °C]	648 (1200)	847 [-44]	3.14	0.54 [1.68]	[73,100]
D $6Me_2BPP$ Stable and crystallized	577 (1500)	847 [-33]	***3.171***	0.50 [1.46]	[169]
E 6MeBQPA	640 (1300)	853 [-45]	3.15	-	[73]

F BnBQA [6 h]	650 (1300)	854 [-47]	3.16	0.55 [1.43]	[101]
***μ*-hydroxo complexes**					
G BnBQA [40 min]	730 (2400)	928 [-53]	3.46	0.57 [1.35] 0.56 [0.96]	[101]
H 6Me$_2$BPP Stable and crystallized	644 (3000)	908 [-47]	***3.395***	0.50 [1.31]	[169]
***μ*-alkoxo complexes**					
I *N*-EtHPTB (μ-O$_2$PPh$_2$) Long-lived at -80 °C in CH$_2$Cl$_2$	678 (2100)	845, 853 [-42]	3.25	-	[148]
J *N*-EtHPTB (μ-O$_2$AsMe$_2$)	632 (2100)	845 [−49]	3.27	0.56 [-1.26]	[148]
K *N*-EtHPTB (η^1-O$_2$PPh$_2$)	621 (1800)	897 [-49]	3.47	0.53 [-1.03]	[148]
L LPh$_4$ (μ-O$_2$CCPh$_3$)	665 (2300)	873 [-50]	***3.307***	0.57 [1.44]	[93,165]

A = $[Fe^{III}_2(\mu\text{-O})(\mu\text{-1,2-O}_2)(OAc)(BPPE)]^+$, BPPE = 1,2-bis[2-(bis(2-pyridyl)methyl)-6-pyridyl]-ethane; **B** = $[Fe^{III}_2(\mu\text{-O})(\mu\text{-1,2-O}_2)(BQPA)_2]^{2+}$, BQPA = bis(2-quinolylmethyl)-*N*-2-pyridylmethylamine; **C** = $[Fe^{III}_2(\mu\text{-O})(\mu\text{-1,2-O}_2)(6\text{-Me}_3TPA)_2]^{2+}$, 6-Me$_3$TPA = tris(6-methyl-2-pyridylmethyl)-amine; **D** = $[Fe^{III}_2(\mu\text{-O})(\mu\text{-1,2-O}_2)(6\text{-Me}_2BPP)_2]^{2+}$, 6-Me$_2$BPP = bis(6-methyl-2-

pyridylmethyl)-3-aminopropionate; **E** = $[Fe^{III}_2(\mu\text{-}O)(\mu\text{-}1,2\text{-}O_2)(6\text{-}Me\text{-}BQPA)_2]^{2+}$, 6-Me-BQPA = bis(2-quinolylmethyl)(6-methylpyridyl-2-methyl)amine]; **F** = $[Fe^{III}_2(\mu\text{-}O)(\mu\text{-}1,2\text{-}O_2)(BnBQA)_2]^{2+}$, BnBQA = *N*-benzyl-*N*,*N*-bis(2-quinolinylmethyl)amine; **G** = $[Fe^{III}(\mu\text{-}OH)(\mu\text{-}1,2\text{-}O_2)((BnBQA)_2]^{3+}$; **H** = $[Fe^{III}_2(\mu\text{-}OH)(\mu\text{-}1,2\text{-}O_2)(6\text{-}Me_2BPP)_2]^{1+}$; **I** = $[Fe^{III}_2(\mu\text{-}1,2\text{-}O_2)(N\text{-}Et\text{-}HPTB)(\mu\text{-}O_2PPh_2)]^{3+}$, *N*-Et-HPTB = tetrakis(2-benzimidazolylmethyl)-2-hydroxy-1,3-diaminopropane; **J** = $[Fe^{III}_2(\mu\text{-}1,2\text{-}O_2)(O_2PPh_2)(N\text{-}Et\text{-}HPTB)]^{2+}$; **K** = $[Fe^{III}_2(O_2)(N\text{-}Et\text{-}HPTB)(\kappa^1\text{–}O_2PPh_2)\text{-}(MeCN)]^{2+}$, **L** = $[Fe^{III}_2(O_2)(LPh_4)(Ph_3CCO_2)]^{2+}$, LPh_4 = *N,N,N′,N′*-tetrakis[(1-methyl-2-phenyl-4-imidazolyl)methyl]-1,3-diamino-2-propanolate.

A comparison of the spectroscopic properties of the (*μ*-oxo)(*μ*-1,2-peroxo)diiron(III) complexes listed in Table 3.5 shows **2** has properties that most closely resemble those of complex **A**, $Fe^{III}_2(\mu\text{-}O)(\mu\text{-}1,2\text{-}O_2)(OAc)(BPPE)]^+$, where BPPE provides 6 pyridines to support a $[Fe^{III}_2(\mu\text{-}O)(\mu\text{-}1,2\text{-}O_2)(\mu\text{-}OAc)$ core. Complexes **2** and **A** are distinct from the others on the list in having blue-shifted peroxo(π_v^*)-to-iron(III) (d_π orbital) charge transfer bands in the visible region, lower *v*(O–O) values, and shorter Fe•••Fe distances. Complex **2** is the only complex on the list with benzimidazole donors, which are more basic than the pyridine and quinoline donors found on the other complexes[180] and thus expected to decrease the Lewis acidity of the iron(III) centers in **2** and give rise to the blue shift of its absorption maximum. In the case of **A**, the addition of a carboxylate bridge serves to lower the Lewis acidity of the metal centers. More importantly, these two complexes resemble each other in having the lowest *v*(O–O) values and the shortest diiron distances in the series (Table 3.5). For **A**, the bridging acetate and the ethylene linker of the dinucleating ligand bring the two iron atoms closer to each other and presumably give

rise to the lower *v*(O–O) observed, but it is quite remarkable that **2** has the same features without similar structural constraints.

The lower *v*(O–O) of **2** suggests that its O–O bond may be weaker than those of the other reported (*μ*-oxo)(*μ*-1,2-peroxo)diiron(III) complexes (Table 3.5). Additionally, the half-life of **2** (13 min at -40 ^{o}C) is also quite short when compared to related complexes in Table 3.5. The weakened bond and short half-life might prime it to undergo O–O bond cleavage by the addition of a suitable acid and convert **2** into a high-valent diiron species.[100,101] This is important because biologically relevant oxidants are generated in analogous ways in enzymes such as sMMO[75,77,161] and class 1a RNR R2[86–88] This aspect is explored in the following sections.

3.2.5 Protonation of 2 as a strategy to achieve O–O bond cleavage

$HClO_4$ is a Bronsted acid that has been used before in similar studies[94,100,101] and chosen to protonate **2** here. When $HClO_4$ is added to a solution of **2** a new chromophore is formed around 640 nm (Figure 3.11). Similar changes are observed when perchloric acid is reacted with [Fe^{III}_2(*μ*-O)(*μ*-O_2)(BnBQA)$_2$].[101] This new intermediate **[2 + H^+]** has been further studied by various spectroscopies and related results are discussed below.

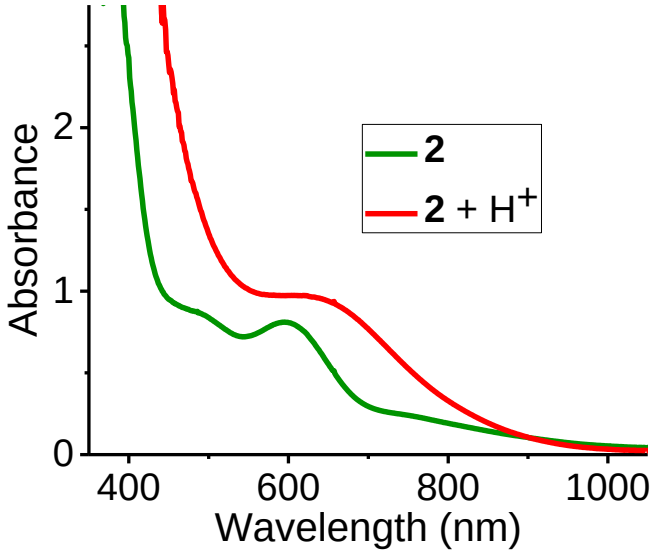

Figure 3.11. UV-vis absorption spectra of **2** (1 mM) and its $HClO_4$ acid (1.5 eq) adduct in CH_3CN at 233 K.

Resonance Raman studies are carried out and resonance-enhanced signals are observed at 820, 527, and 449 cm^{-1}. (Figure 3.12) These vibrations are all isotope sensitive when $^{18}O_2$ is used as the oxidant. This observation suggests that these signals are related to the peroxide moiety and the isotope shifts confirm their assignments as v(O–O), ν_{asym}(Fe−O_2−Fe), and the ν_{sym}(Fe−O_2−Fe) modes. The vibrations of **[2 + H^+]** are very similar to what has been observed for **2**, except for the loss of the ν_{sym}(Fe−O−Fe) and the ν_{asym}(Fe−O−Fe) vibrations. The loss of oxo bridge related vibrations and seemingly unchanged v(O–O) suggests that it is the oxo bridge being affected by strong acid and not the peroxo bridge.

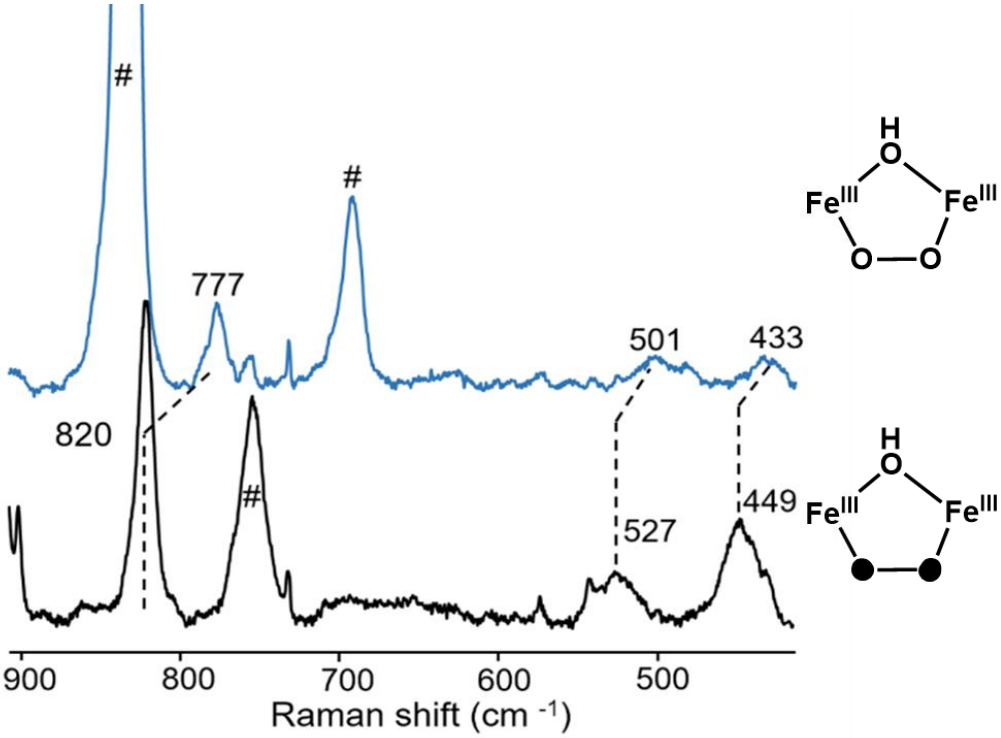

Figure 3.12. Resonance Raman spectra of **[2+H$^+$]** generated by using $^{18}O_2$ (Top) in CD_3CN and $^{16}O_2$ (Bottom) in CH_3CN. The isotope shifts are shown using black dotted lines and the solvent signals are marked by #. Isotopic composition for different spectra are shown on the right-hand side of the figure. Filled oxygen atoms denote ^{18}O-labeled atoms.

XAS studies have been carried out on frozen samples of **[2 + H$^+$].** The XANES spectrum is shown in Figure 3.13 and the region shows similar K-edge energy of 7126.7 eV for **[2 + H$^+$]** like **2** (7126.3 eV) consistent with a +3-oxidation state of each iron atom in both complexes. The protonation of **2** causes the pre-edge area to decrease by 6 units from 18.2 to 12.2 units. (Table 3.6) This reflects a greater symmetry around each iron center. Interestingly, the bond metrics determined by EXAFS give insight into the resonance Raman results. The best fit gives a first shell consisting of 2 N/O scatterers at 1.89 Å (associated with the μ-hydroxo and μ-1,2-peroxo

moieties) and 4 N/O scatterers at 2.09 Å (arising from the supporting ligand) (Figure 3.13). Remarkably, the Fe•••Fe distance remains essentially unchanged at 3.09 Å, which is within the experimental uncertainty of EXAFS analysis. This result is supported by resonance Raman data showing that the ν(O–O) of **[2 + H$^+$]** is only 5 cm^{-1} lower than that for **2**. This is another consequence of the correlation originally developed by Feidler et al. (Figure 3.5).[73] It is worthwhile to mention here that the ν(O–O)'s of other Fe$^{III}_2$(μ-O)(μ-1,2-O$_2$) complexes typically increase by at least 50 cm^{-1} upon treatment with strong acids.[101,169] This is not the case for **2** and is thus a unique feature of this peroxodiiron(III) complex.

Table 3.6. Pre-edge fitting parameters and k-edge energy for **[2 + H$^+$]**

Species	K-edge (eV)	Peak Position (eV)	Area (units)	Relative Area
2 + H$^+$	7126.7	7114.7	9.9	4.3
		7113.3	2.3	1
			Total = 12.2	

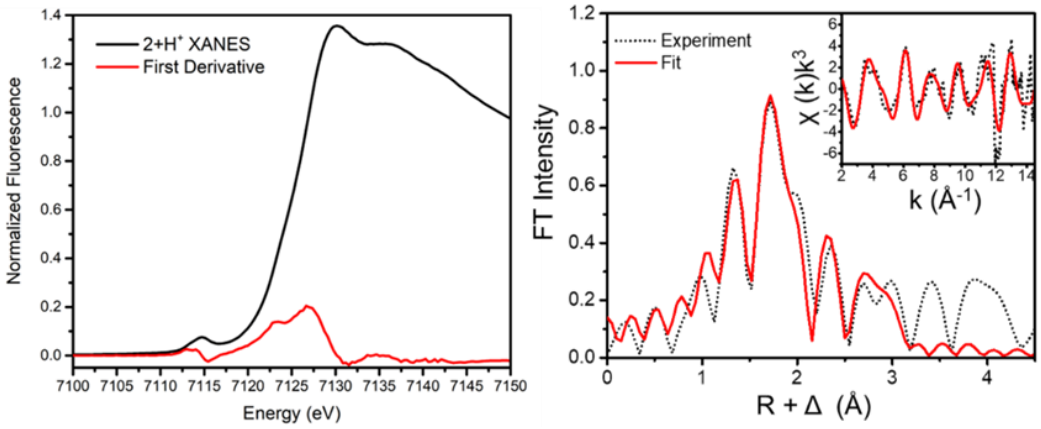

Figure 3.13. (Left) Fe-K edge pre-edge features for **[2 + H$^+$]. (Right)** Fourier-transformed EXAFS data and fit for **[2 + H$^+$]** and k-space data and fit for **[2 + H$^+$]** (inset).

Table 3.7. EXAFS fitting parameters for **[2 + H^+];** best fits in bold font

	Fe-N/O			Fe-O/N			Fe•••C/N			Fe•••Fe				GOF	
Fit	**N**	**R(Å)**	**$\sigma^2(10^{-3})$**	**N**	**R(Å)**	**$\sigma^2(10^{-3})$**	**N**	**R(Å)**	**$\sigma^2(10^{-3})$**	**N**	**R(Å)**	**$\sigma^2(10^{-3})$**	**E_0**	**F**	**F'**
1	4	2.10	3.49										1.91	732	470
2	4	2.09	2.22	2	1.89	5.01							-5.22	648	469
3	4	2.09	2.18	2	1.89	5.25				1	3.07	8.05	-4.69	629	467
4	4	2.08	1.97	2	1.89	4.58	3	2.91	0.29	1	3.06	3.01	-4.89	590	465
5	4	2.09	2.03	2	1.89	4.76	4 3	2.92 3.64	2.03 3.25	1	3.08	2.52	-4.55	593	463
6	4	2.09	1.97	2	1.89	4.80	4 3 5	2.93 3.66 3.91	1.68 2.25 2.04	1	3.08	2.25	-3.92	580	462
7	**4**	**2.08**	**1.78**	**2**	**1.89**	**4.26**	**3**	**2.92**	**0.25**	**1**	**3.08**	**2.85**	**-4.79**	**578**	**462**

Mössbauer spectroscopy of **[2 + H^+]** at 4.2 K and zero applied field reveals two different putative diiron complexes that are generated in a ratio of 7:3. Both species are shown to be typical diiron(III) complexes by their isomer shifts and quadrupole splittings (Major component (70%): δ = 0.56 mms^{-1}, ΔE_Q = 1.17 mms^{-1}; Minor component (30%): δ = 0.46 mms^{-1}, ΔE_Q = 0.69 mms^{-1}) determined by Mössbauer simulations. (Figure 3.14) The former doublet is assigned to the hydroxo-bridged peroxodiiron(III) species as the same is observed by other corroborative spectroscopies, and assumed to be the major component here.

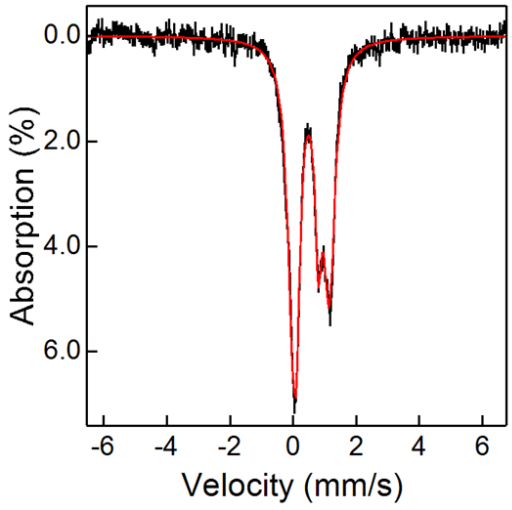

Figure 3.14. Mössbauer spectra of **[2 + H^+]** at 4.2 K and 0 T. Black trace denotes experimental data and the red trace is the simulation of the data.

A unique feature of **[2 + H^+]** ($t_{1/2}$ = 75 min at 233 K) is the longer lifetime compared to its conjugate base **2** ($t_{1/2}$ = 13 min at 233 K). (See Figure 3.15) This is in direct contrast to the BnBQA system where the hydroxo peroxo ($t_{1/2}$ = 40 min at 233 K) is much less stable than the oxo peroxo ($t_{1/2}$ = 6 h at 233 K). Thus, protonation affects the stabilities of the Me_3NTB and BnBQA peroxo complexes in opposite directions for reasons we do not yet fully understand. More examples of oxo and hydroxo bridged pairs need to be studied to shed light on this interesting aspect.

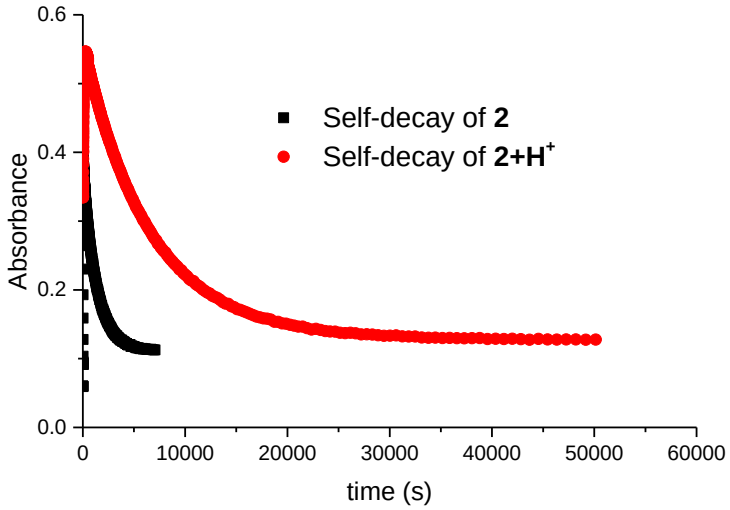

Figure 3.15. Comparison of self-decay curves of **2** and **[2 + H^+]** in CH_3CN at -40 °C.

3.2.6 Lewis acid addition to 2 to achieve O–O bond cleavage

Attempts to use Bronsted acids to induce O–O bond cleavage in **2** to generate a high-valent complex have been unsuccessful. However, the lower *v*(O–O) of **2** points toward a weakened bond, which then must be

primed to undergo O–O bond cleavage. Moving away from Bronsted acids to Lewis acids such as $Sc(OTf)_3$ produces different results. When $Sc(OTf)_3$ is added to a solution of **2**, a deep green chromophore appears (Figure 3.16). When examined using UV-vis absorption spectroscopy at 233 K, the resulting complex exhibits an intense absorption feature at 600 nm (9000 M^{-1} cm^{-1}) that fully forms over an hour.

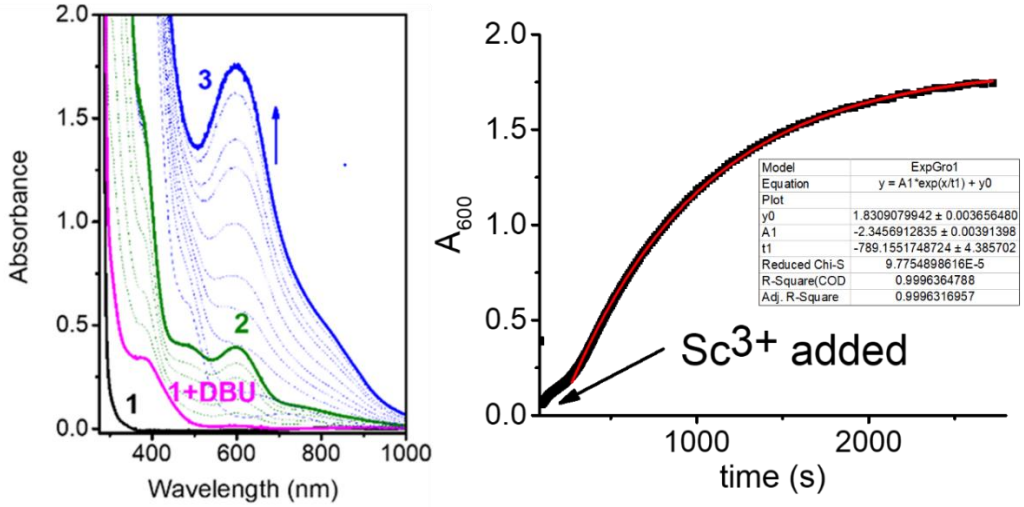

Figure 3.16. UV-vis absorption spectra of **1** (1 mM, black), **[1 + DBU]** (magenta) formed after addition of 1.5 eq DBU, **2** (green) obtained upon oxygenation of **1** in the presence of DBU, and **3** (blue) formed upon addition of 2 eq $Sc(OTf)_3$ to **2**, all in CH_3CN at -40 ºC. The figure on the right shows the 600 nm time trace after the addition of $Sc(OTf)_3$ to **2.** The red trace is the fit of the growth curve using a first-order exponential function.

Excitation of the intense visible chromophore of **3** using a 660-nm laser at 233 K elicits a resonance Raman spectrum with an intense signal at 653 cm^{-1} and a weaker feature at 528 cm^{-1} (Figure 3.17). A Raman spectrum of a sample of ^{18}O-labeled **3** derived from ^{18}O-labeled **2**, generated from the reaction of [**1 + DBU**] with $^{18}O_2$, shows the 653- and 528-cm^{-1} signals to be respectively downshifted to 623 and 511 cm^{-1}. The vibrational

frequency of 653 cm^{-1} with an isotopic shift of 30 cm^{-1} for **3** reflects an Fe–O–Fe angle of close to 100°, characteristic of complexes with an $M_2(\mu\text{-}O)_2$ 'diamond core'.[78,177,181–184] Such an acute angle has thus far only been shown to be enforced by the presence of a second *μ*-oxo bridge. Furthermore, experiments starting with a 1:1 mixture of $^{16}O_2$-labeled **2** and $^{18}O_2$-labeled **2** to form **3** show the formation of $Fe^{IV}_2(\mu\text{-}O)_2$ species having either two ^{16}O atoms or two ^{18}O atoms but with no evidence for a mixed-$^{16}O^{18}O$ complex, which should exhibit an intermediate frequency of 638 cm^{-1} (Figure 3.18). Thus, both oxygen atoms in **3** must derive from the peroxo moiety of one unique molecule of **2** and the oxo-bridged O-atom in **2** must be released from the complex, presumably upon the combination with $Sc(OTf)_3$.

The 653-cm^{-1} Raman band is reminiscent of the 674 cm^{-1} feature reported for $[Fe^{IV}_2(\mu\text{-}O)_2(TPA^*)_2]^{4+}$,[177] which is associated with an A_1 breathing mode of an $Fe_2(\mu\text{-}O)_2$ core that has an Fe−O−Fe angle of 100°.[78,183] Furthermore, the observation of an ^{18}O-isotope shift of ~30 cm^{-1} confirms that this vibration is essentially an Fe–O stretching mode. Interestingly, the 653-cm^{-1} peak falls within error on the higher frequency line in Figure 3.8, which represents the asymmetric Fe–O–Fe modes of the Fe–O–Fe complexes. The corresponding features for $[Fe^{IV}_2(\mu\text{-}O)_2(TPA^*)_2]^{4+}$, $[Fe^{III}Fe^{IV}(\mu\text{-}O)_2(R\text{-}TPA)_2]^{3+}$, and $[Fe^{III}_2(\mu\text{-}O)_2(6\text{-}Me_3\text{-}TPA^*)_2]^{2+}$, shown as triangles, also fall on this line (see Table 3.8 for a comparison of properties for $Fe_2(\mu\text{-}O)_2$ complexes). A similar assignment for the 650-700-cm^{-1} vibration observed in $[Fe^{III}Fe^{IV}(\mu\text{-}O)_2(R\text{-}TPA)_2]^{3+}$ complexes have been made by Solomon and co-workers using normal coordinate analysis.[183]

Complex **3** also exhibits a peak at 528 cm^{-1} with an ^{18}O-isotope shift of 17 cm^{-1}, which would arise from a different Fe_2O_2 mode. Such a feature has

thus far not been observed for any other complex with an $Fe_2(\mu\text{-}O)_2$ core, but all the valence-delocalized $[Fe^{III}Fe^{IV}(\mu\text{-}O)_2(R_3\text{-}TPA)_2]^{3+}$ complexes show a feature near 410 cm^{-1} with comparable ^{18}O-isotope shifts,[78] suggesting that these modes may be related, a notion corroborated by our computational studies (*vide infra*). Clearly, these features do not fall on the lower frequency line of the correlation shown in Figure 3.8 that represents the symmetric Fe–O–Fe modes of the Fe–O–Fe complexes. However, further studies exploring the connection between Fe–O–Fe complexes that have effective C_{2v} symmetry and the diamond core complexes that have effective C_{2h} symmetry are worth pursuing.

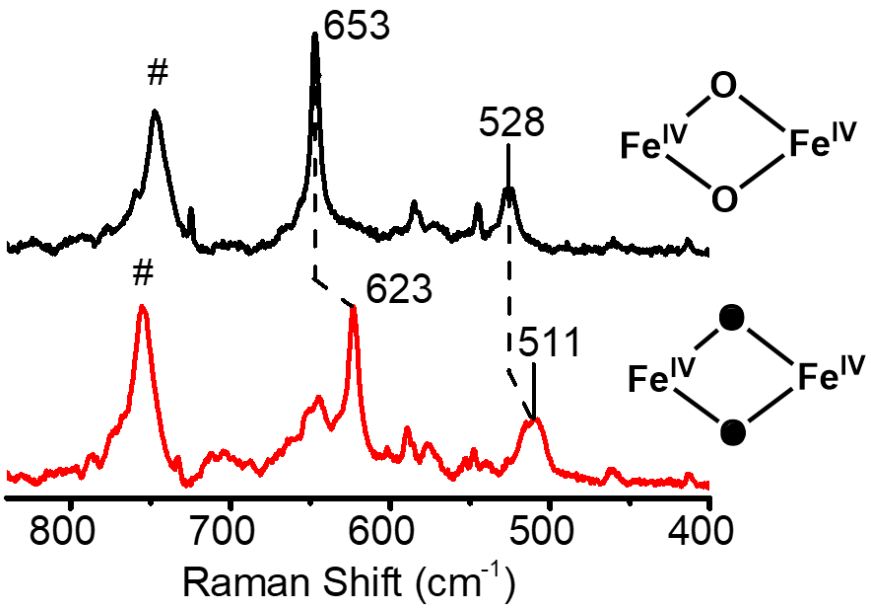

Figure 3.17. Resonance Raman spectra of **3** in CH_3CN derived from $^{16}O_2$ (black) and $^{18}O_2$ (red). The latter was prepared from ^{18}O-labeled **2** generated from the reaction of [**1 + DBU**] with $^{18}O_2$. Dotted lines highlight observed isotope shifts, while # signs correspond to solvent features. Filled oxygen atoms denote ^{18}O isotope incorporation into **3.**

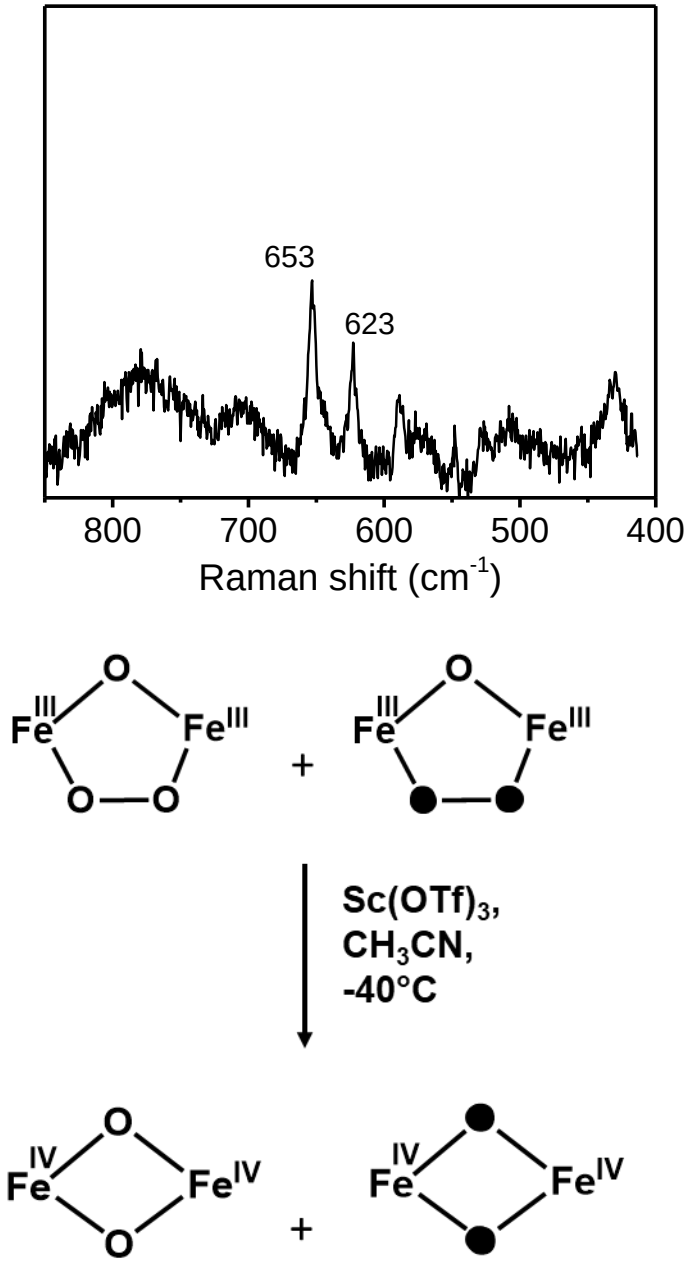

Figure 3.18. (Top) Resonance Raman spectra of **3** generated by adding $Sc(OTf)_3$ to a mixture of $^{16}O_2$-**2** and $^{18}O_2$-**2** in CH_3CN at -40°C, demonstrating that mixed-labeled **3** does not form. (Bottom) Scheme showing the experimental results of the mixed labeling experiment. Filled

oxygen atoms denote ^{18}O isotope and hollow oxygen atoms denote ^{16}O isotope.

Table 3.8. Properties of $Fe_2(\mu\text{-}O)_2L_2$ complexes

Complex	**v(Fe–O) [$\Delta^{18}O$] (cm^{-1})**	**∠Fe–O–Fe (°)**	**d(Fe••Fe) (Å)**	**Ref.**
3	653 [-30] 528 [-17]	97 [a]	2.70	This work
M = Fe^{IV} L = TPA*	674 [-30]	101 [a]	2.73	[177]
M = Fe^{III} L = 6-Me_3TPA	692 [-32]	***92.5*** [b]	***2.714*** [b]	[78,184]
M = $Fe^{3.5}$ L = 5-Et_3-TPA	666 [-35] 411 [-15]	***94.1*** [b]	***2.683*** [b]	[182,183]
M = $Fe^{3.5}$ L = R_3-TPA R = H, 3-Me, or 5-Me	666-668 [-(28 -32)] 404-411 [-(13 -16)]			[78]
sMMO-**Q**	690 [-36]		~3.4	[77,80]

[a] Calculated based on $r_{Fe–O}$ and $r_{Fe•••Fe}$ values obtained from EXAFS data.

[b] Values obtained by X-ray crystallography.

TPA* = tris(3,5-dimethyl4-methoxy-2-pyridylmethyl)amine; 6-Me_3TPA = tris(6-methyl-2-pyridylmethyl)amine; 5-Et_3TPA = tris(5-ethyl-2-pyridylmethyl)amine; TPA = tris(2-pyridylmethyl)amine 3-Me_3TPA = tris(3-methyl-2-pyridylmethyl)amine; 5-Me_3TPA = tris(5-methyl-2-pyridylmethyl)amine; sMMO-**Q** = **Q** intermediate in soluble methane monooxygenase enzyme

---

Mössbauer spectra of ^{57}Fe-enriched **3** have been obtained at 4.2 K and under different applied magnetic fields. The zero-field spectrum of **3** exhibits two quadrupole doublets (Figure 3.19). One doublet exhibits an isomer shift (δ) of -0.04 mm/s and a quadrupole splitting (ΔE_Q) of 2.00 mm/s, nearly identical to those of $[Fe^{IV}_2(O)_2(TPA^*)_2]^{4+}$ (δ = -0.04 mm/s and ΔE_Q = 2.09 mm/s).[177] The other doublet (δ = 0.48 mm/s and ΔE_Q = -1.22 mm/s) has parameters typical of a diferric species.[185,186] The diiron(IV) state in **3** is validated by field-dependent studies performed at 4.2 K with various applied magnetic fields (2.0T, 4.0T, 7.0T) (Figure 3.20). The sample also contains a large fraction of a mononuclear high-spin ferric byproduct. After subtracting out the high-spin ferric component, a cleaner spectrum with only diiron(III) and diiron(IV) complexes can be obtained (Figure 3.21). Analysis of all the spectra from three different samples of ^{57}Fe-enriched **3** shows that the samples contain only ~35% of the diiron(IV) complex, together with 40% of a diferric species and 25% of high-spin ferric components (See Table 3.9 for more details). The diferric species and high-spin ferric components are the decay product as evidenced by the Mössbauer data of the decay product of **3**. (Figure 3.22) The simulation parameters for the diferric and high-spin monoferric components are the same as were used in the simulation of Mössbauer spectra of **3**.

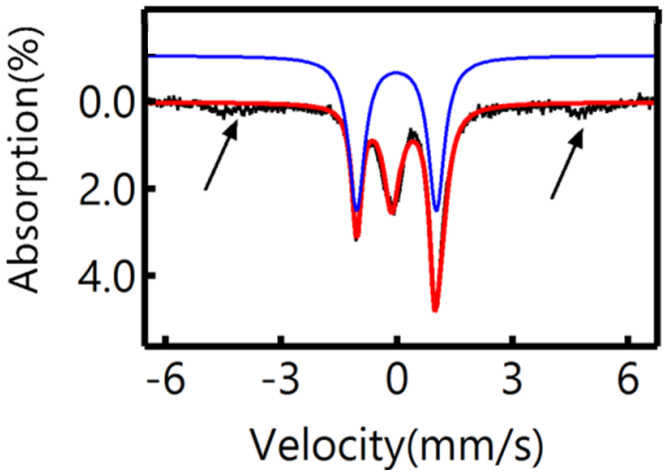

Figure 3.19. Mössbauer spectra of **3** at 4.2 K and 0 T. Black trace denotes experimental data and the red trace is the simulation of the data. The arrows represent features from mononuclear iron(III) impurities. The blue trace shows a simulation of the diiron(IV) component only.

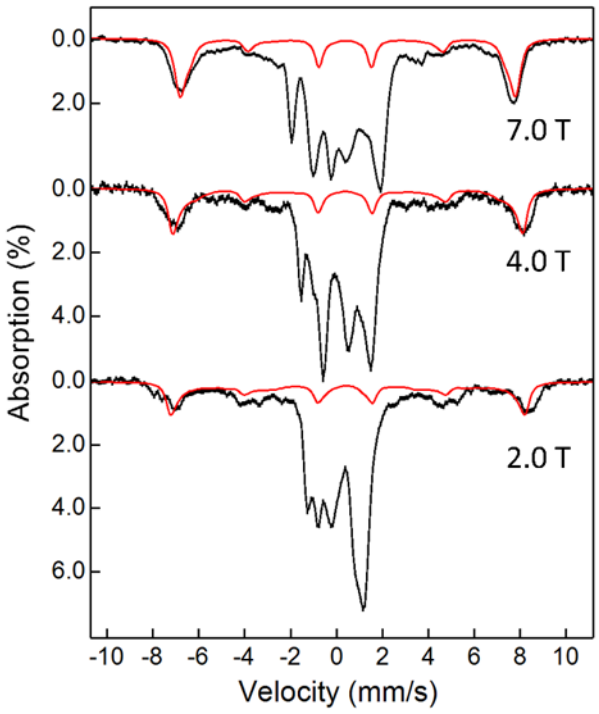

Figure 3.20. 4.2 K Mössbauer spectra of **3** (with various applied magnetic fields (2.0T, 4.0T, 7.0T respectively). Black: experimental spectra of the whole sample; red: theoretical simulation of the high-spin ferric impurity in the sample with the parameters in Table 3.9.

Table 3.9. Theoretical simulation parameters in the spin Hamiltonian for the fit of **3** shown in Figure 3.20.

Species	Diiron(IV) component	Diiron(III) component	High-spin ferric
Spin state	S = 0	S = 0	S = 5/2
Isomer shift (mm/s)	-0.04	0.48	0.44
D (cm^{-1})	-	-	3.0
E/D	-	-	0.15
Quadrupole splitting (mm/s)	2.00	-1.22	-0.24
η	0.4	0.9	0.0
$A_x/g_n\beta_n$ (kG)	-	-	-214
$A_y/g_n\beta_n$ (kG)	-	-	-214
$A_z/g_n\beta_n$(kG)	-	-	-214
Line width (mm/s)	0.3	0.5	0.4
Percentage	35 %	35%	30%

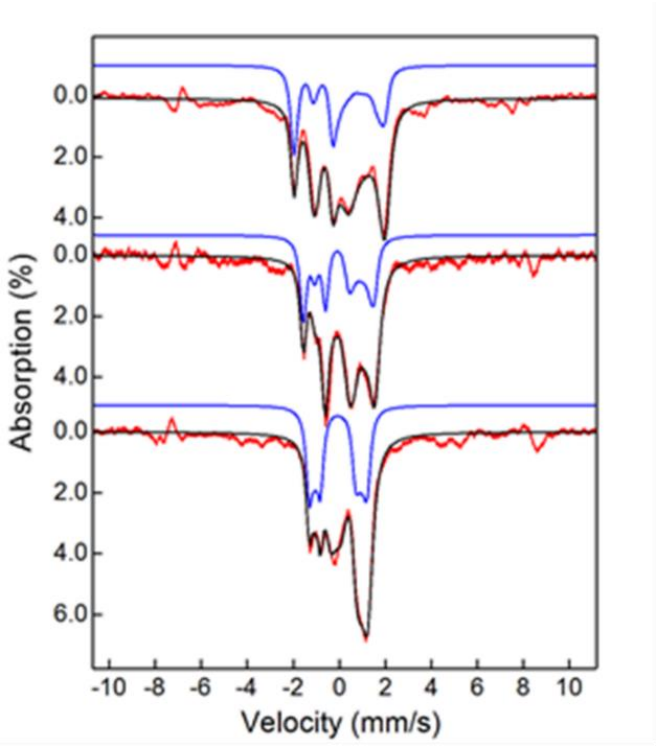

Figure 3.21. 4.2 K Mössbauer spectra of **3** (with various applied magnetic fields (2.0T, 4.0T, 7.0T respectively)). Red: experimental spectra of the whole sample; black: the theoretical simulation of the diiron(III) and diiron(IV) components; blue: the theoretical simulation of the only diiron(IV) component.

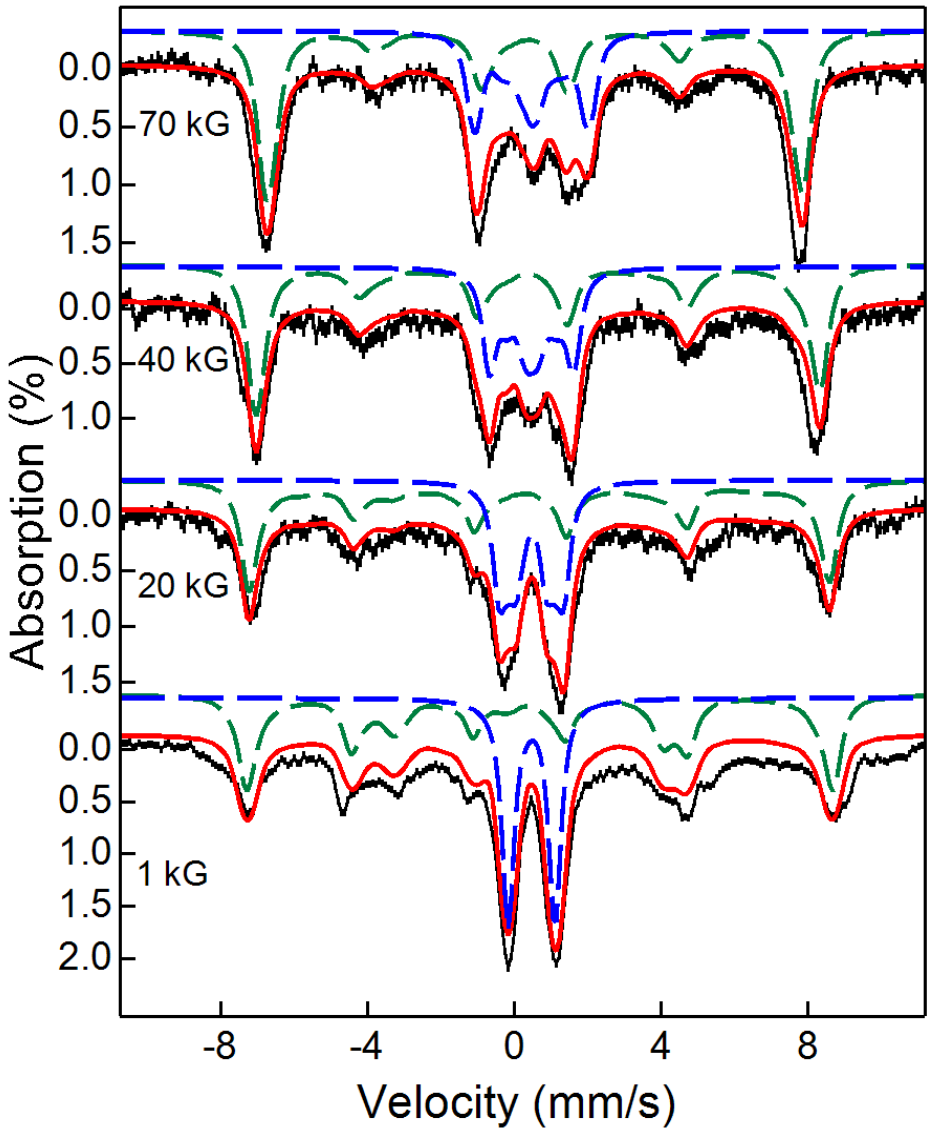

Figure 3.22. 4.2 K Mössbauer spectra of the decayed product of **3** (with various applied magnetic fields (70kG, 40kG, 20kG, 1kG)). Black: experimental spectra of the whole sample; red: the theoretical simulation of the diiron(III) and high-spin mono-ferric species; blue: the theoretical simulation of the diiron(III) species; green: the theoretical simulation of the monoferric species.

XAS studies also support the assignment of **3** as having an $Fe^{IV}_2(\mu\text{-}O)_2$ core. The XANES region in Figure 3.23 shows an increase in the K-edge energy of more than one eV from 7126.3 eV for **2** to 7127.5 eV for **3**, consistent with one-electron oxidation of each iron atom. The K-edge energy value for **3** is not as high as that for $[Fe^{IV}_2(\mu\text{-}O)_2(TPA^*)_2]^{4+}$ (7130.1 eV) due in part to the smaller fraction of **3** (~35%) present in these samples than is found in preparations of $[Fe^{IV}_2(\mu\text{-}O)_2(TPA^*)_2]^{4+}$ (86-90%).[177]

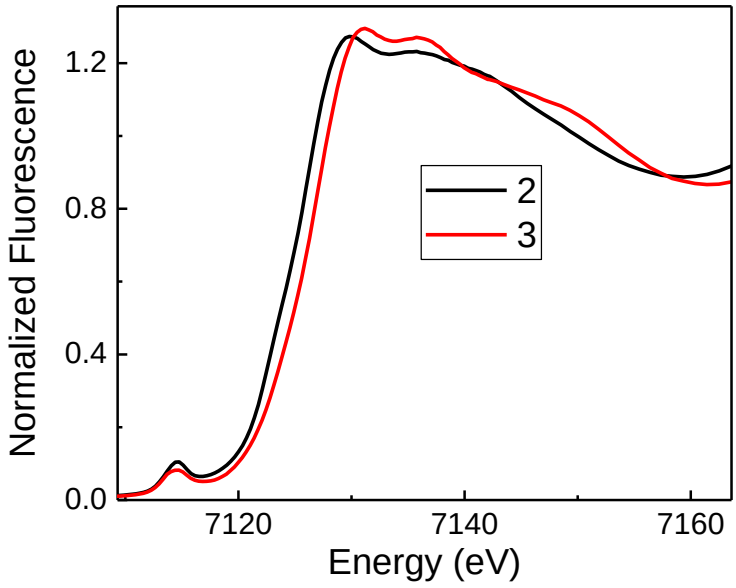

Figure 3.23. Fe K-edge XANES (X-ray Absorption Near-Edge Structures) data of **2** and **3**. The higher oxidation state of the iron centers in **3** is manifested in higher K-edge energy when compared with **2**.

Despite the low yield of **3**, its EXAFS analysis still provides strong support for the assignment of **3** as having an $Fe^{IV}_2(\mu\text{-}O)_2$ diamond core. (Figure 3.24) The primary coordination sphere is composed of 2 N/O scatterers at 1.79 Å, 2 N/O scatterers at 1.97 Å, and 2 N/O scatterers at 2.09 Å. (Table 3.10) The contraction of 4 scatterers in the first shell, 2 from 2.05 to 1.97,

and 2 from 1.83 to 1.79 would be expected upon the oxidation of the iron centers. The remaining scatterers in the first shell at 2.09 Å are consistent with the presence of the diferric and monoferric decay products (previously identified by Mössbauer spectroscopy) in the sample (*vide infra*). More tellingly, the diiron distance contracts significantly from 3.07 Å to 2.70 Å (Figure 3.24), the latter value being almost identical to that reported for $[Fe^{IV}_2(\mu\text{-}O)_2(TPA^*)_2]^{4+}$ (Table 3.11). Because **3** represents only about a third of the iron in the samples, the n value for the iron scatterer at 2.7 Å was constrained to 0.4 in the fitting (Table 3.10). Even with such a small number of short diiron scatterers, the Debye-Waller factor is close to zero (0.07), a behavior consistent with previously reported diferryl diamond core compounds.[177] It is also reflective of the rigidity of the diamond core moiety and explains the large contribution of the diiron feature to the FT EXAFS spectrum (Figure 3.24). The EXAFS analysis of the sample containing **3** also includes a second Fe scatterer at 3.28 Å, which is constrained to n = 0.4 and can be associated with the diiron(III) component observed by Mössbauer spectroscopy. Another piece of evidence that suggests **3** has an $Fe^{IV}_2(\mu\text{-}O)_2$ diamond core is the EXAFS analysis of its thermally decayed product, for which no 2.70 Å scatterer is observed. (Figure 3.24) Instead, the diiron distance found in the sample of decayed **3** is 3.34 Å, similar to the 3.28 Å diiron distance associated with the diiron(III) component found in **3** (Table 3.12). The bond metrics from the EXAFS fit of **3** can be used to calculate an Fe–O–Fe angle of 97°. When this value is plotted against its Fe–O–Fe vibration at 653 cm^{-1} (*represented by a pink triangle*), it fits reasonably on the Sanders-Loehr correlation for the series of Fe–O–Fe complexes shown in Figure 3.25.

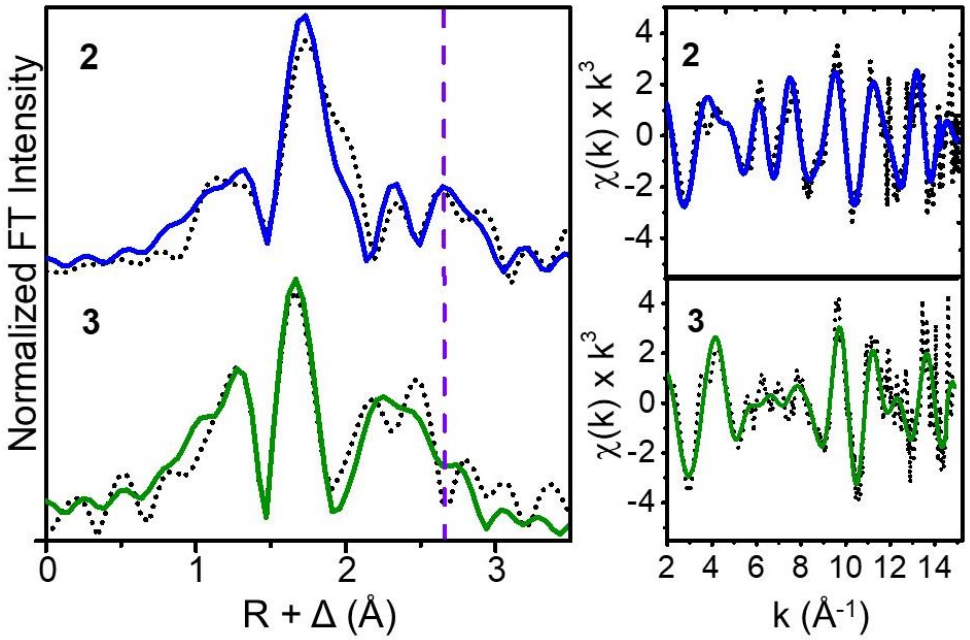

Figure 3.24. Left: Fourier-transformed *k*-space EXAFS data for **2** (top) and **3** (bottom). The vertical dashed purple line highlights the feature associated with the Fe scatterer in **2** and its change between **2** and **3**. **Right:** *k*-space EXAFS data for **2** (top) and **3** (bottom). Data is represented by black dots, and the best fits are blue for **2** and green for **3**.

Table 3.10. EXAFS fitting parameters for **3**; best fits in bold font

3		Fe-N/O			Fe-O/N			Fe•••C/N			Fe•••Fe				GOF	
Fit	N	R(Å)	$\sigma^2(10^{-3})$	N	R(Å)	$\sigma^2(10^{-3})$	N	R(Å)	$\sigma^2(10^{-3})$	N	R(Å)	$\sigma^2(10^{-3})$	E_0	F	F'
1	4	2.09	2.67										67.9	883	631
2	2	2.04	2.34	2	1.81	6.83							-7.39	764	628
3	2	2.01	-0.60	2	1.82	3.61							-2.41	696	626
	2	2.13	0.09												
4	2	1.99	0.54	2	1.81	3.96				0.4	2.70	0.26	-3.95	535	623
	2	2.11	0.57												
5	2	1.99	0.17	2	1.81	3.61				0.4	2.71	0.00	-4.08	522	621
	2	2.11	0.01							0.4	3.28	8.66			
6	**2**	**1.97**	**2.17**	**2**	**1.79**	**4.15**	**2**	**2.90**	**6.40**	**0.4**	**2.70**	**0.07**	**-5.17**	**517**	**618**
	2	**2.09**	**1.94**							**0.4**	**3.28**	**6.97**			

Table 3.11. Comparison of EXAFS-derived iron-scatterer distances for **3** and previously reported closed core diiron(IV) model.

Complex	d(Fe–O) (Å)	d(Fe–N) (Å)	d(Fe••Fe) (Å)	Ref
Diiron(IV) diamond core complexes				
3	2 @ 1.79	2 @ 1.97 2 @ 2.09	2.70	This work
$[Fe^{IV}_2(O)_2$-$(TPA^*)_2]^{4+}$	2 @ 1.78	4 @ 1.97	2.72	[177]

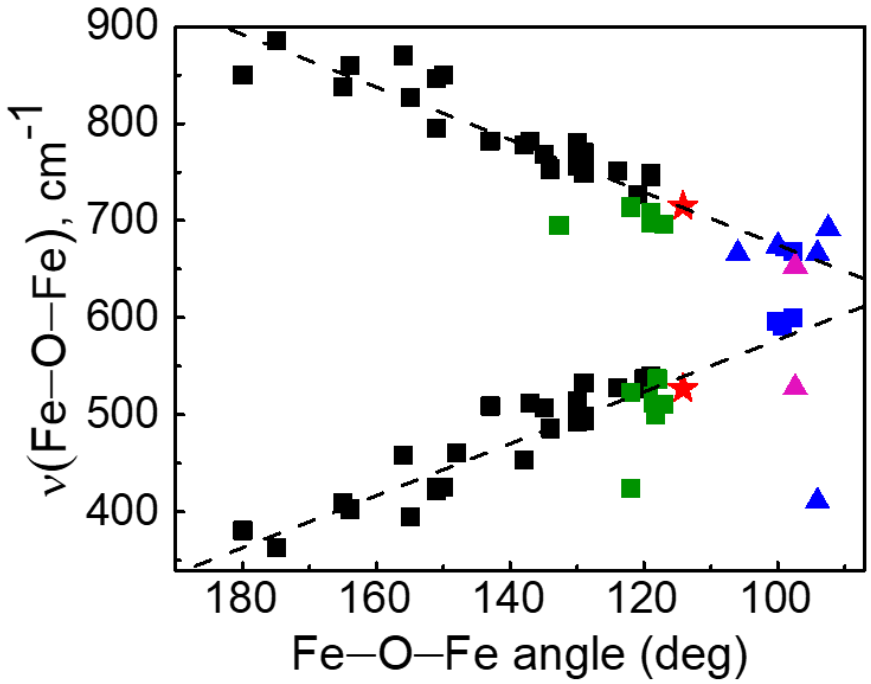

Figure 3.25. Correlation between Fe–O–Fe angles of oxo-bridged diiron complexes and ν_s(Fe–O–Fe) (bottom) and ν_{as}(Fe–O–Fe) values (top). Data from the original Sanders-Loehr study (black),[176] augmented by data for species with $Fe_2(\mu\text{-}O)(\mu\text{-}1,2\text{-}O_2)$ (green)[73,100,101,167,169,170], $Fe_2(\mu\text{-}O)_2$ cores (blue triangles) and $Fe_2(\mu\text{-}O)(\mu\text{-}OH)$ cores (blue squares).[78,177,178] The Fe–O–Fe vibrations of **2** are shown as red stars, while that associated with **3** are indicated by pink triangles. The black dashed lines show the best linear fit of the data points available. The relationship between the vibrations of the Fe–O–Fe unit and the related Fe–O–Fe bond angle has been studied originally using secular equations.[179]

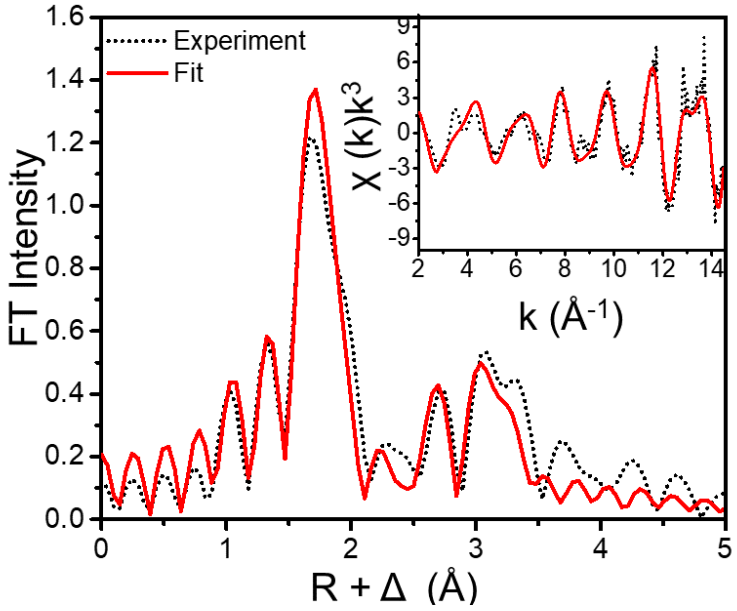

Figure 3.26. Fourier transformed and k-space (inset) EXAFS data (dotted black line) and best fit (red line) for **3 decay.**

Table 3.12. EXAFS fitting parameters for **3 decay**; best fits in bold font

Decayed 3	Fe-N/O			Fe-O/N			Fe•••C/N			Fe•••Fe			GOF		
Fit	**N**	**R(Å)**	**$\sigma^2(10^{-3})$**	**N**	**R(Å)**	**$\sigma^2(10^{-3})$**	**N**	**R(Å)**	**$\sigma^2(10^{-3})$**	**N**	**R(Å)**	**$\sigma^2(10^{-3})$**	**E_0**	**F**	**F'**
1	6	2.07	3.94										-2.45	893	392
2	4	2.07	1.13										-1.70	745	392
3	4	2.05	2.11	1	1.82	-0.80							-4.01	569	391
4	4	2.05	1.84	1 1	1.82 1.71	-1.00 13.82							-5.81	558	389
5	4	2.05	0.94	2	1.83	2.86							-7.61	575	391
6	4	2.06	1.00	2	1.83	3.49				1	3.36	1.44	-4.29	548	389
7	4	2.07	0.92	2	1.83	3.03	4	2.91	2.81	1	3.36	1.89	-3.93	534	387
8	**4**	**2.07**	**0.95**	**2**	**1.83**	**4.07**	**4** **5**	**2.96** **3.17**	**3.46** **0.05**	**1**	**3.34**	**1.01**	**-1.80**	**451**	**386**

Similar spectral changes are seen with $Al(OTf)_3$ as the Lewis acid under the same conditions (Figure 3.27). However, the addition of $Yb(OTf)_3$, $Y(OTf)_3$, $Zn(OTf)_2$, $Ca(OTf)_2$, and $Ba(OTf)_2$ does not result in the formation of **3**, suggesting that there is a threshold in the Lewis acidity of the added metal ion that needs to be crossed to generate **3**. As the Lewis acidities of Sc^{3+} and Al^{3+} ions[187,188],[189] are higher than the other cations mentioned above, a stronger Lewis acid must be required to convert **2** into the diiron(IV) species **3**. Similar effects have been observed for the cleavage of the O–O bond of $[(TMC)Fe^{III}(\eta^2\text{-}O_2)]^+$ with Sc^{3+} and Y^{3+} ions.[190,191],[192] In the latter study, both ions promote O−O bond cleavage to form the $[(TMC)Fe^{IV}(O)]^{2+}$ derivative but the rates depend on the Lewis acidity of the metal ions.

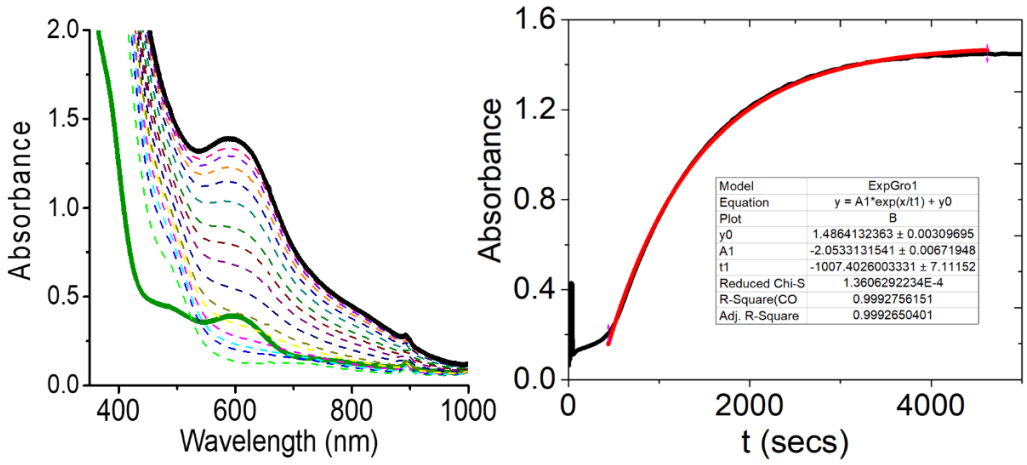

Figure 3.27. UV-vis spectra and 600 nm time trace with a first-order exponential growth curve fit, showing the changes to **2** (0.5 mM, green line) upon the addition of (2 eq) $Al(OTf)_3$ to form **3** (black line) in CH_3CN at -40 °C.

Interestingly, the Lewis acid effect of Sc^{3+} on **2** can be nullified in the presence of 200 mM water (Figure 3.28), and **[2 + H^+]** is formed instead. This effect resembles the effect of treating **2** with $HClO_4$ (Figure 3.11) and suggests that $Sc(OTf)_3$ hydrolyzes under these conditions to produce protons in solution to give rise to **[2 + H^+]**.

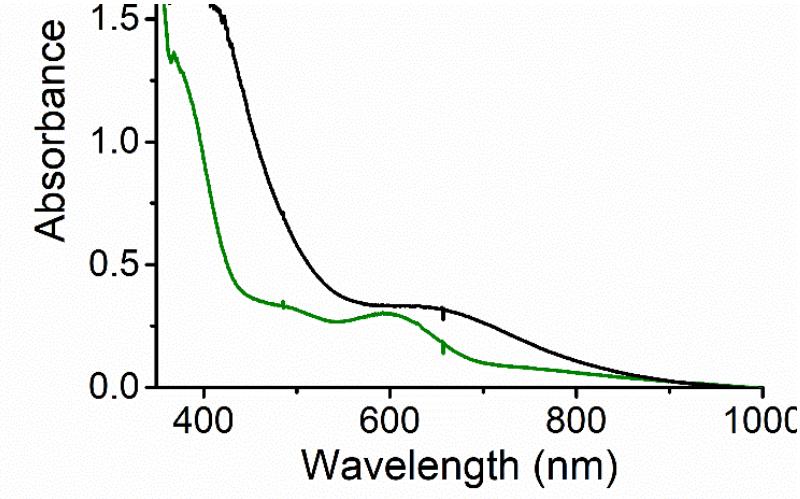

Figure 3.28. UV-vis spectra of the changes to **2** upon the addition of (2 eq) $Sc(OTf)_3$ in the presence of excess water (200 mM) in CH_3CN at -40 °C. The new chromophore (640 nm) seen here is identical to that observed upon protonation of **2**.

As mentioned before, only strong Lewis acids like Sc^{3+} and Al^{3+} generate **3**, whereas weaker Lewis acids like Y^{3+}, Yb^{3+}, Zn^{2+}, $Ca^{2+,}$ and Ba^{2+} do not. Nevertheless, all these Lewis acids do react with **2** except for Ba^{2+}. The reactions of **2** with these Lewis acids almost spontaneously generate **[2 + LA]** adducts. As shown in the UV-vis spectra shown below (Figure 3.29 and 3.30), the charge transfer band of **2** at 595 nm appears to blue shift to higher energy. The spectra of **[2 + Sc]** and **[2 + Al]** are practically the same (Figure 3.29) and successfully generates **3** after standing for an hour at 233 K. Adducts with other cations produce blue-shifted absorption features

(Figure 3.30) that are close to one another. Ba^{2+} is plausibly too big to interact with **2** as no changes are observed when 2 equiv of $Ba(OTf)_2$ is added to a solution of **2**.

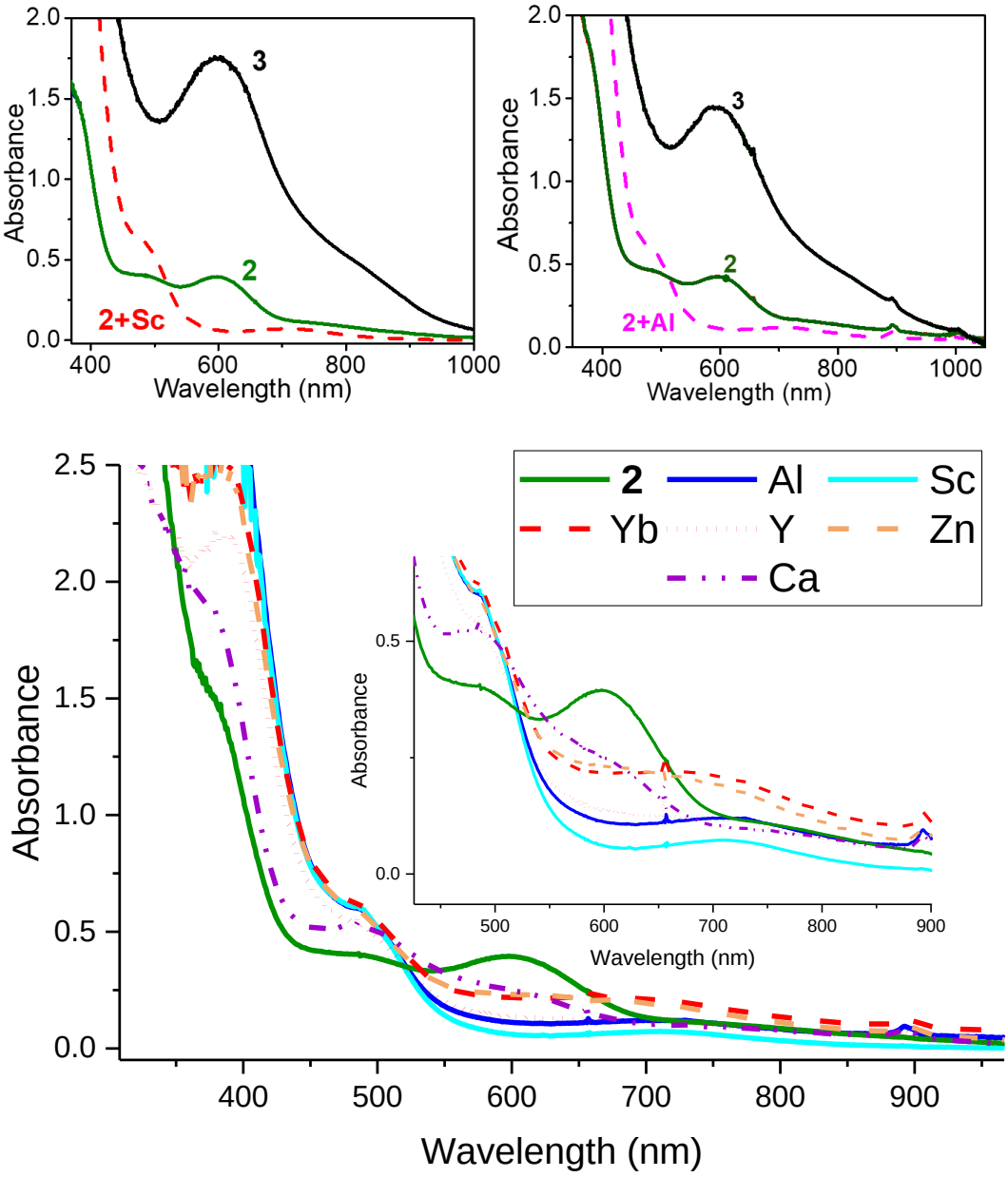

Figure 3.29. (**Top**) UV-vis spectra showing the changes to **2** upon the addition of 2 eq $Sc(OTf)_3$ (left) or $Al(OTf)_3$ (right) in CH_3CN at -40 °C. These figures show the **[2 + Sc]** and **[2 + Al]** adducts before they convert to **3**.

(**Bottom**) UV-vis spectra of the Lewis acid adducts of **2** upon the addition of 2 equiv of the acids in CH_3CN at -40 °C. The legend shows the labeling of different traces that are similar to one another. The spectra are taken right after the addition of Lewis acids in contrast to the top panel where the formation of **3** was followed an hour after the additions.

Mössbauer data has been collected on a sample of **[2 + Sc],** the Sc^{3+} adduct of **2**, which has been frozen before it could transform into **3**. The Mössbauer study of **[2 + Sc]** shows that it is not a pure species (Figure 3.29 bottom panel). There are two diferric components and some ferrous component in the mixture. It is important to note here that none of these parameters match with those of **2** or **[2 + H]**, confirming that there is no unreacted **2** or proton generation after the addition of $Sc(OTf)_3$ under these conditions. An attractive conjecture is that one of these ferric doublets gives rise to **3** within an hour, which may explain a low yield of **3** as detailed before. Mössbauer titrations in the conversion of **2** to **3** are underway to shed light on which of these ferric doublets ultimately converts to **3**. This will also elucidate the mechanism of the formation of **3** from **2**, which is significant if we want to broaden the scope of the ligands used to carry out analogous chemistry as reported here.

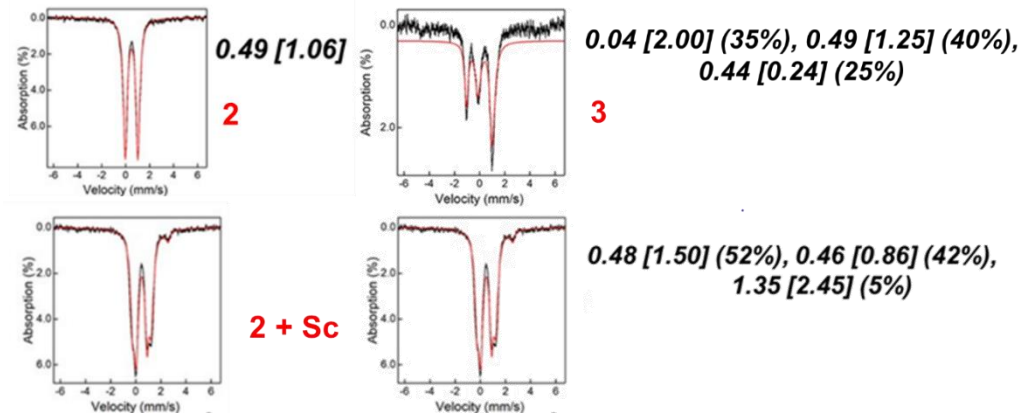

Figure 3.30. Mössbauer analysis of **[2 + Sc] (bottom)** in comparison with Mössbauer data for **2** and **3 (Top)**. Isomer shifts and quadrupole splittings (in square brackets) are listed for each components in these species along with a percentage of the total iron in respective samples.

The temperature dependence for the conversion of **2** to **3** has been investigated to obtain activation parameters. Eyring analysis in the range of 233 to 253 K gives $\Delta H^{\ddagger}$ = 55(2) kJ mol^{-1} and $\Delta S^{\ddagger}$ = -62(10) J mol^{-1} K^{-1} (Figure 3.31). These values are close to activation parameters for the O–O bond homolysis in other iron(III) peroxide complexes (Table 3.13). To date, the only other peroxodiiron(III) complex with such data for comparison is [(TMP)Fe^{III}–O–O–Fe^{III}(TMP)] (TMP = tetramesityl-porphinate dianion), which converts into two mononuclear oxoiron(IV) complexes through O–O bond cleavage.[193] The activation parameters for the latter process ($\Delta H^{\ddagger}$ = 61(4) kJ mol^{-1} and $\Delta S^{\ddagger}$ = -63(4) J mol^{-1} K^{-1}) are quite similar to those for the formation of **3**, lending credence to our proposed O–O bond homolysis mechanism. These values can be also compared with the interesting diiron chemistry reported by Kodera for 6-HPA, an octadentate dinucleating ligand that provides two tertiary amine

and six pyridine donors. This ligand supports a (μ-oxo)diiron(III) center that reacts with H_2O_2 to form a peroxodiiron(III) species and undergoes subsequent O–O bond cleavage to generate a putative (μ-oxo)bis-(oxoiron(IV)) species.[102,172,194] The observed transformation is found to have $\Delta H^{\ddagger}$ = 57 kJ/mol and $\Delta S^{\ddagger}$ = 50 J $K^{-1}mol^{-1}$, values very close to the Eyring parameters obtained for the conversion of **2** to **3**. However, Kodera et al.[172] has classified this step as a *syn*-to-*anti* isomerization of the [$O=Fe^{IV}(\mu\text{-}O)Fe^{IV}=O$] moiety. Nevertheless, a different interpretation can be proposed based on the nearly identical activation parameters determined for this step and the conversion of **2** to **3** and their strong similarity to other entries in Table 3.13 associated with O–O bond homolysis. Therefore, a plausible conjecture is that both **2** and [(6-HPA)Fe^{III}_2(*μ*-O)(*μ*-1,2-O_2)]$^{2+}$ undergo rate-determining O–O homolysis to generate diiron(IV) species.

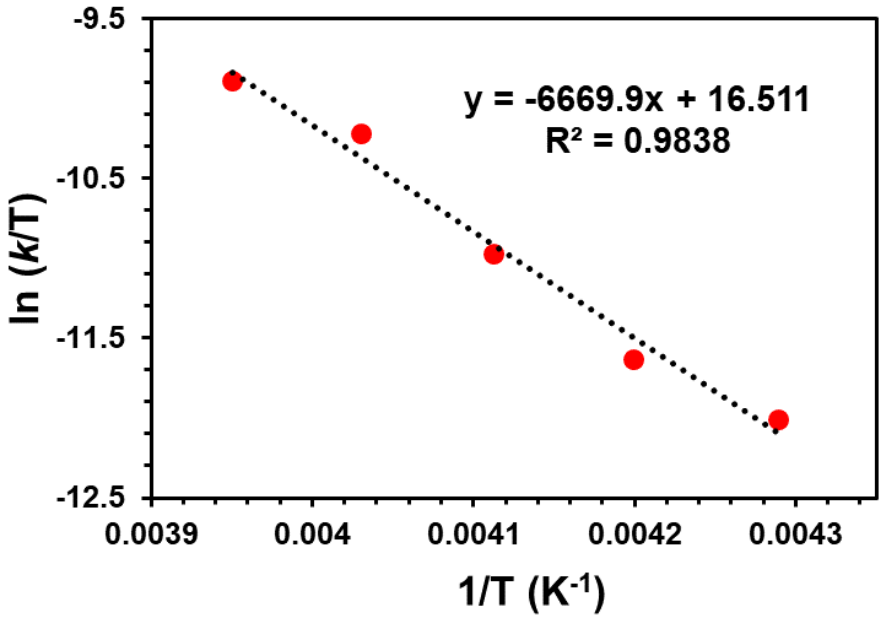

Figure 3.31. Eyring plot for the generation of **3** from **2** in CH_3CN from -40 °C to -20 °C, affording $\Delta H^{\ddagger}$ = 55(2) kJ mol^{-1} and $\Delta S^{\ddagger}$ = -62(10) J K^{-1} mol^{-1}

Table 3.13. Eyring activation parameters for the decay of Fe^{III}–OO(R or Fe^{III}) complexes or formation of high-valent complexes in MeCN unless indicated

Peroxo complex	$\Delta H^{\ddagger}$ kJ mol^{-1}	$\Delta S^{\ddagger}$ J K^{-1} mol^{-1}	Proposed O–O bond cleavage mode	Ref
2 + $Sc^{3+} \rightarrow$ **3**	55(2)	-62(10)	Homolysis	This work
(TMC)Fe^{III}–OOH in acetone/CF_3CH_2OH	56(2)	-75(2)	Homolysis	[195]
[(6-HPA)Fe^{III}_2(μ-O)(μ-1,2-O_2)]$^{2+}$	57	-50	Homo-lysis [a]	[172]
(N4Py)Fe^{III}–OOH in acetone/CF_3CH_2OH	53(1)	-121(2)	Homolysis	[195]
(TPA)Fe^{III}–OO^{t}Bu	52(1)	-74(3)	Homolysis	[196]
(TPA)Fe^{III} (κ^2-$O_2C(CH_3)_2OH$) in acetone	54(3)	-35(13)	Homolysis	[197]
(TPA*)Fe^{III}(κ^2-$O_2C(O)Ar$)	67(3)	12(10)	Homolysis	[198]
(TMP)Fe^{III}–O–O–Fe^{III}(TMP)	61(4)	-63(4)	Homolysis	[193]
sMMO-Q formation (Mc)	111	147		[154]
sMMO-Q formation (Mt)	114	185		[199]

(TMP)$Fe^{III}(O_3CAr)$ in toluene	44(4)	-44(1)	Homolysis	[200]
(TMP)$Fe^{III}(O_3CAr)$ in CH_2Cl_2	15(2)	> -104	Heterolysis	[200]
(TPA)Fe^{III}–OOH	45(2)	-95(10)	Heterolysis	[201]
(TMC)Fe^{III}–OOH + $HClO_4$ in CH_3CN	44(2)	-90(10)	Heterolysis	[190]
(TMP)$Fe^{III}(O_3CAr)$	32(2)	-161(7)	Heterolysis	[202]

[a] See text for another interpretation of the 6-HPA results, which differs from Kodera's.[172]

TMC = 1,4,8,11-tetramethyl-1,4,8,11-tetraazacyclotetradecane; 6-HPA = 1,2-bis{2-[bis(2-pyridylmethyl)-aminomethyl]pyridin-6-yl}ethane; N4Py = 1,1-di(pyridin-2-yl)-*N*,*N*-bis(pyridin-2-ylmethyl)methanamine; TPA = tris(2-pyridylmethyl); TPA* = tris(3,5-dimethyl4-methoxy-2-pyridylmethyl)amine; TMP = tetramesitylporphinato dianion; sMMO-**Q** = **Q** intermediate in soluble methane monooxygenase enzyme

A mechanism for the conversion of **2** to **3** is proposed in Figure 3.32 that accounts for the incorporation of both peroxo oxygen atoms from a unique molecule of **2** into product **3** (Figure 3.17). Intermediate **2** has been shown to have a $Fe^{III}_2(\mu\text{-O})(\mu\text{-1,2-}O_2)$ core by an array of spectroscopic techniques. The fact that the peroxo oxygen atoms in **2** are completely retained in the resultant $Fe^{IV}_2(\mu\text{-O})_2$ core of **3** requires the water-derived oxo bridge of **2** to be lost before the formation of **3**, a disposal function that presumably can be attributed to the highly Lewis acidic Sc^{3+} (or Al^{3+}) ion. Upon loss of the oxo bridge in **2**, both iron coordination spheres become coordinately unsaturated and the peroxo O-atoms remaining on the *μ*-oxo-

depleted **2** are then poised to isomerize from μ-1,2 binding to a μ-η^2:η^2 coordination mode that would set the stage for the subsequent O–O bond cleavage step to generate the bis(μ-oxo)diiron(IV) product **3**. Similar conversions have been well established in dicopper model systems since 1996.[203,204] Treatment with Sc^{3+} (or Al^{3+}) is found to promote O–O bond cleavage in **2**, which is likely to occur homolytically based on the similarity of the activation parameters for the generation of **3** to those of other O–O cleaving reactions (Table 3.13). Further insight into the mechanism is provided by DFT calculations presented in the next section.

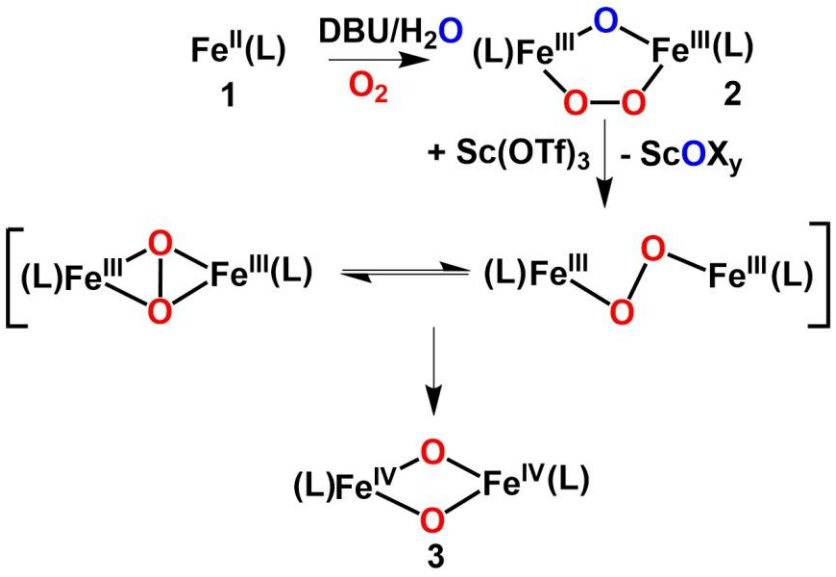

Figure 3.32. Proposed mechanism for the conversion of **2** to **3**. The water-derived O-atom shown in blue is lost during the course of the reaction, possibly by binding to Sc^{3+}.

3.2.7 Theoretical calculations to understand the structure of 2 and formation of 3 through O–O bond cleavage

Insight into how Sc^{3+} may promote the conversion of **2** to **3** has been obtained from DFT calculations at the S12g/TZ2P level of theory.[205,206] To do this, we need to show the computed structures of **2** and **3** and be certain that these are indeed responsible for the measured (vide supra) spectroscopic fingerprints. The optimized structure of **2** (Figure 3.33) shows antiferromagnetic coupling of the high-spin iron(III) atoms, leading to an Fe•••Fe distance of 3.09 Å (in excellent agreement with the EXAFS-derived value of 3.07 Å for **2** (Table 3.3) and an Fe–O–Fe angle of 118°. In this structure, the Me_3NTB ligands adopt a configuration designated as DU, in which one ligand points downwards with the peroxo moiety below the oxo bridge and the other points upwards. Studies of other configurations, namely down-down (DD) and up-up (UU), as well as ferromagnetically (FM) vs. antiferromagnetically (AFM) coupled iron centers for all three ligand configurations, find the AFM-DU isomer to be the most stable (with DD only slightly less stable by ca. 1 $kcal \cdot mol^{-1}$, and UU and ferromagnetically coupled isomers less stable by 10-15 $kcal \cdot mol^{-1}$). The computed Mössbauer parameters for **2-DU** (δ = 0.45-0.47 mm/s, ΔE_Q = 0.80-0.95 mm/s) are in good agreement with the experimental values (δ = 0.49 mm/s, ΔE_Q = 1.06 mm/s) found for **2**.

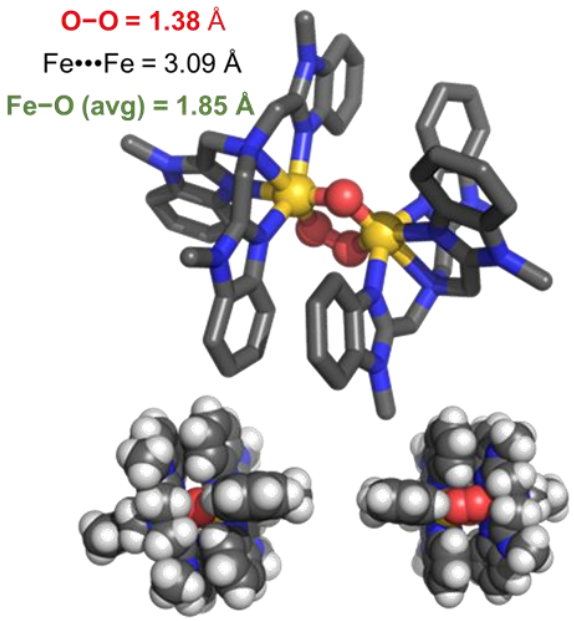

Figure 3.33. (Top) S12g/TZ2P optimized structure for **2. (Bottom)** Spacefill diagrams of **2**, showing the access to the oxo and the peroxo side of the molecule.

For diiron(IV) species **3-DU** isomer, DFT calculations predict Fe–N distances of 1.96-1.97 Å for the benzimidazole donors and 2.13 Å for the amines, an Fe•••Fe distance of 2.70 Å and Fe–O–Fe angles of 98°, in very good agreement with the EXAFS analysis. The **3-DD** form is less stable than **3-DU** by 16.1 kcal/mol, which is consistent with the structures of related crystallographically characterized Fe_2O_2 diamond-core complexes reported so far.[182,184,207,208] As it is difficult to visualize how **2-DD** could easily transform into **3-DU**, we have assumed that both **2** and **3** are in fact in the **DU** form. The computed Mössbauer parameters for **3** (δ = -0.046 $mm \cdot s^{-1}$, ΔE_Q = 2.12 $mm \cdot s^{-1}$) are consistent with experiments.

Adding $Sc(OTf)_3$ to **2** leads to its coordination to the peroxo moiety, which is favored by ca. 44 $kcal \cdot mol^{-1}$ over the binding to the oxo bridge (see

Figure 3.34). Based on the greater accessibility of the peroxo oxygens than that for the oxo bridge, which is shielded by the Me_3NTB ligands (see Figure 3.33 bottom), one might think that the peroxo preference results from steric interactions. Although the Me_3NTB ligands do shield the oxo side quite well, the peroxo binding preference persists even for the simpler model with ammonia ligands (see Figure 3.34), where no such steric interactions are present, favoring the binding of $Sc(OTf)_3$ to the peroxo unit over the oxo bridge by 12 kcal·mol^{-1} in the $[Fe^{III}_2(O_2)(O)(NH_3)_8{\cdot}Sc(OTf)_3]^{2+}$ model. Interestingly, the separation of the interaction between $Sc(OTf)_3$ and the diiron species into deformation energy (or strain) and interaction energy (following the Distortion/Interaction-Activation Strain Model[39]) shows that the intrinsic preference for the peroxo side derives only from deformation. In the process of binding $Sc(OTf)_3$ by **2m**, the diiron species needs to adjust itself only slightly on the peroxo side (deformation of 6.9 kcal·mol^{-1}) versus the oxo side (18.5 kcal·mol^{-1}), which is 2.5 times larger. For both sides, the interaction energy of the $Sc(OTf)_3$ with the **m2** diiron species is the same (-58.1 kcal·mol^{-1}, see Figure 3.35). In the real systems, these energies are larger: for **2** to bind $Sc(OTf)_3$ the deformation energy (8.7 kcal·mol^{-1}, see Figure 3.34) is somewhat larger than that of the model system, but this increase by 1.8 kcal·mol^{-1} is compensated largely by an increase of the interaction energy of 1.3 kcal·mol^{-1}, leading overall to almost similar total binding energies of the $Sc(OTf)_3$ (ca. -51 kcal·mol^{-1}).

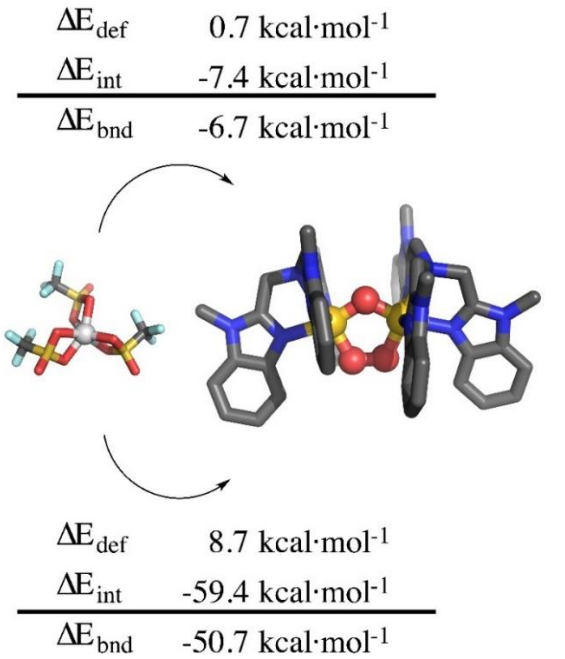

Figure 3.34. DFT structures of **2** indicating the preference of Sc^{3+} for binding to the peroxo ligand over the oxo ligand.

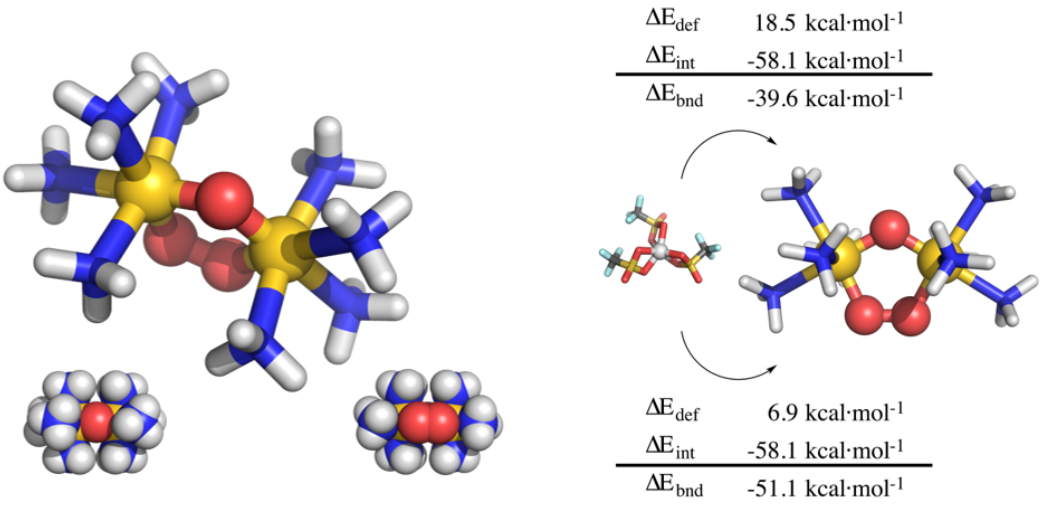

Figure 3.35. DFT structures of **m2**, showing the preference of Sc^{3+} for binding to the peroxo ligand over the oxo ligand

3.2.8 Reactivity of 3 towards C–H bond cleavage

The identification of a second example of a tetradentate tripodal N4 ligand able to support bis(*μ*-oxo)diiron(IV) core opens the door for comparing the C–H bond oxidative power of **3** relative to that of $[Fe^{IV}_2(\mu\text{-}O)_2(TPA^*)_2]^{4+}$ as well as their mononuclear $[Fe^{IV}(O)(N4)]^{2+}$ counterparts. This question has been explored with 1,4-cyclohexadiene (CHD; BDE = 78 kcal mol^{-1}) as a substrate. At 233 K, the addition of CHD to a solution of **3** in CH_3CN results in the first-order decay of its 600-nm chromophore and a second-order rate constant (k_2) of 7 * 10^{-4} $M^{-1}s^{-1}$ (Figure 3.36). This value is comparable to the k_2 value of 10^{-4} M^{-1} s^{-1} reported for the oxidation of 9,10-dihydroanthracene by $[Fe^{IV}_2(\mu\text{-}O)_2(TPA^*)_2]^{4+}$ at 193 K,[56] after extrapolation to 233 K by assuming that rates double with every 10 K increase in temperature to give a value of 1.6 x 10^{-3}, making the k_2 for **3** at 233 K only a factor of 2 smaller than that for $[Fe^{IV}_2(\mu\text{-}O)_2(TPA^*)_2]^{4+}$.

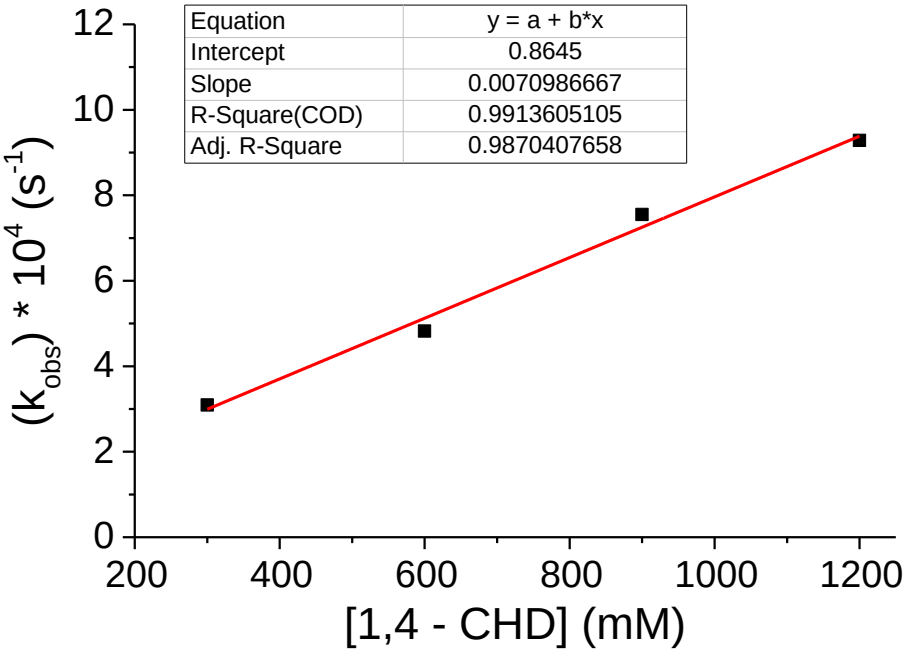

Figure 3.36. Second-order rate constant determination for the reaction of **3** with 1,4-cyclohexadiene in CH_3CN at -40°C.

In contrast, the corresponding mononuclear complex $[Fe^{IV}(O)(Me_3NTB)]^{2+}$ is one of the most reactive nonheme $Fe^{IV}(O)$ complexes described to date, with $k_2 = 9.4 * 10^2\ M^{-1}s^{-1}$ for 1,4-CHD oxidation in CH_3CN at 233 K,[57] nearly 10^7-fold more reactive towards 1,4-CHD than **3**. This result suggests that a terminal oxo is more reactive towards C–H bonds than a bridging oxo if other variables such as oxidation states and spin states of the iron center are kept constant.[56] For comparison, the mononuclear $[Fe^{IV}(O)(TPA^*)]^{2+}$ is 1000-fold more reactive than the corresponding dinuclear $[Fe^{IV}_2(\mu\text{-}O)_2(TPA^*)_2]^{4+}$ complex.[56] These complexes represent the only two pairs of iron(IV)-oxo complexes supported by the same ligand framework but differ in having a terminal or bridging oxo units. The 10^4-fold greater reactivity difference found for the Me_3NTB pair of complexes is quite amazing, and a phenomenon that deserves further scrutiny.

Lastly, it needs to be emphasized here that **3** and $[Fe^{IV}_2(\mu\text{-}O)_2(TPA^*)_2]^{4+}$ are far less reactive than sMMO intermediate **Q**, where the latter can oxidize the strong and unactivated C–H bonds of methane efficiently at 4 °C. This disparity may stem from differences in the spin states of the iron(IV) centers, $S = 1$ for both **3** and $[Fe^{IV}_2(\mu\text{-}O)_2(TPA^*)_2]^{4+}$, and $S = 2$ for the much more reactive **Q.**[46,54,56] There are also differences in the diiron(IV) core structures deduced from resonance Raman and X-ray absorption spectroscopy that have yet to be resolved.[77,80] Further scrutiny of these structure-reactivity correlations is desirable.

3.3 Discussion

The use of benzimidazoles is rare in modeling diiron chemistry and the use of the same in the Me_3NTB ligand framework made the generation of the diiron(II) precursor from a monoiron(II) complex different from the previously reported models, where the most commonly used base is

triethylamine (pKa = 18.82 in CH_3CN[168]). The use of a much stronger base, DBU (pKa = 24.34 in CH_3CN[168]) is an important discovery and it is only with a strong base that this extensive diiron chemistry is possible. The use of triethylamine did not generate the chromophore of the diiron(II) complex (λ_{max} = 395 nm). This follows from the use of more basic donors in benzimidazoles[168] when compared with pyridines and quinolines, where the use of triethylamine was successful in carrying out dioxygen activation through the generation of diiron(II) complex in solution.[101,167] The increased basicity decreases the Lewis acidity of the iron center in (Me_3NTB)Fe(II) complex and hence increases the pKa of the water molecule attached to it in solution. This makes it more difficult for the deprotonation step that needs to happen to lead to *μ*-hydroxido bridge formation that will ultimately lead to the (bis-*μ*-hydroxido)diiron(II) complex. (Figure 3.37)

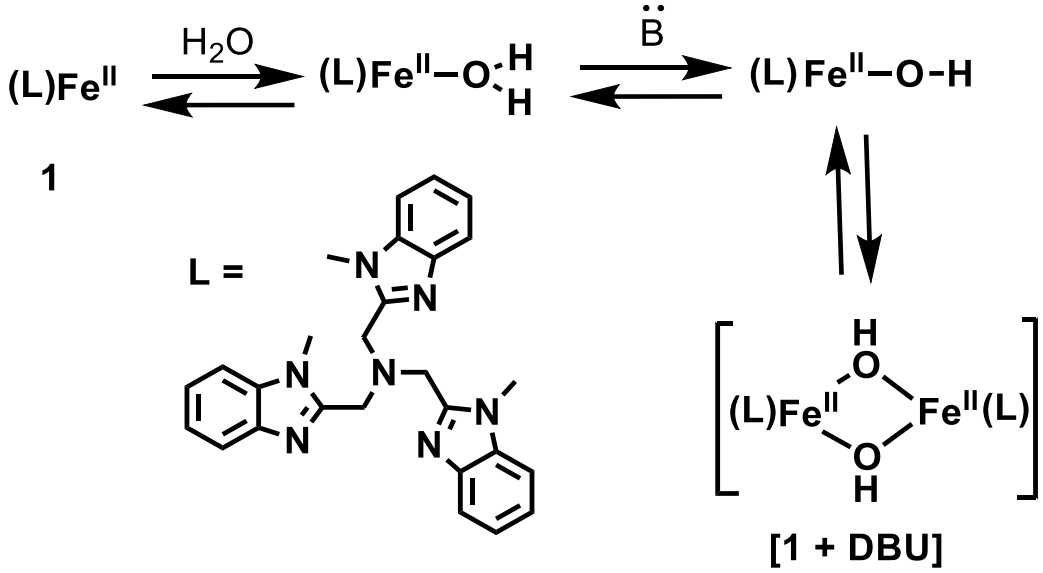

Figure 3.37. Scheme of the proposed reaction that gives rise to the in-situ diiron(II) precursor before oxygen exposure.

The structure of the peroxodiiron(III) complex **2** from **[1 + DBU]** allows us to make use of excellent correlations developed by Sanders Loehr[176] and Fiedler[73] for diiron complexes. EXAFS characterization of **2** produced a shorter diiron distance and lower O–O stretching frequency than most of the related models. This underlies the uniqueness of the Me_3NTB system that already has a weaker O–O bond and two iron centers closer than systems reported before. The weaker O–O bond increases the likelihood that **2** will form a high-valent complex whereas the shorter diiron distance reduces the reorganization energy needed to form a “diamond” core structure observed in **3**. The actual structure of the diiron(IV) core for **Q** is currently not settled, where resonance Raman data support a closed-core structure[77] but recent XAS data[80] favor an open-core structure.

Nevertheless, our study is unique in that it involves the conversion of a peroxodiiron(III) complex to a diiron(IV) complex analogous to the diiron center in the **sMMO** enzyme. Also, it was shown that the two oxygen atoms of O_2 are retained in the closed-core structure of **3**, reminiscent of similar observations through mixed-labeling experiments in **sMMO-Q**.[77] This further highlights the mechanistic similarity of the conversion of **2** to **3** and **sMMO-P** to **sMMO-Q**. The strategy to utilize Lewis acids to carry out O–O bond cleavage is unprecedented in systems that have two basic sites (oxo and peroxo) like **2**. And when compared with Bronsted acids, Lewis acids produce a different result. The study presented here will drive the search for other peroxodiiron(III) systems that can be treated with strong Lewis acids to form similar high-valent complexes. This will enhance the understanding of the structure and reactivity of such models that are still rare in the current literature. Our investigation thus underscores the complexities of the chemistry involved in activating the peroxo O–O bond to generate high-valent oxidants in nonheme iron catalysts and highlights

Nature's ability to deliver a key proton to a particular site to elicit the desired transformation.

3.4 Conclusion

In summary, **3** represents the first diiron(IV) complex to be generated by acid-assisted cleavage of the O−O bond of a peroxodiiron(III) complex like sMMO, which is derived from the reaction of O_2 with a diiron(II) precursor. Indeed, there are few examples in which an observed peroxodiiron(III) complex is converted into a higher-valent diiron derivative upon treatment with acid. For two $[Fe^{III}_2(O)(O_2)(L)_2]^{2+}$ complexes with L = 6-Me$_3$TPA (= tris(6-methyl-2-pyridylmethyl)amine) and BnBQA (= N-benzyl-N,N-bis(2-quinolinylmethyl)amine), it has been observed that the addition of acid results in the formation of a high-valent diiron(III,IV) complex (black pathway in Figure 3.38).[100][101] In another example (along the pink path in Figure 3.38), the reaction of stoichiometric H_2O_2 with $[Fe^{III}_2(\mu\text{-}O)(TPA^*)_2(OH)(OH_2)]^{3+}$ (TPA* = tris(4-methoxy-3,5-dimethyl-2-pyridylmethyl)amine) directly form a diiron(IV) intermediate with an open $O{=}Fe^{IV}{-}O{-}Fe^{IV}{-}OH$ core via a presumed but unobserved diferric-peroxo intermediate in ~70% yield.[209] Upon treatment with 1 eq. $HClO_4$, the nascent diiron(IV) complex converts into a complex with an $Fe^{IV}_2(\mu\text{-}O)_2$ diamond core. A fourth example (along the blue path in Figure 3.38) describes the reaction of $[Fe^{III}_2(\mu\text{-}O)(6\text{-HPA})(OH_2)_2]^{4+}$ (6-HPA = 1,2-bis{2-[bis(2-pyridylmethyl)-aminomethyl]pyridin-6-yl}-ethane) with H_2O_2 and 2 eq. Et_3N to generate a (μ-oxo)(μ-1,2-peroxo)-diiron(III) derivative that is in equilibrium with a diiron(IV) intermediate with an $O{=}Fe^{IV}{-}O{-}Fe^{IV}{=}O$ core.[172] The present study, however, shows that moving to Lewis acids is a viable way to convert a peroxodiiron(III) complex into a diiron(IV) complex. To the best of our knowledge, this is the first time a Lewis acid-mediated strategy has been used to break the O-O bond in a diiron system.

Importantly, this study shows, with support from theoretical models, that Sc^{3+} prefers binding the peroxide bridge over a more basic oxo bridge, which assists in the induction of O-O bond cleavage to generate **3**. Interestingly, in the presence of excess water, Sc^{3+} changes its role and acts as a proton donor, which generates an analogous species as a Bronsted acid such as perchloric acid. This is an important result and is an intriguing contrast to the recently reported acid effects observed with the reaction of H_2O_2 and $[Fe(\beta\text{-BPMCN})(CH_3CN)_2]^{2+}$, where the $HClO_4$ and Sc^{3+} showed similar effects.[210] On a similar note, Browne and co-workers have also provided strong evidence that the $Sc(OTf)_3$-enhanced olefin epoxidation by the combination of $[Mn^{IV}_2(\mu\text{-}O)_3(tmtacn)_2]^{2+}$ (where tmtacn = 1,4,7-trimethyl-1,4,7-triazacyclononane) and H_2O_2 results from Bronsted acid formation upon hydrolysis of $Sc(OTf)_3$ by water present in the reaction mixture.[211] The uniqueness of **2**, when compared to these results, is the fact that acids (Bronsted or Lewis) have a choice of attack, and depending on that choice, the outcomes have been shown to be very different.

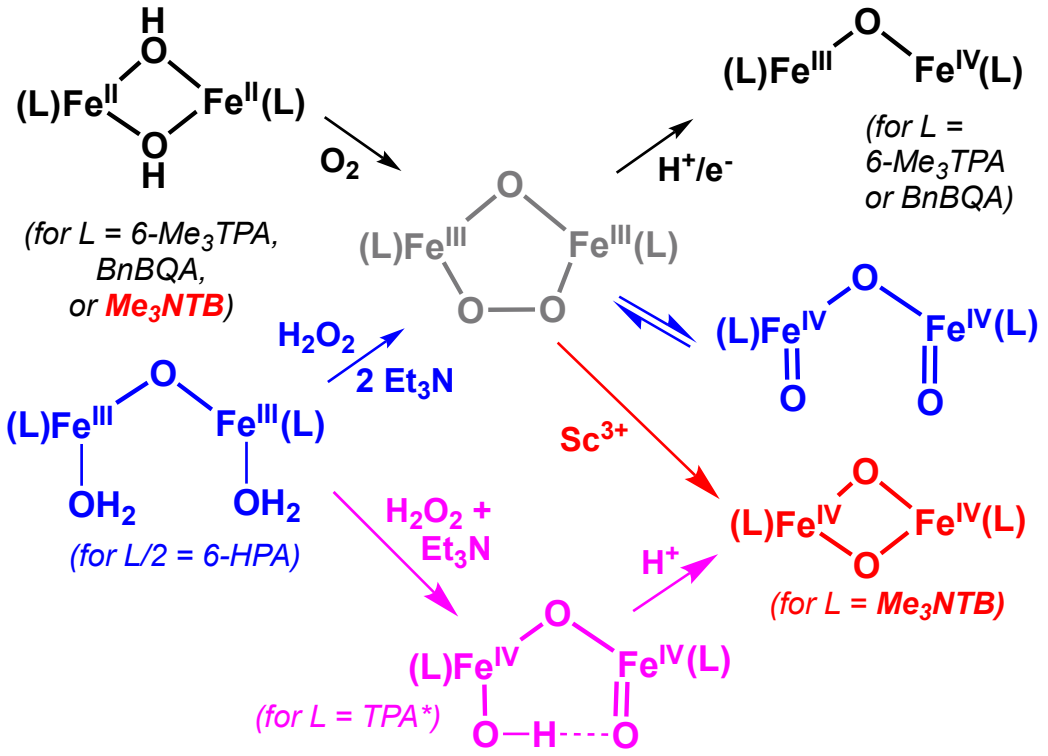

Figure 3.38. Formation of high-valent diiron species from the reaction of a diiron(II) precursor with O_2 or a diiron(III) precursor with H_2O_2. For L = 6-Me$_3$TPA and BnBQA (black), an Fe^{III}–O–Fe^{IV} species is formed upon protonation of the peroxo intermediate.[30,32] For the dinucleating 6-HPA (blue), an O=Fe^{IV}–O–Fe^{IV}=O species is formed in equilibrium with the peroxo intermediate.[172] For L = TPA* (pink), an HO–Fe^{IV}–O–Fe^{IV}=O species is proposed to form from an unobserved (μ-oxo)(μ-1,2-hydroperoxo)diiron(III) species and then convert into an $Fe^{IV}_2(\mu\text{-O})_2$ core upon protonation.[209] For L = Me$_3$NTB (red), a (μ-oxo)(μ-1,2-peroxo)diiron(III) intermediate **2** is formed upon exposure of its diiron(II) precursor to O_2 and is converted to **3**, a complex with an $Fe^{IV}_2(\mu\text{-O})_2$ diamond core upon addition of Sc^{3+}.

3.5 Experimental Section

3.5.1 Materials

Commercially available chemicals such as DBU (1,8-Diazabicyclo[5.4.0]undec-7-ene), Scandium triflate, Aluminium triflate, Yttrium triflate, perchloric acid, and solvents were used without further purification unless noted. $[Fe^{II}(Me_3NTB)(CH_3CN)](CF_3SO_3)_2$ (**1**) was synthesized as previously reported.[57]

3.5.2. Sample preparation procedures

A 4-mM solution of **1** in CH_3CN or CD_3CN was prepared in a 1-cm cuvette in a nitrogen containing glovebox and then treated with 1.5 equiv DBU/H_2O to generate the putative diron(II) species [**1+DBU**] at -40 °C in a UV-vis cuvette. At this stage, a balloon containing moisture-free oxygen gas was used to purge the headspace of the cuvette to produce a deep-green solution of $[Fe_2^{III}(\mu\text{-}O)(\mu\text{-}O_2)(Me_3NTB)]^{2+}$ (**2**). This process was monitored by UV-vis absorption spectroscopy. When the yield of **2** was maximized, pre-cooled pipettes were used to transfer the solution into NMR tubes and then frozen at 77 K for resonance Raman studies. XAS samples of **2** were prepared similarly, except the solutions of **2** were frozen in XAS cups. Mössbauer samples of **2** were prepared starting with a 2-mM solution of ^{57}Fe-enriched **1** in CH_3CN and treated with 1.5 equiv DBU/H_2O followed by O_2 before being transferred into Mössbauer cups and frozen at 77 K. Corresponding samples of **3** were obtained by treating solutions of **2** with 2 equivalents of $Sc(OTf)_3$ and transferring them into appropriate sample cups after an hour reaction time.

3.5.3. Physical methods

UV-vis absorption spectra were recorded with an HP 8453A diode array spectrophotometer equipped with a cryostat from UNISOKU Scientific

Instruments, Japan. All UV-vis absorption experiments were carried out in 1-cm path length cuvettes. Resonance Raman spectra were obtained at room temperature with excitation at 561 nm (50 mW at source, Cobolt Lasers) or 661 nm (60 mW at source, Ar+ laser, SpectraPhysics) through the sample in a flat bottom NMR tube using a 90° backscattering arrangement (parallel to the slit direction). Resonance Raman spectra on frozen samples (at 77 K) were obtained using a 135° back scattering arrangement. The collimated Raman scattering was collected using two Plano convex lenses (f = 12 cm, placed at an appropriate distance) through appropriate long pass edge filters (Semrock) into an Acton AM-506M3 monochromator equipped with a Princeton Instruments ACTON PyLON LN/CCD-1340x400 detector. The detector was cooled to -120 °C before the experiments. Spectral calibration was performed using the Raman spectrum of acetonitrile/toluene 50:50 (v:v).[212] Each spectrum was accumulated, typically 60 times with 5 s acquisition time, resulting in a total acquisition time of 5 min per spectrum. The collected data was processed using Spekwin32,[213] and a multi-point baseline correction was performed for all spectra. Iron K-edge X-ray absorption spectra for **2** and **3** were collected on SSRL beamline 9−3 using a 100-element solid-state Ge detector (Canberra) with a SPEAR storage ring current of ∼500 mA at a power of 3.0 GeV. The incoming X-rays were unfocused using a Si(220) double crystal monochromator, which was detuned to 70% of the maximal flux to attenuate harmonic X-rays. Between 6 and 8 scans of the fluorescence excitation spectra for each sample were collected from 6882 to 8000 eV at a temperature (10 K) that was controlled by an Oxford Instruments CF1208 continuous-flow liquid helium cryostat. An iron foil was placed in the beam pathway before the ionization chamber I_0 and scanned concomitantly for energy calibration, with the first inflection point of the edge assigned to 7112.0 eV. A 3 μm, 6 μm, or 9 μm Mn filter and a Soller

slit were used to increase the signal-to-noise ratio of the spectra. Photoreduction was monitored by scanning the same spot on the sample twice and comparing the first derivative peaks associated with the edge energy during collection, but none was observed in the present study. The detector channels from the scans were examined, calibrated, averaged, and processed for EXAFS analysis using EXAFSPAK[140] to extract χ(k). Theoretical phase and amplitude parameters for a given absorber−scatterer pair were calculated using FEFF 8.40[141] and were utilized by the “opt” program of the EXAFSPAK package during curve fitting. In all analyses, the coordination number of a given shell was a fixed parameter and was varied iteratively in integer steps, while the bond lengths (R) and mean-square deviation (σ^2) were allowed to freely float. The amplitude reduction factor S_0 was fixed at 0.9, while the edge-shift parameter E_0 was allowed to float as a single value for all shells. Thus, in any given fit, the number of floating parameters was typically equal to (2 × num shells) + 1. The k range of the data is 2−15 $Å^{-1}$. The pre-edge analysis was performed on data normalized in the “process” program of the EXAFSPAK package, and pre-edge features were fit between 7108 and 7118 eV for all samples using the Fityk[142] program with pseudo-Voigt functions composed of 50:50 Gaussian/Lorentzian functions. Mössbauer spectra were recorded with two spectrometers using Janis Research (Wilmington, MA) SuperVaritemp dewars that allow studies in applied magnetic fields up to 7.5 T in the temperature range from 1.5 to 200 K. Mössbauer spectral simulations were performed using the WMOSS software package (SEE Co, Edina, MN).[143]

3.6 Acknowledgments

I am thankful for grants from the U. S. National Institutes of Health (R01 GM-38767 and R35 GM-131721 to L.Q.), the U. S. National Science

Foundation (CHE1654060 to Y.G.), and MICINN (CTQ2017-87392-P to M.S.) for support of this work. XAS data were collected at the Stanford Synchrotron Radiation Lightsource Beamline 9-3. Use of the Stanford Synchrotron Radiation Lightsource, SLAC National Accelerator Laboratory, is supported by the U.S. Department of Energy, Office of Science, Office of Basic Energy Sciences under Contract No. DE-AC02-76SF00515. The SSRL Structural Molecular Biology Program is supported by the DOE Office of Biological and Environmental Research, and by the National Institutes of Health, National Institute of General Medical Sciences (P41GM103393). The contents of this publication are solely my responsibility and do not necessarily represent the official views of NIGMS or NIH. I am grateful to have worked with immensely helpful collaborators – Dr. Apparao Draksharapu for being an excellent mentor and help with Raman results, Patrick Crossland for XAS related studies and assisting me with the manuscript preparation of this work, Dr. Ruixi Fan and Prof. Yisong Guo for Mössbauer spectroscopy collaboration and Prof. Marcel Swart for theoretical insights into experimental observations – in this work. I acknowledge several insightful discussions with Dr. Andrew Jasniewski that helped in developing the study presented here.

Chapter 4:

Characterization of Quinoline-containing Diiron Complexes Involved in Dioxygen Activation

4.1 Introduction

As mentioned in the previous chapter, diiron enzymes such as soluble methane monooxygenase (sMMO), ribonucleotide reductase (RNR), fatty acid desaturases, human deoxyhypusine hydroxylase (hDOHH) and others.[67,68,89,152] are involved in various important transformations such as the conversion of methane to methanol, the conversion of ribonucleotides to deoxyribonucleotides, the desaturation of fatty acids and the selective hydroxylation of the eukaryotic initiation factor 5a. High-valent intermediates in sMMO and RNR enzymes play key roles in enzyme action, such as the diiron(III,IV) species "**X**" in RNR class 1A[86–88] or the diiron(IV) species "**Q**" in sMMO.[75,77,161] A key feature of these high-valent intermediates is that they possess high-spin or S = 2 iron(IV) centers, and studies have shown that high-spin oxoiron(IV) complexes are more reactive than intermediate-spin (S = 1) ones.[45,46,54–56]

Various synthetic models have been produced to mimic dioxygen activation steps in nonheme diiron enzymes[67,152,162] and they have been discussed in chapter 3 in addition to a study of a (μ-1,2-peroxo)diiron(III) species and its conversion to a diiron(IV) complex supported by Me_3NTB ligand framework. Despite the unprecedented formation of a bis-(μ-oxo)diiron(IV) complex from a diferric peroxo, the sluggish reactivity of the iron(IV) complex raised questions about whether having an S = 1 spin-state is a challenge or not. To explore this aspect more, we need ligand frameworks that can support S = 2 iron centers in bis-(μ-oxo)diiron(IV) complexes. Unfortunately, there is no report in the current literature of such a complex. However, Kodera et al. developed a 6-HPA system that supports a (μ-oxo)bis(oxoiron(IV)) complex, which contains S = 2 iron(IV) centers and exhibits significant oxidative reactivity. Additional studies have shown that diiron complexes that contain S = 2 are more reactive compared to ones

that have *S* = 1 centers.[56] This calls for a strategy to utilize ligands that may give rise to *S* = 2 iron(IV) centers in high-valent diiron complexes. Using quinolines to exert steric interactions to weaken the ligand field around the metal center has proved to be effective in transforming *S* = 1 iron(IV) centers into *S* = 2 iron(IV) centers.[54] Similar strategies have been attempted here to develop systems that can activate dioxygen and give rise to model intermediates that have *S* = 2 iron centers. Quinoline containing ligands explored here is TQA that provides us with a strategy to access high-spin iron centers as evidenced by its recent success in modeling myonuclear enzymes[54].

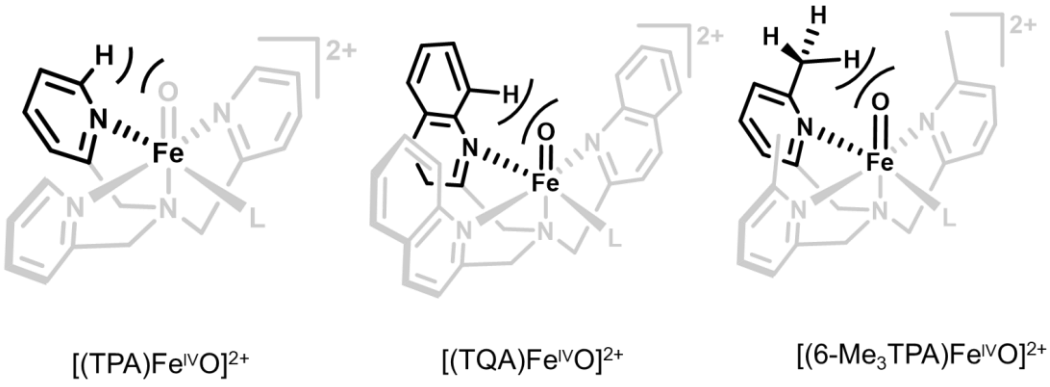

Figure 4.1. Synthetic strategy where increasing the steric congestion at α-carbon of the pyridines weakens the ligand field and changes the spin-state of the iron(IV) center from *S* = 1 (TPA) to *S* = 2 (TQA and 6-Me$_3$TPA)[46]

4.2 Results

4.2.1 Generation of a diiron(II) species 1 and related characterization

A yellow colored 1-mM solution of [(TQA)Fe^{II}(OTf)$_2$] prepared in CH_3CN under N_2 at -40 °C turns dark purple upon the addition of 1 equiv. NEt_3/H_2O, corresponding to the appearance of an absorption band around 505 nm (Ɛ = 2000 M^{-1} s^{-1}) to form **1** (Figure 4.2). Similar spectral changes have been

observed when related $Fe^{II}(N4)$ complexes are treated with Et_3N to form dihydroxo-bridged diiron(II) complexes.[101,167] In this case, the stronger base DBU, which was needed to form a similar species with Me_3NTB is not necessary for the corresponding TQA complex, due to the lower basicity of quinolines in comparison to benzimidazoles[180]. Isolation of **1** has been successful, which was not the case with the Me_3NTB ligand framework. This is another contrast between these two related systems. Upon treatment with NEt_3/H_2O, a 10-mM solution of $[(TQA)Fe^{II}(OTf)_2]$ in CH_3CN converts into a dark purple solution, which is left in an Et_2O bath at 233 K to give rise to purple solids in a couple of days. Based on its elemental analysis (see experimental section) **1** is formulated as $[(TQA)_2Fe^{II}_2(OH)_2](OTf)_2$ with additional solvent molecules.

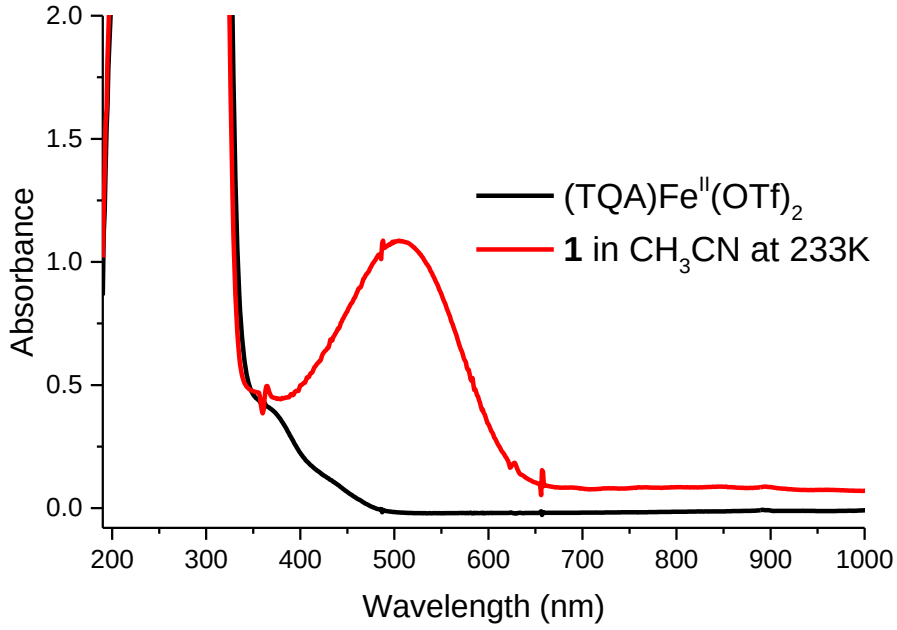

Figure 4.2. UV-vis absorption spectrum of **1** formed after the addition of 1 equiv. NEt_3/H_2O to a 1 mM solution of $(TQA)Fe^{II}(OTf)_2$ in CH_3CN at -40 ^oC.

The UV-vis spectrum of **1** shows the absorption band centered around 505 nm. By analogy to previously studied related complexes,[167] this feature has been empirically assigned to metal-to-ligand charge transfer (MLCT) transitions. These transitions connect high-lying occupied orbitals of the iron(II) center to low-lying empty π-acceptor orbitals of the quinolines in TQA. In comparing absorption features of related complexes (Table 4.1), we find that quinoline-based systems like **1**, BQPA and BnBQA have MLCT features around 500 nm, whereas systems containing more basic pyridines such as TPA and 6Me$_3$TPA have the same feature blue-shifted to 465 nm or lower. Interestingly, the BQPA ligand, which has both pyridines and quinolines has two MLCT features corresponding to transitions connecting these heterocycles with the iron(II) center. An interesting comparison here is with the diiron(II) complex supported by the Me$_3$NTB ligand framework, where the MLCT band is at 390 nm. This is expected when we consider the order of the basicity of nitrogen-containing heterocycles discussed here (benzimidazoles 6-Me-pyridines> pyridines > quinolines).[180] An important caveat is that there will also be ligand-to-metal charge transfer (LMCT) transitions involving the high-lying occupied orbitals of bridging hydroxide ligands to low-lying empty d-orbitals of the iron(II) center in **1**. Related molecular orbital investigations have been carried out for more prevalent diiron(III) complexes by the Solomon group.[214] Intense MLCT transitions of **1** in the visible region may obscure the appearance of the LMCT transitions in its UV-vis spectrum.

Table 4.1. Comparison of the absorption features of different diiron(II) complexes.

Diiron(II) complex with ligands **L**	λ_{max} (nm), Ɛ (M^{-1} cm^{-1})	References
L = TQA (**1**)	505 (2000)	This work
L = $6Me_3TPA$	420 (2400)	[167,215]
L = BnBQA	518 (2400)	[101,167]
L = BQPA	445 (2900), 550 (2100)	[167]
L = TPA	465 (2800)	[167]
L = Me_3NTB**	390 (800)	[216]

** Only non-isolated diiron(II) complex in this table without any elemental analysis or related compositional analysis. Hence, the molar extinction coefficient is less reliable.

We have not been successful in obtaining diffraction quality crystals of **1**. However, based on the similarities between the UV-vis spectrum of **1** and previously reported diiron(II) complexes[167], whose crystal structures are known, we can assume that **1** has a bis-(μ-OH)diiron(II) core. ESI-MS measurements support this notion and show the presence of a bis-(μ-OH)diiron(II) core with triflate as a counter-anion. (See figure 4.3 below) However, major peaks correspond to $[(TQA)Fe^{II}]^+$ and $[(TQA)Fe^{II}(OH)]^+$, which is most likely the result of the dication $[(TQA)_2Fe^{II}_2(OH)_2]^{2+}$ falling apart under the ionization conditions in the ESI-MS chamber. We also observe partially decomposed $[Fe^{II}_2(O)(TQA)_2(OTf)]^+$ cations. These MS assignments are also supported by ^{18}O labeling studies. Finally, the

elemental analysis also supports the formulation of **1**, which is reported in the experimental section.

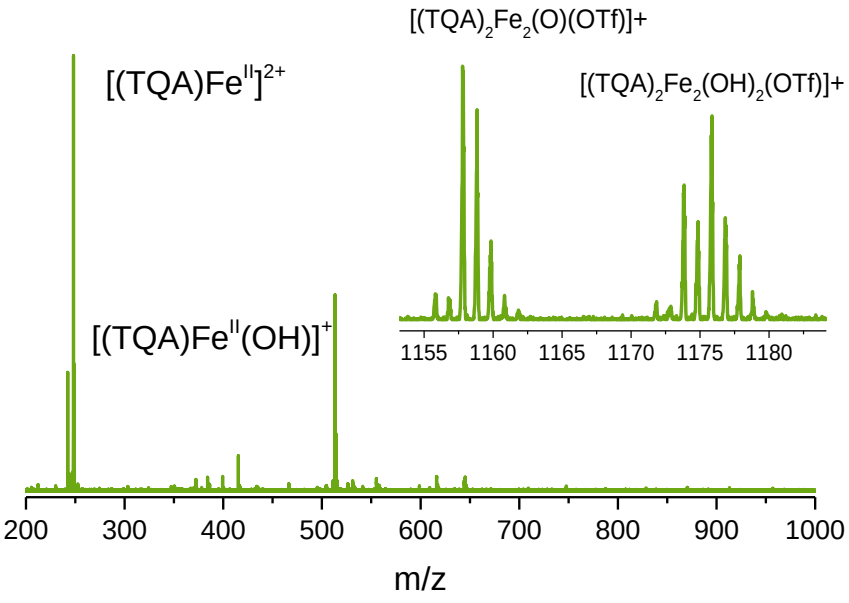

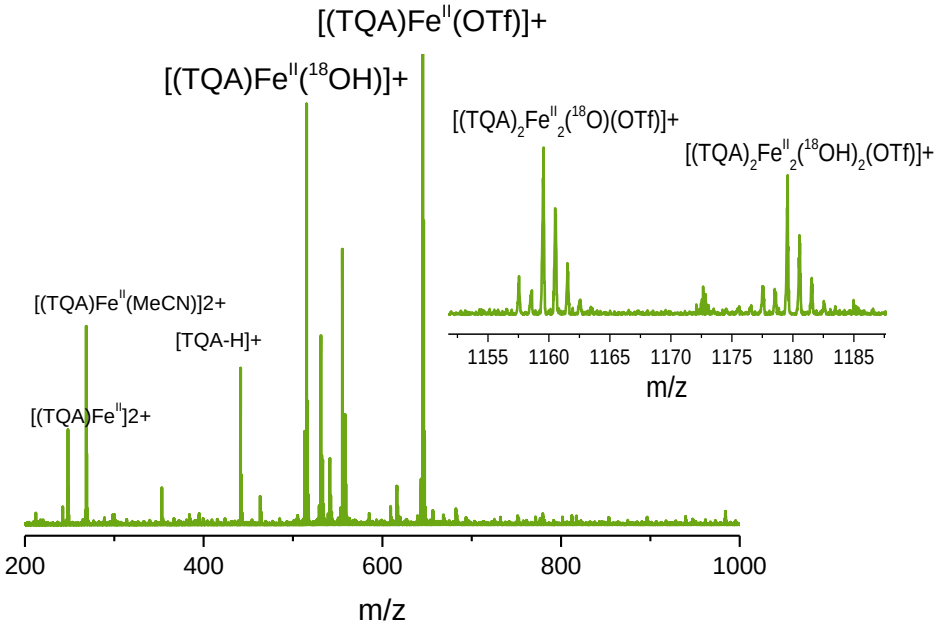

Figure 4.3. ESI-MS of **1** in MeCN at room temperature, showing the presence of the diiron(II) complex, and the dissociated monoiron(II) species that may have been generated under the ionization conditions of the instrument. (**Top**) Signals have oxygen atoms ^{16}O labeled and (**bottom**) ^{18}O labeled.

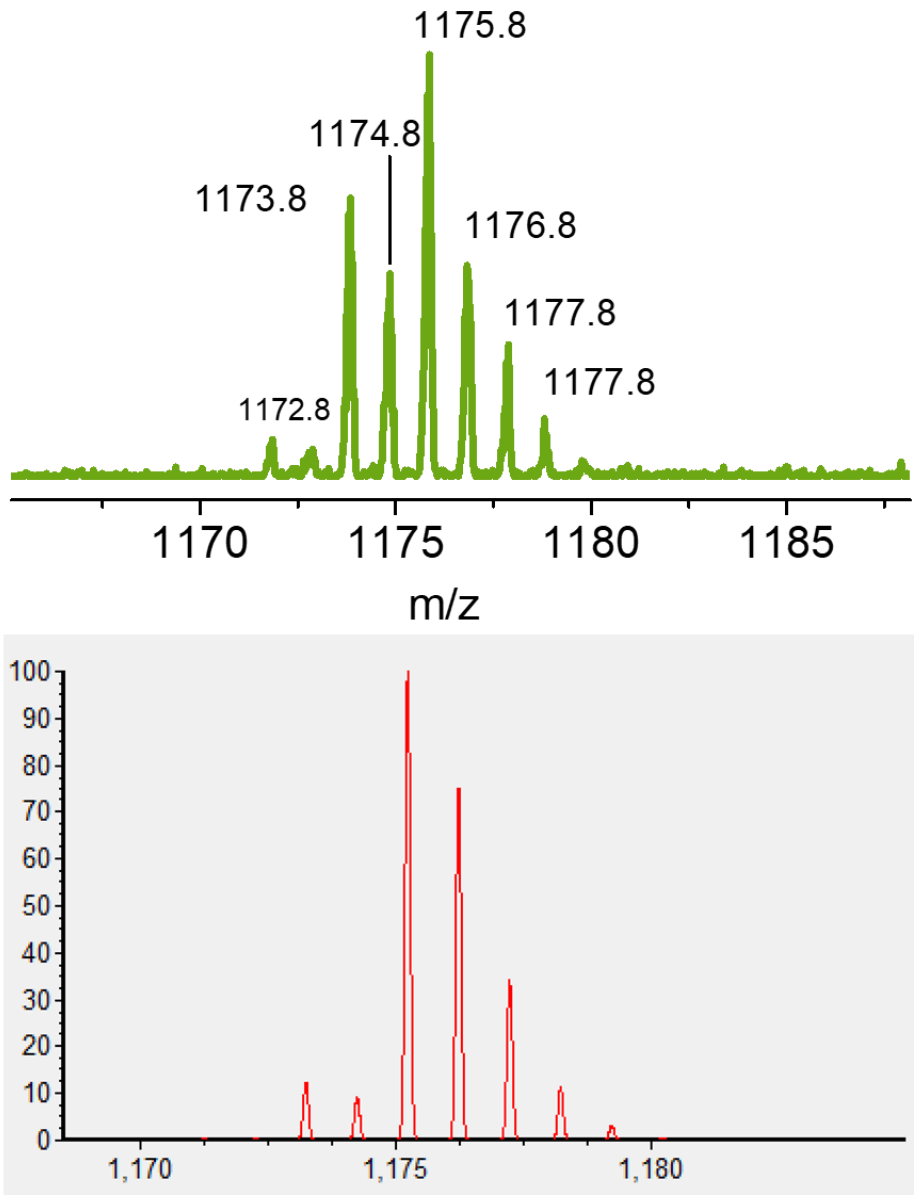

Figure 4.4. Magnified ESI-MS of **1** in MeCN at room temperature (top) and an IsoPro simulation of the mass-spectrum of $[Fe^{II}_2(OH)_2(TQA)_2(OTf)]^+$ cation (bottom). The peaks at m/z = 1173.8 and 1174.8 are bigger owing to the oxidation of **1** under the ESI-MS conditions to generate diiron(III) complex $[Fe^{III}_2(O)_2(TQA)_2(OTf)]^+$. This is further supported by the observation of the same signal in the fully oxidized solution of **1** (see a later section for details).

Resonance Raman characterization of **1** was carried out using a 515-nm excitation source to probe its intense visible chromophore at 505 nm. This type of transition has been empirically assigned to an MLCT transition by Kryatov et al.[167], and is expected to produce resonance-enhanced quinoline-iron based vibrations. Upon irradiation with a 515-nm laser source, an intense signal at 631 cm^{-1} is observed (Figure 4.5) among other resonance-enhanced signals. Interestingly, the position of the intense 631 cm^{-1} signal is reminiscent of $M_2(\mu\text{-}OR)_2$ cores in synthetic models.[78,181] However, no other nonheme diiron(II) bis-(μ-OH) complexes have been studied vibrationally before. Therefore, without labeling studies, no confirmatory assignment is possible at this point. Future experiments with ^{18}O labeled water will shed more light on the specific assignments.

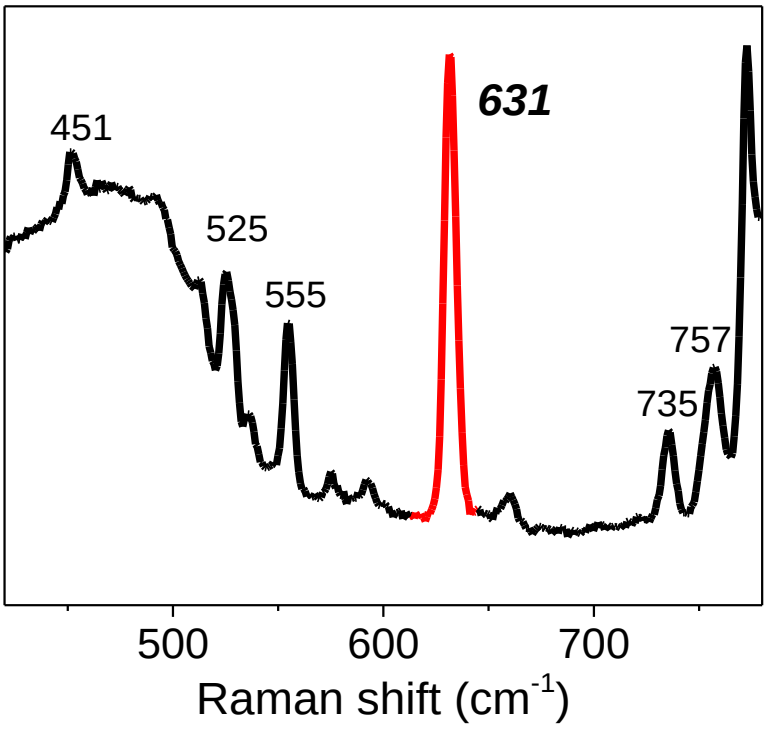

Figure 4.5. Resonance Raman spectrum of **1** in CH_3CN collected at 77 K using a 515 nm laser source.

The ^1H NMR spectrum of **1** shows paramagnetically shifted peaks as expected for high-spin iron(II) complexes.[60] The peaks are well-resolved and sharp, which span a 200-ppm range starting from –60 ppm and going up to 130 ppm (Figure 4.6). The total number of protons after integrating all 20 signals (43) signifies the presence of some asymmetry in the diiron(II) assembly or the presence of other complexes in solution. This follows from the fact that we would expect to observe a maximum of 31 protons in a centrosymmetric configuration of **1**. This also follows by comparing the total signal integration to the expected number of ligand-based signals in a completely asymmetric assembly (62) including the protons from the hydroxide bridges in **1**. The NMR spectrum of **1** can be compared with that of the monomeric $[(TQA)Fe^{II}(OTf)_2]$ complex, also shown in Figure 4.7. This

monoiron(II) spectrum shows 6 signals, which suggests either fortuitous overlapping of resonances or fluxional behavior resulting in peak averaging. This is because the solid-state structure of this complex suggests more than 6 NMR signals owing to the involved asymmetry in the crystal structure[54]. This further underscores the differences in the solution structure of **1** where the degree of asymmetry is higher than expected for a purely symmetric dimerization of two $[(TQA)Fe]^{2+}$ units.

As seen from the bottom panel of figure 4.7, the paramagnetic shifts are far greater for **1** than the monoiron(II) complex. While the most downfield shifted signal in **1** extends up to 130 ppm, $[(TQA)Fe^{II}(OTf)_2]$ has a much narrower range with the most downfield signal at 50 ppm. On the tentative assumption that these signals arise from the same ring protons on the bound TQA ligand in the two complexes, the threefold larger paramagnetic shift observed for **1** (This follows from the fact that the aromatic protons of TQA ligand appear around 8 ppm. Subtracting 8 ppm from the observed shifts of 130 and 50 ppm gives us the paramagnetic shifts, which are 122 and 42 respectively, and produces the threefold enhancement as discussed here) suggests that the magnetic susceptibility of **1** is roughly threefold larger than its monomeric counterpart. Such a change would easily be rationalized by assuming a system of two uncoupled high-spin iron(II) centers in **1** to give rise to an effective $S = 4$ system versus $S = 2$ for the monomeric complex. In this context, the spin-only magnetic susceptibility of a paramagnetic system can be calculated by applying the formula $\chi = n(n+2)$ where n = the total number of unpaired electrons. Thus, applying this simple formula to the $S = 4$ ground state proposed for **1** gives a magnetic susceptibility of 80, which if divided by 24 for the value of the magnetic susceptibility for an $S = 2$ center gives rise to a factor of 3.3 difference in magnetic susceptibility. This ratio is the paramagnetic shift difference observed for the most downfield shifted peaks in the two

complexes, suggesting that there exists no antiferromagnetic coupling between the iron centers. This is because any antiferromagnetic coupling would have mitigated the paramagnetism experienced by the protons in **1**. Mössbauer studies are underway to further confirm these observations.

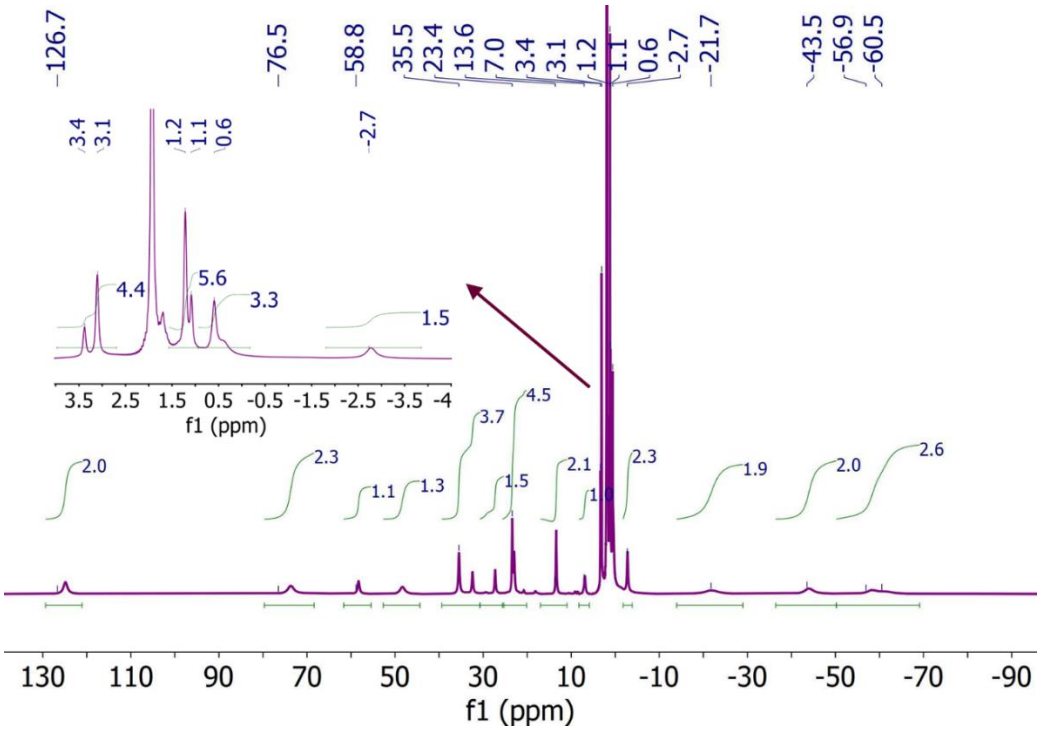

Figure 4.6. ^{1}H NMR spectrum of **1** in CD_3CN at 298 K. The chemical shifts are shown on top of the picture and the relative integrations are shown by the sigmoid curves. The inset picture shows the magnified version of the signals between -4 to +4 ppm.

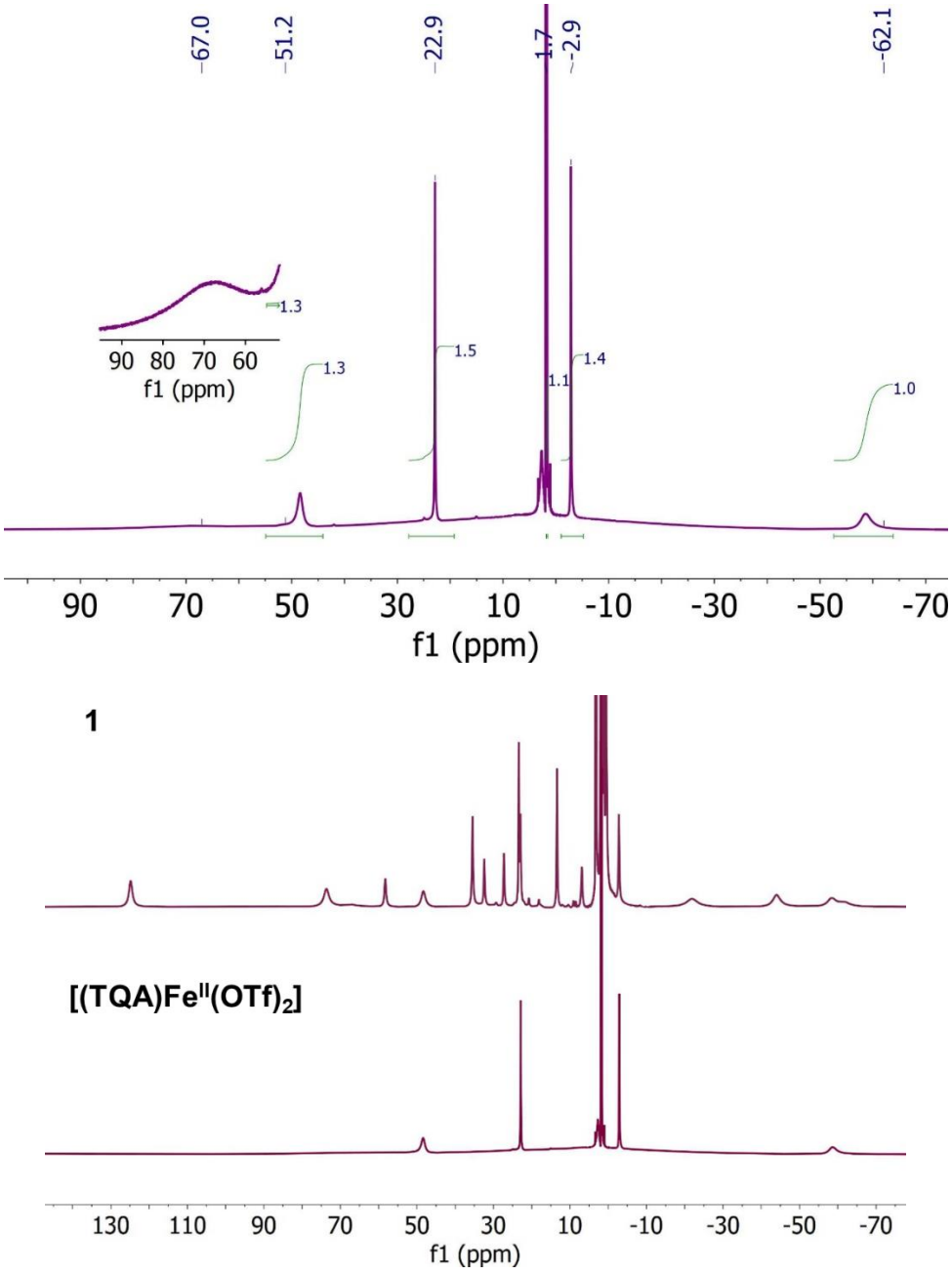

Figure 4.7. (**Top**) ^{1}H NMR spectrum of [(TQA)Fe^{II}(OTf)$_2$] in CD_3CN at 298 K. The chemical shifts are shown on top of the picture and the relative integrations are shown by the sigmoid curves. The broad signal at 67 ppm is shown as an inset picture. (**Middle**) ^{1}H NMR of **1** in CD_3CN at 298 K. (**Bottom**) ^{1}H NMR of [(TQA)Fe^{II}(OTf)$_2$] in CD_3CN at 298 K. The above

comparison of NMR spectra of **1** and [(TQA)$Fe^{II}(OTf)_2$] clearly shows the difference in the paramagnetic shifts between these two complexes besides a larger number of signals in **1**.

Variable temperature NMR studies have been performed on **1** to shed light on how the diiron unit affects magnetic susceptibility as a function of temperature. As seen in Figure 4.8, the NMR signals in **1** move farther from the diamagnetic region with a decrease in temperature, as expected for Curie behavior, underscoring the increase in magnetic susceptibility with the lowering of temperature. Besides the change in paramagnetic shifts, the signals become broader with a lowering in temperature following the expected lowering of transverse spin-spin relaxation time (T_2) with temperature.

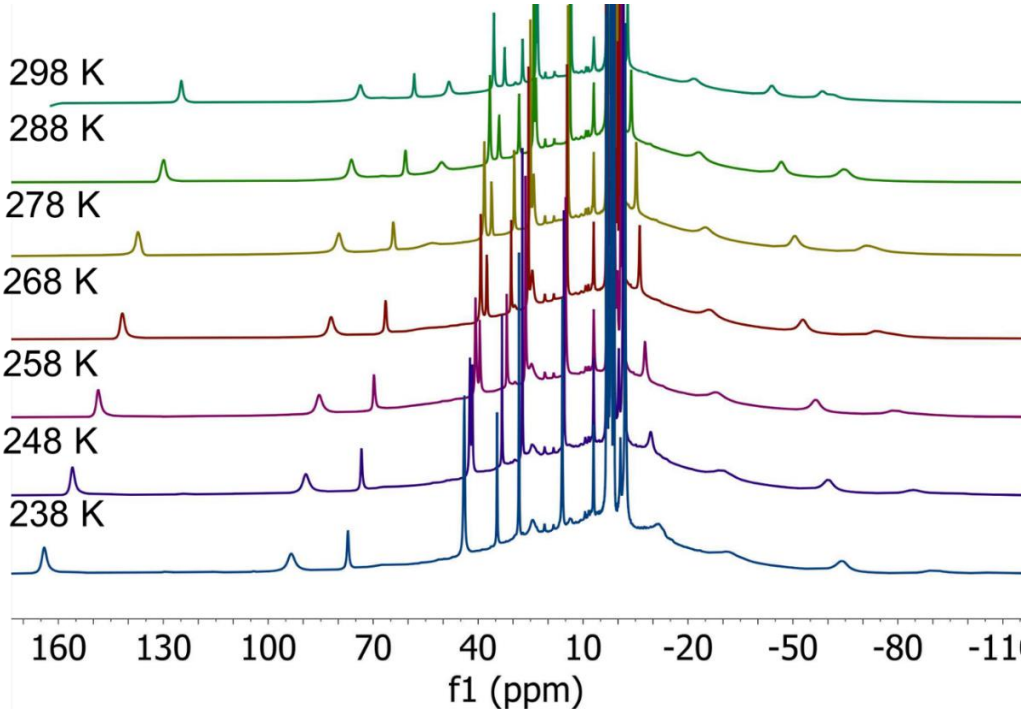

Figure 4.8. Variable temperature NMR spectra of **1** in CD_3CN in the temperature range of 238 - 298 K.

For comparison, the variable temperature behavior of [(TQA)$Fe^{II}(OTf)_2$] is shown in Figure 4.9. The paramagnetic shifts and the line broadening of the signals increase with the lowering of temperature. However, these changes differ from changes in **1** by the extent of dependence of these variables upon temperature. Figure 4.10 shows that the increase in paramagnetism in **1** is far greater than in [(TQA)$Fe^{II}(OTf)_2$] within the same temperature range. More interestingly, the overall line broadening effect is much more apparent in [(TQA)$Fe^{II}(OTf)_2$] than in **1**. The rationale behind this intriguing observation is not clear but possibly related to the differences in the mechanism of electronic relaxation in **1** compared to [(TQA)$Fe^{II}(OTf)_2$].

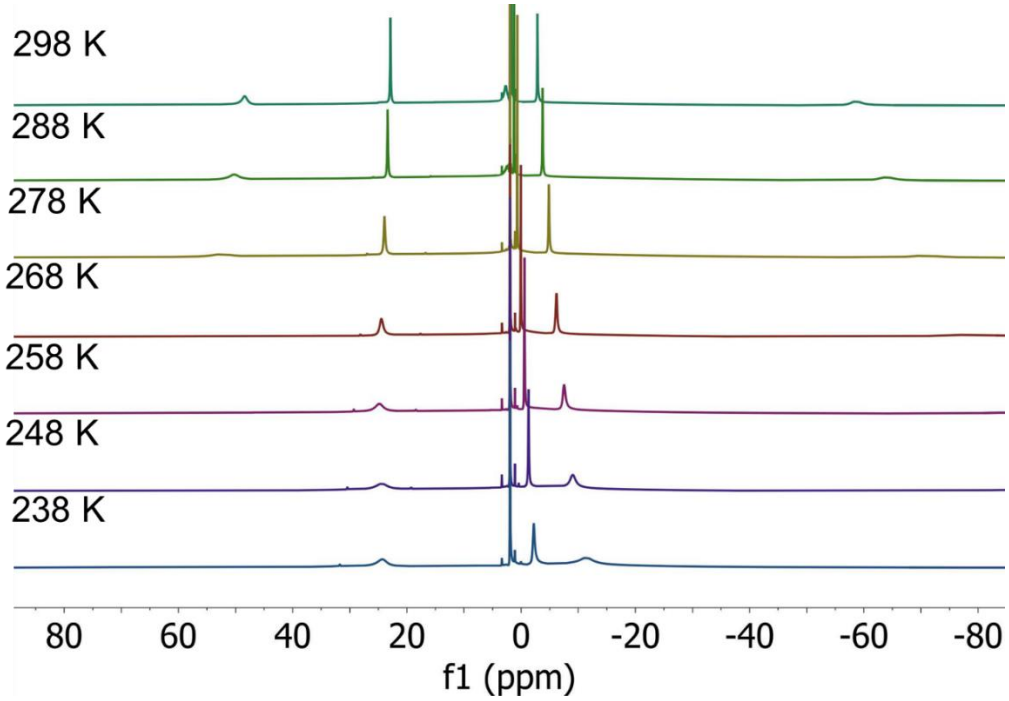

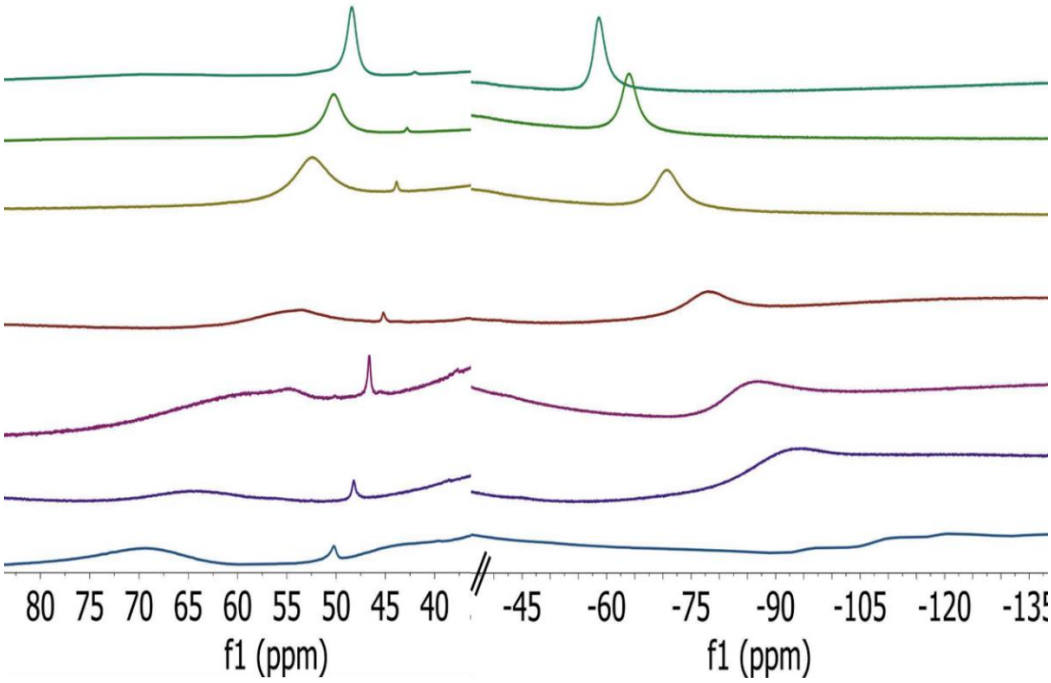

Figure 4.9. Variable temperature NMR spectra of [(TQA)$Fe^{II}(OTf)_2$] in CD_3CN obtained in the temperature range of 238 - 298 K. Regions from 40 – 80 ppm and -45 – 135 ppm have been magnified to show the broadness of the related peaks more clearly.

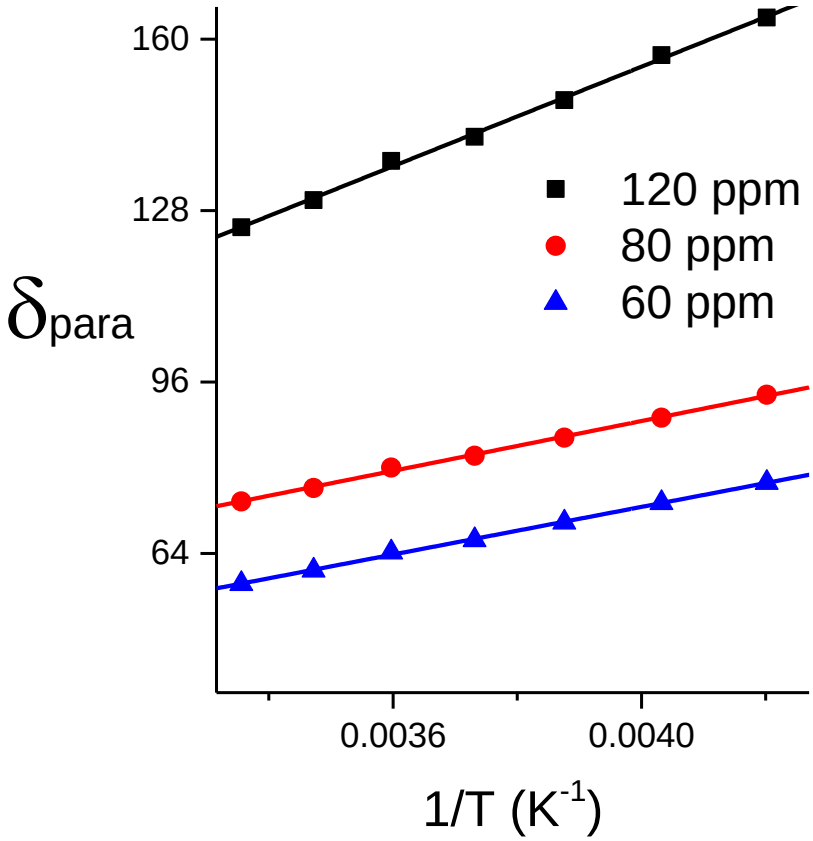

Figure 4.10. Plots of paramagnetic shifts of different signals in **1** versus the inverse of temperature. The lines connecting the dots are the linear fit of the corresponding sets of data. As expected from Curie's law, the relationships are mostly linear and signify that the paramagnetic shifts are inversely proportional to temperature.

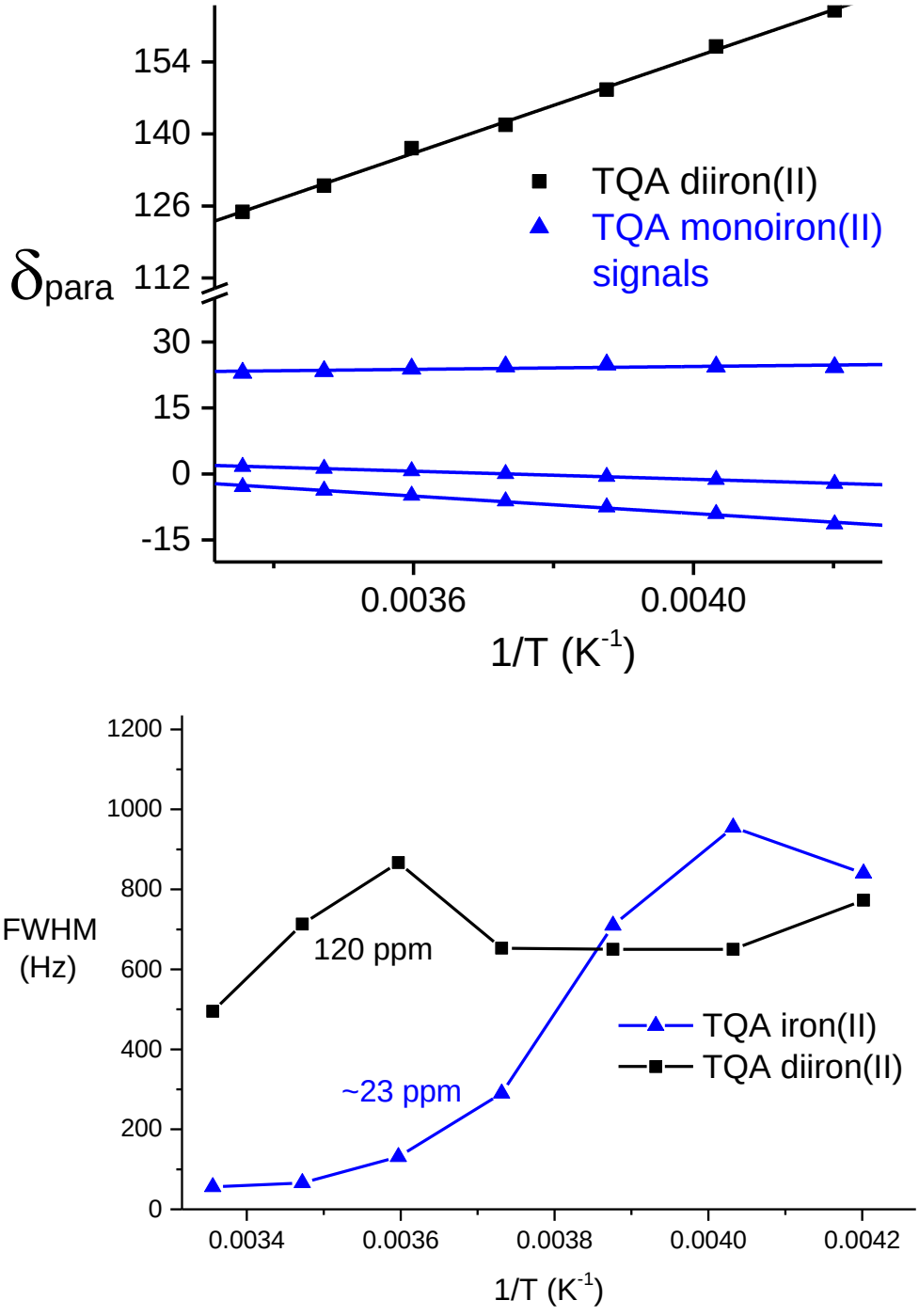

Figure 4.11. (Top) Comparative plots of paramagnetic shifts of different signals in **1 (black squares)** and different signals in [(TQA)Fe^{II}(OTf)$_2$] **(blue diamonds)** versus the inverse of temperature. As expected from Curie's

law, the relationships are mostly linear, and this is emphasized by the linear fits of the available datasets with solid lines. (**Bottom**) Plots of the full peak widths at half-maxima (FWHMs) or linewidths (indirect T_2 measurements) versus the inverse of temperature. At 298 K, the NMR signal at 23 ppm in the monoiron(II) complex is sharper than the signal at 120 ppm in the diiron(II) complex **1**. The choice of 23 ppm and 120 ppm follows from the fact that they are the most downfield shifted peaks that are legible across the temperature range in the respective complexes. However, the temperature dependence of the signals of these two complexes is drastically different. The maximum change in linewidths of the monoiron(II) complex is almost double the change observed in the diiron(II) complex **1**.

4.2.2 Oxygen activation of 1 and related characterization of the O_2 adducts

Upon reaction with O_2 at room temperature, the color of an acetonitrile solution of **1** changes from dark red-purple to brown yellow within minutes. When followed by UV-vis absorption spectroscopy, the spectrum of **1** changes rapidly to generate a significant increase in absorption around 400 nm (Figure 4.12). Related oxygenation studies on diiron systems by Kryatov et al.[167] showed the presence of similar absorption changes that were related to the formation of (μ-oxo)diiron(III) products. Indeed, ESI-MS analysis of the solution of oxidation of **1** shows an m/z signal corresponding to $[(TQA)_2Fe_2^{III}(\mu\text{-}O)_2(OTf)]^+$ (Figure 4.13). The presence of this intense signal in the final oxidized product mixture suggests that it might be possible to isolate this species. Interestingly, there is only one report of an isolated nonheme bis(μ-oxo)diiron(III) complex, and that was not prepared using oxygen activation. It is highly significant that a bis(μ-oxo)diiron(III) complex can be formed in the oxygen activation of a diiron(II) precursor such as **1**, as similar core structures have been characterized in oxygen

activating enzymes, including diiron enzyme **sMMO**.[67,68] Therefore, the isolation of this complex will provide additional structural data, which can be used to shed light on similar structures in Nature. The challenge lies in the difficulty in generating these bis(μ-oxo)diiron(III) complexes in pure form to be recrystallized from the solution. If the oxidation of **1** is expressed as a chemical reaction (see below), then we notice that water is being formed as a by-product that may be capable of protonating the rather basic oxygen atoms in $[(TQA)_2Fe_2^{III}(\mu\text{-}O)_2]^{2+}$ to generate at least in some fraction of its conjugate acid.

$$2\,[(TQA)_2Fe_2^{II}(\mu\text{-}OH)_2]^{2+} + O_2 \longrightarrow 2\,[(TQA)_2Fe_2^{III}(\mu\text{-}O)_2]^{2+} + 2H_2O$$

To avoid this issue, aerial oxidation of an acetonitrile solution of **1** is carried out in the presence of an excess base (NEt_3) where the dark red-purple color of **1** changed in brown yellow. The resulting solution is placed in an ether bath overnight at 233 K. This produces yellow-colored crystals, which are characterized by X-ray diffraction. The resulting crystal structure confirms the presence of a bis(μ-oxo) diiron core (Figure 4.15) and the presence of two triflate anions confirms the total charge of the cation to be +2. The overall charge is consistent with the bis(μ-oxo)diiron(III) formulation. This isolated complex **2** is the first crystal structure of a bis-(μ-oxo)diiron(III) complex resulting from oxygen activation.

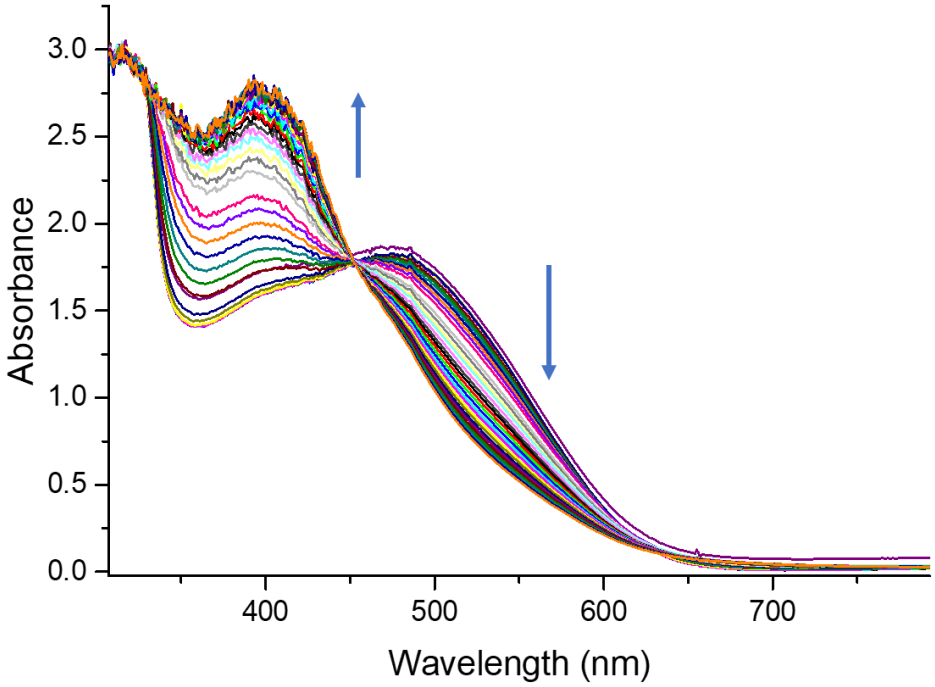

Figure 4.12. UV-vis absorption spectra of the aerial oxidation of **1** (1 mM) in CH_3CN at 298 K. The spectra were collected over 4 minutes as **1** was being oxidized to **2.** An isosbestic point at 453 nm was observed.

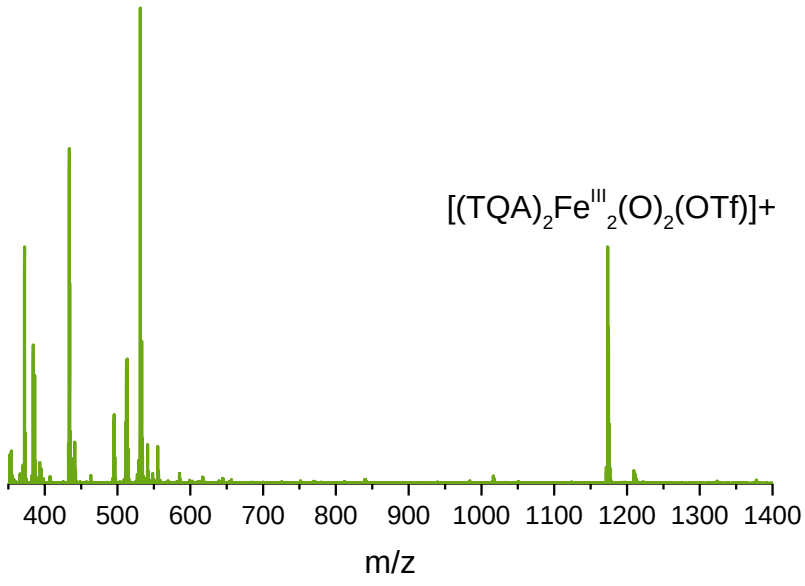

Figure 4.13. ESI-MS of the oxygenated solution of **1** in MeCN at room temperature, with the signal for m/z 550 for the $[(TQA)_2Fe_2^{III}(\mu\text{-}O)_2(OTf)]^+$ cation labeled. The signals below m/z = 550 in the oxidized solution of **1** have not been assigned.

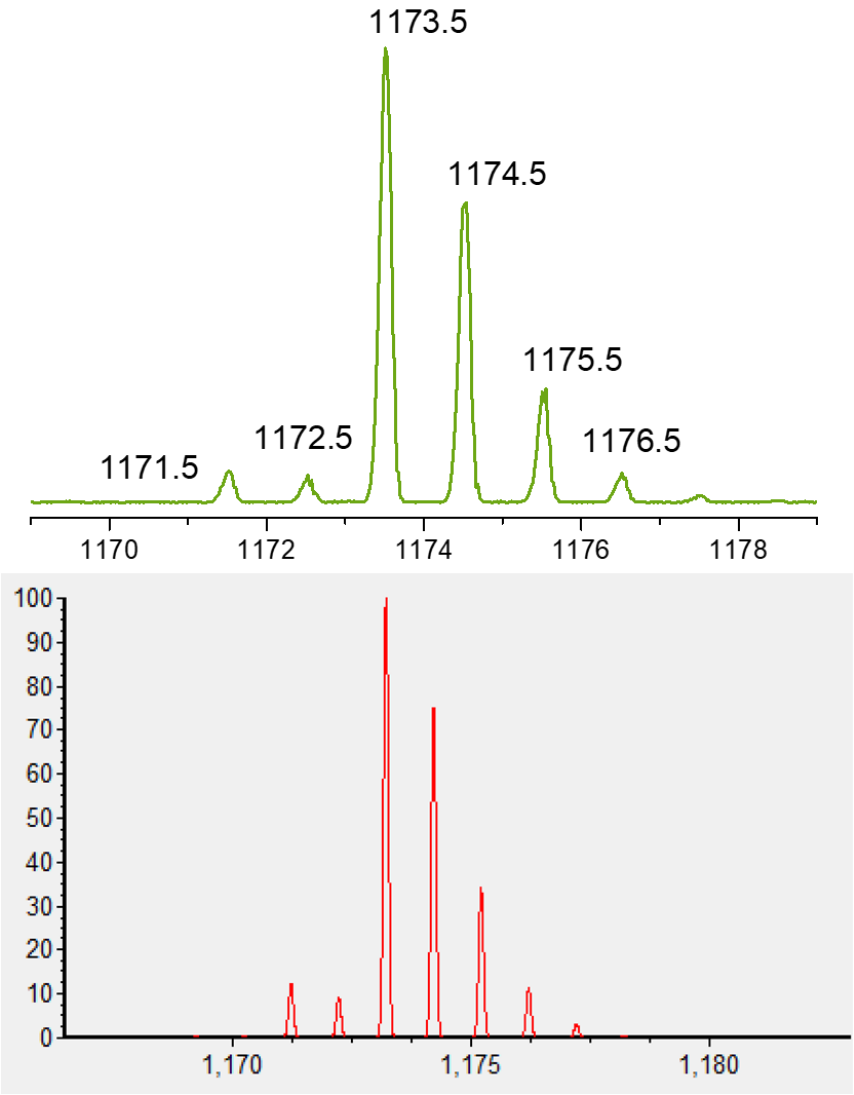

Figure 4.14. Magnified ESI-MS of the $[(TQA)_2Fe_2^{III}(\mu\text{-}O)_2(OTf)]^+$ cation signal (top) and an IsoPro simulation of the mass spectrum (bottom).

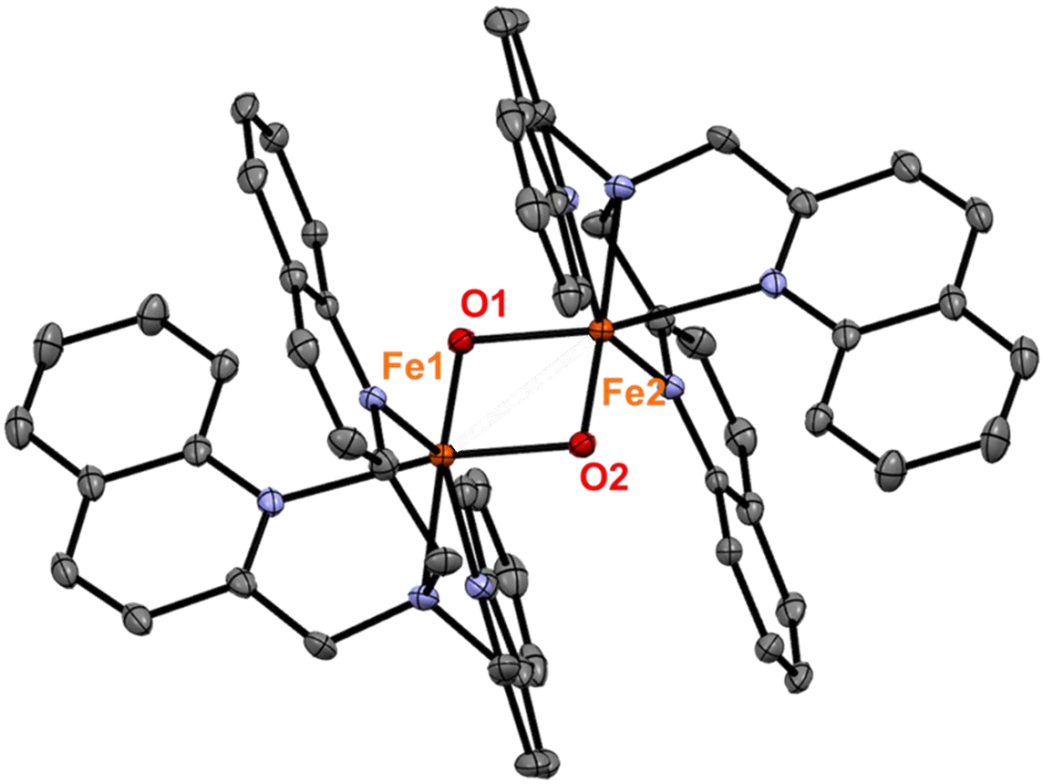

Figure 4.15. Structure of the cationic form of **2** ($[(TQA)_2Fe_2(\mu\text{-}O)_2]^{2+}$) with thermal ellipsoids drawn to the 50% probability level. Triflate anions and hydrogen atoms have been removed for clarity. The presence of an inversion center at the center of the Fe_2O_2 core results in one-half of the molecule being unique. Iron atoms are shown in golden yellow; oxygen atoms are in red, nitrogen atoms are in blue and carbon atoms are shown in grey.

X-ray crystallography shows **2** to be best formulated as $[(TQA)_2Fe_2(\mu\text{-}O)_2](OTf)_2$. There is one unique molecule in the unit cell with an inversion center at the Fe_2O_2 core. Each iron atom is in a distorted octahedral environment consisting of the four nitrogens from TQA and two bridging oxygen atoms. Compared to single oxo-bridged diiron(III) complexes[217], **2**

shows some unique features. The Fe–O distances in **2**, Fe–μ-O bond *trans* to a quinoline (1.84 Å) and the Fe–μ-O bond *trans* to an amine (1.92 Å) are longer than previously reported diiron(III) complexes with single oxo bridges (range 1.73 – 1.83 Å).[217] This results from the decrease in Lewis acidity of the iron(III) centers upon coordination with two oxygen atoms versus one. Similar differences in Mn–μ-O distances have been observed with $[Mn^{III}_2(\mu\text{-}O)_2]$ complexes exhibiting longer Mn–μ-O bonds than $[Mn^{III}_2(\mu\text{-}O)]$ complexes.[218–220] However, the degree of asymmetry in the oxo-bridges for $[Mn^{III}_2(\mu\text{-}O)_2]$ complexes is not as pronounced as observed in **2** and other $[Fe^{III}_2(\mu\text{-}O)_2]$ and $[Fe^{III}_2(\mu\text{-}OR)_2]$ units[221,222]. Interestingly, the Fe–O bond distances found for **2** are almost identical to those of the previously reported $[(6Me_3TPA)_2Fe_2(\mu\text{-}O)_2]^{2+}$ complex[222] (see Table 4.2 below). Next, **2** has a distinctly small Fe–O–Fe bond angle (90.5°), which is smaller than found for any other (μ-oxo)diiron(III) complexes. It is even smaller than the $[(6Me_3TPA)_2Fe_2(\mu\text{-}O)_2]^{2+}$ complex (Table 4.2). The shorter angle in **2** reflects a greater amount of electronic repulsion between two oxo bridges and minimization of steric congestion between two TQA ligands. This is also manifested in the shorter diiron distance (2.67 Å) in **2**, which is the shortest separation ever observed for (μ-oxo)diiron(III) complexes.

Table 4.2. Comparison between the two bis-(μ-oxo)diiron(III) complexes.

Complex	**$[(6Me_3TPA)_2Fe_2(\mu\text{-}O)_2]^{2+}$**	**2**
Fe·····Fe	2.714 (1)	2.669 (8)
Fe–O1	1.842 (5)	1.839 (3)
Fe–O2	1.917 (4)	1.917 (3)
∠Fe–O–Fe	92.43 (2)	90.48 (1)
Fe–N (avg)	2.241 (5)	2.254 (3)

The UV-vis absorption spectrum of **2** shows absorption features that are reminiscent of the previously reported $[(6Me_3TPA)_2Fe_2(\mu\text{-}O)_2]^{2+}$ complex[223]. It has intense absorption at around 320 nm together with broad features at 380 nm (1500 M^{-1} cm^{-1}) assigned to an LMCT transition from quinoline to Fe(III) d-orbitals. The 470 nm (370 M^{-1} cm^{-1}) feature (Figure 4.16) has been assigned to an LMCT transition from the oxo ligands to the Fe(III) center. Similar features have been reported for $[(6Me_3TPA)_2Fe_2(\mu\text{-}O)_2]^{2+}$ complex at 375 nm (2000 M^{-1} cm^{-1}) and 470 nm (560 M^{-1} cm^{-1}).[223] The similarity of these bands is a testament to similar ligand donor capabilities of quinolines and 6-methyl-pyridine moieties.

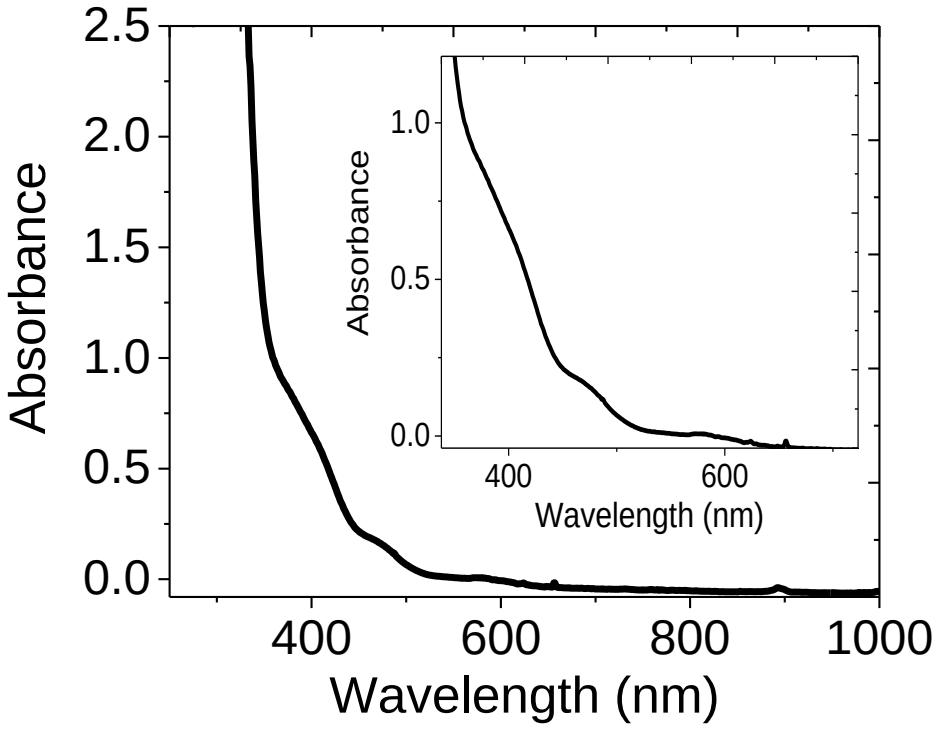

Figure 4.16. UV-vis absorption spectrum of **2** (0.5 mM) in CH_3CN at 298 K.

The ^1H NMR spectrum of **2** shows well-resolved relatively sharp features from 0 to 70 ppm (Figure 4.17). This range of paramagnetic shifts is comparable to what has been previously reported for (μ-oxo)(μ-hydroxo)- and bis-(μ-oxo)diiron(III) complexes[223,224] but much larger than what was observed for single-bridged (μ-oxo)diiron(III) complexes[225]. This follows from the stronger anti-ferromagnetic coupling interaction in single-bridged (μ-oxo)diiron(III) complexes. The two broad signals at 34 ppm and 68 ppm most likely originate from the methylene groups in the TQA ligand framework, whereas the sharper signals belong to the ring protons of quinolines. Relatively sharper signals between 18 and 30 ppm likely originate from C7-H protons on the quinoline moieties, and with the

increase in distance from the iron center, the other ring protons (C6-H, C5-H, and C4-H in that order) appear closer to the diamagnetic region with a decrease in paramagnetic shifts. Similar NMR analyses have been reported with ^{1}H NMR spectra for closed core diiron(III) complexes with 6Me$_3$TPA as the supporting ligand[223,224]. The C8-H protons of the quinolines are too close to the iron(III) center and too broad to observe, analogous to α-protons on pyridine rings.[224] Although there are very few reports on iron-quinoline NMR studies, unpublished data can be used here for reference from work carried out by Rasheed et al.[226] These studies showed the absence of C8-H proton signals, presumably due to their broadness, and can be used as a comparison for the current set of data, although the NMR data reported by Rasheed et al. is not for iron(III) centers. Absolute assignments of NMR signals of **2** will not be significantly beneficial for our goals here and hence, have not been pursued.

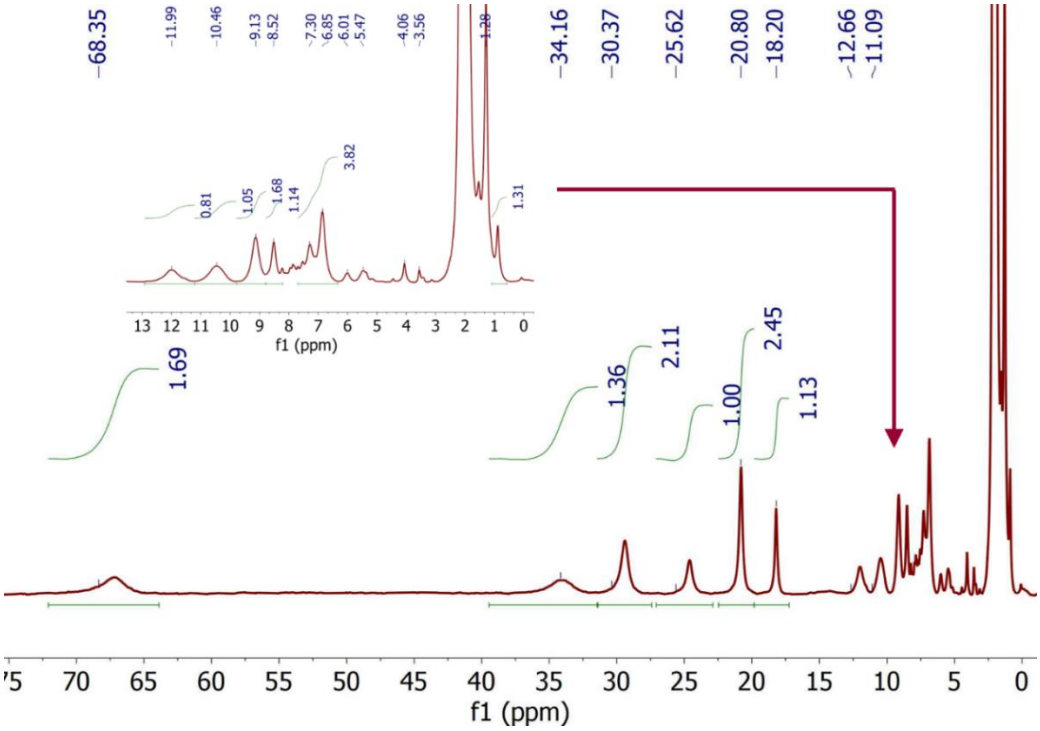

Figure 4.17. ^{1}H NMR spectrum of **2** in CD_3CN at 298 K. Inset shows the magnified region from 0 to 14 ppm.

Variable temperature data on **2** have also been collected and exhibit remarkable differences upon comparison with the diiron(II) precursor **1** and the related mononuclear complex [(TQA)Fe^{II}(OTf)$_2$]. As seen in Figure 4.18., neither the chemical shifts nor the linewidths vary much with the lowering of temperature. This is in sharp contrast with the variable temperature behavior of **1** where a shift of 40 ppm is observed within the same temperature range (Figure 4.9 and 4.10). This suggests that there must be weak anti-ferromagnetic coupling between the iron centers in **2**, which mitigates the paramagnetism experienced by the protons when compared with the diiron(II) complex **1**. The magnitude of this coupling (indicated by *J* value) has not been measured in **2**. However, our NMR observations are reminiscent of the weak anti-ferromagnetic coupling in the

$[(6Me_3TPA)_2Fe_2(\mu\text{-}O)_2]^{2+}$ complex (J = 54 cm^{-1}) where NMR signals are found between -5 and 80 ppm[23] in contrast to strong coupling interactions in single bridged diiron(III) TPA complexes[36].

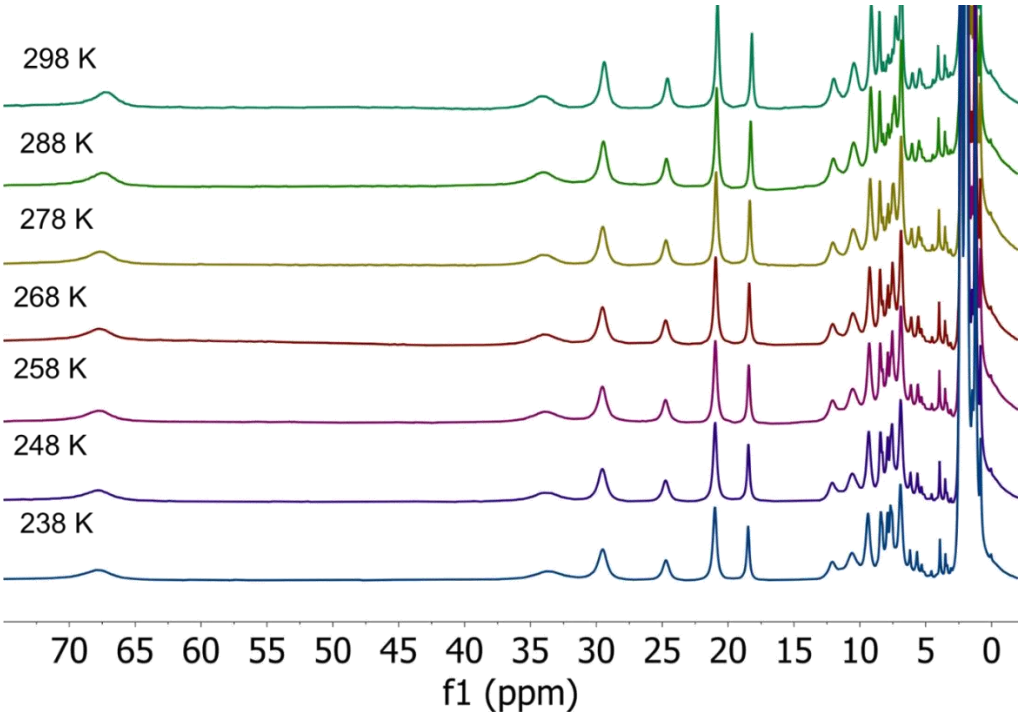

Figure 4.18. ^{1}H-NMR spectra of **2** in CD_3CN from 238 to 298 K.

A vibrational study on **2** using FTIR spectroscopy shows a distinct feature at 673 cm^{-1}, which is absent in mononuclear $[(TQA)Fe^{II}(OTf)_2]$ complex (Figure 4.19). Furthermore, this signal disappears upon ^{18}O labeling of **2** with the addition of $H_2{}^{18}O$. It needs to be mentioned here that there are additional changes upon ^{18}O labeling in the IR spectra that are currently unexplained. The crystal structure of **2** confirms the presence of a Fe_2O_2 core. As we are aware of the characteristic position of an M_2O_2 vibration, which usually appears between 600 to 700 cm^{-1} region[78,99], we tentatively assigned the 673 cm^{-1} signal to the 'breathing' motion of the Fe_2O_2 core in **2**.

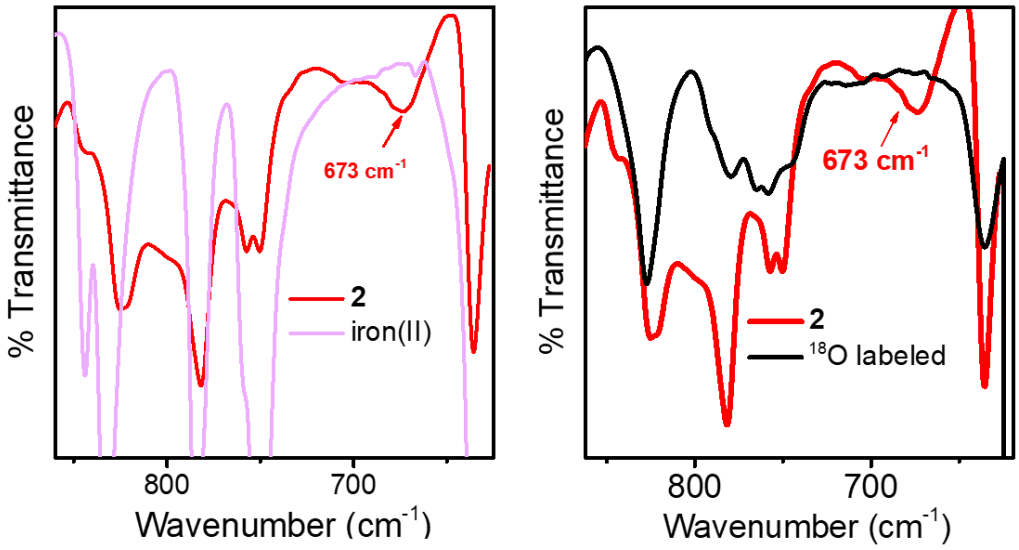

Figure 4.19. FTIR spectra showing the vibrational signatures of **2** (red) as compared with the iron(II) complex [(TQA)$Fe^{II}(OTf)_2$] (pink in the left panel) and the ^{18}O-labeled **2** (black in the right panel), after treatment of **2** with 300 equiv of $H_2{}^{18}O$.

Confirmation of this IR observation with Raman spectroscopy is highly desired, but the lack of intense absorption in the visible region makes it difficult to obtain resonance enhancement for the vibrations in **2** with the available laser sources in the Que group. However, with suitable UV lasers, the 380 nm absorption can be exploited to obtain a resonance-enhanced vibrational spectrum of **2**. Efforts are underway to acquire such a laser source in the Que group. Nonetheless, the 673 cm^{-1} signal obtained from IR spectroscopy matches quite well with the 90.5° Fe—O—Fe bond angle in **2** obtained from its crystal structure (see Sanders Loehr plot in Figure 4.20. below).

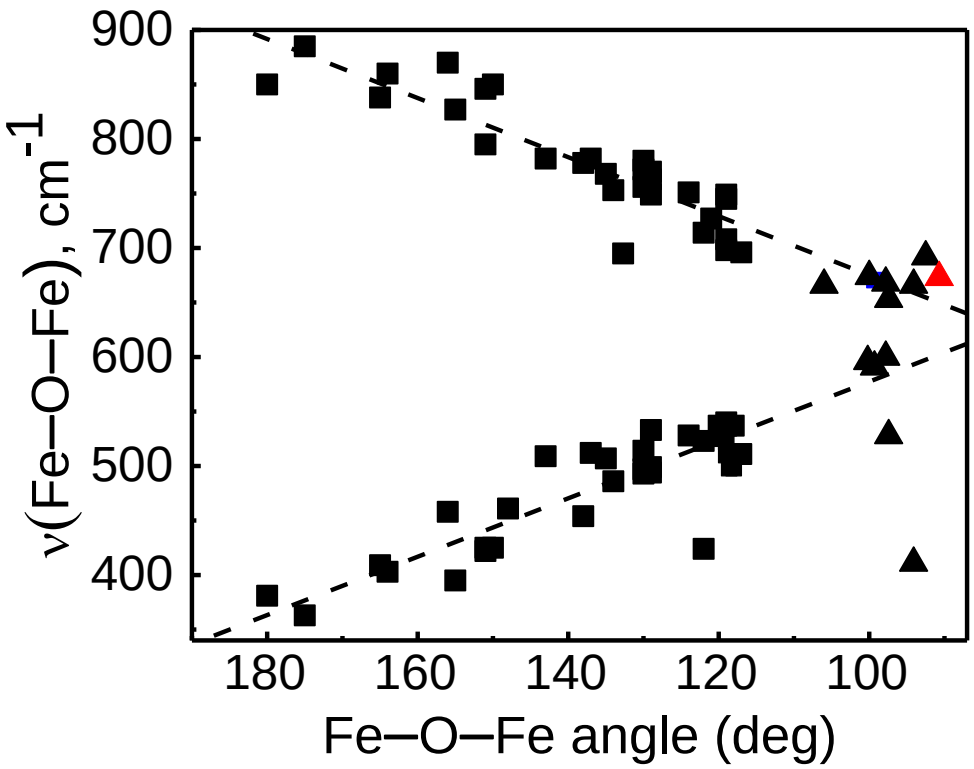

Figure 4.20. Sanders-Loehr plot showing the correlation of the Fe–O–Fe vibrations with Fe–O–Fe angles. **2** is shown with the red diamond symbol. The black squares in the linear correlations represent oxo-bridged diiron(III) complexes and peroxodiiron(III) complexes. The closed core diiron complexes are shown as solid triangles to focus on the current discussion and emphasize the excellent agreement of the structural and vibrational data of **2** with the previously reported diiron complexes. The closed core outlier around 400 cm^{-1} is reported for $[(Me_3NTB)_2Fe^{IV}_2(O)_2]^{4+}$ complex[216].

While we now have a much better understanding of the final product of the oxygenation of **1**, we need to search for fleeting intermediates during the oxygenation of **1** before it is converted to oxodiiron(III) species like **2**. To

achieve this, the temperature was lowered down to 233 K to stabilize any intermediates that may have been difficult at room temperature. Similar systems have been shown to form peroxodiiron(III) intermediates starting from diiron(II) complexes such as **1** at lower temperatures[167]. However, when **1** was exposed to oxygen at 233 K, no characteristic absorption features were observed that would point toward a peroxodiiron(III) complex (Figure 4.21). Synthetic peroxodiiron(III) complexes are well studied in the literature[67] and provide us with a good idea about the UV-vis absorption spectra of these species. More importantly, the BnBQA framework (a tridentate quinoline-rich ligand quite similar to TQA in terms of N-donation capabilities) has supported a (μ-oxo)peroxodiiron(III) complex that has intense absorption at 650 nm[101,167] (reproduced in figure 4.23). It is expected that the absorption features of a peroxodiiron(III) complex supported by TQA would have similar characteristics as BnBQA. However, no such features are observed in the oxygenation of **1** at 233 K. What is observed is an increase in absorption around 400 nm region, which signifies the formation of oxo bridged diiron(III) complexes, reminiscent of what is observed at room temperature (as discussed before using figure 4.12).

The mechanism of dioxygen activation in the diiron models has been shown by Kryatov et al.[167] to proceed by inner-sphere electron transfer involving an initial binding of dioxygen to the iron center. Assuming that a similar mechanism operates for **1**, it is not surprising that no accumulation of a peroxo-like intermediate for **1** is observed even at lower temperatures despite successes with related systems.[73,167,216] Indeed, sterically hindered systems like BQPA and 6Me$_3$TPA did not yield significant amounts of peroxodiiron(III) intermediates in coordinating solvents like acetonitrile. As explored in these studies, factors can be changed like the solvent and the use of additives. Upon changing the solvent from MeCN to

a DCM:MeCN mixture with a strong base as an additive, we start seeing the formation of peroxo-like features with TQA (Figure 4.22). This is reminiscent of what was observed by Kryatov et al. for 6Me$_3$TPA in similar solvent mixtures[215].

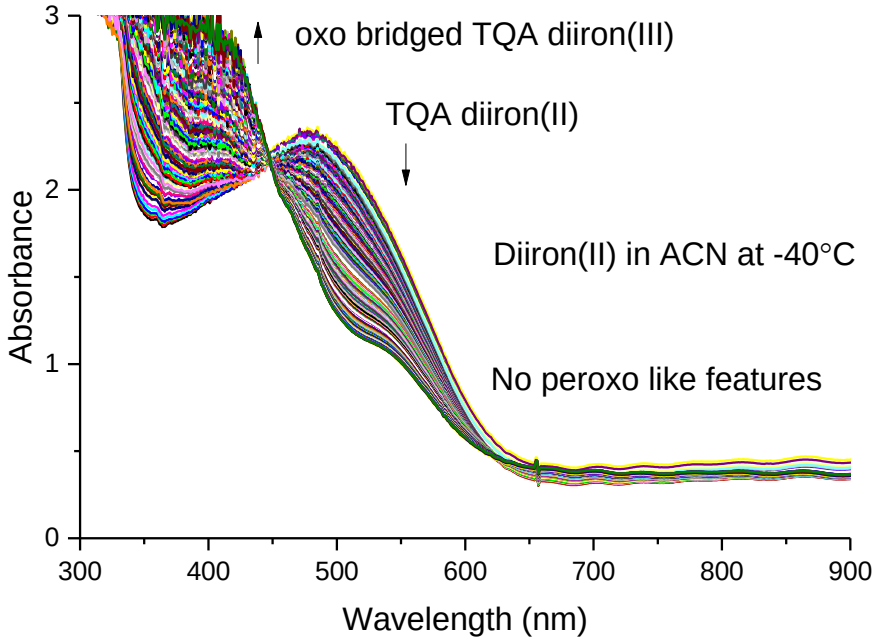

Figure 4.21. UV-vis spectra of the oxygenation of **1** (1.2 mM) in ACN at 233 K, showing the formation of characteristic features of (μ-oxo)diiron(III) complexes[167].

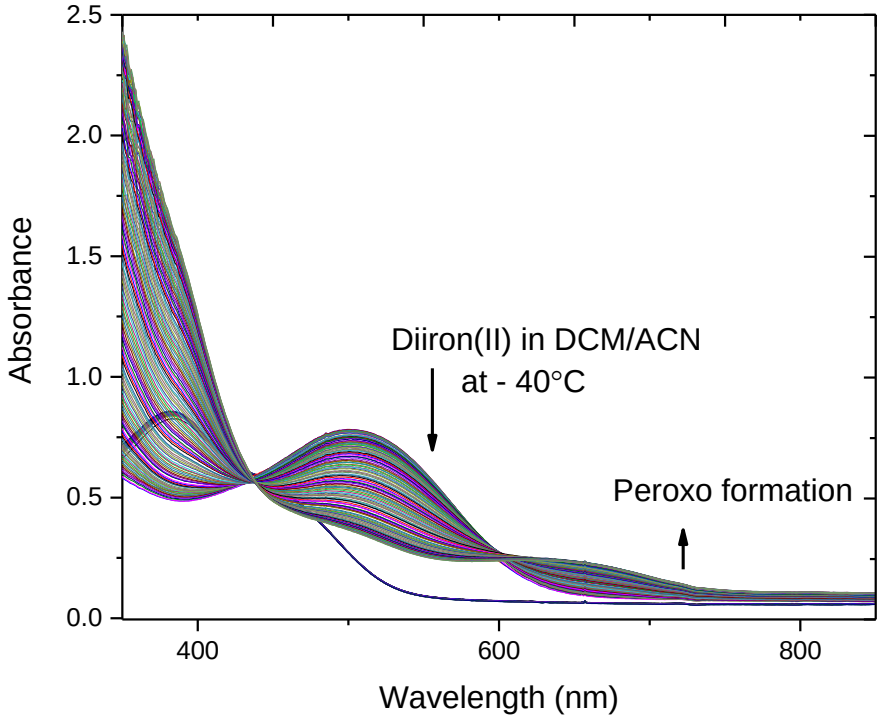

Figure 4.22. UV-vis spectra of the oxygenation of **1** (0.4 mM) in 9:1 DCM:ACN at 233 K in the presence of DBU as an additive, showing the formation of characteristic features of (μ-oxo)(μ-1,2-peroxo)diiron(III) complexes[167].

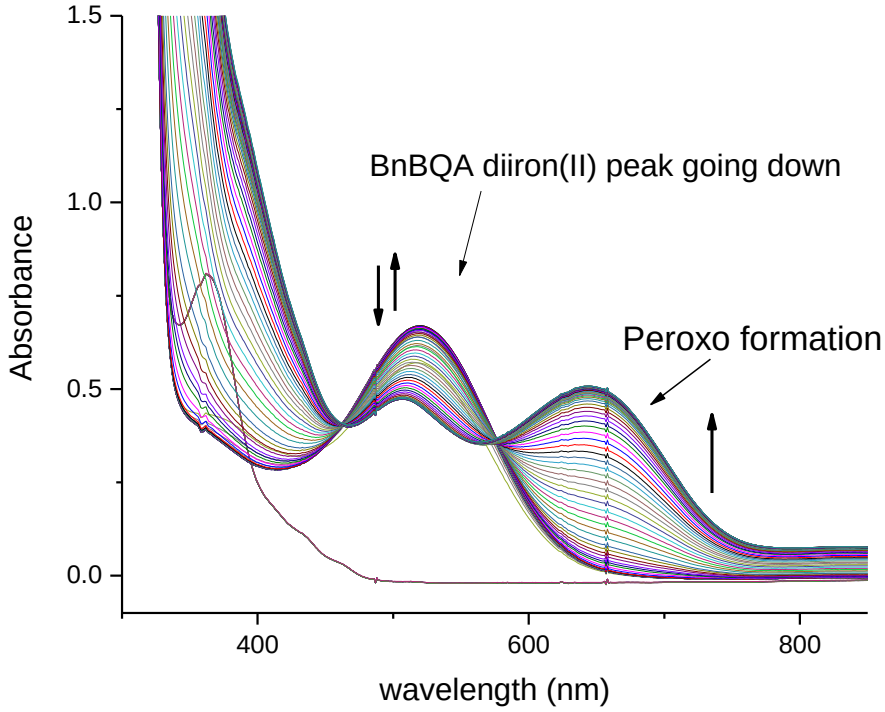

Figure 4.23. UV-vis spectra of the oxygenation of diiron(II) **[(BnBQA)$_2$Fe$^{II}_2$(OH)$_2$]$^{2+}$** complex in ACN at 233 K, showing the formation of characteristic features of the corresponding (μ-oxo)(μ-1,2-peroxo)diiron(III) complex[101,167]. The feature at 650 nm is like what is observed during the oxygenation of **1** in Figure 4.22 under modified conditions.

4.3 Discussion

It is worth emphasizing the origin of the differences between the two sets of conditions. Most importantly, regardless of the conditions, oxygenation of **1** still takes place and this implies that oxygen still binds with the iron center because an outer sphere electron transfer is not plausible based on detailed studies reported by Kryatov et al.[167]. The steric demands of the TQA ligand arguably prevent the oxygen molecule from binding to both of the iron centers at the same time to generate peroxodiiron(III)

intermediates in observable amounts. The use of non-coordinating solvents like DCM makes it easier for oxygen to bind to both the iron centers, consistent with the appearance of peroxodiiron(III) features upon using DCM in the solvent mixture. Next, the use of base promotes the formation of peroxodiiron(III) intermediate owing to the presence of proton sensitive steps in the oxygen activation of **1**. Similar observations were made with related systems that had significant steric demands[167]. Lastly, even with the improved conditions, **1** can only provide roughly 25% formation of the peroxodiiron(III) complex at 233 K. Further lowering of temperature and a detailed study of other solvents and additives to improve the yield of this intermediate is desired. This will allow spectroscopic characterization of this species and will aid in comparing the same with previously reported models[67]. Moreover, a greater accumulation of the peroxodiiron(III) intermediate will allow us to utilize what we learned from Chapter 3 about strategies to break the O-O bonds in diiron systems to generate high-valent intermediates. Also, moving to even lower temperatures than 233 K may allow us to observe reactive high-valent diiron species before they decay to oxodiron(III) intermediates like **2**.

The use of a strong base to enhance the formation of a peroxodiiron(III) species needs to be discussed further. Oxygen activation by a diiron system is proposed to proceed by initial O_2 binding to generate a superoxide species **S**, which converts into a hydroperoxide **H** (see below). A competing reaction is the formation of bis(μ-oxo)diiron(III) complexes like **2**. It is the presence of base that mitigates the accumulation of species like **H**, which in turn helps to form the peroxodiiron(III) complex **P** in figure 4.24 below. In coordinating solvents like MeCN, there is a considerable accumulation of **H**, which then reacts with the residual diiron(II) complex **1** to generate oxodiiron(III) species.

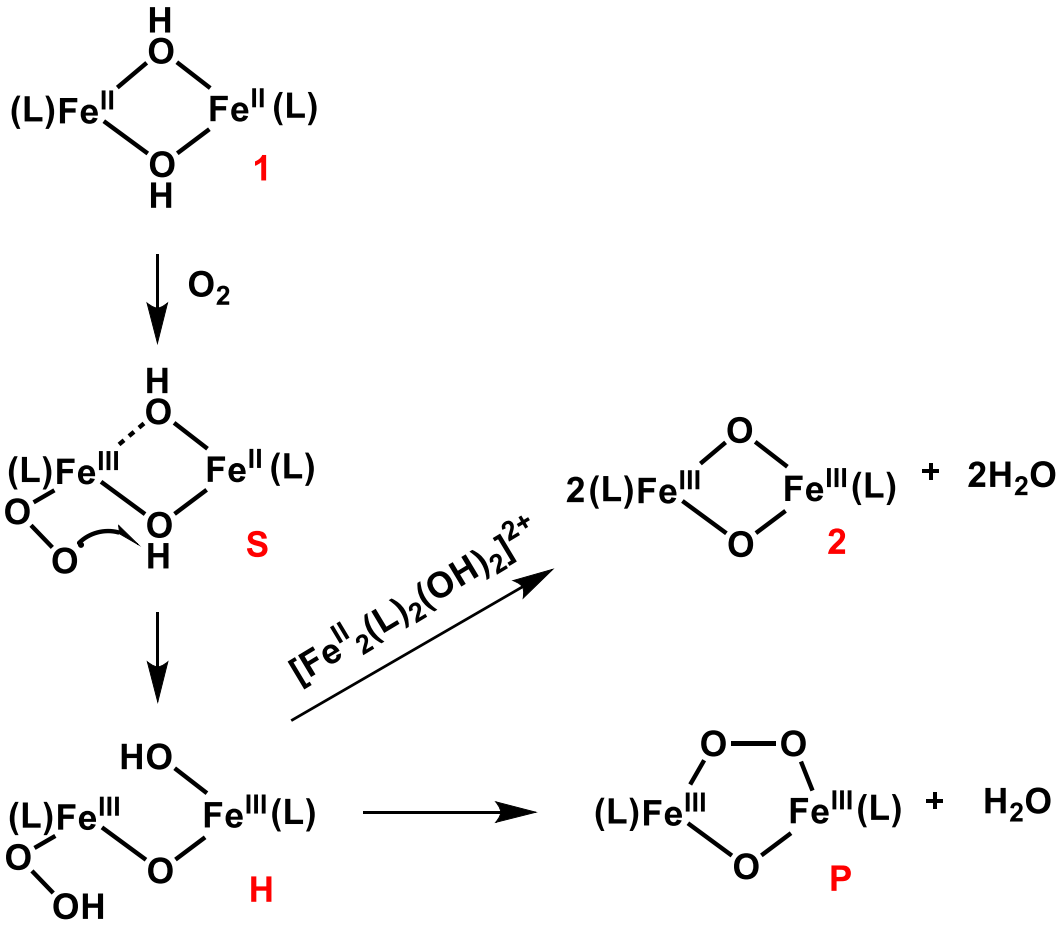

Figure 4.24. Proposed oxygen activation pathway of diiron center **1**. The figure is reprinted (adapted) with permission from S. V. Kryatov, S. Taktak, I. V. Korendovych, E. V. Rybak-Akimova, J. Kaizer, S. Torelli, X. Shan, S. Mandal, V. L. MacMurdo, A. Mairata I Payeras, L. Que, *Inorg. Chem.* **2005**, *44*, 85–99. Copyright 2005 American Chemical society.

4.4 Conclusion

In the process of moving towards weak-field ligands like quinolines, we have observed unique differences between the diiron chemistry of the TQA ligand framework and the Me_3NTB ligand framework. A major difference lies in the isolation of the diiron(II) precursor complex supported by these

two systems. While the diiron(II) complex of Me_3NTB can be only generated in situ, the diiron(II) complex with TQA **1** can be isolated as a solid. Secondly, the oxygen activation results are quite different in acetonitrile for **1** and the corresponding diiron(II) precursor of Me_3NTB as discussed in chapter 3.[227] While there is no sign of a peroxodiiron(III) formation with **1**, the diiron(II) complex with the Me_3NTB framework forms a peroxodiiron(III) species in ~80% yield at the same temperature and solvent. Lastly, the isolation of **2** marks the first bis-(μ-oxo)diiron(III) complex formed as a result of oxygen activation. Similar isolation attempts have not been successful so far with the Me_3NTB framework.

4.5 Experimental Section

4.5.1 Materials

Commercially available chemicals such as DBU (1,8-diazabicyclo[5.4.0]undec-7-ene) and solvents were used without further purification unless noted. $[Fe^{II}(TQA)(CF_3SO_3)_2]$ was synthesized as previously reported.[54] All oxygen- and moisture-sensitive compounds were synthesized in a nitrogen-filled glovebox.

4.5.2. Physical methods

UV-vis absorption spectra were recorded with an HP 8453A diode array spectrophotometer equipped with a cryostat from UNISOKU Scientific Instruments, Japan. All UV-vis absorption experiments were carried out in 1-cm path length cuvettes. Resonance Raman spectra on frozen samples of **1** (at 77 K) were obtained using a 135° back scattering arrangement. The collimated Raman scattering was collected using two Plano convex lenses (f = 12 cm, placed at an appropriate distance) through appropriate long pass edge filters (Semrock) into an Acton AM-506M3 monochromator equipped with a Princeton Instruments ACTON PyLON LN/CCD-1340x400

detector. The detector was cooled to -120 °C before the experiments. Spectral calibration was performed using the Raman spectrum of acetonitrile/toluene 50:50 (v:v).[212] Each spectrum was accumulated, typically 60 times with 5 s acquisition time, resulting in a total acquisition time of 5 min per spectrum. The collected data was processed using Spekwin32,[213] and a multi-point baseline correction was performed for all spectra. Elemental analyses were carried out by Atlantic Microlab (Norcross, GA). Electrospray ionization mass spectrometry (ESI-MS) experiments were performed on a Bruker BioTOF II mass spectrometer using a spray chamber voltage of 4000 V and a carrier gas temperature of 200 °C. Mass spectra were simulated using IsoPro 3.1 software.[228] IR spectra of **2** were recorded on a Nicolet iS5 FT-IR spectrometer with an ATR source. NMR spectra were recorded on a Bruker 400 MHz spectrometer at 298 K unless otherwise mentioned. Chemical shifts (in ppm) were referenced to the residual protic solvent peaks.

Synthesis of complex 1

To a solution of $[Fe^{II}(TQA)(CF_3SO_3)_2]$ (0.3 g, 10 mM) in CH_3CN in a nitrogen-filled glovebox was added NEt_3 dropwise until the solution turned dark red-purple. The solution was stirred overnight, passed through a syringe filter to remove any undissolved solids, and then placed in a diethyl ether bath in a freezer that is kept at 233 K to yield a purple solid. Anal. calcd. for **1**·$(OTf)_2$·CH_3CN·H_2O ($C_{64}H_{55}F_6Fe_2N_9O_9S_2$): C, 55.54; H, 4.01; N, 9.11. Found: C, 55.36; H, 3.94; N, 9.25. ^{1}H NMR (400 MHz, CD_3CN) δ = -60.5, -56.9, -43.5, -21.7, -2.7, 0.6, 1.1, 1.2, 3.1, 3.4, 7.0, 13.6, 23.4, 35.5, 58.8, 76.5, 126.7. UV-vis, CH_3CN: λ_{max}, nm (Ɛ, M^{-1} cm^{-1}), 505 (2000)

Synthesis of complex 2

To a 2 ml solution of **1** in CH_3CN (10 mM), excess NEt_3 (5 equiv) was added and the resultant solution was subjected to aerial oxidation when the dark red-purple color of **1** changed into brown yellow. This solution was passed through a syringe filter and then kept in a diethyl ether bath at 233 K overnight to yield yellow crystals suitable for X-ray diffraction. Anal. calcd. for **2**·$5H_2O$ ($C_{62}H_{56}F_6Fe_2N_8O_{12}S_2$): C, 52.70; H, 4.14; N, 7.93. Found: C, 52.75; H, 3.61; N, 7.99. ^{1}H NMR (400 MHz, CD_3CN) δ = 0.9, 1.3, 6.8, 7.3, 8.5, 9.1, 10.5, 12.0, 18.2, 20.8, 25.6, 30.4, 34.2, 68.4. UV-vis, CH_3CN: λ_{max}, nm (Ɛ, M^{-1} cm^{-1}), 380 (1500) and 470 (370)

4.6 Acknowledgments

I am thankful for grants from the U. S. National Institutes of Health (R01 GM-38767 and R35 GM-131721 to L.Q.) for support of this work. The Bruker Avance III HD nanobay 400 MHz NMR spectrometer used in this study was purchased from funds provided by the Office of the Vice President of Research, the College of Science and Engineering, and the Department of Chemistry at the University of Minnesota. I am grateful to have worked with immensely helpful collaborators like Shuangning Xu for help with Raman results, Dr. Waqas Rasheed for X-ray diffraction results. I would like to thank Prof. Steven Kass and Curtis Payne for the use of their FTIR spectrometer. I also must thank Yuan Sheng for helping me with TQA ligand in the preliminary stages of this project and later sharing his synthetic experience with a modified synthesis for TQA.

Chapter 5:

Summary and Future Perspectives

5.1 Thesis Summary

This thesis focuses on the generation, characterization, and reactivity of synthetic nonheme mono- and dinuclear complexes that mimic similar intermediates identified in nonheme iron-containing enzymes.

Chapter 2 introduces one of the most reactive mononuclear oxoiron(IV) models[229] and discusses the lack of understanding of its structure in solution. The only rationale for its high reactivity follows from DFT calculations.[230] Reaction condition optimizations and lowering of reaction temperature aided in increasing the stability of this high-valent complex. Furthermore, ^{1}H NMR spectroscopy is used to study the solution-state structure of this complex at temperatures as low as 193 K. This strategy also involves the use of synthesis and NMR study of related oxoiron(IV) complexes, which helps us assign most of the NMR signals in these complexes. One key achievement of our study in this chapter is presenting evidence that S = 1 iron(IV) centers can be as reactive as S = 2 iron(IV) centers. This is highly significant as all the biological oxoiron(IV) species have S = 2 centers[231] and it has been thought that the spin state is key to unlocking high reactivity in nonheme models.[232] Our study clearly shows that it is far more complicated than that, and more factors need to be considered before making structure-reactivity correlations. Lastly, our experimental results contradict theoretical calculations that have been put forward in the literature for this model.[229,230] This highlights the need to use better theoretical methods to accurately predict spin states of the iron(IV) centers in nonheme models. Notably, such studies are already underway through recent efforts of Comba et al.[233].

While chapter 2 focuses on mononuclear iron-oxo chemistry, chapters 3 and 4 focus on dinuclear iron-oxo chemistry. Chapter 3 describes the

development of a dinuclear system supported by the Me_3NTB ligand framework, the same ligand that supported the mononuclear oxoiron(IV) complex from chapter 2. It underscores the challenges of generating a diiron(II) precursor with this ligand and oxidation of the same using oxygen. Oxidation of the diiron(II) precursor leads to a peroxodiiron(III) complex, which is observed at cryogenic temperatures, and possess unusual properties compared to related models in the literature. Its short lifetime even at 233 K coupled with low O-O stretching frequency and a short diiron distance suggests that it is well-positioned to convert into a high-valent intermediate through appropriate strategies. The obvious strategy here is to model Nature and use protons to carry out O-O bond scission to generate reactive high-valent intermediates. Such attempts fail to generate high-valent intermediates with the Me_3NTB system. Moving away from protons, we decide to use redox-inactive metal ions as Lewis acids to achieve O-O bond scission, a strategy unprecedented in nonheme diiron model systems. Strong Lewis acids like scandium and aluminum triflates achieve the O-O bond scission to generate a high-valent bis-(μ-oxo)diiron(IV) complex. This is the first time such a complex has been generated from a peroxodiiron(III) species using oxygen as the oxidant.[227] This biomimetic approach is closely related to analogous processes in the diiron enzyme soluble methane monooxygenase. Spectroscopic characterization of this high-valent intermediate adds valuable structural data in the inventory of rare high-valent diiron compounds. This chemistry also represents the first example where the treatment of protons and Lewis acids yield significantly different results. Finally, the characterization of high-valent mono- and diiron complexes with the same nonheme ligand is achieved using results from chapters 2 and 3. This provides a rare opportunity to study their reactivities and better understand their roles in biology. Upon carrying out this exercise, we observe that the bis-(μ-

oxo)diiron(IV) complex is roughly ten million times less reactive than the mononuclear oxoiron(IV) complex supported by Me_3NTB ligand. This suggests that bridged oxo units are far less reactive than terminal oxos. This raises the question of what the actual structure of **Q** in **sMMO** is. Resonance Raman studies suggest the presence of bridging oxo units in **Q**[234,235] but X-ray absorption studies suggest an open core structure[235,236] containing terminal oxo units. The best conjecture is an equilibrium between a less reactive closed core **Q** and highly reactive open core **Q**, which is capable of cleaving unactivated C-H bonds in methane. The reactivity discrepancy between bridging and terminal oxo units in mono- and diiron models have also been observed in TPA* framework[237], although there is only a thousand-fold difference, which is much less drastic when compared to the Me_3NTB case.[227] In the same context, recent developments in nonheme cobalt chemistry have been very intriguing.[238–240] When the reactivities of mono- and dicobalt oxos are compared it is the bridging oxos that are more reactive than the terminal ones, although the supporting ligands are different in this comparison. More examples of mono- and dinuclear oxos using the same ligand will help us understand these trends better.

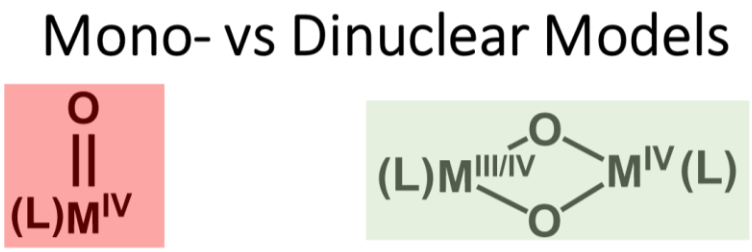

Ligand	Organic Substrate	C-H BDE (kcal/mol)	k_2 (M^{-1} s^{-1})	k_2 (M^{-1} s^{-1})	Ratio
Me_3NTB	1,3-CHD	78	940	0.0007	~ 10^7
TPA*	DHA	78	2	0.0016	~ 10^3
TPA based $Co_2^{III,IV}$	DHA	78	0.008 – 0.2	1.5 at 213 K	0.005< x <0.1

Figure 5.1. Comparison of the reactivity of high-valent mono- and dinuclear complexes that show opposite trends for iron-containing and cobalt-containing complexes. Please note that the ligands supporting mono- and dicobalt complexes are different, unlike the two iron-containing examples. Rate constants are extracted from these references [229,227,239,240,238].

Chapter 4 starts with a goal of understanding how spin-state plays a role in the reactivity of high-valent diiron models after results in chapter 2 confirmed that the spin-state is not the only determining factor in governing reactivity of high-valent monoiron models. This chapter introduces a quinoline rich TQA ligand framework, which supports *S* = 2 high-valent iron centers in mononuclear models[241,242] owing to the weak field nature of quinolines. Despite the success of this ligand in mononuclear oxoiron(IV) modeling, no attempts have been made to explore its diiron chemistry. We must pursue this because there is no report of a bis-(μ-oxo)diiron(IV) complex with *S* = 2 iron(IV) centers. Resonance Raman results show **sMMO-Q** to be a bis-(μ-oxo)diiron(IV) unit with *S* = 2 iron(IV) centers.[234,235]

So far, synthetic models of closed core **Q** have been sluggish oxidants[237] and have *S* = 1 iron(IV) centers. Incorporating *S* = 2 iron(IV) centers in these diiron models will help us understand whether the oxidation capability of closed core **Q** is strong enough to carry out methane oxidation in methanotrophs or open core **Q** is necessary. We have isolated the diiron(II) precursor of TQA and characterized it using multiple techniques. This allows comparison with other related diiron(II) complexes. Oxygen activation is found to be quite different than what has been observed for a similar diiron(II) precursor with the Me_3NTB system.[227] No peroxodiiron(III) species is observed with TQA under similar conditions. Upon moving to a different solvent and using a strong base, a peroxodiiron(III) species is observed in low yield that will need further exploration. Nonetheless, oxygen activation using TQA led us to isolate the first bis-(μ-oxo)diiron(III) complex using oxygen as the oxidant. The crystal structure of this complex revealed that it has the shortest Fe-O-Fe angle ever reported for (μ-oxo)diiron(III) complexes. More importantly, similar diiron cores have been implicated in the catalytic cycle of various diiron enzymes including **sMMO**.[243] The formation of this diiron(III) complex provides indirect evidence of the presence of the same Fe_2O_2 core in a higher-valent state, which may be observed at lower temperatures. Our results in this chapter provide a great foundation for a study to generate a rare bis-(μ-oxo)diiron(IV) complex with *S* = 2 iron(IV) centers.

5.2 Future Perspectives

Studies of mono- and diiron complexes with the same ligand Me_3NTB in chapters 2 and 3 represent a significant advance in bioinorganic chemistry. We tried to take it another step forward by employing TQA to explore diiron chemistry and compare it with its reported mononuclear chemistry. Even

though significant progress has been made through these efforts, many unanswered questions remain about these synthetic complexes.

One key direction to move forward with our results from chapter 2 would be to strategize ways to measure thermodynamic driving forces behind the reactivity of nonheme oxoiron(IV) models. This relationship is used to rationalize the reactivity of high-valent heme models, however, it has not been explored in detail for nonheme systems. Mayer and others have proposed that there exist thermodynamic driving forces behind HAT reactivity such as the strength of the O–H bond after HAT.[119] To achieve a better understanding of this factor, it will require a knowledge of both the $Fe^{IV/III}$ $E_{1/2}$ of the oxoiron(IV) complex, as well as the pKa of the resulting hydroxoiron(III) species. A big challenge is the instability of the nonheme $Fe^{III}O–H$ species that is formed after an oxoiron(IV) reacts with a C–H bond. Indeed, there are only a handful of these species even though there are close to a hundred model oxoiron(IV) complexes. Que group has recently reported a putative iron(III)-OH complex based on the TMC-Py framework.[244] Moreover, Goldberg[245] and Fout[246] have shown that intelligent ligand design can stabilize these complexes and provide us with important information. These developments encourage the bioinorganic community to follow these studies with more reports on nonheme $Fe^{III}O–H$ complexes. These complexes can be effectively utilized in a square scheme using Hess's law to experimentally measure the bond strengths. Indeed, Borovik has excellently utilized this strategy to measure the pK_a and the redox potential associated with the HAT reaction to calculate the O–H bond strengths of a $Fe^{III}O–H$ complex. Unfortunately, the related oxoiron(IV) model is not very reactive. Nonetheless, similar strategies may be used to synthesize a $Fe^{III}O–H$ complex supported by the Me_3NTB framework and then measure the corresponding O–H bond strength. By following similar routes

like Goldberg[245,247] and Fout[246], the plan should be to introduce secondary coordination sphere interactions on the benzimidazole rings that will stabilize the hydroxide bond in the proposed $Fe^{III}O$–H complex supported by a modified Me_3NTB framework. The secondary coordination sphere interactions will be introduced by synthesizing novel benzimidazole derivatives with hydrogen bonding donors from the aromatic ring. The synthons for these benzimidazoles can be either synthesized or purchased from commercial vendors. We expect these interactions will stabilize the hydroxide complex, allow us to measure the pK_a and the redox potential, which will then lead to the calculation of the O-H bond strength (See figure 5.2 below). A caveat to this strategy is the possibility that we are significantly changing the oxidizing power of the parent model, thus it would be necessary to carry out substrate reactivity studies with the modified oxoiron(IV) complex.

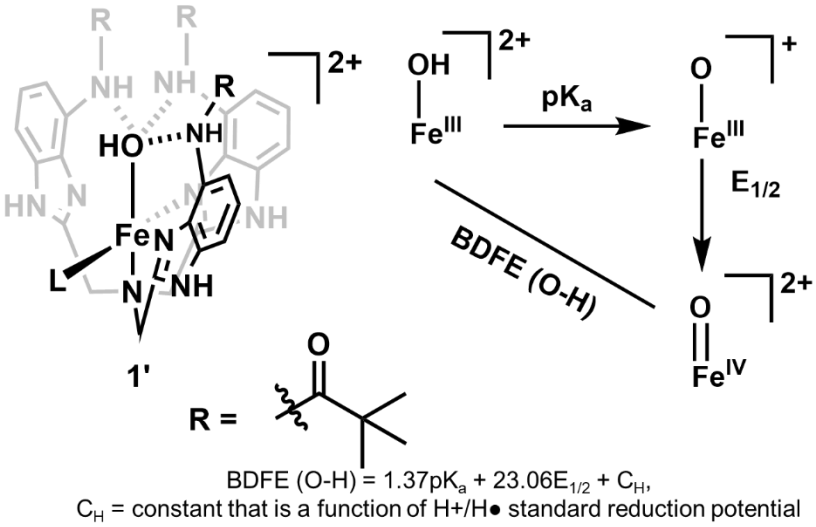

Figure 5.2. A proposed strategy of stabilizing a hydroxoiron(III) complex and measuring the O-H bond strength for shedding light on thermodynamic factors behind HAT reactivity.

Next, our results in chapter 2 show that serious review is needed to update the theoretical methods used to predict spin states of oxoiron(IV)

complexes. Comba et al. have already shown inconsistencies between experimental and traditional DFT predictions in their latest work.[233] A collaboration of experimental and theoretical chemists such as Prof. Marcel Swart will be necessary to achieve a harmony between theory and experiments for structure-reactivity correlations in nonheme iron-oxygen chemistry.

Another productive extension of our results would be to expand the reactivity of $[(Me_3NTB)Fe^{IV}(O)(CH_3CN)]^{2+}$ beyond stoichiometric oxidations and attempt to carry out catalytic reactions. While enzymatic oxoiron(IV) species are often implicated in biological catalysis, synthetic oxoiron(IV) models have fallen short in this department. Recent developments by Ray and his group in Berlin have demonstrated a rare study of an oxoiron(IV) model performing catalytic reactions using H_2O_2 or iodosylbenzene derivatives as oxidants.[248] Similar strategies must be explored with the Me_3NTB system and explore whether its high reactivity in stoichiometric reactions can be transferred to catalytic reactions.

Our diiron results in chapter 3 open the door for utilizing Lewis acids to break the O-O bond in peroxodiiron(III) complexes. Understanding O-O bond scission and how that may generate high-valent diiron intermediates will take us closer to modeling biologicals systems. In that context, reported peroxodiiron(III) intermediates supported by diverse frameworks must be treated with strong Lewis acids and the resulting intermediates studied. The discrepancy between the number of reported peroxodiiron(III) models and high-valent oxodiiron models is significant, mostly because of the lack of understanding of the O-O bond breaking that can generate high-valent species. Our Lewis acid-mediated O-O bond scission and generation of the first bis-(μ-oxo)diiron(IV) complex using oxygen as the oxidant provides a

way to test similar chemistry with other established systems. These can include but are not limited to N-EtHPTB, TPA*, BQPA, BnBQA, and 6Me$_3$TPA. More specifically, BnBQA and 6Me$_3$TPA systems will enforce *S* = 2 iron centers, which have the potential to generate reactive species. Our results in this chapter also highlight the difference in reactivity between bridging oxos and terminal oxos in high-valent iron chemistry. The comparison is simpler as the same ligand is used to support mono- and diiron systems in chapters 2 and 3. This is only the second time that this feat is achieved in the literature. To further extend these correlations, other ligands can be explored that can support both mono- and dinuclear oxidants. This is especially necessary as opposite trends in reactivity are observed for cobalt-based high-valent complexes.[238–240]

The discovery of only the second nonheme ligand that can support a bis-(μ-oxo)diiron(IV) complex in chapter 3 demands attempts to synthesize open core versions of this complex. Similar studies have been successful with TPA* ligand where the addition of F^- and OH^- successfully generated reactive open core diiron(IV) complexes.[237] Along the same lines, we can use appropriate reductants to achieve 1-e^- reduction of the diiron(IV) complex to generate mixed valent diiron(III,IV) species, which will mimic similar intermediates found in the class 1A **RNR R2** enzyme.[243]

Relevant to our results in chapter 4, progress needs to be made on the foundation of the diiron chemistry of the TQA ligand framework. This will involve characterizing the diiron(II) complex with X-ray diffraction, which will add important structural information and enable comparison with similar complexes supported by related systems. Oxygen activation in acetonitrile has been shown to generate a biologically relevant bis-(μ-oxo)diiron(III) complex with TQA. Our results can be used to isolate similar

complexes with other ligand frameworks. This will be very useful for the bioinorganic community as there exist only two examples of bis-(μ-oxo)diiron(III) complexes and increasing this number will enhance our understanding of this motif that is critical in enzymes. Next, isolation of a bis-(μ-oxo)diiron(III) complex allows us to generate high-valent diiron intermediates using electrochemical methods and appropriate 1-e^- oxidizing agents. Similar studies have been reported for $6Me_3TPA$ ligand framework[249] and can be attempted with TQA framework. We have been successful in changing conditions to observe fleeting intermediates in the oxygen activation of this framework. Unfortunately, the yield of the peroxodiiron(III) species is low (~25%) and not ideal for spectroscopic and reactivity studies. More reaction conditions should be explored to increase the yield of the peroxodiiron(III) intermediate and utilize O-O bond scission lessons from chapter 3 to generate high-valent diiron intermediates.

I wish the best of luck to future scientists who decide to explore these challenges, and I hope that my results guide them in their explorations.

References

[1] J. M. Lippard, S. J.; Berg, University Science Books, Mill Valley, California, **1994**.

[2] R. M. Roat-Malone, *Bioinorganic Chemistry: A Short Course*, John Wiley And Sons, Hoboken, NJ, USA, **2007**.

[3] D. C. Rees, *Annu. Rev. Biochem.* **2002**, *71*, 221–246.

[4] J. T. Groves, *Proc. Natl. Acad. Sci. U. S. A.* **2003**, *100*, 3569–3574.

[5] M. A. Greenough, J. Camakaris, A. I. Bush, *Neurochem. Int.* **2013**, *62*, 540–555.

[6] M. Costas, M. P. Mehn, M. P. Jensen, L. Que, *Chem. Rev.* **2004**, *104*, 939–86.

[7] A. R. McDonald, L. Que, *Coord. Chem. Rev.* **2013**, *257*, 414–428.

[8] S. Kal, L. Que, *J. Biol. Inorg. Chem.* **2017**, *22*, 339–365.

[9] C. Krebs, D. Galonić Fujimori, C. T. Walsh, J. M. Bollinger, D. G. Fujimori, C. T. Walsh, J. M. Bollinger, *Acc. Chem. Res.* **2007**, *40*, 484–92.

[10] J. C. Price, E. W. Barr, B. Tirupati, J. M. Bollinger, C. Krebs, *Biochemistry* **2003**, *42*, 7497–7508.

[11] P. J. Riggs-Gelasco, J. C. Price, R. B. Guyer, J. H. Brehm, E. W. Barr, J. M. Bollinger, C. Krebs, *J. Am. Chem. Soc.* **2004**, *126*, 8108–8109.

[12] D. A. Proshlyakov, T. F. Henshaw, G. R. Monterosso, M. J. Ryle, R. P. Hausinger, *J. Am. Chem. Soc.* **2004**, *126*, 1022–1023.

[13] D. P. Galonić, E. W. Barr, C. T. Walsh, J. M. Bollinger, C. Krebs, *Nat. Chem. Biol.* **2007**, *3*, 113–116.

[14] M. L. Matthews, C. M. Krest, E. W. Barr, F. H. Vaillancourt, C. T. Walsh, M. T. Green, C. Krebs, J. M. Bollinger, *Biochemistry* **2009**, *48*, 4331–4343.

[15] A. J. Panay, M. Lee, C. Krebs, J. M. Bollinger, P. F. Fitzpatrick, *Biochemistry* **2011**, *50*, 1928–1933.

[16] W. C. Chang, Y. Guo, C. Wang, S. E. Butch, A. C. Rosenzweig, A. K. Boal, C. Krebs, J. M. Bollinger, *Science* **2014**, *343*, 1140–1144.

[17] L. M. Hoffart, E. W. Barr, R. B. Guyer, J. M. Bollinger, C. Krebs, *Proc. Natl. Acad. Sci. U. S. A.* **2006**, *103*, 14738–14743.

[18] B. E. Eser, E. W. Barr, P. A. Frantom, L. Saleh, J. M. Bollinger, C. Krebs, P. F. Fitzpatrick, *J. Am. Chem. Soc.* **2007**, *129*, 11334–5.

[19] C. Krebs, J. C. Price, J. Baldwin, L. Saleh, M. T. Green, J. M. Bollinger, *Inorg. Chem.* **2005**, *44*, 742–757.

[20] S. Sinnecker, N. Svensen, E. W. Barr, S. Ye, J. M. Bollinger, F. Neese, C. Krebs, J. M. Bollinger, F. Neese, C. Krebs, *J. Am. Chem. Soc.* **2007**, *129*, 6168–6179.

[21] J. M. Bollinger, J. C. Price, L. M. Hoffart, E. W. Barr, C. Krebs, *Eur. J. Inorg. Chem.* **2005**, *2005*, 4245–4254.

[22] J. C. Price, E. W. Barr, T. E. Glass, C. Krebs, J. M. Bollinger, *J. Am. Chem. Soc.* **2003**, *125*, 13008–9.

[23] J. M. Bollinger, C. Krebs, *J. Inorg. Biochem.* **2006**, *100*, 586–605.

[24] L. C. Blasiak, F. H. Vaillancourt, C. T. Walsh, C. L. Drennan, *Nature* **2006**, *440*, 368–371.

[25] C. Wong, D. G. Fujimori, C. T. Walsh, C. L. Drennan, *J. Am. Chem. Soc.* **2009**, *131*, 4872–4879.

[26] D. Khare, B. Wang, L. Gu, J. Razelun, D. H. Sherman, W. H. Gerwick, K. Håkansson, J. L. Smith, *Proc. Natl. Acad. Sci. U. S. A.* **2010**, *107*, 14099–14104.

[27] A. Busche, D. Gottstein, C. Hein, N. Ripin, I. Pader, P. Tufar, E. B. Eisman, L. Gu, C. T. Walsh, D. H. Sherman, F. Löhr, P. Güntert, V. Dötsch, *ACS Chem. Biol.* **2012**, *7*, 378–386.

[28] A. J. Mitchell, Q. Zhu, A. O. Maggiolo, N. R. Ananth, M. L. Hillwig, X. Liu, A. K. Boal, *Nat. Chem. Biol.* **2016**, *12*, 636–640.

[29] J. Fauvarque, *Pure Appl. Chem.* **1996**, *68*, 1713.

[30] S. Stavber, M. Jereb, M. Zupan, *Synthesis* **2008**, *2008*, 1487–1513.

[31] D. G. Fujimori, E. W. Barr, M. L. Matthews, G. M. Koch, J. R. Yonce, C. T. Walsh, J. M. Bollinger, C. Krebs, P. J. Riggs-Gelasco, *J. Am. Chem. Soc.* **2007**, *129*, 13408–13409.

[32] S. D. Wong, M. Srnec, M. L. Matthews, L. V. Liu, Y. Kwak, K. Park, C. B. Bell, E. E. Alp, J. Zhao, Y. Yoda, S. Kitao, M. Seto, C. Krebs, J. M. Bollinger, E. I. Solomon, *Nature* **2013**, *499*, 320–3.

[33] M. Srnec, S. D. Wong, M. L. Matthews, C. Krebs, J. M. Bollinger, E. I. Solomon, *J. Am. Chem. Soc.* **2016**, *138*, 5110–5122.

[34] T. Borowski, H. Noack, M. Radoń, K. Zych, P. E. M. Siegbahn, *J. Am. Chem. Soc.* **2010**, *132*, 12887–12898.

[35] O. A. Andersen, A. J. Stokka, T. Flatmark, E. Hough, *J. Mol. Biol.* **2003**, *333*, 747–757.

[36] A. J. Panay, P. F. Fitzpatrick, *J. Am. Chem. Soc.* **2010**, *132*, 5584–5585.

[37] J. U. Rohde, J. H. In, M. H. Lim, W. W. Brennessel, M. R. Bukowski, A. Stubna, E. Münck, W. Nam, L. Que, *Science* **2003**, *299*, 1037–1039.

[38] J. E. M. N. Klein, L. Que, *Encycl. Inorg. Bioinorg. Chem.* **2016**, DOI 10.1002/9781119951438.eibc2344.

[39] D. Janardanan, Y. Wang, P. Schyman, L. Que, S. Shaik, *Angew. Chem. Int. Ed.* **2010**, *49*, 3342–3345.

[40] M. Hee Lim, J.-U. U. Rohde, A. Stubna, M. R. Bukowski, M. Costas, R. Y. N. N. Ho, E. Münck, W. Nam, L. Que, M. H. Lim, J.-U. U. Rohde, A. Stubna, M. R. Bukowski, M. Costas, R. Y. N. N. Ho, E. Munck, W. Nam, L. Que, *Proc. Natl. Acad. Sci. U. S. A.* **2003**, *100*, 3665–70.

[41] J.-U. Rohde, A. Stubna, E. L. Bominaar, E. Münck, W. Nam, L. Que, *Inorg. Chem.* **2006**, *45*, 6435–45.

[42] A. Decker, J.-U. Rohde, Que Lawrence, E. I. Solomon, *J. Am. Chem. Soc.* **2004**, *126*, 5378–5379.

[43] A. Decker, J. U. Rohde, E. J. Klinker, S. D. Wong, L. Que, E. I. Solomon, *J. Am. Chem. Soc.* **2007**, *129*, 15983–15996.

[44] T. K. Paine, M. Costas, J. Kaizer, L. Que, *J. Biol. Inorg. Chem. JBIC Publ. Soc. Biol. Inorg. Chem.* **2006**, *11*, 272–6.

[45] H. Hirao, D. Kumar, L. Que,, S. Shaik, *J. Am. Chem. Soc.* **2006**, *128*, 8590–8606.

[46] M. Puri, L. Que, *Acc. Chem. Res.* **2015**, *48*, 2443–52.

[47] O. Pestovsky, A. Bakac, *J. Am. Chem. Soc.* **2004**, *126*, 13757–13764.

[48] O. Pestovsky, S. Stoian, E. L. Bominaar, X. Shan, E. Münck, L. Que, A. Bakac, *Angew. Chem. Int. Ed.* **2005**, *44*, 6871–6874.

[49] J. England, M. Martinho, E. R. Farquhar, J. R. Frisch, E. L. Bominaar, E. Münck, L. Que, *Angew. Chem. - Int. Ed.* **2009**, *48*, 3622–3626.

[50] D. C. Lacy, R. Gupta, K. L. Stone, J. Greaves, J. W. Ziller, M. P. Hendrich, A. S. Borovik, *J. Am. Chem. Soc.* **2010**, *132*, 12188–90.

[51] J. P. Bigi, W. H. Harman, B. Lassalle-Kaiser, D. M. Robles, T. A. Stich, J. Yano, R. D. Britt, C. J. Chang, *J. Am. Chem. Soc.* **2012**, *134*, 1536–42.

[52] J. England, Y. Guo, K. M. Van Heuvelen, M. A. Cranswick, G. T. Rohde, E. L. Bominaar, E. Münck, L. Que, *J. Am. Chem. Soc.* **2011**, *133*, 11880–11883.

[53] J. England, Y. Guo, E. R. Farquhar, V. G. Young Jr., E. Münck, L. Que Jr., *J. Am. Chem. Soc.* **2010**, *132*, 8635–8644.

[54] A. N. Biswas, M. Puri, K. K. Meier, W. N. Oloo, G. T. Rohde, E. L. Bominaar, E. Münck, L. Que, *J. Am. Chem. Soc.* **2015**, *137*, 2428–2431.

[55] S. Shaik, H. Hirao, D. Kumar, *Acc. Chem. Res.* **2007**, *40*, 532–542.

[56] G. Xue, R. De Hont, E. Münck, L. Que, *Nat. Chem.* **2010**, *2*, 400–405.

[57] M. S. Seo, N. H. Kim, K. Bin Cho, J. E. So, S. K. Park, M. Clémancey, R. Garcia-Serres, J. M. Latour, S. Shaik, W. Nam, *Chem. Sci.* **2011**, *2*, 1039–1045.

[58] S. H. Bae, M. S. Seo, Y. M. Lee, K. B. Cho, W. S. Kim, W. Nam, *Angew Chem Int Ed* **2016**, *55*, 8027–8031.

[59] N. Y. Lee, D. Mandal, S. H. Bae, M. S. Seo, Y.-M. Lee, S. Shaik, K.-B. Cho, W. Nam, *Chem. Sci.* **2017**, *8*, 5460–5467.

[60] L. Que, *Physical Methods in Bioinorganic Chemistry: Spectroscopy and Magnetism*, University Science Books, Sausalito, Calif., **2000**.

[61] Y. Zang, J. Kim, Y. Dong, E. C. Wilkinson, E. H. Appelman, L. Que, *J. Am. Chem. Soc.* **1997**, *119*, 4197–4205.

[62] E. J. Klinker, J. Kaizer, W. W. Brennessel, N. L. Woodrum, C. J. Cramer, L. Que, *Angew. Chem Int. Ed.* **2005**, *44*, 3690–3694.

[63] E. A. Duban, K. P. Bryliakov, E. P. Talsi, *Eur. J. Inorg. Chem.* **2007**, *2007*, 852–857.

[64] Y. M. Lee, H. Kotani, T. Suenobu, W. Nam, S. Fukuzumi, *J. Am. Chem. Soc.* **2008**, *130*, 434–435.

[65] J. Prakash, G. T. Rohde, K. K. Meier, E. Münck, L. Que, *Inorg. Chem.* **2015**, *54*, 11055–11057.

[66] B. J. Wallar, J. D. Lipscomb, *Chem. Rev.* **1996**, *96*, 2625–2658.

[67] A. J. Jasniewski, L. Que, *Chem. Rev.* **2018**, *118*, 2554–2592.

[68] R. Banerjee, J. C. Jones, J. D. Lipscomb, *Annu. Rev. Biochem.* **2019**, *88*, 409–431.

[69] R. S. Hanson, T. E. Hanson, *Microbiol. Mol. Biol. Rev.* **1996**, *60*.

[70] J. D. Lipscomb, *Annu. Rev. Microbiol.* **1994**, *48*, 371–399.

[71] P. Nordlund, P. Reichard, *Annu. Rev. Biochem.* **2006**, *75*, 681–706.

[72] E. Torrents, *Front. Cell. Infect. Microbiol.* **2014**, *4*, DOI 10.3389/fcimb.2014.00052.

[73] A. T. Fiedler, X. Shan, M. P. Mehn, J. Kaizer, S. Torelli, J. R. Frisch, M. Kodera, L. Que, *J. Phys. Chem. A* **2008**, *112*, 13037–13044.

[74] C. E. Tinberg, S. J. Lippard, *Biochemistry* **2009**, *48*, 12145–12158.

[75] S. K. Lee, J. D. Lipscomb, *Biochemistry* **1999**, *38*, 4423–4432.

[76] S. K. Lee, W. A. Froland, J. D. Lipscomb, B. G. Fox, E. Münck, *J. Am. Chem. Soc.* **1993**, *115*, 6450–6451.

[77] R. Banerjee, Y. Proshlyakov, J. D. Lipscomb, D. A. Proshlyakov, *Nature* **2015**, *518*, 431–434.

[78] E. C. Wilkinson, *J. Am. Chem. Soc.* **1998**, *120*, 955–962.

[79] L. Shu, J. C. Nesheim, K. Kauffmann, E. Münck, J. D. Lipscomb, L. Que, *Science* **1997**, *275*, 515–518.

[80] G. E. Cutsail, R. Banerjee, A. Zhou, L. Que, J. D. Lipscomb, S. Debeer, *J. Am. Chem. Soc.* **2018**, *140*, 16807–16820.

[81] J. C. Nesheim, J. D. Lipscomb, *Biochemistry* **1996**, *35*, 10240–10247.

[82] B. J. Brazeau, B. J. Wallar, J. D. Lipscomb, *J. Am. Chem. Soc.* **2001**, *123*, 10421–10422.

[83] J. T. Groves, *J. Inorg. Biochem.* **2006**, *100*, 434–447.

[84] J. Baldwin, C. Krebs, L. Saleh, M. Stelling, B. H. Huynh, J. M. Bollinger, P. Riggs-Gelasco, *Biochemistry* **2003**, *42*, 13269–13279.

[85] P. Moënne-Loccoz, J. Baldwin, B. A. Ley, T. M. Loehr, J. M. Bollinger, *Biochemistry* **1998**, *37*, 14659–14663.

[86] W. H. Tong, S. Chen, S. G. Lloyd, D. E. Edmondson, B. H. Huynh, J. Stubbe, *J. Am. Chem. Soc.* **1996**, *118*, 2107–2108.

[87] D. Burdi, J. P. Willems, P. Riggs-Gelasco, W. E. Antholine, J. Stubbe, B. M. Hoffman, *J. Am. Chem. Soc.* **1998**, *120*, 12910–12919.

[88] B. E. Sturgeon, D. Burdi, S. Chen, B. H. Huynh, D. E. Edmondson, J. A. Stubbe, B. M. Hoffman, *J. Am. Chem. Soc.* **1996**, *118*, 7551–7557.

[89] J. A. Cotruvo, J. Stubbe, *Annu. Rev. Biochem.* **2011**, *80*, 733–767.

[90] L. M. K. Dassama, A. Silakov, C. M. Krest, J. C. Calixto, C. Krebs, J. M. Bollinger, M. T. Green, *J. Am. Chem. Soc.* **2013**, *135*, 16758–16761.

[91] N. Mitić, M. D. Clay, L. Saleh, J. M. Bollinger,, E. I. Solomon, *J. Am. Chem. Soc.* **2007**, *129*, 9049–9065.

[92] P. E. Doan, M. Shanmugam, J. Stubbe, B. M. Hoffman, *J. Am. Chem. Soc.* **2015**, *137*, 15558–15566.

[93] M. Sekino, H. Furutachi, R. Tojo, A. Hishi, H. Kajikawa, T. Suzuki, K. Suzuki, S. Fujinami, S. Akine, Y. Sakata, T. Ohta, S. Hayami, M. Suzuki, *Chem. Commun.* **2017**, *53*, 8838–8841.

[94] X. Zhang, H. Furutachi, S. Fujinami, S. Nagatomo, Y. Maeda, Y. Watanabe, T. Kitagawa, M. Suzuki, *J. Am. Chem. Soc.* **2005**, *127*, 826–827.

[95] P. Moënne-Loccoz, J. Baldwin, B. A. Ley, T. M. Loehr, J. M. Bollinger, *Biochemistry* **1998**, *37*, 14659–14663.

[96] A. Ghosh, F. T. De Oliveira, T. Yano, T. Nishioka, E. S. Beach, I. Kinoshita, E. Münck, A. D. Ryabov, C. P. Horwitz, T. J. Collins, *J. Am. Chem. Soc.* **2005**, *127*, 2505–2513.

[97] G. Xue, D. Wang, R. De Hont, A. T. Fiedler, X. Shan, E. Munck, L. Que, *Proc. Natl. Acad. Sci.* **2007**, *104*, 20713–20718.

[98] G. Xue, A. T. Fiedler, M. Martinho, E. Münck, L. Que, *Proc. Natl. Acad. Sci.* **2008**, *105*, 20615–20620.

[99] L. Q. Jr, W. B. Tolman, *Angew. Chem. Int. Ed.* **2002**, *41*, 1114–1137.

[100] Y. Dong, Y. Zang, L. Shu, E. C. Wilkinson, L. Que, K. Kauffmann, E. Münck, *J. Am. Chem. Soc.* **1997**, *119*, 12683–12684.

[101] M. A. Cranswick, K. K. Meier, X. Shan, A. Stubna, J. Kaizer, M. P. Mehn, E. Münck, L. Que, *Inorg. Chem.* **2012**, *51*, 10417–10426.

[102] M. Kodera, Y. Kawahara, Y. Hitomi, T. Nomura, T. Ogura, Y. Kobayashi, *J. Am. Chem. Soc.* **2012**, *134*, 13236–13239.

[103] C. Krebs, D. G. Fujimori, C. T. Walsh, J. M. Bollinger, *Acc. Chem. Res.* **2007**, *40*, 484–492.

[104] J. C. Price, E. W. Barr, B. Tirupati, J. M. Bollinger, C. Krebs, *Biochemistry* **2003**, *42*, 7497–508.

[105] E. Eichhorn, J. R. Van Der Ploeg, M. A. Kertesz, T. Leisinger, *J. Biol. Chem.* **1997**, *272*, 23031–23036.

[106] X. Engelmann, I. Monte-Pérez, K. Ray, *Angew Chem Int Ed* **2016**, *55*, 7632–7649.

[107] M. Puri, L. Que, *Acc. Chem. Res.* **2015**, *48*, 2443–2452.

[108] S. H. Bae, M. S. Seo, Y. M. Lee, K. Bin Cho, W. S. Kim, W. Nam, *Angew Chem Int Ed* **2016**, *55*, 8027–8031.

[109] A. Decker, J. U. Rohde, E. J. Klinker, S. D. Wong, L. Que, E. I. Solomon, *J. Am. Chem. Soc.* **2007**, *129*, 15983–15996.

[110] Y. Dong, S. Yan, V. G. Young, L. Que, *Angew. Chem. Int. Ed. Engl.* **1996**, *35*, 618–620.

[111] W. Rasheed, A. Draksharapu, S. Banerjee, V. G. Young Jr, R. Fan, Y. Guo, M. Ozerov, J. Nehrkorn, J. Krzystek, J. Telser, L. Que, *Angew Chem Int Ed* **2018**, *57*, 9387–9391.

[112] B. Kwak, K. Woong Cho, M. Pyo, M. Soo Lah, *Inorganica Chim. Acta* **1999**, *290*, 21–27.

[113] E. J. Klinker, J. Kaizer, W. W. Brennessel, N. L. Woodrum, C. J. Cramer, L. Que, *Angew. Chem Int. Ed.* **2005**, *44*, 3690–3694.

[114] E. A. Duban, K. P. Bryliakov, E. P. Talsi, *Eur. J. Inorg. Chem.* **2007**, *2007*, 852–857.

[115] Y. M. Lee, H. Kotani, T. Suenobu, W. Nam, S. Fukuzumi, *J. Am. Chem. Soc.* **2008**, *130*, 434–435.

[116] J. Prakash, G. T. Rohde, K. K. Meier, E. Münck, L. Que, *Inorg. Chem.* **2015**, *54*, 11055–11057.

[117] M. Mitra, H. Nimir, S. Demeshko, S. S. Bhat, S. O. Malinkin, M. Haukka, J. Lloret-Fillol, G. C. Lisensky, F. Meyer, A. A. Shteinman, W. R. Browne, D. A. Hrovat, M. G. Richmond, M. Costas, E. Nordlander, *Inorg. Chem.* **2015**, *54*, 7152–7164.

[118] A. Borgogno, F. Rastrelli, A. Bagno, *Chem Eur J* **2015**, *21*, 12960–12970.

[119] C. T. Saouma, J. M. Mayer, *Chem. Sci.* **2014**, *5*, 21–31.

[120] F. G. Bordwell, *Acc. Chem. Res.* **1988**, *21*, 456–463.

[121] K. A. Gardner, J. M. Mayer, *Science* **1995**, *269*, 1849–1851.

[122] J. M. Mayer, *Acc. Chem. Res.* **1998**, *31*, 441–450.

[123] J. P. Roth, J. C. Yoder, T. J. Won, J. M. Mayer, *Science* **2001**, *294*, 2524–2526.

[124] J. M. Mayer, *Acc. Chem. Res.* **2011**, *44*, 36–46.

[125] D. C. Lacy, Ph.D. Thesis, University of California—Irvine, Irvine, CA, **2012**.

[126] D. Usharani, D. C. Lacy, A. S. Borovik, S. Shaik, *J. Am. Chem. Soc.* **2013**, *135*, 17090–17104.

[127] X. Wang, S. Peter, M. Kinne, M. Hofrichter, J. T. Groves, *J. Am. Chem. Soc.* **2012**, *134*, 12897–12900.

[128] J. Serrano-Plana, W. N. Oloo, L. Acosta-Rueda, K. K. Meier, B. Verdejo, E. García-España, M. G. Basallote, E. Münck, L. Que, A. Company, M. Costas, *J. Am. Chem. Soc.* **2015**, *137*, 15833–15842.

[129] J. Kaizer, E. J. Klinker, N. Y. Oh, J.-U. Rohde, W. J. Song, A. Stubna, J. Kim, E. Münck, W. Nam, L. Que, *J. Am. Chem. Soc.* **2004**, *126*, 472–3.

[130] K. A. Gardner, L. L. Kuehnert, J. M. Mayer, *Inorg. Chem.* **1997**, *36*, 2069–2078.

[131] S. Korcek, J. H. B. Chenier, J. A. Howard, K. U. Ingold, *Can. J. Chem.* **1976**, *50*, 2285–2297.

[132] I. W. C. E. Arends, P. Mulder, K. B. Clark, D. D. M. Wayner, *J. Phys. Chem.* **1995**, *99*, 8182–8189.

[133] L. M. Dorfman, I. A. Taub, D. A. Harter, *J. Chem. Phys.* **1964**, *41*, 2954–2955.

[134] X. Wang, R. Ullrich, M. Hofrichter, J. T. Groves, *Proc. Natl. Acad. Sci.* **2015**, *112*, 3686–3691.

[135] D. Macikenas, E. Skrzypczak-Jankun, J. D. Protasiewicz, *J. Am. Chem. Soc.* **2011**, *133*, 4151–4151.

[136] D. Macikenas, E. Skrzypczak-Jankun, J. D. Protasiewicz, *J. Am. Chem. Soc.* **1999**, *121*, 7164–7165.

[137] L. K. Thompson, B. S. Ramaswamy, E. A. Seymour, *Can. J. Chem.* **1977**, *55*, 878–888.

[138] B.-T. Chen, N. Morlanés, E. Adogla, K. Takanabe, V. O. Rodionov, *ACS Catal.* **2016**, *6*, 4647–4652.

[139] K. S. Hagen, *Inorg. Chem.* **2000**, *39*, 5867–5869.

[140] G. N. George, **2000**.

[141] A. Ankudinov, B. Ravel, *Phys. Rev. B - Condens. Matter Mater. Phys.* **1998**, *58*, 7565–7576.

[142] M. Wojdyr, *J. Appl. Crystallogr.* **2010**, *43*, 1126–1128.

[143] D. T. Petasis, M. P. Hendrich, *Methods Enzymol.* **2015**, *563*, 171–208.

[144] F. Rastrelli, A. Bagno, *Chem. - Eur. J.* **2009**, *15*, 7990–8004.

[145] F. Rastrelli, A. Bagno, *Magn. Reson. Chem.* **2010**, *48*, DOI 10.1002/mrc.2666.

[146] A. Borgogno, F. Rastrelli, A. Bagno, *Dalton Trans.* **2014**, *43*, 9486–9496.

[147] M. Reiher, *Inorg. Chem.* **2002**, *41*, 6928–6935.

[148] J. R. Frisch, V. V. Vu, M. Martinho, E. Münck, L. Que, *Inorg. Chem.* **2009**, *48*, 8325–8336.

[149] I. Bertini, C. Luchinat, G. Parigi, *Solution NMR of Paramagnetic Molecules: Applications to Metallobiomolecules and Models*, Elsevier, **2001**.

[150] I. Bertini, C. Luchinat, G. Parigi, *Prog. Nucl. Magn. Reson. Spectrosc.* **2002**, *40*, 249–273.

[151] P. Hrobárik, R. Reviakine, A. V. Arbuznikov, O. L. Malkina, V. G. Malkin, F. H. Köhler, M. Kaupp, *J. Chem. Phys.* **2007**, *126*, 24107.

[152] A. Trehoux, J. P. Mahy, F. Avenier, *Coord. Chem. Rev.* **2016**, *322*, 142–158.

[153] S. K. Lee, J. C. Nesheim, J. D. Lipscomb, *J. Biol. Chem.* **1993**, *268*, 21569–21577.

[154] K. E. Liu, A. M. Valentine, A. Salifoglou, S. J. Lippard, D. Wang, B. H. Huynh, D. E. Edmondson, *J. Am. Chem. Soc.* **1995**, *117*, 10174–10185.

[155] P. Moënne-Loccoz, J. Baldwin, B. A. Ley, T. M. Loehr, J. M. Bollinger, *Biochemistry* **1998**, *37*, 14659–14663.

[156] J. A. Broadwater, J. Ai, T. M. Loehr, J. Sanders-Loehr, B. G. Fox, *Biochemistry* **1998**, *37*, 14664–14671.

[157] J. A. Broadwater, C. Achim, E. Münck, B. G. Fox, *Biochemistry* **1999**, *38*, 12197–12204.

[158] V. V. Vu, J. P. Emerson, M. Martinho, S. K. Yeon, E. Münck, H. P. Myung, L. Que, *Proc. Natl. Acad. Sci. U. S. A.* **2009**, *106*, 14814–14819.

[159] Z. Han, N. Sakai, L. H. Böttger, S. Klinke, J. Hauber, A. X. Trautwein, R. Hilgenfeld, *Structure* **2015**, *23*, 882–892.

[160] A. J. Jasniewski, L. M. Engstrom, V. V. Vu, M. H. Park, L. Que, *J. Biol. Inorg. Chem.* **2016**, *21*, 605–618.

[161] C. E. Tinberg, S. J. Lippard, *Biochemistry* **2009**, *48*, 12145–12158.

[162] E. Y. Tshuva, S. J. Lippard, *Chem. Rev.* **2004**, *104*, 987–1012.

[163] Y. Dong, S. Ménage, B. A. Brennan, T. E. Elgren, H. G. Jang, L. L. Pearce, L. Que, *J. Am. Chem. Soc.* **1993**, *115*, 1851–1859.

[164] T. Ookubo, H. Sugimoto, T. Nagayama, H. Masuda, T. Sato, K. Tanaka, Y. Maeda, H. Okawa, Y. Hayashi, A. Uehara, M. Suzuki, *J. Am. Chem. Soc.* **1996**, *118*, 701–702.

[165] M. Yamashita, H. Furutachi, T. Tosha, S. Fujinami, W. Saito, Y. Maeda, K. Takahashi, K. Tanaka, T. Kitagawa, M. Suzuki, *J. Am. Chem. Soc.* **2007**, *129*, 2–3.

[166] J. S. Pap, A. Draksharapu, M. Giorgi, W. R. Browne, J. Kaizer, G. Speier, *Chem. Commun.* **2014**, *50*, 1326–1329.

[167] f

[168] I. Kaljurand, A. Kütt, L. Sooväli, T. Rodima, V. Mäemets, I. Leito, I. A. Koppel, *J. Org. Chem.* **2005**, *70*, 1019–1028.

[169] X. Zhang, H. Furutachi, S. Fujinami, S. Nagatomo, Y. Maeda, Y. Watanabe, T. Kitagawa, M. Suzuki, *J. Am. Chem. Soc.* **2005**, *127*, 826–827.

[170] J. S. Pap, M. A. Cranswick, É. Balogh-Hergovich, G. Baráth, M. Giorgi, G. T. Rohde, J. Kaizer, G. Speier, L. Que, *Eur. J. Inorg. Chem.* **2013**, *2013*, 3858–3866.

[171] M. Kodera, Y. Taniike, M. Itoh, Y. Tanahashi, H. Shimakoshi, K. Kano, S. Hirota, S. Iijima, M. Ohba, H. Okawa, *Inorg. Chem.* **2001**, *40*, 4821–4822.

[172] M. Kodera, S. Ishiga, T. Tsuji, K. Sakurai, Y. Hitomi, Y. Shiota, P. K. Sajith, K. Yoshizawa, K. Mieda, T. Ogura, *Chem. - Eur. J.* **2016**, *22*, 5924–5936.

[173] N. Kitajima, N. Tamura, H. Amagai, H. Fukui, K. Heerwegh, C. a Reed, C. R. Randall, L. Que, K. Tatsumi, *J. Am. Chem. Soc.* **1994**, *116*, 9071–9084.

[174] F. A. Chavez, R. Y. N. Ho, M. Pink, V. G. Young, S. V. Kryatov, E. V. Rybak-Akimova, H. Andres, E. Münck, L. Que, W. B. Tolman, *Angew. Chem. - Int. Ed.* **2002**, *41*, 149–152.

[175] A. M. Khenkin, M. Vedichi, L. J. W. Shimon, M. A. Cranswick, J. E. M. N. Klein, L. Que, R. Neumann, *Isr. J. Chem.* **2017**, *57*, 990–998.

[176] J. Sanders-Loehr, W. D. Wheeler, A. K. Shiemke, B. A. Averill, T. M. Loehr, *J. Am. Chem. Soc.* **1989**, *111*, 8084–8093.

[177] G. Xue, D. Wang, R. De Hont, A. T. Fiedler, X. Shan, E. Munck, L. Que, *Proc. Natl. Acad. Sci.* **2007**, *104*, 20713–20718.

[178] H. Zheng, Y. Zang, Y. Dong, V. G. Young, L. Que, *J. Am. Chem. Soc.* **1999**, *121*, 2226–2235.

[179] R. M. Wing, K. P. Callahan, *Inorg. Chem.* **1969**, *8*, 871–874.

[180] M. Lõkov, S. Tshepelevitsh, A. Heering, P. G. Plieger, R. Vianello, I. Leito, *Eur. J. Org. Chem.* **2017**, *30*, 4475–4489.

[181] L. Que, Jr., W. B. Tolman, L. Que Jr., W. B. Tolman, *ChemInform* **2010**, *33*, no-no.

[182] H. F. Hsu, Y. Dong, L. Shu, V. G. Young, L. Que, *J. Am. Chem. Soc.* **1999**, *121*, 5230–5237.

[183] A. J. Skulan, M. A. Hanson, H. F. Hsu, L. Que, E. I. Solomon, *J. Am. Chem. Soc.* **2003**, *125*, 7344–7356.

[184] Y. Zang, Y. Dong, L. Que, K. Kauffmann, E. Münck, *J. Am. Chem. Soc.* **1995**, *117*, 1169–1170.

[185] K. E. Kauffmann, C. V. Popescu, Y. Dong, J. D. Lipscomb, L. Que, E. Münck, *J. Am. Chem. Soc.* **1998**, *120*, 8739–8746.

[186] D. Lee, B. Pierce, C. Krebs, M. P. Hendrich, B. H. Huynh, S. J. Lippard, *J. Am. Chem. Soc.* **2002**, *124*, 3993–4007.

[187] S. Fukuzumi, K. Ohkubo, *Chem. - Eur. J.* **2000**, *6*, 4532–4535.

[188] S. Fukuzumi, K. Ohkubo, *J. Am. Chem. Soc.* **2002**, *124*, 10270–10271.

[189] M. Sankaralingam, Y. M. Lee, Y. Pineda-Galvan, D. G. Karmalkar, M. S. Seo, S. H. Jeon, Y. Pushkar, S. Fukuzumi, W. Nam, *J. Am. Chem. Soc.* **2019**, *141*, 1324–1336.

[190] F. Li, K. M. Van Heuvelen, K. K. Meier, E. Münck, L. Que, *J. Am. Chem. Soc.* **2013**, *135*, 10198–10201.

[191] Y. M. Lee, S. Bang, Y. M. Kim, J. Cho, S. Hong, T. Nomura, T. Ogura, O. Troeppner, I. Ivanović-Burmazović, R. Sarangi, S. Fukuzumi, W. Nam, *Chem. Sci.* **2013**, *4*, 3917–3923.

[192] S. Bang, Y. M. Lee, S. Hong, K. Bin Cho, Y. Nishida, M. S. Seo, R. Sarangi, S. Fukuzumi, W. Nam, *Nat. Chem.* **2014**, *6*, 934–940.

[193] A. L. Balch, *Inorganica Chim. Acta* **1992**, *198–200*, 297–307.

[194] M. Kodera, T. Tsuji, T. Yasunaga, Y. Kawahara, T. Hirano, Y. Hitomi, T. Nomura, T. Ogura, Y. Kobayashi, P. K. Sajith, Y. Shiota, K. Yoshizawa, *Chem. Sci.* **2014**, *5*, 2282–2292.

[195] L. V. Liu, S. Hong, J. Cho, W. Nam, E. I. Solomon, *J. Am. Chem. Soc.* **2013**, *135*, 3286–3299.

[196] J. Kaizer, M. Costas, L. Que, *Angew. Chem. - Int. Ed.* **2003**, *42*, 3671–3673.

[197] A. Mairata i Payeras, R. Y. N. Ho, M. Fujita, L. Que, *Chem. - Eur. J.* **2004**, *10*, 4944–4953.

[198] W. N. Oloo, K. K. Meier, Y. Wang, S. Shaik, E. Münck, L. Que, *Nat. Commun.* **2014**, *5*, 3046.

[199] B. J. Brazeau, J. D. Lipscomb, *Biochemistry* **2000**, *39*, 13503–13515.

[200] J. T. Groves, Y. Watanabe, *J. Am. Chem. Soc.* **1988**, *110*, 8443–8452.

[201] W. N. Oloo, A. J. Fielding, L. Que, *J. Am. Chem. Soc.* **2013**, *135*, 6438–6441.

[202] K. Yamaguchi, Y. Watanabe, I. Morishima, *J. Am. Chem. Soc.* **1993**, *115*, 4058–4065.

[203] J. A. Halfen, S. Mahapatra, E. C. Wilkinson, S. Kaderli, V. G. Young, L. Que, A. D. Zuberbühler, W. B. Tolman, *Science* **1996**, *271*, 1397–1400.

[204] J. Cahoy, P. L. Holland, W. B. Tolman, *Inorg. Chem.* **1999**, *38*, 2161–2168.

[205] M. Swart, *Chem. Phys. Lett.* **2013**, *580*, 166–171.

[206] M. Swart, M. Gruden, *Acc. Chem. Res.* **2016**, *49*, 2690–2697.

[207] H. Zheng, Y. Zang, Y. Dong, V. G. Young, L. Que, *J. Am. Chem. Soc.* **1999**, *121*, 2226–2235.

[208] Y. Honda, H. Arii, T. Okumura, A. Wada, Y. Funahashi, T. Ozawa, K. Jitsukawa, H. Masuda, *Bull. Chem. Soc. Jpn.* **2007**, *80*, 1288–1295.

[209] G. Xue, A. T. Fiedler, M. Martinho, E. Munck, L. Que, *Proc. Natl. Acad. Sci.* **2008**, *105*, 20615–20620.

[210] S. Kal, A. Draksharapu, L. Que, *J. Am. Chem. Soc.* **2018**, *140*, 5798–5804.

[211] J. D. Steen, S. Stepanovic, M. Parvizian, J. W. De Boer, R. Hage, J. Chen, M. Swart, M. Gruden, W. R. Browne, *Inorg. Chem.* **2019**, *58*, 14924–14930.

[212] A. International, *ASTM Int.* **2002**, *96*, 1–11.

[213] F. Menges, "'Spekwin32 – optical spectrscopy software', Version 1.72.1, 2016.," can be found under http://www.effemm2.de/spekwin/, **2016**.

[214] R. C. Reem, J. M. McCormick, D. E. Richardson, F. J. Devlin, P. J. Stephens, R. L. Musselman, E. I. Solomon, *J. Am. Chem. Soc.* **1989**, *111*, 4688–4704.

[215] S. V. Kryatov, E. V. Rybak-Akimova, V. L. MacMurdo, L. Que, *Inorg. Chem.* **2001**, *40*, 2220–2228.

[216] S. Banerjee, A. Draksharapu, P. M. Crossland, R. Fan, Y. Guo, M. Swart, L. Que, *J. Am. Chem. Soc.* **2020**, DOI 10.1021/jacs.9b12081.

[217] D. M. Jr, Kurtz, "Oxo- and hydroxo-bridged diiron complexes: a chemical perspective on a biological unit | Chemical Reviews," can be found under https://pubs.acs.org/doi/pdf/10.1021/cr00102a002, **n.d.**

[218] K. Wieghardt, *Angew. Chem. Int. Ed. Engl.* **1989**, *28*, 1153–1172.

[219] P. A. Goodson, A. R. Oki, J. Glerup, D. J. Hodgson, *J. Am. Chem. Soc.* **1990**, *112*, 6248–6254.

[220] J. Glerup, P. A. Goodson, A. Hazell, R. Hazell, D. J. Hodgson, C. J. McKenzie, K. Michelsen, U. Rychlewska, H. Toftlund, *Inorg. Chem.* **1994**, *33*, 4105–4111.

[221] S. Menage, L. Que, *Inorg. Chem.* **1990**, *29*, 4293–4297.

[222] Y. Zang, Y. Dong, L. Que, K. Kauffmann, E. Münck, *J. Am. Chem. Soc.* **1995**, *117*, 1169–1170.

[223] H. Zheng, Y. Zang, Y. Dong, V. G. Young, L. Que, *J. Am. Chem. Soc.* **1999**, *121*, 2226–2235.

[224] Y. Zang, G. Pan, L. Que, B. G. Fox, E. Munck, *J. Am. Chem. Soc.* **1994**, *116*, 3653–3654.

[225] Y. Dong, H. Fujii, M. P. Hendrich, R. A. Leising, G. Pan, C. R. Randall, E. C. Wilkinson, Y. Zang, L. Que, *J. Am. Chem. Soc.* **1995**, *117*, 2778–2792.

[226] W. Rasheed, PhD Thesis: Structural- and Spectroscopic-Reactivity Relationships of Nonheme Oxoiron(IV) Complexes, PhD Thesis, University of Minnesota—Twin Cities, Minneapolis, MN, **2019**.

[227] S. Banerjee, A. Draksharapu, P. M. Crossland, R. Fan, Y. Guo, M. Swart, L. Que, *J. Am. Chem. Soc.* **2020**, *142*, 4285–4297.

[228] “IsoPro 3.1,” can be found under https://sites.google.com/site/isoproms/, **2009**.

[229] M. S. Seo, N. H. Kim, K. B. Cho, J. E. So, S. K. Park, M. Clémancey, R. Garcia-Serres, J. M. Latour, S. Shaik, W. Nam, *Chem. Sci.* **2011**, *2*, 1039–1045.

[230] N. Y. Lee, D. Mandal, S. H. Bae, M. S. Seo, Y.-M. Lee, S. Shaik, K.-B. Cho, W. Nam, *Chem. Sci.* **2017**, *8*, 5460–5467.

[231] S. Kal, L. Que, *JBIC J. Biol. Inorg. Chem.* **2017**, *22*, 339–365.

[232] H. Hirao, D. Kumar, L. Que, S. Shaik, *J. Am. Chem. Soc.* **2006**, *128*, 8590–8606.

[233] P. Comba, D. Faltermeier, S. Krieg, B. Martin, G. Rajaraman, *Dalton Trans.* **2020**, *49*, 2888–2894.

[234] R. Banerjee, Y. Proshlyakov, J. D. Lipscomb, D. A. Proshlyakov, *Nature* **2015**, *518*, 431–434.

[235] R. Banerjee, J. C. Jones, J. D. Lipscomb, *Annu. Rev. Biochem.* **2019**, *88*, 409–431.

[236] G. E. Cutsail, R. Banerjee, A. Zhou, L. Que, J. D. Lipscomb, S. Debeer, *J. Am. Chem. Soc.* **2018**, *140*, 16807–16820.

[237] G. Xue, R. De Hont, E. Münck, L. Que, *Nat. Chem.* **2010**, *2*, 400–405.

[238] S. Hong, F. F. Pfaff, E. Kwon, Y. Wang, M.-S. Seo, E. Bill, K. Ray, W. Nam, *Angew. Chem. Int. Ed.* **2014**, *53*, 10403–10407.

[239] B. Wang, Y.-M. Lee, W.-Y. Tcho, S. Tussupbayev, S.-T. Kim, Y. Kim, M. S. Seo, K.-B. Cho, Y. Dede, B. C. Keegan, T. Ogura, S. H. Kim, T. Ohta, M.-H. Baik, K. Ray, J. Shearer, W. Nam, *Nat. Commun.* **2017**, *8*, 1–10.

[240] Y. Li, S. Handunneththige, E. R. Farquhar, Y. Guo, M. R. Talipov, F. Li, D. Wang, *J. Am. Chem. Soc.* **2019**, *141*, 20127–20136.

[241] M. Puri, A. N. Biswas, R. Fan, Y. Guo, L. Que, *J. Am. Chem. Soc.* **2016**, *138*, 2484–2487.

[242] A. N. Biswas, M. Puri, K. K. Meier, W. N. Oloo, G. T. Rohde, E. L. Bominaar, E. Münck, L. Que, *J. Am. Chem. Soc.* **2015**, *137*, 2428–2431.

[243] A. J. Jasniewski, L. M. Engstrom, V. V. Vu, M. H. Park, L. Que, *J. Biol. Inorg. Chem.* **2016**, *21*, 605–618.

[244] W.-M. Ching, A. Zhou, J. E. M. N. Klein, R. Fan, G. Knizia, C. J. Cramer, Y. Guo, L. Que, *Inorg. Chem.* **2017**, *56*, 11129–11140.

[245] V. Yadav, J. B. Gordon, M. A. Siegler, D. P. Goldberg, *J. Am. Chem. Soc.* **2019**, *141*, 10148–10153.

[246] M. J. Drummond, C. L. Ford, D. L. Gray, C. V. Popescu, A. R. Fout, *J. Am. Chem. Soc.* **2019**, *141*, 6639–6650.

[247] L. R. Widger, C. G. Davies, T. Yang, M. A. Siegler, O. Troeppner, G. N. L. Jameson, I. Ivanović-Burmazović, D. P. Goldberg, *J. Am. Chem. Soc.* **2014**, *136*, 2699–2702.

[248] X. Engelmann, D. D. Malik, T. Corona, K. Warm, E. R. Farquhar, M. Swart, W. Nam, K. Ray, *Angew. Chem. Int. Ed.* **2019**, *58*, 4012–4016.

[249] H. Zheng, S. J. Yoo, E. Münck, L. Que, *J. Am. Chem. Soc.* **2000**, *122*, 3789–3790.